UNIVERSITÉ LAVAL

Gasification Reactions of Carbon Anodes; Multi Scale Reaction Model

Thèse

Mohammad Kavand

Doctorat en génie des matériaux et de la métallurgie
Philosophiæ doctor (Ph. D.)

Québec, Canada

Gasification Reactions of Carbon Anodes; Multi Scale Reaction Model

Thesis

Mohammad Kavand

Under the direction of:

Houshang Alamdari, Supervisor

Faïçal Larachi, Co-Supervisor

Réactions de gazéification des anodes de carbone ; modèle de réaction multi-échelle

Thesis Ph.D.

Mohammad Kavand

Resume

La réactivité des anodes de carbone avec le CO_2 est l'une des principales préoccupations des alumineries utilisant le procédé Hall-Héroult. Une telle réactivité n'est pas souhaitable car elle augmente la consommation nette de carbone et raccourcit ainsi la durée de vie des anodes. La surconsommation d'anode est affectée par la réactivité intrinsèque de l'anode et les phénomènes de transport de masse.

Différents modèles mathématiques du processus de gazéification ont été développés pour différentes géométries et techniques :

La première partie de ce travail se concentre sur la gazéification d'une seule particule d'anode de carbone avec du CO_2, en utilisant un modèle de réaction-transport détaillé, basé sur la cinétique intrinsèque de la réaction et le transport des espèces gazeuses. Le modèle comprend les équations de conservation de la masse pour les composants gazeux et les particules solides de carbone, ce qui donne un ensemble d'équations différentielles partielles non linéaires, résolues à l'aide de techniques numériques. Le modèle peut prédire le taux de génération de gaz, les compositions de gaz et le taux de consommation de carbone pendant la gazéification d'une particule de carbone. Différents modèles cinétiques ont été comparés pour décrire le comportement de gazéification des particules de carbone. Il a été constaté que le modèle de

pores aléatoires (RPM) fournissait la meilleure description de la réactivité des particules d'anode. Le modèle a également prédit le retrait des particules pendant le processus de gazéification. Le modèle a été validé à l'aide de résultats expérimentaux obtenus avec différentes gammes de tailles de particules. Un bon accord entre les résultats du modèle et les données expérimentales a montré que cette approche pouvait quantifier avec succès la cinétique de gazéification et la distribution du gaz au sein de la particule anodique. De plus, le modèle Langmuir-Hinshelwood (L-H) est utilisé afin de capturer l'effet d'inhibition du monoxyde de carbone sur la réaction de gazéification.

Dans la deuxième partie, la simulation du processus de gazéification de l'anode avec du CO_2, en tant que lit de particules d'anode a été considérée. Le modèle numérique de la méthode des éléments discrets CFD multi-échelles (DEM) a été développé sur la base d'un concept eulérien-lagrangien. Le modèle comprend une méthode des éléments finis eulériens (FEM) pour le gaz et les particules solides, et un DEM lagrangien pour la phase particulaire, cette dernière visant à capturer l'effet de retrait des particules (mouvement des particules lors de la gazéification). Les propriétés physiques des particules, telles que la porosité et la surface spécifique, et les propriétés thermochimiques des particules, telles que la chaleur de réaction, sont finalement suivies. Les changements géométriques des particules, le transfert de chaleur et de masse, le retrait des particules et les réactions chimiques sont pris en compte lors de la gazéification de l'anode avec du CO_2. Les profils dynamiques de concentration et de température du réactif et des gaz produits ainsi que la conversion solide ont été modélisés à la fois dans les vides entre les particules et les pores à l'intérieur de chaque particule. Pour valider le modèle, des tests expérimentaux ont été réalisés à l'aide d'un lit de particules anodiques.

Dans la dernière partie, une simulation d'une dalle d'anode a été réalisée. Le modèle contient la masse et les équations de transfert de chaleur pour les composants gazeux et les particules solides de carbone, ce qui donne un ensemble d'équations différentielles partielles non linéaires, résolues à l'aide de techniques numériques. Le modèle peut prédire le taux de génération de gaz, les compositions de gaz et le taux de consommation de carbone, la chute

de pression et la distribution de température pendant la gazéification d'une particule de carbone.

Mots clés: anode, réactivité, modèle multi-échelle, porosité, phénomènes de transport de masse; rétrécissement; CFD; DEM; FEM.

Gasification Reactions of Carbon Anodes; Multi Scale Reaction Model,

Thesis Ph.D.

Mohammad Kavand

Abstract

The reactivity of carbon anodes with CO_2 is one of the main concerns in aluminum smelters using the Hall-Héroult process. Such reactivity is not desirable because it increases the net carbon consumption and thus shortens the lifetime of the anodes. Anode overconsumption is affected by anode intrinsic reactivity and mass transport phenomena.

Different mathematic models of the gasification process were developed for different geometries and technics:

The first part of this work focuses on the gasification of a single carbon-anode particle with CO_2, using a detailed reaction-transport model, based on the reaction intrinsic kinetics and transport of gaseous species. The model includes the mass conservation equations for the gas components and solid carbon particles, resulting in a set of nonlinear partial differential equations, being solved using numerical techniques. The model may predict the gas generation rate, the gas composition, and the carbon consumption rate during the gasification of a carbon particle. Various kinetic models were compared to describe the gasification behavior of carbon particles. It was found that the Random pore model (RPM) provided the best description of the reactivity of anode particles. The model also predicted the particle

shrinkage during the gasification process. The model was validated using experimental results obtained with different particle size ranges. Good agreement between the model results and the experimental data showed that this approach could quantify with success the gasification kinetics and the gas distribution within the anode particle. In addition, the Langmuir-Hinshelwood (L-H) model is used in order to capture the inhibition effect of carbon monoxide on the gasification reaction.

In the second part, the simulation of the gasification process of anode with CO_2, as an anode particle bed, was considered. Numerical multiscale CFD-discrete element method (DEM) model was developed based on an Eulerian-Lagrangian concept. The model includes an Eulerian finite element method (FEM) for the gas and solid particles, and a Lagrangian DEM for the particle phase, the latter intending to capture the particle shrinkage effect (movement of particles during gasification). The physical properties of particles, such as porosity and specific surface area, and the thermochemical properties of particles, such as the heat of reaction, are ultimately tracked. Geometric changes in particles, heat and mass transfer, particle shrinkage and chemical reactions are considered during anode gasification with CO_2. The dynamic concentration and temperature profiles of the reactant and product gases as well as the solid conversion were modeled both in the voids between the particles and the pores inside each particle. To validate the model, experimental tests were performed using a bed of anode particles.

In the last part, a simulation of the anode slab was carried out. The model contains the mass, and heat transfer equations for the gas components and solid carbon particles, resulting in a set of nonlinear partial differential equations, which are solved using numerical techniques. The model can predict the gas generation rate, gas compositions, and carbon consumption rate, pressure drop, and temperature distribution during the gasification of an anode slab.

Key Words: Anode, Reactivity, Multi-scale model, Porosity, mass transport phenomena; shrinkage; CFD; DEM; FEM

Table of Content

Page

List of Tables

Page

List of Figures

Page

List of Abbreviations

Fixed bed Reactor: FBR

Pseudo-empirical approach: PEA

Rigorous approach: RA

Combined approach: CA

Thermo gravimetric analyzer: TGA

Finite element method: FEM

Discrete element method: DEM

Critical pore size: CPS

Computational fluid dynamics: CFD

Volumetric model: VM

Shrinking core model: CM

Random pore model: RPM

Modified random pore model: MRPM

Traditional model: TM

Partial differential equations: PDEs

Ordinary differential equations: ODEs

Langmuir-Hinshelwood: L-H

Two-fluid model: TFM

Dedication

Dedicated to my parents, sisters, and brother

Acknowledgments

I have worked with a large number of people throughout my Ph.D. program, without whose kind support, I would not have been able to finish the present work. I would like to express my words of thanks here to some of them. Mention some of them here.

First and foremost, my deep and sincere gratitude would go to my thesis director, Professor Houshang Alamdari, for his confidence in me by giving me the opportunity to be part of his group and conduct this project. I would also like to sincerely thank my co-director, Professor Faïçal Larachi, for the insights, support, and valuable comments he provided me with over the years culminating in the present thesis.

I would like to extend my gratitude to my co-director in Alcoa, Dr. Donald Ziegler, for his insights and support and to Dr. Roozbeh Mollaabbassi for the insightful discussions he had with me all along with this project.

My thanks would also go to Alcoa, Natural Sciences and Engineering Research Council of Canada (NSERC), and Fonds de Recherche du Québec-Nature et Technologies (FRQ-NT) for the financial support they provided through the intermediary of the Aluminum Research Centre – REGAL.

I wish to thank Donald Picardand Guillaume Gauvin for their constant help and guidance and their time to this project. My Special thanks to my friends and colleagues Francois Chevarin, Ramzi Ishak, and Asem Hussein for their kind support and professional suggestions concerning this project.

Last but certainly not least, I express my heartful gratitude to my parents, sisters, and brother for all their love, support, and encouragement to help me fulfill my dream.

Preface

This doctoral thesis is written as a ‘thesis by articles’ consisting of four chapters. It begins with the introduction, which includes the statement of the problem and the research objectives. Chapter 1 includes a presentation of the effective parameters in the gasification process and a review of the different models proposed so far as well as the literature on the main topics related to this research. Chapters 2 and 3 attend to the research results, presented as two published research papers (see below) in scientific journals. Appendix A deals explicitly with the results of the anode slap simulation. Appendix B is included supplementary information and also some corrections related to chapter 3. Each chapter ends with its own list of references. The thesis concludes with a conclusion and suggestions for further research. The articles that makeup two chapters of this doctoral thesis are:

1. (presented as Chapter 2): "Reaction-diffusion model for gasification of shrinking single carbon-anode particle.” Mohammad Kavand (main author), Roozbeh Mollaabbasi, Donald Ziegler, Faïçal Larachi, Donald Picard, Houshang Alamdari (corresponding author) (Omega ACS-accepted)

2. (presented as Chapter 3). “Multi-scale CFD-DEM Model for Gasification Reactions of Carbon Anode.” Mohammad Kavand (main and corresponding author) (Fuel-accepted)

Introduction

History

Aluminum is one of the metals found abundantly on the earth's surface. This metal is light, has a good thermal and electrical conductivity, and is resistant to corrosion by forming a thin, invisible protective layer of aluminum oxide on its surface [1, 2]. This layer is formed spontaneously upon contact with air or pure water at room temperature [1, 3]. Due to such qualities, aluminum is used in many fields such as the shipping industry, air transport, road transport, and packaging of edible products, to name just a few.

As can be seen in the world map below (Figure I), according to the current statistics provided by Mannweiler Consulting, aluminum production was almost doubled over 10 years (i.e., from 2010 to 2020), rising from 40 to 70 million tonnes a year. During this period, China was constantly the world's largest producer, and countries of North America countries gave up their second place to those from the Middle East and Russia.

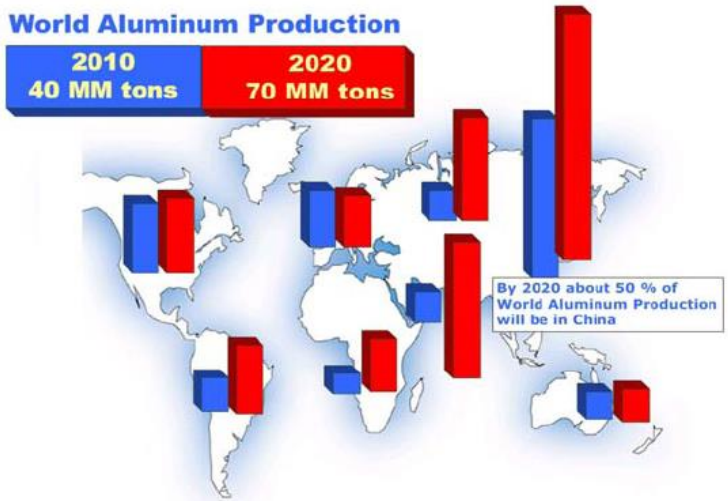

Figure I. The world map of aluminum production [4]

Figure II shows alumina refinery and smelters in Canada. Canada's primary aluminum production in 2019 was estimated at 2.85 million tonnes. One alumina refinery is located in Quebec. Also located in this province are 10 aluminum smelters (on 9 sites), with the Alouette facility in Sept-Îles being the largest, capable of producing as many as 602,000 tonnes per year. There is also another smelter is in British Columbia (on one site) [5].

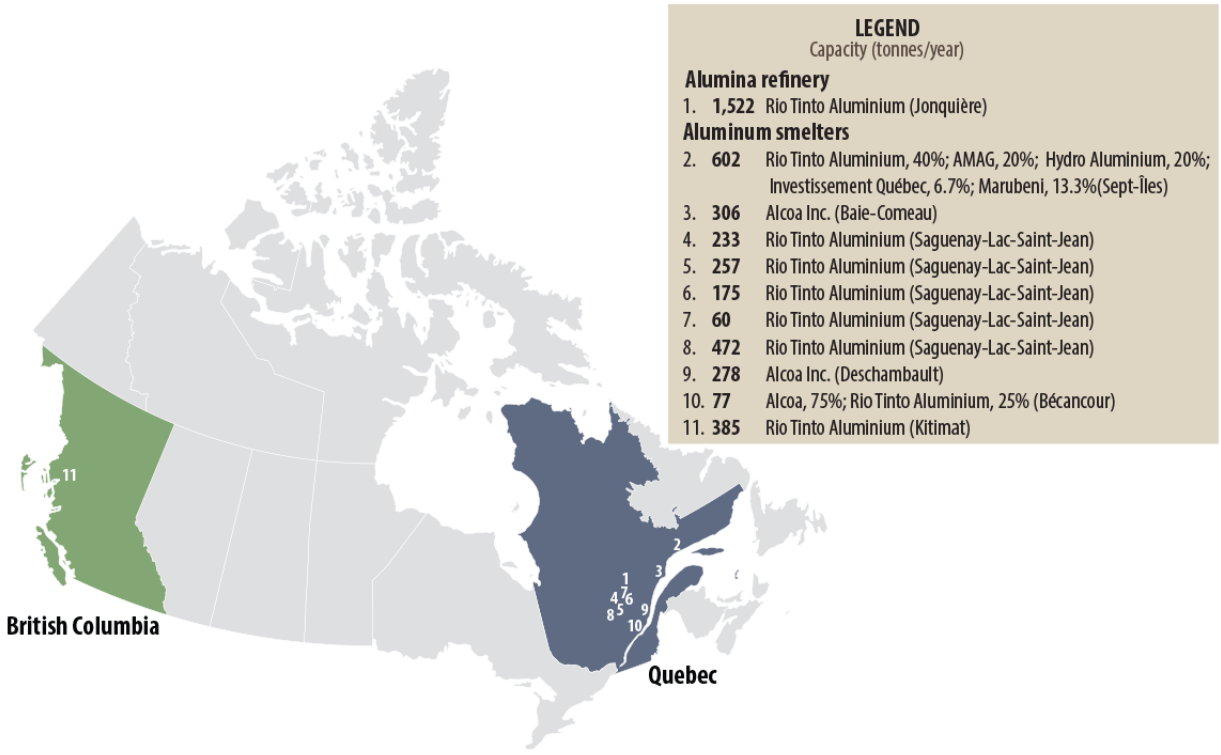

Figure II. Canadian aluminum refinery and smelters' estimated capacity [5]

A common process involved in aluminum production is the Hall-Héroult. As far back as 1886, Paul (Louis-Toussaint) Héroult discovered in France the cryolite bath technology associated with electrolysis to dissolve alumina in oxygen and metallic aluminum. In the same year, Charles Martin Hall independently invented at United States the same technology. Industrial exploitation of this discovery began in 1889 in France and the United States.

In the electrolytic cell, the temperature of the cryolite bath is approximately 960 °C. The addition of certain salts lowers the temperature of the melting point of cryolite, which is about 1010 °C and allows the dissolution of alumina. It is a chemical compound that occurs naturally in Greenland [6-8]. With its limited quantities and high extraction price, this natural compound has been replaced by an artificial mixture of sodium, aluminum, and calcium fluorides [3]. To obtain 1 ton of aluminum, 2 tons of alumina [approximately 4 to 5 tons of bauxite is required for 2 tons of alumina], half a ton of anode, and 13 MWh of electrical energy are needed [9]. Figure III illustrates the Hall-Héroult technology, which is a fundamental part of obtaining commercially pure aluminum. A carbon-containing electrolysis cell is fed by alumina, with the electrolysis reaction that takes place being as follows [9]:

$$2\ Al_2O_3\ (diss) + 3\ C\ (s) \rightarrow 4\ Al\ (m) + 3\ CO_2\ (g), \qquad (I)$$

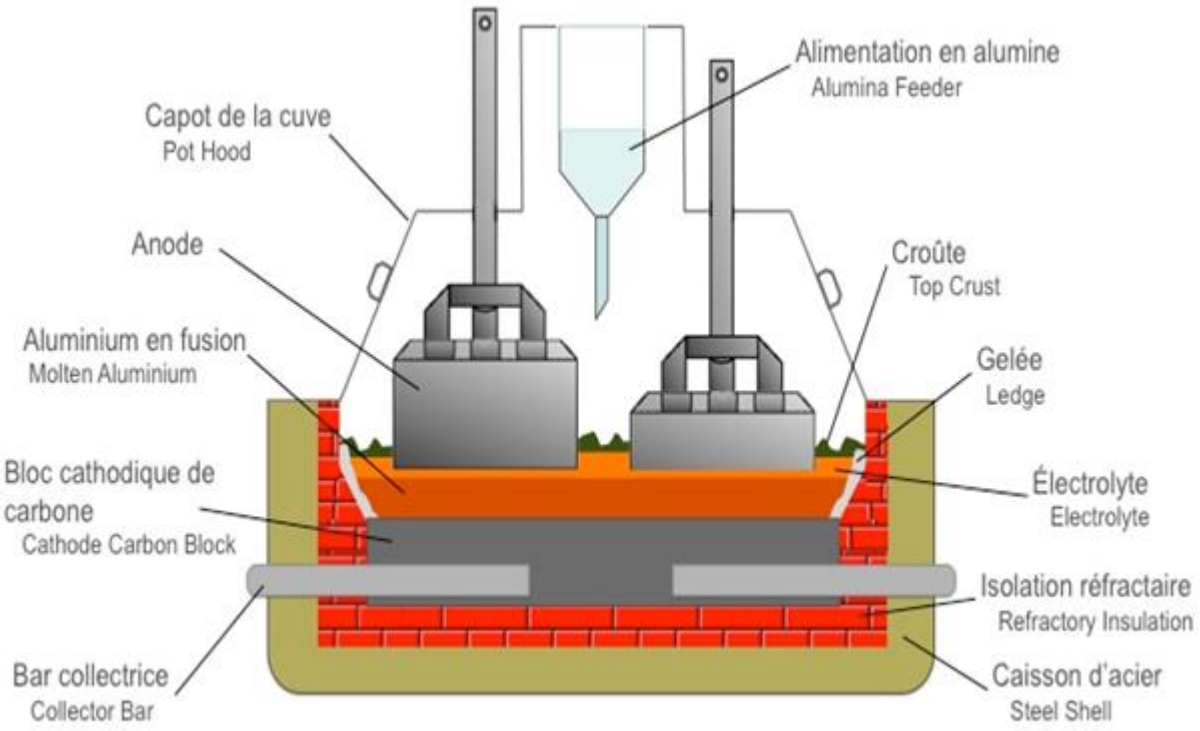

Figure III. Schematic representation of aluminum electrolysis cell with anodes [10]

The cells contain carbon anodes and cathodes, and the electrolysis leads to aluminum production in the Hall-Herault cell. The cathode placed at the bottom of the electrolysis cell is made of anthracite or graphite and a pitch as a binder. Cathodes are classified under 3 categories: semi-graphitized, graphitic, and graphitized. The graphitized coke is heat-treated between 2400 and 3000°C, while the semi-graphitic and graphitic coke are calcined at around 1200 °C before being crushed and sieved. These aggregates are then mixed with coal-tar pitch, extruded, and baked. Carbon cathodes require a good electrical conductivity and high resistance to wear. The required components for the production of anodes are petroleum coke (60-70 wt.%), coal tar pitch (14-17 wt.%), and anode scrap (15-20 wt.%). The filler is the coal-tar pitch, which serves to fill the void between the solid petroleum coke particles.

The process of chemical reactions consumes approximately 75% of the anodes. The rest stem from the reactions occurring between the anode with either air above the cell or carbon dioxide produced in electrolysis reactions. This surplus of anode consumption markedly pertains to process economics.

‘Dusting’ is one of the implications that happens as the carbon anode reacts with CO_2. This occurs as the mechanical dislodging of particulate carbon, which is loosened by the reaction during the cell’s normal operation, and the particulates drop into the electrolyte. Dust formation is thought to occur due to preferential oxidation of the more reactive pitch coke, allowing for the disintegration of the rest of the anode structure for which the pitch coke acts as the glue [11, 12].

Solid carbon is oxidized to carbon dioxide gas at the carbon anodes, which is then released into the atmosphere. At the carbon cathode, aluminum ions are reduced to elemental aluminum. More dense liquid aluminum sinks to the vessel's bottom, where it can be siphoned off periodically in a process called tapping. The consumption of carbon anode Follows the process and lasts almost 25 days in the pot. Consequently, a new anode should replace it. Once one-third to one-fourth of anode's original size has been consumed, the residual anode is removed, crushed, and recycled as raw material to produce new anodes [13, 14].

Statement of the Problem

Multiple drawbacks still exist in aluminum industries, including pollutant emissions, high-energy consumption, and carbon anode overconsumption. In general, the sum of the following contributes to the anode consumption:

- Electrochemically forming carbon dioxide,
- Electrochemically forming carbon monoxide,
- The carboxy reaction (Boudouard),
- Air burn, and
- Preferential oxidation yielding dusting [15].

Equation II represents the alumina-to-aluminum electrolytic conversion of theoretical carbon consumption. In addition to the main reaction, a number of side reactions may occur in this process, which is listed in Table I. Because of the reoxidation reaction, current efficiency loss is taken into consideration Based on electrolytic carbon loss [15];

$$2Al + 3CO_2 \rightarrow Al_2O_3 + 3CO \qquad (II)$$

Generated carbon monoxide mass makes up 7.1 % of CO_2 mass during this process. The reaction of the anode with air to produce CO_2 possibly occurs in addition to electrolytic reactions. As these reactions lead to increased net carbon consumption, they are undesirable [16, 17]. The theoretical carbon consumption for aluminum electrolysis is 0.334 kg per kg of Al produced. However, since the cell efficiency is usually less than 100 %, the real electrolytic consumption of carbon is around 0.41 kg per kg of Al produced. Keller et al. [18] reported that the extra cost associated with the overconsumption of one kg of anode per one tonne of produced aluminum is around $2 US. The overconsumption of a midsize smelter (producing 300,000 tonnes of aluminum and requiring 150,000 anodes per year) is approximately 40 kg per anode. Therefore, the estimated extra cost could amount to $12 million US per year [17, 18]. The oxidation of carbon with oxygen in the air is the basis of the air reactivity:

$$C\,(s) + O_2\,(g) \rightarrow CO_2(g), \qquad (III)$$

and

$2C\ (s) + O_2\ (g) \rightarrow 2CO(g).$ (IV)

The electrochemical reaction at the anode bottom generates CO_2 molecules, which react with the anode surface. This inevitable reaction is called ”Boudouard” [16], is impossible to prevent and is represented by Equation V. Furthermore, CO_2 diffusion may occur through the porous structure, a process responsible for the consumption of the anode’s interior:

$C\ (s) + CO_2\ (g) \leftrightarrows 2CO\ (g).$ (V)

A gas bubble layer existing beneath the carbon anode bottom surface impedes the reaction of CO_2 with the anode carbon [11]. However, the diffusion of CO_2 through the anode takes place while afterward reacting at a chemically active surface; CO is generated as a result [19, 20]. Therefore, the chemical reaction and the mass transport play a significant role in the anode mass loss.

Table I. Carbon anode consumption [15]

Mechanism	Anode consumption, mass %
Basic reaction:	66 to 76
$2Al_2O_3 + 3C \rightarrow 4Al + 3CO_2$	
Excess consumption:	8 to 15
$C + O_2 \rightarrow CO_2$	
and	
$2C + O_2 \rightarrow 2CO$	
CO_2 burning:	5 to 6
$CO_2 + C \leftrightarrow 2CO$	
Unreacted dust	0.3
Re-oxidation of metal	7 to 8
Pyrolysis and vaporization	0.2
Sulphu, impurities and carbon loss	3.5 to 4.5
Net Carbon consomption [kg C/t Al]	400 to 450

Hypothesis and Objectives

With a very long history of the Hall-Héroult process (over 125 years), the experience of specialists in aluminum production makes it possible to rely on formulate the following hypothesis:

The overall reactivity of carbonaceous materials is controlled by weighting the effect of the chemical reaction and the mass transport phenomenon on the reactivity of the anode to CO_2 at 960 ° C. It will be possible to identify the most significant criterion in the overall reactivity of anodes to increase the latter's service life. This weighting is fundamental for the manufacture and baking of carbon anodes because it would make it possible to produce anodes with physicochemical properties, which would promote low reactivity or, on the contrary, in the case of an increase, to minimize the effects. This assessment could make it possible to model CO_2 gasification with emphasis on chemical reaction and mass transfer phenomenon and the structural parameters as key effective factors on the mass transfer and the chemical reaction.

A lot of research has been carried out on how to decrease the excess carbon consumption caused by gasification through oxidation and CO_2 as well as dusting. Except for improving the anode structure, cell design, and operation, it is also essential to comprehend the gasification mechanisms appropriately.

In order to decrease the overall reactivity of the anodes, the study of their physicochemical characteristics has been the subject of much research. However, since these studies were primarily based on determining the overall reactivity of the anodes based on their properties, they did not selectively determine the essential parameter controlling this reactivity.

The principal objective of this study is to conduct and build a comprehensive model of the CO_2 gasification of carbon anode in the Hall-Hearoult process. The gasification modeling of the anode has been studied in three geometries; single-particle, bed of particles, and real anode slab. By estimating the weighting of these two factors (chemical reaction and mass transfer), we should be able to identify the structural parameters influencing the overall reactivity. As a result, this project will improve our understanding of the reactivity of anodes

to CO2 through its scientific approach, adapted reactivity tests, and adequate samples representative of the industry while reducing the environmental impact of the Hall-Héroult process.

The second objective of the model is to examine the structural parameters affecting the overall reactivity and monitor changes in these parameters during the process. Through the use of the model, the user will be able to observe the various structural parameters throughout the experiment, including the porosity of micro and macro scales, permeability, particle size, and specific surface area in the passing direction of each particle.

Finally, the distribution of operating parameters in solid and gas phases such as gas concentrations, chemical reaction rate, solid conversion, pressure drop, velocity, and temperature are other objectives of this works.

Thesis outline

Since anode gasification is studied in various geometries and requires different approaches to solve, the thesis outline can be divided into the following parts:

1. The development of a method that makes it possible to solve a non-catalytic gas-solid reaction of a single particle based on the reaction intrinsic kinetics and transport of gaseous species. The model will include the mass conservation equations for the gas components and solid carbon particles, resulting in a set of partial differential equations using numerical techniques. The model will predict the gas generation rate, the gas compositions, and the carbon consumption rate during the gasification of a carbon particle.

2. As the real process is to be carried out on an industrial scale, the determination of reactivity using lab devices has limitations. Employing a lab-scale fixed-bed reactor overcomes many of the drawbacks associated with these devices. A multi-scale model

with non-catalytic reaction was developed to investigate fixed-bed reactors and apply a new approach to consider solid structural changes during gasification. In this method, the solid particles were considered a discrete part, and the flow in the space between the particles was considered a continuum phase. The Eulerian finite-element method (FEM) served as the basis for the proposed mathematical method to model the fluid phase. Besides, the discrete element method (DEM) was applied to model the anode particles' dynamics.

3. And finally, the simulation of anode slab in unsteady, non-isothermal conditions will be studied. The model includes the finite element method (FEM) for the gas and solid phases. The solid phase's physical properties, including porosity and specific surface area, and the thermochemical properties of particles, such as the heat of reaction, are ultimately tracked. Geometric changes in the anode slab, heat and mass transfer, and chemical reactions are considered during anode gasification with CO_2. The dynamic concentration and temperature profiles of the anode will be modeled.

References

1. Kelly, T.D. and G.R. Matos, *Historical Statistics for Mineral and Material Commodities in the United States*, in *Copper statistics*, N.M.I. Center, Editor. 2015, U.S. Geological Survey Data Series 140. p. 4.
2. Azari, K., *Investigation of the materials and paste relationships to improve forming process and anode quality*, in *Material and Metallurgy Department* 2013, Laval Uinversity: Canada.
3. MacKenzie, D.S.T., G.E., *Handbook of Aluminum: Vol. 1: Physical Metallurgy and Processes (1st ed.).* 2003.
4. Consulting, M. *Sourcing Anodes as a Production Option: A Viable and Economic Alternative with Proven Sucess*. in *15th World Aluminium Conference*. 2010. Oslo, Sweden.
5. *Aluminum facts*. 2019; Available from: https://www.nrcan.gc.ca/our-natural-resources/minerals-mining/minerals-metals-facts/aluminum-facts/20510.
6 Flem Peltier, B. Eline., *Heats in Cryolite Melts with Alumina*, 1996, Universitetet I Trondheim, Ph.D. dissertation, Norway
7. Azari, K., et al., *Compaction properties of carbon materials used for prebaked anodes in aluminum production plants.* Powder Technology, 2013. **246**(C): p. 650-657.
8. Azari, K., et al., *Influence of coke particle characteristics on the compaction properties of carbon paste material.* Powder Technology, 2014. **257**: p. 132-140.

9. Azari, K., *Investigation of the materials and paste relationships to improve forming process and anode quality*. 2013, Laval Uinversity: Canada.
10. http://mace3.fsg.ulaval.ca/
11. Sadler, B.A. and S.H. Algie. *Porosimetric study of sub-surface carboxy oxidation in anodes*. in *TMS Annual Meeting*. 1991. New Orleans, LA, USA.
12. Ziegler, D.P., *Sub-surface carbon dioxide reaction in anodes,* in *Light Metals 2011*. 2011, Springer. p. 901-906.
13. HOUSTON, G. and H. Øye, *Carbon losses caused by gaseous oxidation during aluminium electrolysis. Pt. 2.* Aluminium (Düsseldorf), 1985. **61**(8): p. 589-591.
14. Engvoll, M.A., H.A. Oye, and M. Srlie. *Gas reactivity inside industrial anodes*. in *TMS*. 2002. Seattle, WA, USA.
15. B.A, S., *An investigation into reducing the consumption of carbonaceous anodes during aluminium electrolysis* in *Department of Mining and Metallurgical Engineering*. 1989, University of Queensland: Saint Lucia.
16. Azari, K., *Investigation of the materials and paste relationships to improve forming process and anode quality*, in *Material and Metallogy Department* 2013, Ph.D. dissertation, Laval Uinversity: Canada.
17. Chevarin, F., et al., *Active pore sizes during the CO_2 gasification of carbon anode at 960°C.* Fuel, 2016. **178**: p. 93-102.
18. Keller, F., U. Mannweiler, and E. Knall, *Anode for the aluminum industry*. Constructing and Operating Anode Plants: What Top Management Needs to Know; R & D Carbon Ltd.: Sierre, Switzerland, 1995: p. 217-224.
19. Mani, T., N. Mahinpey, and P. Murugan, *Reaction kinetics and mass transfer studies of biomass char gasification with CO_2.* Chemical Engineering Science, 2011. **66**(1): p. 36-41.
20. Chevarin, F., et al., *Characterization of carbon anode constituents under CO_2 gasification: A try to understand the dusting phenomenon.* Fuel, 2015. **156**: p. 198-210.

Chapter 1

Literature review

This section provides a general view of the gasification process by looking at the literature on this phenomenon. It also presents definitions of the parameters that can affect CO_2 gasification of carbon anode.

1.1 Gasification Mechanism

The mechanism of gasification starts with the thermochemical degradation of the anode to CO_2. Carbon gasification reactions are sensitive to the effects of mass transfer. Below, a list of processes that can affect control the gasification rate [1]:

1. Gaseous reactants diffusion-induced mass transfer from the bulk gas phase to the surface of carbon;
2. Reactant adsorption on the carbon surface;
3. Chemical rearrangements (reactions) on the surface and the mobility and formation of adsorbed products;
4. Desorption of products; and
5. Diffusion induced mass transport of the gaseous reaction product(s) distancing from the surface of the carbon.

Both process parameters and carbon properties play a significant role in the gasification process. The former mostly affects the temperature of the reaction, pressure, and particle size, and the latter principally impact porosity, presence of catalytic impurities, and active impurities site concentration.

1.1.1 Gasification reaction rate

The intrinsic rate of gasification reaction' is the function of three variables: the temperature, the bulk gas' concentration, and the activated reaction surface. Generally, the product of these three - parameters are addressed in the formulation of kinetic models for heterogeneous reactions' intrinsic rates [2],

$$R=k(T)f(C)S(X) \quad (1.1)$$

in which, f(C) represents the gas concentration effect on the reaction rate. Several models have been perused to detail the CO_2 gasification kinetics. In the next chapter (Table), these models are summarized. The volumetric reaction model, the shrinking core model, the modified volumetric model, and the random pore model have been extensively used by researchers.

The next function, S, the specific reactive surface area, which is related to the structural evolution of the particles during the gasification, defines the change in the geometrical property of the anode particle as the gasification proceeds. Different models have been proposed in the literature for the function of S. For instance, the random pore model(RPM) assumes that the pore structure of porous particles consists of cylindrical channels having different sizes and that the reaction takes place on the wall surfaces. According to this model, the relationship between the internal surface area of a particle and its porosity can be shown by [3, 4]:

$$S(X) = S_0(1-X)\sqrt{1-\psi\, ln(1-X)}, \quad (1.2)$$

where S_0 is the initial surface area, ψ is a dimensionless parameter indicating the nature of pore structure (i.e., RPM structural parameter [5],

$$\psi = \frac{4\pi L_0(1-\varepsilon_0)}{S_0^2}, \quad (1.3)$$

where L_0, ε_0 and S_0 represent the total pore length per unit volume, the initial porosity, and initial surface area ($m^2.kg^{-1}$), respectively.

The Arrhenius equation could compute the constant rate k. The following relationship can use the rate constant to evaluate the activation energy [6]:

$$k(T) = k_0 e^{\frac{-E_a}{RT}} \tag{1.4}$$

where, E_a indicates the apparent activation energy (J/mol), T and R are the reaction temperature (K) and the gas constant (8.314 J/ (mol K)), respectively.

Plotting the logarithmic reaction rate as a function of the reciprocal temperature (idealized Arrhenius plots) may visualize the process's activation energy (E). This plot can be used to describe the effect of temperature on the reactivity of porous anode materials (Figure 1.1). The effect of temperature on the reactivity of carbon anode particles has been studied by several researchers [7]. The temperature scale is split into three zones in terms of multiple rate-specifying steps. The curve-slope (d log (rate)/d (1/T)) in each zone is tantamount to the rate-determining process's activation energy. The chemical reaction rate drops at low temperatures (zone 1) while chemically controlling the gasification rate over the entire available carbon surface.

Furthermore, the reactant gas concentration uniformly distributes across the bulk carbon sample and sets to the concentration of the bulk gas phase (C_b). In this zone, the activation energy measured is identical to the actual chemical activation energy ($E_{obs} = E_A$). Pore diffusion partly controls the gasification rate at intermediate temperatures (zone 2). At some point in the pore system, the gaseous reactant concentration remains zero with the apparent activation energy less than that of zone 1 ($E_{obs} = 0.5 \cdot (E_A + E_D)$, E_D = diffusion activation energy). High temperatures are accompanied by very high chemical reaction rates in zone 3, while the bulk gas to the carbon surface is limited in the bulk diffusion rate. A gas concentration gradient is gradually amassed on the surface, and the apparent activation energy equalizes the diffusion's activation energy (E_D) [8].

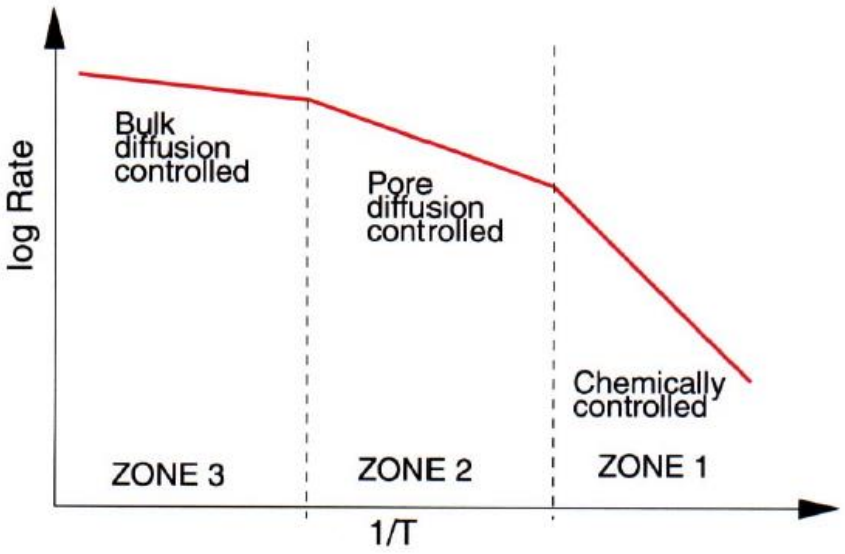

Figure 1.1. A porous carbon's gasification reaction rate as a function of temperature [1]

1.1.2 Internal and external gasification

The anode's total gasification can be split into two internal and external parts. The internal gasification includes solid particles' consumption within the porosity. In contrast, the external part is defined by the consumption of carbon in both particles' external surface and the surface-linked very large pores. The critical pore size (CPS) is utilized to distinguish between types of gasification. As the gasification reaction progresses from steps X_1 to X_2 (owing to the internal reaction), the enlargement of smaller pores (than CPS) is observed antithetical to the entire shrinkage of particles caused by the external reaction. The particle's external surface is used to measure open larger-than-CPS pores (Figure 1.2) [9]. Increased external surface with gasification progress demonstrates that the particles' external surface is directly related to reaction Progression. To explain this fact, two parameters should be considered. First, the particles shrink as gasification progresses, leading to an increase in the particle volume ratio of the external surface. Secondly, as pores become larger near the external surface, the CPS is violated, they are regarded as external surfaces, and therefore, the external contribution increases.

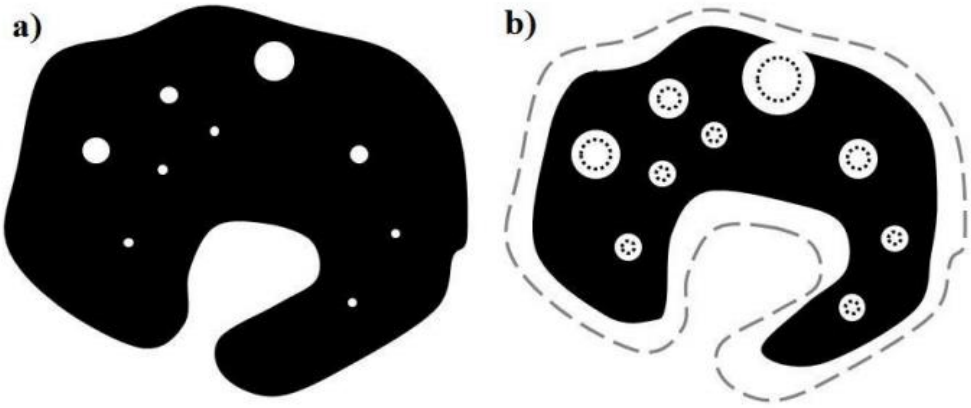

Figure 1.2. Schematic demonstration of the anode particle gasification under CO_2 at 960 °C: a) the anode particle at the initial state, X_1; b) Gasification percentage-consumed anode particle, X_2 [9]

The particles' external surface and the open pores with entrance diameters greater than the critical size are primarily responsible for CO_2 reaction. Determined by F. Chavarin et al. [9], the critical pore size ranges from 20 to 40 microns. As the particle size increases, the contribution of the internal reaction gradually decreases. The small ratio of the internal reaction to anode particles' total gasification is attributed to the significance of mass transport constraints in the fine pores. The pores greater than the critical size can be more conveniently eschewed from decreasing the anodes' CO_2 reaction. In addition, the CO_2 gasification is influenced by the mass transport inside the anode pores, leading both chemical reaction and mass transport to be seen as paramount in this phenomenon.

1.2 Reactivity's Effective Parameters

The limitations of chemical reactivity and mass transport mainly influence carbon materials' reactivity. The chemical reactivity is chiefly affected by graphitization and impurity, while the mass transport phenomena are impressed more by gas concentration gradient (diffusion) and pressure gradient (convection) [1, 10].

1.2.1 Chemical reactivity

1.2.1.1 Graphitization

Graphitization (L_C) and reactivity are specifically related to each other. A rise in graphitization lets the ratio of graphene's edge carbon atoms decrease versus carbon atoms' global quantity. Carbon graphitization decreases the air, and CO_2 reactivity as the edge carbon atoms continue to be highly reactive compared to graphene's plane carbon atoms. Larger graphite crystals with a higher crystallite height (Lc) value exhibit less reactivity with respect to air and CO_2. This is due to the decrease in the total number of accessible surface active sites, which are essentially located at the edge of the graphite crystallite. [7]. Lavigne and Castonguay [11] related the L_C of calcined coke to its reactivity. The authors concluded that the higher the L_C is, the lower the reactivity towards CO_2 (Figure 1.3).

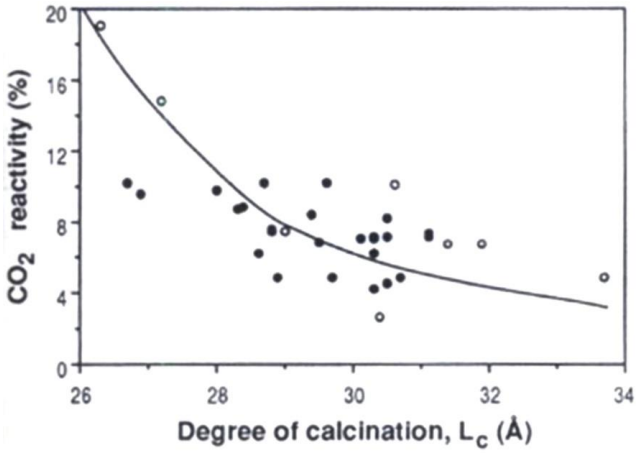

Figure 1.3 Effects of degree of calcination on CO_2 reactivity [12].

1.2.1.2 Level of impurities

The effects of several impurities on the CO_2 and O_2 reactivity of carbon have been determined by several researchers [13, 14]. The presence of impurities in the raw materials used to

manufacture the anodes or those contained in the electrolysis bath can vary the kinetics of the Boudouard reaction. They classified Si, Fe, V, Ni, Na, Ca, Pb, Cu, Cr, Ti, and Al into the group of carbon-O_2 reaction catalysts. Except for Si, Zn, Cr, and Ti, these compounds catalytically affect the carbon-CO_2 reaction. On the other hand, inactive complexes formed by sulfur cause a drop in the gasification rate. In addition to sulfur, boron, aluminum fluoride, and phosphor have been reported to behave as deterrents to either C-O_2 or C-CO_2 reactions.

1.2.2 Mass Transfer Mechanisms

To evaluate the reactivity of carbonaceous materials in this project, the global and intrinsic reactivities were studied. It will be seen that the overall reactivity of the anodes is controlled by the chemical reaction and by the transport of gases in the anode. Therefore, the assessment of mass transport is essential in understanding overall responsiveness.

In aluminum smelters, carbon anodes are identified by many analytical techniques (mechanical tests, levels of impurities, etc.). The reactivity of the anodes in the air or CO_2 is also evaluated. The reactivity of anodes is defined as the loss of mass caused by the attack of air and CO_2 on the anode for a defined period and at a given temperature[13, 15, 16]. These mass losses are in the form of gas as well as coal in the electrolysis tanks.

A better understanding of the phenomena would allow more efficient interaction with the industrial process to reduce the overconsumption of raw materials generated by the reactivity between the gases and carbon. Understanding these reactivities is, therefore, a major objective for the industry. The two groups of reactions for the reactivity of the anodes are chemical reactions for reactivity in air and CO_2, in the top and bottom of the anode, respectively [13, 15-17].

Determining the type of regime controlling the kinetics of these reactions is essential because it makes it possible to understand the overall reactivity of the anodes. The anode gasification reactions are sensitive to mass-transfer effects. A schematic illustration of the gasification

rate is provided in Figure 1.4. It may take place through physical and chemical processes from the bulk gas phase to the carbon surface.

Determination of the gas flow in-situ in the anodes: In the literature, several hypotheses are proposed to determine the flow types that control the overall reactivity of the anodes in the electrolytic cells. Below, the reasoning for the cases of O_2 and CO_2 is summarized.

In the case of O_2: According to Bonal [18], the overall air reactivity of carbon anode at 550 °C and the atmospheric pressure is controlled by chemical reactions and gas diffusion simultaneously. As a result of calculating the mean free path of O_2 between 400 °C and 600 °C at atmospheric pressure, the transport in the anode is caused by sliding flow. Therefore, two opposite conclusions are reached for the O_2 flux in the carbonaceous material.

In the case of CO_2: In the same way, there appears to be disagreement over the transport of CO_2 in anodes at high temperatures. Sadler [19] argues that the overall reactivity of the anode to CO_2 is controlled by the chemical reaction and by a viscous CO_2 flow regime dependent on the anode's permeability. Sadler justifies this hypothesis by setting up a manipulation allowing the anode to react on only one side. This one-dimensional attack brings closer to industrial scale, measures the depth of gasification, and relates mass transport to overall responsiveness. He thus measures the impact of convective transport on the total mass loss of the sample by the end of the test. This technique allows Sadler to semi-quantitatively correlate the loss of mass in the form of CO as a function of the initial permeability of the sample. However, according to the author, if the mass loss is correlated with permeability, mass transport is controlled by convective gas transport.

Conversely, Ziegler [20] suggests that the permeability of the gas through the anode (that is, the gas moving under a convective flow) plays no role in the reactivity of the anodes to CO_2. He proposes that it is the diffusion that controls the kinetics of the Boudouard reaction in the material. The Boudouard reaction causes a CO_2 molecule and a carbon atom to react to give two CO molecules. At the initial carbon site, a deficit in CO_2 concentration is created between the surface of the anode (saturated with CO_2) and the reaction site (in the pores). Fick's first law, therefore, governs this concentration gradient. As a result, CO_2 is supplied by diffusion. There is then a transport of molecules step by step. Diffusion, however, is not controlled by

permeability, which impedes the reasoning and results of Sadler's manipulation. Ziegler justifies the inconsistency of the reactivity/permeability relationship because permeability is related to bulk density in an exponential (and a nonlinear) form [21]. However, it is known that the bulk density is related to the reactivity in a linear fashion. Therefore, the linear Reactivity/Permeability relationship is considered to be only incidental. Oliveira [22] corroborates Ziegler's conclusion on the control of diffusion mass transport for carbonaceous materials. This author has studied the phenomena involved in the reactivity to CO_2 at 1000 ° C at atmospheric pressure for two metallurgical coke scales; a piece of coke (wafer) and a bed of coke. Experimental measurement and simulation show that platelets with a maximum thickness of 6 mm would make it possible to neglect the effects of gas transport in the kinetics of the reaction, which would then be controlled only by the chemical reaction. In contrast, for the coke bed, the overall kinetics are affected by both the chemical reaction and gas diffusion. Oliviera [22] considers the presence of a concentration gradient, which develops throughout the coke bed, and the grain size, which imposes resistance to the internal diffusion of the reactive gas, to be the cause of this double phenomenon.

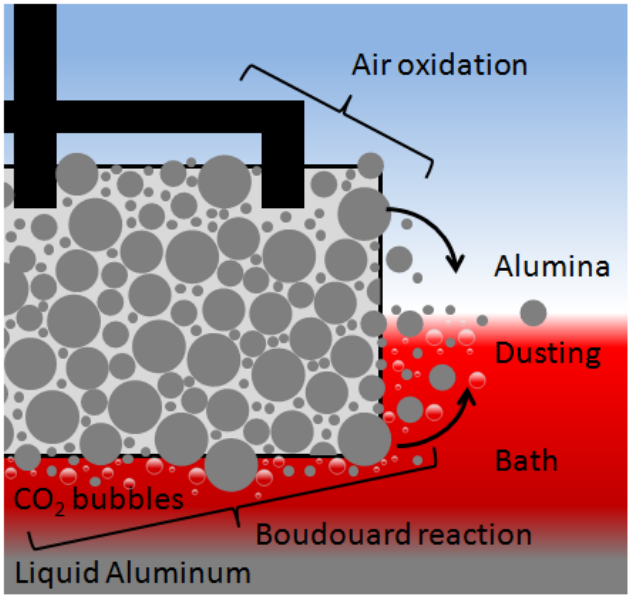

Figure 1.4 Schematic of an anode slab under CO_2 and O_2 reactivity in bottom and top, respectively [15].

1.2.2.1 Pressure gradient and convection

Convection is defined as mass transport caused by a bulk fluid motion. Proportional to the fluid velocity u, the convective flux vector behaves in the same direction as this velocity does. The following cases list the physics interfaces for Porous Media Flow [23, 24];

- Navier Stokes: Free flow
- Brinkman equation: Fast flow in porous media
- Richard's equation: changeably saturated porous media
- Darcy's law: Slow flow in porous media
- Fracture Flow: Flow in line with surfaces

Depending on the size of the pores involved, both Darcy's law and Brinkman's extension can model flow in the porous media. Because of the slow flow in porous media (where fluid velocities are small), the inertial forces in the momentum conservation equation are negligible compared to forces for the body and viscous forces in Darcy's law [23]. The Brinkman equations can be applied if the pores' size is large enough for the fluid to impose momentum variations through shear impacts. Sadler and Algie [17] showed that CO_2 mass transport flow passing via the anode pore structure remained mainly viscous and imputed to the anode permeability. In another study, Engvall [25] approved that the majority of the pores they observed in industrial anodes had a size of at least 5 μm and that gas permeability, including the viscous flow, could control the main transport. In this way, Darcy's law models the convective velocity [9].

Porous material permeability (K) determines how readily a fluid will cross its pore space as long as an external driving force exists. A critical property is permeability to define the porous sample's flow capacity, and Darcy, who noted linearly increasing flow rate with applied pressure gradient in a set of fluid flow experiments via a packed gravel bed, notably defined it. The following relationship represents Darcy's equation based on this observation [24],

$$u = -\frac{\beta}{\mu L}\nabla P \qquad (1.5)$$

In this formula, β is permeability, which is independent of the nature of the fluid, but which depends on the geometry of the medium. It has dimensions (length)^2. P is pressure, μ is dynamic viscosity (Pa.s).

In general, for simple structures, the correlation between permeability and specific surface area could be established. This correlation was initially intended to employ the Kozeny-Carman relationship, equation 1.6, between two parameters to exclude one of them from the model [20].

$$\beta = \frac{196.\varepsilon^3}{S^2(1-\varepsilon)^2} \quad (1.6)$$

In this equation, S (m^2.kg^{-1}) and ε (-) represent the specific surface area and porosity, respectively.

1.2.2.2.Concentration gradient and diffusion

Diffusion is defined as the movement of molecules from a high-concentration zone to a low-concentration zone. Diffusion's distinctive characteristic is its mixing or mass transport, irrespective of the bulk motion (bulk flow). The (diagonal) Fick diffusion is an approximation of Maxwell-Stefan diffusion and only coincides with it when the molar masses and the binary diffusivities of the component gases are identical [26]. Here are the two equations:

Fick equation: $J = -C_t D_{ij} \nabla x$ (1.7)

Maxwell-Stefan equation: $J = -\sum_{j \neq i}^{n} \frac{x_j N_i - x_i N_j}{C_t D_{ij}}$ (1.8)

Where J_i is the diffusion flux vector of the ith species, D_{ij} is diffusion constant, the index i denotes the ith species, and C is the concentration (mol/m^3).

The effective diffusion coefficient in the porous statement differs from the actual one. This results from the fact that diffusion's possible cross-section is more limited than that of the existing fluid, as well as from the fact that the lag between one point and the other in the

porous body continues to be lower than the path a molecule needs to travel between these points (as the molecule must travel between the material's solid portions). Therefore, the real concentration gradient becomes smaller than the apparent one. E. Putri et al. applied the effective diffusion coefficient to measure the CO_2 diffusion coefficient. Multiplication of the diffusion coefficient by a tortuosity ($\tau > 1$) formulates this effect into Fick's first law [26]:

$$D_e = \frac{\varepsilon . D_{ij}}{\tau} \tag{1.9}$$

where ε is the particle porosity (-), τ is torousity (-), D_e is effective diffusion coefficient constant ($m^2 \cdot s^{-1}$), and D_{ij} ($m^2 \cdot s^{-1}$) is diffusion coefficient constant, the

Once path-free molecular mean gets much larger than the pore diameter within which the diffusing molecules are present, the collision of molecules with the wall becomes more prevalent than with other molecules. This phenomenon has been dubbed Knudsen diffusion, D_k, which assumes relations of the cylindrical pore, and is expressed as follows [10];

$$D_k = \frac{d_p}{3} \sqrt{\frac{8 R_g T}{\pi M_w}} \tag{1.10}$$

where d_p is the pore diameter (m), R_g is the gas constant ($J \cdot kMol^{-1} \cdot K^{-1}$), T is the temperature (K), and M_w is the molecular weight ($kg \cdot Kmol^{-1}$).

In general, the Knudsen diffusion becomes more prominent at small pressures and low pore diameters. If competition between Knudsen diffusion and molecular diffusion happens through a "resistances in series" approach, the total diffusivity can be expressed as [27]:

$$D^t = \frac{1}{1/D_m + 1/D_k} \tag{1.11}$$

where D^t is the total diffusivity measured in the experiment; D_m is the apparent molecular coefficient, which depends on intermolecular collisions; and D_k is the Knudsen coefficient, which depends on collisions with the pore walls. Therefore, the effective diffusion coefficient is computed by [27]:

$$D_e^t = (\frac{\varepsilon}{\tau})D^t \quad (1.12)$$

Researchers have found that the CO_2 flow in the anode pores is related to pore size. Using mercury porosimetry, Sadler [17] determined that viscous flow could start with pores larger than 40 mm in size. This was based on the pore size being significantly greater than the mean free path of CO_2 molecules, which is 0.44 μm at 960 °C and 1.05 atm [28]. Sadler and Algie [29] determined that CO_2 mass transport through the anode pore structure was predominantly a viscous flow and hence related to the anode permeability. In the current study, as CO_2 molecules' path-free mean equals 0.44 μm at a temperature of 960 °C under 1.05 atm, the pore size was far smaller than the average (20 μm). As a result, the Knudsen diffusion is supported [9].

1.2.3 Effect of pore size of the anode

When the dominant pore size of the anode is between 5 and 50 μm and with the average free path of around 0.5 μm for CO_2, the slippery flow will dominate the gas transport in the anodes. However, it should be considered that in pores smaller than 0.1 μm, the diffusion of gases would partially control the overall reactivity. Such pore sizes are present throughout the anode. Finally, the gas viscous flow controls the overall reactivity of the anodes in large pores (> 100 μm). These pores are present on the surface of the anode. They are formed during the gasification of the anode. This reaction causes the pores to enlarge. However, permeability is influenced by pores with sizes greater than 50 μm [30]. This means that the overall reactivity kinetics are controlled by permeability only at the surface and at a very shallow depth of the material.

1.2.4 Effect of porosity on reactivity

The porosity of carbon anodes also has an impact on their reactivity with CO_2. It can be determined by reference to the specific surface, the pores' size distribution, the real and apparent densities, the tortuosity, and the permeability.

1.2.5 Effect of particle size

Particle size is one of the most important factors that determine the apparent reactivity of porous carbon materials. There may also be closed pores within large particles apart from the concentration gradient within their pores that affect their reaction rate. During the reaction, the closed pores may open, creating new specific surface areas. The comparison between the reaction rates observed with and without limitation of mass transport makes it possible to demonstrate the retarding effect of mass transport on the overall reactivity of carbonaceous material[9].

Kovacik et al. [31] evaluated (Using thermogravimetric analyser (TGA), at 900 °C and under CO_2) the mass transport occurring during the gasification of carbon particles whose size varied between 0.074 and 2.4 mm. They revealed that mass transport had a significant effect when the particle size was larger than 0.1mm. F. Chavarin et al. [9] measured the mass loss of anode particles at 960 °C under CO_2 (Figure 1.5); they demonstrated that the percentage of gasification increased with an increase in reaction time a decrease in particle size.

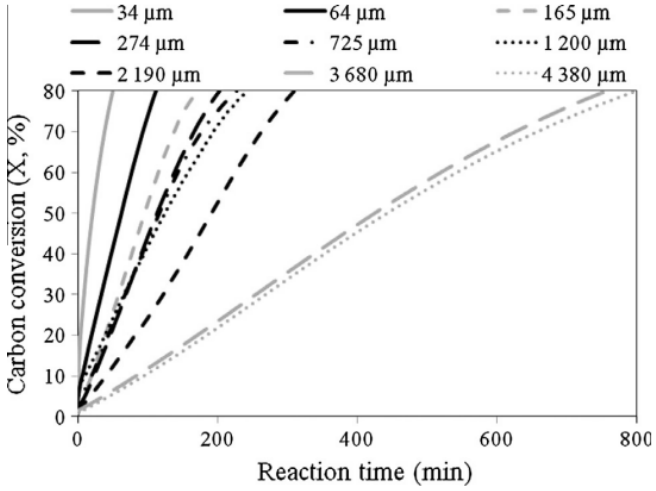

Figure 1.5 Experimental anode particle conversion versus reaction time under CO_2 flow at 960 °C, done using TGA[9]

1.3 CO_2 gasification models of Carbon Anodes

Although several experimental studies have been done on anode gasification of the Hall-Heroult process, only a little research has been done on modeling the reactivity of the process. The models proposed for a single particle and bed of particles for CO_2 gasification of porous materials are summarized here.

Several process variables, including particle size, the anode's mineral content, anode porosity, temperature, and partial pressure of the gasifying reactant and products, influence anode's gasification rate in a gasifier, many of which carry a complex effect on the process. A few remarkable studies have been published on the gasification of carbon anodes on the aluminum electrolysis cell. Therefore, one of the original points of the present study is developing a mathematical model for the gasification of porous materials in aluminum electrolysis cells based on modifications and updates of previous work. A series of simplifications led to a more tractable model, representing the key factor affecting the gasification of the anode particles.

1.3.1 Single-particle model

Determination of macro kinetic data is not feasible under entire conditions that could dominate a fixed bed [32]. To this end, as a single anode particle's conversion process is described, spatial discretization becomes necessary. Many process variables affect the anode's gasification rate, such as particle size, char porosity, mineral content, temperature, and partial pressure. Several of these variables have complicated effects on the process. In practice, therefore, several simplifications are used to attain a more tractable expression rate. In the case of diffusional films and intraparticle mass- and heat-transfer processes that are not rapid enough, the actual gasification rate will differ from the intrinsic one. As a result, the overall gasification rate of particles is determined by combining intrinsic chemical reactions with intraparticle and external diffusion rates[22, 33].

A one-dimensional transient model is used to project each particle's conversion process to compromise computation time and description precision. Two models are available to solve the reaction-diffusion equation inside the anode particle: the structural and the volumetric models. The structural models account for the changes in the structure of carbon during the process. Throughout the reaction, the internal pore structure changes over time [27, 34-42]. Conversely, in the volumetric models, experimental correlations are used to consider the porous structural changes [4, 33, 34, 39, 43-45]. In this latter approach, the problem is addressed by feeding the model with mechanical properties or other experimental data. These models explicitly refer to the solid microstructure changes during the reaction and the influence of the microstructure evolution on reactivity. Despite the changes in the structure, the particle size during the process remains invariant. The literature abounds with simplified techniques to circumvent mathematical and computational difficulties. Jamshidi and Ale Ebrahim [46-48] developed a semi-analytical, semi-numerical method, the Quantize Method (QM), with simplified assumptions. Their model leads to acceptable results based on the experimental data, though without mentioning the effect of solid structural changes on the solid volume. Thus, the particle radius remained fixed during the gasification, which does not correctly represent the real gasification conditions.

In a non-catalytic carbon-CO_2 reaction, it is essential to consider the solid structural changes as the reaction progresses since the reaction rate is a function of both gas and solid concentrations [33-35]. From a mathematical point of view, this aspect leads to integrating the gas-solid conservation equations into the model, which will increase the complexity of the problem. Researchers have extensively studied the computational aspects of single-particle models. Still, only limited research data is available on single-particle reactions that pay heed to gas-solid conservation equations [34-37, 39]. It is therefore essential to develop models for such practical systems. An accurate model for a particle reaction could generate valuable insights into modeling the whole anode reaction.

For cases in which gas and carbon material are reacted, several equations can Represent the reaction. The shrinking core models are based on removing the external particle with the time that is named exposed shrinking-core model (SCM). The external core surface just examines the external mass transfer and intrinsic kinetics [49]. In addition, the particles' external surface hosts their reaction with gas reactants. Then the interior is occupied step by step, contributing to a layer formation in their reacted covering and simultaneously an un-reacted core which has been formed in the inside. At the same time, the unreacted core radius decreases by progressing the gasification reaction. A semi-empirical model, the modified volumetric model (MVM), has been modified by adding a new parameter. In the Random Pore Model (RPM), it is assumed that the pore structure of porous particles consists of cylindrical channels having different sizes and that the reaction takes place on the wall surfaces [2, 13, 25, 49-52]. Main structural reaction models for gasification rate are presented in chapter 2.

In this study, we attempted to reduce the gap between theory and experiment by providing a model that considers diffusion and pore growth during the reaction of an anode particle. Throughout the gasification process, the anode particles are consumed, and the apparent radius of the carbon anode decreases gradually while the porosity of the particle increases. Hence, the effect of shrinkage and particle porosity is considered in the mathematical modeling. To this end, suitable numerical methods were implemented in the mathematical model to solve the governing transfer equations. First, the intrinsic kinetics of CO_2 gasification was experimentally investigated by using thermogravimetric analysis. Then, a

global reaction model was developed by considering all the above-mentioned aspects. The suitability of the existing structural reaction models for our global reaction model was examined. For more details on modeling, various models incorporating more structural parameters and complicated chemical reactions will be discussed in chapter 2. The kinetic parameters result of the single-particle model will be applied at the next step for the bed of particle model.

1.3.2 Bed of particles model

One of the main criteria for the evaluation of any mathematical model is its mathematical feasibility. On the one hand, a model must explicitly include as many relevant physical-chemical processes as possible. On the other hand, more detailed models involve more complicated differential equations and, consequently, are computationally more demanding. Needless to say, the first step to take is determining the level of details captured by the model in terms of the presence of accurate kinetic expressions and model parameters. However, the model's applicability has also to be considered, as it can be limited by the difficulties associated with its mathematical handling.

The gas entering the solid phase from the bottom of the anode has two paths: moving up among particles and penetrating them. Figure 1.6.a shows the slices in the middle of the anode. The light gray points are anode particles, which are surrounded by the binder. Figure 1.6.b illustrates the zoom-in of one carbon particle and its encircled area. The impacts of different microstructural scales are considered by several models, such as the ones defining reactions in particles' beds [53-59]. The compliance of such a model with anodes may be employed for anode modeling through the structure simplification by taking a bed of particles into account. In this study, the porosity within the particle demonstrates the small pores, while the voids between the particles indicate the large pores (Figure 1.7).

Furthermore, the active particle sites have the potential to allow the reaction to happen. Such a reaction would indicate a robust function of particles' temperature and species partial pressures, which are influenced by the flow patterns transported into the reactor. In such a

manner, the multi-scale base particle modeling of continuous bed reactors, which represent the most widely used for heterogeneous reactions, requires an improvement in perception and design [53-57, 59-61].

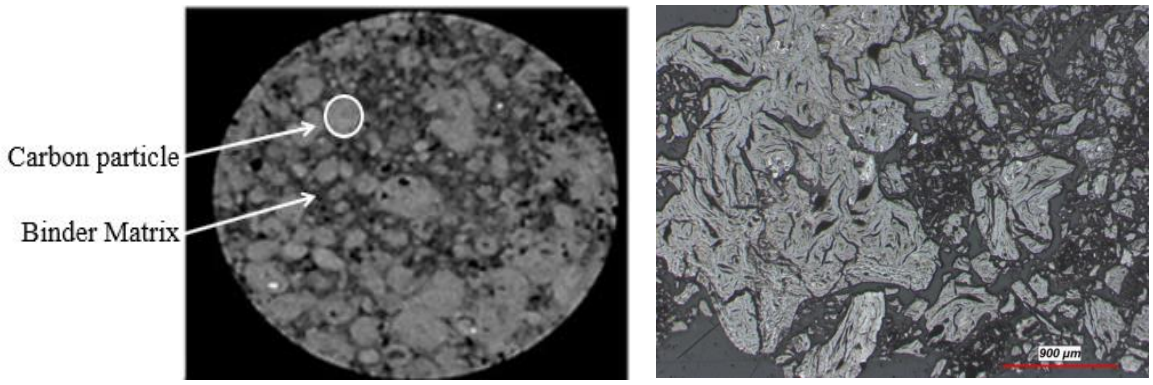

a) b)

Figure 1.6 a) Global image; Slices in the middle of an anode (CT with the voxel resolution of 0.15 × 0.15 × 0.6 mm^3); b) zoom in one carbon particle and its surrounded area [62]

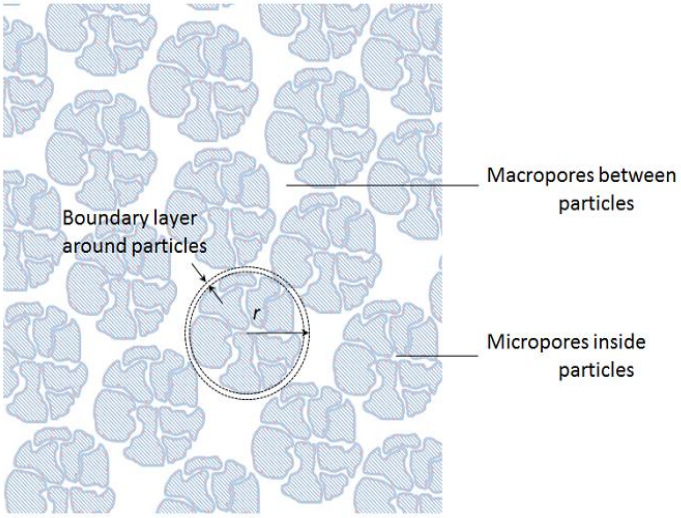

Figure 1.7 Macro and micropores between and inside the particle [63].

1.3.3 Strategies used to include the particle model in the bed of particles

The sophistication of a model depends on its assumptions and, consequently, on how various phenomena are incorporated into it. Numerous surveys have covered steady-state models and

simulations of fixed bed reactors. For example, Froment [64] and Hofmann and Hlavacek [65, 66] have proposed a general classification of the fixed bed reactor. Two of these are presented below.

1. *Pseudo-HomogeneousAapproach (PHA)*: The pseudo-homogeneous incorporation comes into the model by integrating the properties of the solid (particles) and fluid (exhaust gas) into a single governing equation while assuming a negligible pressure drop. This approach assumes that the solid surface is completely exposed to the bulk fluid conditions when there are no resistances between the particles and fluid [65, 66]. The high level of uncertainty associated with FB gasifier models benefiting this approach springs from the lack of records about how physical effects influence either the lab-specified reactivity or the gasifier conditions.
2. *Heterogeneous Approach (HA)*: On the other hand, heterogeneous models take conservation equations for the two phases into account separately [64]. The reactivity is acquired free from diffusional impacts at a laboratory base. When the reactor is modeled, the reactivity is applied in-situ at any position within an anode particle. To assess the anode particle's overall gasification rate, formulating a kinetic-particle model follows the overall reactor model. Although the method is a rigorous one, it is computationally too complicated. Therefore, this method is theoretically preferred when diffusional effects are likely to exist [65, 66].

1.3.3.1 Pseudo-Homogeneous Approach (PEA)

Due to its simplified assumptions of single-phase equations, which incorporate effective properties for fluid and solid phases, the pseudo-homogeneous model is most commonly used to design packed bed reactors. This model assumes that the solid surface is completely exposed to the bulk fluid conditions that there are no resistances between the particles and the fluid. A pseudo-homogenous condition assumes that chemical reaction occurs at the particle's surface and not within the particle. When pore diffusion is not rate-limiting in particle systems, pseudo-homogeneous conditions can be accepted as accurate [64]. Most

studies have used a pseudo-homogeneous one-dimensional model, which only considers the plug flow in the axial direction.

In one-dimensional models, resistance to heat and mass transfer in the radial direction is omitted, and the temperature and conversion rates are predicted to be uniform. In the case of reactions that involve a pronounced heat effect, this is a simplification. The design of such reactors must be directed toward avoiding adverse over-temperature on the axis by using a model that predicts the detailed temperatures and conversion patterns in the reactor. Two-dimensional models have thus been proposed. The flux of mass or heat in the radial direction is modeled using the effective transport concept in these models.

A summary of the paramount FB biomass gasifier models that have been published from the early 1980s to date is presented in Table 1.1. The table shows that an intrinsic kinetic approach has been broadly applied to model the anode particles' gasification in FB gasifiers. Occasionally, the treatment given to the anode gasification reactions has not been transparently specified (or justified) [67-71]. Application of kinetic reactivity of coal as biomass systems are modeled typical [67, 72, 73]. For instance, Petersen and Werther [85, 86] have applied the L-H kinetics achieved by Matsui et al. [74-76] for coal chars to model the sewage sludge char gasification in a CFB[77].

Harriott et al. [91] introduced a simple model for estimating gasification by injecting lime slurry into a series of boilers fired with coal. Lee and Koon [92] examined the reaction at low temperatures. Using a sharp interface model, they perused the impact of temperature, relative humidity, and O_2 concentration on a packed bed reactor's breakthrough curves. Wu et al. [78] proposed an experimental method to solve the problem of incomplete conversion in the gasification reaction. The problem pertained to pore mouth blockage was settled, and in this way, the complete conversion was acquired.

Srinivasan [79] developed a one-dimensional pseudo-homogeneous packed bed reactor to investigate the reduced reaction of nitric oxide with carbon monoxide over rhodium-alumina and platinum-alumina catalysts. The results demonstrated that conversion characteristics depend on the diffusion and thermal conductivity models but that the choice of a specific

model does not largely influence the conversion profiles because of the similar effective transport values.

Table 1.1 Selected FB gasifier models for Pseudo-empirical approach

	Solid material	T (K)	Remarks
[80]	catalyst pellet	300-900	Bubbling fluidized-bed reactors (BFBR) for solid-catalyzed gas (diff-conv-reaction model)
[81]	Oxidation	700-1400	Continuum Model of an Unsteady State Fixed Bed Reactor for Lean CH_4 Oxidation
[82]	coked Cr-Mg catalyst	533-673	regeneration of coked Cr-Mg catalyst in fixed bed reactors
[83]	Coal	973-1273	coal pyrolysis in fixed bed reactor
[84]	different pellet	500-800	2D flow fields in a fixed-bed reactor
[85]		300-453	Dynamic experiments in a nonadiabatic packed bed to evaluate wall temperature and inlet airflow rate
[86]	catalyst pellet	273-973	existing physical phenomena in the catalyst along with the corresponding numerical models
[87]	Peat, sawdust	1100-1200	Atmospheric and pressurized BFB
[27]	Biomass char	600-800	Kinetic-diffusion using FBR
[88]	Black liquor	760-820	Three-phase fluid dynamic model, simulate commercial BFB
[89]	Wood Miscanthus	1036-1160	FB conversion of coal and biomass Fuel sizes between 0.17- 1.89 mm
[90]	Biomass	1173-1273	Gasification in bubbling and circulating fluidized bed
[91]	Woody Biomass fuel	1025-1175	Gasification of biomass, applying empirical factor in reactivity

1.3.3.2 Heterogenous approach in the bed of particle

The heterogeneous models can Explain massive and exciting results, including mass and heat transfer distributions and velocity profiles during gasification. The heterogeneous approaches consider temperature and concentration differences between the fluid bulk and catalyst surfaces [64-66].

The first aspect to consider for heterogeneous models is the generation of representative geometry. This can be achieved by scanning an original sample, creating a regular arrangement, or generating a bed structure synthetically. The second step involves the use of discretization since the Navier-Stokes equations must be solved iteratively. A mesh or a number of grid points is generated based on a numerical method. As the next step, chemical reactions must be coupled with the flow field, species concentrations, temperature distribution, and chemical kinetics. The last step in the workflow is to analyze and extract the data and visualize the results. There are challenges associated with each of those steps that have to be overcome. Many of them are addressed in the following sections [64-66].

Ziarati et al. [92] extended their works on CO_2 gasification of char by a rigorous heterogeneous approach. This method includes an Eulerian-Lagrangian method for solid and fluid phases. Particle tracking is another interesting result that a rigorous approach can obtain.

Several researchers have studied the affinity between the local heat and flow flux in a bed of spheres [54, 56, 92-97]. They have employed a simulation approach based on the Eulerian–Eulerian approach for investigating the fluid flow and heat transfer mechanisms in fixed-bed reactors (Table 1.1). In general, the early field-associated practices on modeling are imputed to the fluid flow and heat transfer in gas-solid, two-phase, and fixed-bed reactors.

Subagjo et al. [81] studied the application of lean methane oxidation using pseudo-homogeneous and heterogeneous models, both for mass and heat balances. The result showed that the pseudo-homogeneous model in a temperature profile was similar to the temperature profile of the heterogeneous model when operated under a steady state. Conversely, in an unsteady state, the difference between the pseudo-homogeneous and heterogeneous models of the heat balance ranged from 23% to 38%.

Table 1.2 Selected FB gasifier models Based on the heterogeneous approach

Reference	scale	Particle-reactor Model	Solid material	T (K)	Remarks
[97]	Multi- scale	Eulerian-Eulerian	Coal-biomass	900-1100	multiphase interactions of soft solid bodies in fluids
[98]	Multi- scale	Eulerian-Lagrangian	Char	973-1181	formulation, implementation of multiphase flows
[99]	Multi- scale	Eulerian-Eulerian	Charcoal	650-800	Pressure drop and fluid flow in a packed pebble bed reactor Oxygen gasification
[3]	Multi- scale	Eulerian-Eulerian	coal and biomass blend chars	1100-1373	kinetics and producer gas compositions of steam gasification
[87]	Multi- scale	Eulerian-Eulerian	Peat, sawdust	1100-1300	hydrodynamics of fine particles deposition in packed-bed reactors
[93]	Multi- scale	Eulerian-Eulerian	Agricultural Waste	1000-1050	CFD modeling of gas flow in porous medium and catalytic coupling reaction
[92]	Multi- scale	Eulerian-Lagrangian	Char	1200-1290	Methanol—Steam Reforming in Packed-Bed Reactors
[100]	Multi- scale	Eulerian-Lagrangian	Catalytic effect	1020-1210	Numerical evaluation on the intraparticle transfer in butylene
[76]	Multi- scale	Eulerian-Lagrangian	Charcoal	1023-1173	Pressure Drop in Fixed Bed Reactor Using a Computational Fluid Dynamics (CFD) Code
[101]	Multi- scale	Eulerian-Eulerian	Pinewood CFB	1073	CO_2- kinetics model
[77]	Multi- scale	Eulerian-Lagrangian	Catalytic	1200	Numerical simulations of catalytic fixed-bed reactors
[57]	Multi- scale	Eulerian-Lagrangian	Char-CO_2-CH_4 reactions	900-1200	Packed Bed Chemical

					Looping Reforming (PBCLR) Reactor
[102]	Multi- scale	Eulerian-Lagrangian	Char	900-1150	A parallel dual-grid multiscale approach

1.3.4 Multi-scale Reaction Model

Several scholars have modeled fixed-bed reactors based on axial, radial, and circumferential profiles [56, 58, 59, 61, 103]. A few studies have combined macro-and micro-scale fluid dynamics and particle reaction with fixed beds since a complex equation system would be expanded with species conservation equations. Furthermore, the majority of previous studies have addressed catalytic reactions [57, 104, 105]. However, particles' structural property and solid size remained unchanged over the process. Because anode gasification represents a non-catalytic reaction, it is imperative to use a new scheme for considering solid structural variations throughout the gasification. Many studies have incorporated non-catalytic reactions into the fixed-bed reaction, while this kinetics has often been restricted to a specific scope of process parameters [92, 102, 103, 106-112].

The coupling procedure plays a pivotal role in modeling the gasification process. The models involved in this process are computationally more advanced and more committed than those proposed by earlier studies. They allow simulation of both fluid-solid and solid-solid interactions in the anode and the control volume. They receive support from a newly developed approach and can provide detailed information concerning the complex structural solid characteristics and fluid dynamics. Recently, an Eulerian-Lagrangian approach has been employed for the simulation of porous particles. The Eulerian Finite Element Method (FEM) has developed a mathematical method for modeling the fluid phase. In addition, the Discrete Element Method (DEM) has been used to model the dynamics of anode particles. Both approaches involve a coupling that allows tracking the particles' motions and the fluid phase's dynamics.

With the multi-scale approach, the geometric structure of particle beds enables the effective solving of momentum and heat transport and species mass transfer between particles. In addition, resolving heat and species mass transports in the particles' interior (intraparticle transport) is possible. As shown in Figure 1.8 , the model for porous media benefits from bed morphology's averaged values. No transparent distinction exists between the phases. Figure 1.8 illustrates the corresponding porosity of the two approaches.

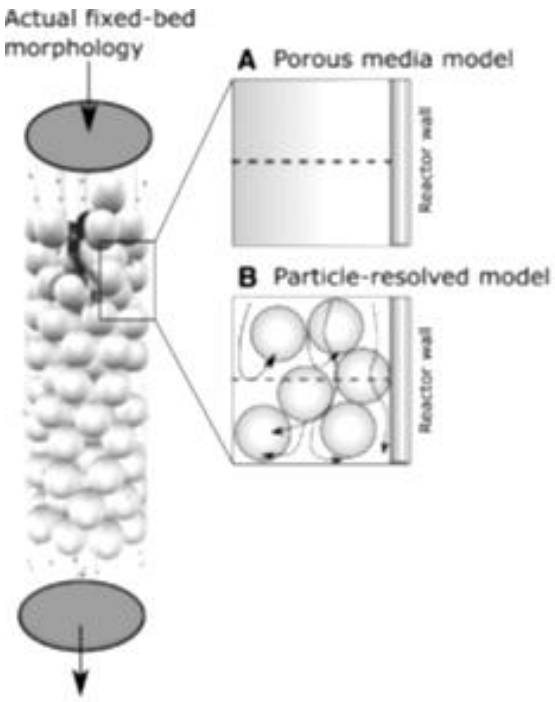

Figure 1.8. A) Conventional porous media model, and B) particle resolved CFD simulating inside of the fixed-bed reactor and spherical particles [113]

1.4 Conclusions and significance

In an FB gasifier, an anode particle's actual reaction rate at a specified position and instance depends on the gas species concentration, the anode particle size, its burn-off history, and the position-specific temperature in the reactor. For assessing the anode particles reactivity in an FB gasifier, two main approaches have been identified: a heterogenous approach (HA) and a

pseudo-homogenous approach (PHA). The PHA approach avoids the requirement of solving a particle model for the anode particles, a fact that accounts for its extensive use. The approach also suffers from a high level of uncertainty when applied to FB gasifier models. On the other hand, despite its computationally complicated nature, the HA approach is precise and consistent. Theoretically, this approach is preferred when diffusional effects are likely to exist. A summary of these approaches is presented in Table 1.3.

Table 1.3 Comparison of different model approaches

proach	**Difficulty**	**Method of solution**	**Certainty**	**Limitation**
Pseudo-empirical approach (PEA)	Easy to solve	Finite difference method	high uncertainty	particle equation- pore diffusion
Rigorous approach (RA)	complicated	Finite element- Finite element Finite element- Discrete element	precise and consistent	High number of particle- need long time to proceed

1.5 Gap of knowledge in modeling of the Hall- Heroult process

A lot of research has been done on carbon anodes that have been applied to the Hall-Heroult process, including the physicochemical characteristics of anodes, CO_2 and O_2 reactions, raw materials, and their modification to reduce overall reactivity. Most of these studies are primarily based on determining the overall reactivity, with only a few dealing with the essential parameters, controlling the reactivity of the anodes based on their properties. However, A handful of studies have been conducted to model carbon anode gasification. This work focuses on the numerical problems associated with CO_2 gasification of carbon anode in the Hall-Heroult process to cover the gap between industrial work and academic researches. This study proposes developed models in 3 parts: single anode particle, bed of anode particles, and the anode slab.

An accurate model for a particle reaction could generate valuable insights into modeling the whole anode reaction in the future. In this part, we have attempted to reduce the gap between theory and experiment by providing a model that considers diffusion and pore growth during the reaction of an anode particle. By starting the gasification process, the anode particles are consumed, and the apparent radius of the carbon anode decreases gradually while the porosity of the particle increases. Hence, the effect of shrinkage and particle porosity should be considered in the mathematical modeling. This work is a novel approach to solving mass transfer equations in gasification by applying particle shrinkage to numerical modeling.

In the second part of the thesis, a multi-scale model with a non-catalytic reaction was developed to investigate anode's reactivity and apply a new approach to consider structural changes in anode particles during the gasification. Although CO_2 gasification of various materials has been reported in fixed bed reactors, modeling carbon anodes with their specific properties is a completely new project. Thus, mathematical modeling was adopted and specified according to the anode's structural characteristics. As temperature and concentration differences between the fluid bulk and anode surfaces need to be considered, the heterogeneous approaches were applied. The most challenging part of the work was the change of structural parameters during the gasification process, especially for anodes' particle size. To overcome this problem, in addition to moving the boundary condition of each particle, the movement equations for each particle were applied. So, the solid particles were considered a discrete part, and the flow in the space between the particles was considered a continuum phase. An Eulerian Finite-Element Method (FEM) served as the basis for the proposed mathematical method to model the fluid phase, while a discrete-element method (DEM) was employed to model the anode particles' dynamics and particle shrinkage, which provided the possibility of tracking the particles' motion and of the dynamics of the fluid. Communication between the two length scales was achieved through an interpolation strategy, and a dual-grid multi-scale scheme was originally proposed to couple DEM with FEM. To facilitate data conversion between continuum models derived from FEM and DEM, an interface was defined. This process was the key point for modeling gasification and allowed the investigation of particle–fluid interaction without missing the information on particles.

In the last part of the thesis, the mathematical model was developed for large-scale modeling of anode slab. The only reported work on anode slab is that by D. Ziegler [20], done under isothermal steady-state and first-order conditions. In this study, a model was developed in an unsteady-state condition. To address the inherent effect of CO on the gasification process, L-H mechanism is used as the gas part of the chemical reaction rate, and RPM as the solid part to consider structural parameters. The model includes a finite element method (FEM) for the gas and solid phases (anode). In addition, the anode disappearing has been included in the model by adding the burning rate of the anode and the moving boundary condition.

The present work can open a new window for addressing one of the most critical issues in aluminum smelters and a better understanding of the CO_2 gasification process.

References

1. Engvoll, M.A., *Reactivity of anode raw materials and anodes for production of aluminium*. 2001, The Norwegian university of science and technology (NTNU): Norway.
2. Xie, Y. and X. Xue, *Multi-scale electrochemical reaction anode model for solid oxide fuel cells.* Journal of Power Sources, 2012. **209**: p. 81-89.
3. Xu, Q., S. Pang, and T. Levi, *Reaction kinetics and producer gas compositions of steam gasification of coal and biomass blend chars, part 2: Mathematical modelling and model validation.* Chemical Engineering Science, 2011. **66**(10): p. 2232-2240.
4. Mandapati, R.N., et al., *Experiments and Kinetic Modeling for CO2 Gasification of Indian Coal Chars in the Context of Underground Coal Gasification.* Industrial & Engineering Chemistry Research, 2012. **51**(46): p. 15041-15052.
5. Liu, L., et al., *Structure Characterization and CO_2 Gasification Kinetics of Tri-High Coal-Chars Derived from High-Temperature Pyrolysis.* ACS omega, 2019. **4**(21): p. 19030-19036.
6. Levenspiel, O., *Chemical reaction engineering*. 3rd ed. 1999, New York: Wiley.
7. Chevarin, F., *Relation entre les propriétés physico-chimiques de l'anode en carbone et sa vitesse de réaction sous CO_2*, in *Metallurgy and Materials Department*. 2016, Laval University: Quebec, Canada.
8. Walker, P.L., F. Rusinko, and L.G. Austin, *Gas Reactions of Carbon*, in *Advances in Catalysis*, D.D. Eley, P.W. Selwood, and P.B. Weisz, Editors. 1959, Academic Press. p. 133-221.
9. Chevarin, F., et al., *Active pore sizes during the CO_2 gasification of carbon anode at 960°C.* Fuel, 2016. **178**: p. 93-102.
10. Gudekar, K.G., *B.S modeling, control, and optimization of fixed bed reactors*. 2002, Texas Tech University: USA.
11. de Koranyi, A., *The relationship between specific reactivity and the pore structure of coal chars during gasification.* Carbon, 1989. **27**(1): p. 55-61.

12. Malekshahian, M. and J.M. Hill, *Effect of Pyrolysis and CO2 Gasification Pressure on the Surface Area and Pore Size Distribution of Petroleum Coke.* Energy & Fuels, 2011. **25**(11): p. 5250-5256.
13. HOUSTON, G. and H. Øye, *Carbon losses caused by gaseous oxidation during aluminium electrolysis. Pt. 2.* Aluminium (Düsseldorf), 1985. **61**(8): p. 589-591.
14. Khaji, K. and M. Al Qassemi, *The Role of Anode Manufacturing Processes in Net Carbon Consumption.* Metals, 2016. **6**(6): p. 128.
15. Chevarin, F., *Relation entre les propriétés physico-chimiques de l'anode en carbone et sa vitesse de réaction sous CO2*. 2016, Université Laval.
16. Chevarin, F., et al., *Air and CO_2 reactivity of carbon anode and its constituents: an attempt to understand dusting phenomenon*, in *Light Metals 2015*. 2015, Springer. p. 1147-1152.
17. Sadler, B.A. and S.H. Algie. *Porosimetric study of sub-surface carboxy oxidation in anodes*. in *TMS Annual Meeting*. 1991. New Orleans, LA, USA.
18. Bensah, Y.D. and T. Foosnaes, *The nature and effect of sulphur compounds on CO_2 and air reactivity of petrol coke.* 2010.
19. Fischer, W. and R. Perruchoud, *Factors Influencing the Carboxy- and Air-Reactivity Behavior of Prebaked Anodes in Hall--Heroult Cells.* Light Metals 1986., 1986. **2**: p. 575-580.
20. Ziegler, D.P., *Sub-surface carbon dioxide reaction in anodes*, in *Light Metals 2011*. 2011, Springer. p. 901-906.
21. Azari, K., et al., *Effects of Physical Properties of Anode Raw Materials on the Paste Compaction Behavior*, in *Light Metals 2011*, S.J. Lindsay, Editor. 2016, Springer International Publishing: Cham. p. 1161-1164.
22. Gómez-Barea, A., P. Ollero, and C. Fernández-Baco, *Diffusional Effects in CO2 Gasification Experiments with Single Biomass Char Particles. 1. Experimental Investigation.* Energy & Fuels, 2006. **20**(5): p. 2202-2210.
23. Ingham, D.B., et al., *Transport phenomena in porous media*. 1st ed. ed. 1998, Oxford: Pergamon.
24. Nield, D.A. and A. Bejan, *Convection in porous media*. 2017, Springer: Cham, Switzerland.
25. Engvoll, M.A., H.A. Oye, and M. Srlie. *Gas reactivity inside industrial anodes*. in *TMS*. 2002. Seattle, WA, USA.
26. Stockie, J.M., K. Promislow, and B.R. Wetton, *A finite volume method for multicomponent gas transport in a porous fuel cell electrode.* International Journal for Numerical Methods in Fluids, 2003. **41**(6): p. 577-599.
27. Mani, T., N. Mahinpey, and P. Murugan, *Reaction kinetics and mass transfer studies of biomass char gasification with CO2.* Chemical Engineering Science, 2011. **66**(1): p. 36-41.
28. Tordai, T., *Anode dusting during the electrolytic production of aluminium*. 2007, EPFL.
29. Tordai, T., *Anode dusting during the electrolytic production of aluminium*. EPFL.
30. Lavigne, L. and L. Castonguay, *Prediction of anode performance from calcined coke properties*. Light Metals 1993, 1993: p. 569-575.
31. Kovacik, G., A. Chambers, and B. Özüm, *CO_2 gasification kinetics of two Alberta coal chars.* The Canadian Journal of chemical engineering, 1991. **69**(3): p. 811-815.
32. Gottifredi, J.C. and E.E. Gonzo, *Approximate expression for the effectiveness factor estimation and a simple numerical method for concentration profile calculation in porous catalyst.* Chemical Engineering Journal, 2005. **109**(1): p. 83-87.
33. Gómez-Barea, A. and P. Ollero, *An approximate method for solving gas–solid non-catalytic reactions.* Chemical Engineering Science, 2006. **61**(11): p. 3725-3735.
34. Zou, J.H., et al., *Modeling reaction kinetics of petroleum coke gasification with CO_2.* Chemical Engineering and Processing: Process Intensification, 2007. **46**(7): p. 630-636.

35. Rafsanjani, H.H. and E. Jamshidi, *Kinetic study and mathematical modeling of coal char activation.* Chemical Engineering Journal, 2008. **140**(1): p. 1-5.
36. Wu, Y., S. Wu, and J. Gao, *A Study on the Applicability of Kinetic Models for Shenfu Coal Char Gasification with CO_2 at Elevated Temperatures.* Energies, 2009. **2**(3): p. 545.
37. Zhang, Y., et al., *Modeling of catalytic gasification kinetics of coal char and carbon.* Fuel, 2010. **89**(1): p. 152-157.
38. Fei, H., et al., *A New Mathematical Model Study on CO_2 Gasification Reaction of Typical Agricultural Residues.* Industrial & Engineering Chemistry Research, 2012. **51**(42): p. 13619-13626.
39. Tomaszewicz, M., et al., *The kinetics of CO_2 gasification of coal chars.* Journal of Thermal Analysis and Calorimetry, 2013. **113**(3): p. 1327-1335.
40. Huo, W., et al., *Mechanism analysis and experimental verification of pore diffusion on coke and coal char gasification with CO_2.* Chemical Engineering Journal, 2014. **244**: p. 227-233.
41. Prabhakar, A., et al., *Modeling and Experimental Studies on CO_2 Gasification of Coarse Coal Char Particle.* Energy & Fuels, 2017. **31**(3): p. 2652-2662.
42. Keller, F., F. Küster, and B. Meyer, *Determination of coal gasification kinetics from integral drop tube furnace experiments with steam and CO_2.* Fuel, 2018. **218**: p. 425-438.
43. G.S., L., et al., *Modeling of Infra-Particle C-CO_2 Reaction: An Application of the Random Pore Model.* Developments in Chemical Engineering and Mineral Processing, 1999. **7**(5-6): p. 525-536.
44. Matsumoto, K., et al., *Gasification reaction kinetics on biomass char obtained as a by-product of gasification in an entrained-flow gasifier with steam and oxygen at 900–1000°C.* Fuel, 2009. **88**(3): p. 519-527.
45. Reyes, S. and K.F. Jensen, *Percolation concepts in modelling of gas-solid reactions—II. Application to char gasification in the diffusion regime.* Chemical Engineering Science, 1986. **41**(2): p. 345-354.
46. Jamshidi, E. and H. Ale Ebrahim, *An incremental analytical solution for gas-solid reactions, application to the grain model.* Chemical Engineering Science, 1996. **51**(18): p. 4253-4257.
47. Jamshidi, E. and H. Ale Ebrahim, *A new solution technique of moving boundary problems for gas-solid reactions; application to half-order volume reaction model.* The Chemical Engineering Journal and the Biochemical Engineering Journal, 1996. **63**(2): p. 79-83.
48. Jamshidi, E. and A.A. Ebrahim, *Erratum to 'A quantized solution for the nucleation model in gas—solid reactions' [Chemical Engineering Journal 68 (1997) 1–6].* Chemical Engineering Journal, 1998. **70**(3): p. 245.
49. Liu, H. and B.M. Gibbs, *Modeling NH_3 and HCN emissions from biomass circulating fluidized bed gasifiers.* Fuel, 2003. **82**(13): p. 1591-1604.
50. Jahrsengene, G., et al., *A XANES Study of Sulfur Speciation and Reactivity in Cokes for Anodes Used in Aluminum Production.* Metallurgical and Materials Transactions B, 2018. **49**(3): p. 1434-1443.
51. Wakao, N. and J.M. Smith, *Diffusion in catalyst pellets.* Chemical Engineering Science, 1962. **17**(11): p. 825-834.
52. Thunman, H., *Principles and models of solid fuel combustion*. 2001, Chalmers University of Technology: Gothenburg, Sweden.
53. Schwidder, S. and K. Schnitzlein, *A new model for the design and analysis of trickle bed reactors.* Chemical Engineering Journal, 2012. **207-208**: p. 758-765.
54. Behnam, M., et al., *A New Approach to Fixed Bed Radial Heat Transfer Modeling Using Velocity Fields from Computational Fluid Dynamics Simulations.* Industrial & Engineering Chemistry Research, 2013. **52**(44): p. 15244-15261.

55. Bruch, C., B. Peters, and T. Nussbaumer, *Modelling wood combustion under fixed bed conditions.* Fuel, 2003. **82**(6): p. 729-738.
56. Fedkiw, R.P., *Coupling an Eulerian Fluid Calculation to a Lagrangian Solid Calculation with the Ghost Fluid Method.* Journal of Computational Physics, 2002. **175**(1): p. 200-224.
57. Singhal, A., et al., *Verification of heat and mass transfer closures in industrial scale packed bed reactor simulations.* Energies, 2018. **11**(4): p. 805.
58. Thomas, J.R. and F. Fucher, *Thermal Modeling of Microwave Heated Packed and Fluidized Bed Catalytic Reactors.* Journal of Microwave Power and Electromagnetic Energy, 2000. **35**(3): p. 165-174.
59. Jiang, Y., et al., *CFD modeling of multiphase flow distribution in catalytic packed bed reactors: scale down issues.* Catalysis Today, 2001. **66**(2): p. 209-218.
60. Potapov, A.V., M.L. Hunt, and C.S. Campbell, *Liquid–solid flows using smoothed particle hydrodynamics and the discrete element method.* Powder Technology, 2001. **116**(2): p. 204-213.
61. Salmi, T. and J. Wärmå, *Modelling of catalytic packed-bed reactors—comparison of different diffusion models.* Computers & Chemical Engineering, 1991. **15**(10): p. 715-727.
62. Azari, K., *Investigation of the materials and paste relationships to improve forming process and anode quality*, in *Material and Metallurgy Department* 2013, Laval Uinversity: Canada.
63. *https://www.comsol.com/model/download/684061/heterogeneous_catalysis_pellet.pdf*.
64. Froment, G.F., K.B. Bischoff, and J. De Wilde, *Chemical reactor analysis and design*. Vol. 2. 1990: Wiley New York.
65. Hlavacek, V. and H. Hofmann, *Modeling of chemical reactors—XVI Steady state axial heat and mass transfer in tubular reactors An analysis of the uniqueness of solutions.* Chemical Engineering Science, 1970. **25**(1): p. 173-185.
66. Hlavacek, V., *STEADY STATE OPERATION OF FIXED BED REACTORS AND MONOLITHIC STRUCTURES.* 1976.
67. Thunman, H., K. Davidsson, and B. Leckner, *Separation of drying and devolatilization during conversion of solid fuels.* Combustion and Flame, 2004. **137**(1): p. 242-250.
68. Thunman, H., et al., *Composition of Volatile Gases and Thermochemical Properties of Wood for Modeling of Fixed or Fluidized Beds.* Energy & Fuels, 2001. **15**(6): p. 1488-1497.
69. Turkdogan, E.T. and J.V. Vinters, *Effect of carbon monoxide on the rate of oxidation of charcoal, graphite and coke in carbon dioxide.* Carbon, 1970. **8**(1): p. 39-53.
70. van den Aarsen, F.G., *Fluidised bed wood gasifier performance and modeling*. 1985, University of Twente: Netherlands.
71. Alopaeus, V., et al., *Modeling of Gas−Liquid Packed-Bed Reactors with Momentum Equations and Local Interaction Closures.* Industrial & Engineering Chemistry Research, 2006. **45**(24): p. 8189-8198.
72. Comiti, J. and M. Renaud, *A new model for determining mean structure parameters of fixed beds from pressure drop measurements: application to beds packed with parallelepipedal particles.* Chemical Engineering Science, 1989. **44**(7): p. 1539-1545.
73. Gudekar, K.G., *Modeling, control, and optimization of fixed bed reactors*, in *Chemical Engineering*. 2002, Texas Tech University: United States.
74. Magoo, A.K., A. Mittal, and S. Roy, *Modeling Packed Bed Fischer–Tropsch Reactors with Phase Evolution.* Indian Chemical Engineer, 2013. **55**(1): p. 29-37.
75. Lane, N.M., *Numerical studies of flow in porous media using an unstructured approach*, in *The Gordon A. and Mary Cain Department of Chemical Engineering*. 2011, Louisiana State University and Agricultural and Mechanical College: Louisiana, USA.
76. Ahmadi, S. and F. Sefidvash, *Study of pressure drop in fixed bed reactor using a Computational Fluid Dynamics (CFD) code.* ChemEngineering, 2018. **2**(2): p. 14.

77. Wehinger, G.D., T. Eppinger, and M. Kraume, *Detailed numerical simulations of catalytic fixed-bed reactors: Heterogeneous dry reforming of methane.* Chemical Engineering Science, 2015. **122**: p. 197-209.
78. Wu, S., M.A. Uddin, and E. Sasaoka, *Effect of Pore Size Distribution of Calcium Oxide High-Temperature Desulfurization Sorbent on Its Sulfurization and Consecutive Oxidative Decomposition.* Energy & Fuels, 2005. **19**(3): p. 864-868.
79. Srinivasan, A., *One-dimensional pseudo-homogeneous packed bed reactor modeling including no-co kinetics*. 2011, University of Kansas.
80. Bizon, K., *Application of Pseudohomogeneous and Heterogeneous Models in Assessing the Behavior of a Fluidized-Bed Catalytic Reactor*. Energies, 2021. **14**(1): p. 208.
81. S, S., et al. *Homogeneity of Continuum Model of an Unsteady State Fixed Bed Reactor for Lean CH_4 Oxidation*. Journal of Engineering and Technological Sciences, 2014. **46**, 195-210 DOI: 10.5614/j.eng.technol.sci.2014.46.2.6.
82. Reshetnikov, S.I., et al., *Mathematical modeling of regeneration of coked Cr-Mg catalyst in fixed bed reactors.* Chemical Engineering Journal, 2020. **380**: p. 122374.
83. Qian, Y., et al., *CFD model of coal pyrolysis in fixed bed reactor.* Chemical Engineering Science, 2019. **200**: p. 1-11.
84. Donaubauer, P.J., L. Schmalhorst, and O. Hinrichsen, *2D flow fields in fixed-bed reactor design: a robust methodology for continuum models.* Chemical Engineering Science, 2019. **208**: p. 115137.
85. Jorge, L.M.d.M., R.M.M. Jorge, and R. Giudici, *Experimental and numerical investigation of dynamic heat transfer parameters in packed bed.* Heat and Mass Transfer, 2010. **46**(11): p. 1355-1365.
86. Depcik, C. and D. Assanis, *One-dimensional automotive catalyst modeling.* Progress in Energy and Combustion Science, 2005. **31**(4): p. 308-369.
87. Hamel, S. and W. Krumm, *Mathematical modelling and simulation of bubbling fluidised bed gasifiers.* Powder Technology, 2001. **120**(1): p. 105-112.
88. Chen, G., J. Andries, and H. Spliethoff, *Biomass conversion into fuel gas using circulating fluidised bed technology: the concept improvement and modelling discussion.* Renewable Energy, 2003. **28**(6): p. 985-994.
89. de Jong, W., et al., *Thermochemical conversion of brown coal and biomass in a pressurised fluidised bed gasifier with hot gas filtration using ceramic channel filters: measurements and gasifier modelling.* Applied Energy, 2003. **74**(3): p. 425-437.
90. Gómez-Barea, A. and B. Leckner, *Modeling of biomass gasification in fluidized bed.* Progress in Energy and Combustion Science, 2010. **36**(4): p. 444-509.
91. Liu, H. and B.M. Gibbs, *Modeling NH3 and HCN emissions from biomass circulating fluidized bed gasifiers ☆.* Fuel, 2003. **82**(13): p. 1591-1604.
92. Ziarati, M., M.A. Ghafouri Roozbahani, and N. Khandan, *New Method of Rigorous Modeling and CFD Simulation for Methanol—Steam Reforming in Packed-Bed Reactors.* Chemical Engineering Communications, 2016. **203**(10): p. 1359-1373.
93. Gao, X., Y.-P. Zhu, and Z.-h. Luo, *CFD modeling of gas flow in porous medium and catalytic coupling reaction from carbon monoxide to diethyl oxalate in fixed-bed reactors.* Chemical Engineering Science, 2011. **66**(23): p. 6028-6038.
94. Hou, Q., D. E, and A. Yu, *Discrete particle modeling of lateral jets into a packed bed and micromechanical analysis of the stability of raceways.* AIChE Journal, 2016. **62**(12): p. 4240-4250.
95. Ku, X., T. Li, and T. Løvås, *CFD–DEM simulation of biomass gasification with steam in a fluidized bed reactor.* Chemical Engineering Science, 2015. **122**: p. 270-283.

96. Rabbani, S., M. Sassi, and T. Shamim, *Modeling of hydrodynamics of fine particles deposition in packed-bed reactors.* The Journal of Computational Multiphase Flows, 2017. **9**(4): p. 157-168.
97. Valkov, B., C.H. Rycroft, and K. Kamrin, *Eulerian Method for Multiphase Interactions of Soft Solid Bodies in Fluids.* Journal of Applied Mechanics, 2015. **82**(4).
98. Norouzi, H.R., et al., *Coupled CFD-DEM modeling: formulation, implementation and application to multiphase flows*. 2016: John Wiley & Sons.
99. Abdulmohsin, R.S. and M.H. Al-Dahhan, *Pressure Drop and Fluid Flow Characteristics in a Packed Pebble Bed Reactor.* Nuclear Technology, 2017. **198**(1): p. 17-25.
100. Huang, K., et al., *Numerical evaluation on the intraparticle transfer in butylene oxidative dehydrogenation fixed-bed reactor over ferrite catalysts.* Journal of Industrial and Engineering Chemistry, 2015. **29**: p. 172-184.
101. Sadooghi, P. and R. Rauch, *Experimental and modeling study of catalytic steam reforming of methane mixture with propylene in a packed bed reactor.* International Journal of Heat and Mass Transfer, 2014. **78**: p. 515-521.
102. Pozzetti, G., et al., *A parallel dual-grid multiscale approach to CFD–DEM couplings.* Journal of Computational Physics, 2019. **378**: p. 708-722.
103. Potapov, A.V., M.L. Hunt, and C.S. Campbell, *Liquid–solid flows using smoothed particle hydrodynamics and the discrete element method.* Powder Technology, 2001. **116**(2-3): p. 204-213.
104. Singhal, A., et al., *Multiscale modeling of a packed bed chemical looping reforming (pbclr) reactor.* Energies, 2017. **10**(12): p. 2056.
105. Wehinger, G., T. Eppinger, and M. Kraume, *Detailed numerical simulations of catalytic fixed-bed reactors: Heterogeneous dry reforming of methane. Chemical Engineering Science*, 2015. **122**: p. 197-209.
106. Ortiz-Arroyo, A., et al., *CFD modeling and simulation of clogging in packed beds with nonaqueous media.* AIChE Journal, 2002. **48**(8): p. 1596-1609.
107. Pirnia, P., et al., *ICY: An interface between COMSOL multiphysics and discrete element code YADE for the modelling of porous media.* Computers & Geosciences, 2019. **123**: p. 38-46.
108. Romkes, S.J.P., et al., *CFD Modeling and Experimental Validation of Particle-to-Fluid Mass and Heat Transfer in a Packed Bed at Very Low Channel to Particle Diameter Ratio.* Chem. Eng. J., 2003. **96**: p. 3.
109. Santana, E.R., G. Pozzetti, and B. Peters, *Application of a dual-grid multiscale CFD-DEM coupling method to model the raceway dynamics in packed bed reactors.* Chemical Engineering Science, 2019. **205**: p. 46-57.
110. Taskin, M.E., et al., *CFD Study of the Influence of Catalyst Particle Design on Steam Reforming Reaction Heat Effects in Narrow Packed Tubes.* Ind. Eng. Chem. Res., 2008. **47**: p. 5966.
111. Wolfrum, C., A. Josten, and P. Götz, *Optimization and scale-up of oligonucleotide synthesis in packed bed reactors using computational fluid dynamics modeling.* 2014. **30**(5): p. 1048-1056.
112. Zhu, Y.-P., G.-Q. Chen, and Z.-H. Luo, *Iterative Multiscale Computational Fluid Dynamics–Single-Particle Model for Intraparticle Transfer and Catalytic Hydrogenation Reaction of Dimethyl Oxalate in a Fluidized-Bed Reactor. Industrial & Engineering Chemistry Research*, 2013. **53**(1): p. 110-122.
113. Jurtz, N., M. Kraume, and G.D. Wehinger, *Advances in fixed-bed reactor modeling using particle-resolved computational fluid dynamics (CFD).* Reviews in Chemical Engineering, 2019. **35**(2): p. 139-190.

Chapter 2

Reaction-diffusion model for gasification of shrinking single carbon-anode particle

Mohammad Kavand[1], Roozbeh Mollaabbasi[1], Donald Ziegler[2], Faïçal Larachi[3], Donald Picard[1], Houshang Alamdari[,1]*

[1] Aluminum Research Centre REGAL, Université Laval, 1065 avenue de la Médecine, Québec, Québec, G1V 0A6

[2] Alcoa corporation, Alcoa Technical Centre, 859 White Cloud Road, New Kensington, PA, 15068, USA

[3] Department of Chemical Engineering, Université Laval, 1065 avenue de la Médecine, Québec, Québec, G1V 0A6

[*]Corresponding author: houshang.alamdari@gmn.ulaval.ca

Abstract

The present work focuses on the gasification of a single carbon-anode particle with CO_2, using a detailed reaction-transport model, based on the reaction intrinsic kinetics and transport of gaseous species. The model includes the mass conservation equations for the gas components and solid carbon particles, resulting in a set of nonlinear partial differential equations, being solved using numerical techniques. The model may predict the gas generation rate, the gas compositions, and the carbon consumption rate during the gasification of a carbon particle. Five kinetic models were compared to describe the gasification behavior of carbon particles. It was found that the random pore model (RPM) provided the best description of the reactivity of anode particles. The model also predicted the particle shrinkage during the gasification process. The model was validated using experimental results obtained with different particle size ranges, being gasified with CO_2 at

1233 K. The experiments were performed in a thermo-gravimetric analyzer (TGA). Good agreement between the model results and the experimental data showed that this approach could quantify with success the gasification kinetics and the gas distribution within the anode particle. In addition, the Langmuir-Hinshelwood (L-H) model is used in order to capture the inhibition effect of carbon monoxide on the gasification reaction. The effectiveness factor and Thiele modulus simulated for various particle sizes helped assessing the evolution of the relative dominance of diffusion and chemical reactions during the gasification process.

Résumé

Le présent travail se concentre sur la gazéification d'une seule particule d'anode de carbone avec du CO_2, en utilisant un modèle de transport-réaction détaillé, basé sur la cinétique intrinsèque de la réaction et le transport des espèces gazeuses. Le modèle comprend les équations de conservation de la masse pour les composants gazeux et les particules solides de carbone, ce qui donne lieu à un ensemble d'équations aux dérivées partielles non linéaires, résolues à l'aide de techniques numériques. Le modèle peut prédire le taux de génération de gaz, les compositions de gaz ainsi que le taux de consommation de carbone pendant la gazéification d'une particule de carbone. Cinq modèles cinétiques ont été comparés pour décrire le comportement de gazéification des particules de carbone. Il est ressorti que le modèle de pores aléatoires (RPM) fournissait la meilleure description de la réactivité des particules d'anode. Le modèle a également prédit le rétrécissement des particules pendant le processus de gazéification. Le modèle a été validé à l'aide de résultats expérimentaux obtenus avec différentes gammes de tailles de particules, ayant été gazéifiées avec du CO_2 à 1233 K. Les expériences ont été réalisées dans un analyseur thermo-gravimétrique (TGA). Une similitude des résultats du modèle et ceux des données expérimentales a montré que cette approche pourrait quantifier avec succès la cinétique de gazéification et la distribution du gaz au sein de la particule anodique. De plus, le modèle Langmuir-Hinshelwood (L-H) est utilisé afin de capturer l'effet d'inhibition du monoxyde de carbone sur la réaction de gazéification. Le facteur d'efficacité et le module de Thiele simulés pour différentes tailles de particules ont

aidé à évaluer l'évolution de la dominance relative de la diffusion et des réactions chimiques au cours du processus de gazéification.

Keywords: carbon anode; single-particle shrinkage; gasification; diffusion; inhibition; modeling

Nomenclature

Latin symbols

A	stoichiometric coefficient, (-)
B	stoichiometric coefficient, (-)
C_C	concentration of anode reactant, ($mol \cdot m^{-3}$)
C	concentration of gaseous species, ($mol \cdot m^{-3}$)
C(O)	surface concentration of carbon-oxygen complex, ($mol \cdot m^{-2}$)
D	diffusion coefficient, ($m^2 \cdot s^{-1}$)
D_e	effective diffusion coefficient, ($m^2 \cdot s^{-1}$)
k	reaction rate constant, $(mol \cdot m^{-3})^{((1-n)\cdot s^{-1})}$
k_0	preexponential factor, ($bar^{-n} \cdot s^{-1}$)
L_0	pore length, ($m \cdot kg^{-1}$)
H	number of experimental data, (-)
M	molecular weights, ($kg \cdot mol^{-1}$)
m	mass of anode particle, (kg)
N	number of samples, (-)
n	partial reaction order, (-)

P	pressure, ($kg \cdot m^{-2} \cdot s^{-2}$)
r	spherical coordinate (m)
r_0	particle radius, (m)
R	chemical reaction rate, ($mol \cdot s^{-1} \cdot m^{-3}$)
R_m	gas constant ($kJ \cdot mol^{-1} \cdot K^{-1}$)
S	specific surface area, (m^{-1})
t	reaction time, (s)
T	temperature, (K)
v	pore volume ($m^3 \cdot kg^{-1}$)
X	gasification conversion of anode particle, (-)
x	value of each sample
$\overline{x}$	mean of samples
Greek symbols	
α	modified random pore model constant, (s^{-1})
ε	void fraction, (-)
φ	Thiele module, (-)
η	effectiveness factor, (-)
λ	modified Thiele module, (-)
ρ	density, ($kg \cdot m^{-3}$)
σ	Lennard-Jones collision diameter, (m)
Ω_D	collision integral for molecular diffusion, (-)

τ	tortuosity, (-)
ω	power-law constant, (-)
ψ	structural parameter, (-)
Subscripts	
Abs	absolute
Ap	apparent
Ave	average
C	carbon
CO	carbon monoxide
CO_2	carbon dioxide
Diss	dissolved
F	active carbon site
G	gas phase
I	gas specie
J	gas specie
M	molten
S	solid phase
Sh	shrinkage start point
t	instantaneous
0	initial

2.1 Introduction

Carbon anode reactivity is of considerable concern for most aluminum smelters using the Hall-Héroult electrolysis process. In this process, anodes are partially submerged into the electrolyte solution, which is made up of molten cryolite. Molten aluminum is produced by the reduction of dissolved alumina in the cryolite, and the anode is electrochemically oxidized, generating CO_2. The stoichiometry of this overall electrolysis reaction in shown as Equation (2.1). The generated CO_2 at the anode surface, directly escapes to the electrolysis cell headspace. However, part of the generated CO_2 diffuses into the porous structure of the carbon anode due to the electrolyte hydrostatic head and the concentration gradient. Consequently, it reacts with the solid carbon through the Boudouard reaction [1]. The Boudouard reaction is not desirable because it results in an increase in the net carbon consumption and may contribute to the generation of carbon dust in the pots which is an operational problem [1, 2]. The carbon dust is principally generated by selective burning of the anode components that are in contact with air or CO_2. For instance, it is believed that the binder matrix within the anode is preferentially burnt, causing detachment of the carbon particles from the anode surface, which then fall into the electrolyte bath [3].

$$2Al_2O_{3(diss)} + 3C_{(s)} \rightarrow 4Al_{(m)} + 3CO_{2(g)} \qquad (2.1)$$

The combustion reactions occur either at the anode surface or within the anode bulk. For a given anode formulation, the reaction rate is a function of temperature, pore structure, permeability, and intrinsic reactivity of the anode constituents [3-5]. The minimum theoretical carbon consumption for aluminum electrolysis is 0.334 kg per kg of Al produced. However, since the cell efficiency is usually less than 100 %, the real electrolytic consumption of carbon is around 0.41 kg per kg of Al produced. Keller et al. reported that the extra-cost associated with the overconsumption of one kg anode per one ton of produced aluminum is around US$ 2. The overconsumption of a midsize-smelter (producing 300,000 tons of aluminum per year, and needing 150,000 anodes per year), is approximately 40 kg per anode. Therefore the estimated extra cost could be about US$ 12 million per year [6]Gasification of anode by air and CO_2 greatly contributes to this carbon overconsumption.

Several authors [7-10] discussed the influence of anode properties on its air and CO_2 reactivity and the net carbon consumption. The present work will mainly emphasize the quantification of the structural changes of anode particles during CO_2 gasification and its effect on the gasification reactions.

The electrolysis cell (which is called *pot*) is composed of prebaked carbon anodes, molten cryolite, and a liquid layer of aluminum lying on cathode carbon blocks. The carbon anode is consumed during the process, and it should be replaced by a new one approximately every 25 days. The anodes in the electrolysis cell are in contact with CO_2 at high temperatures (typically 1233 K). At temperatures higher than 1073 K, the apparent rate of carbon-CO_2 gasification reaction becomes more significant due to the combined chemical reaction and the mass transfer effects. It is worth mentioning that the diffusion is the main part of the mass transfer [11, 12] and its effect on the gasification rate becomes more significant for particles larger than 0.1 mm [12, 13].

In order to estimate the anode consumption rate, numerous mathematical models have been introduced in the literature such as the grain model (GM) [14, 15], the volume reaction model (VM) [8, 10, 15], the nucleation model, the single-pore model (SPM) [8], the modified grain model (MGM) [16], and the random pore model (RPM) [8, 9, 15, 17]. Broadly, these models can be divided into two main categories: structural and volumetric models. The structural models account for the changes in the structure of carbon in the process. During the reaction, the internal pore structure is changing over time [11, 15, 18-25]. In the volumetric models, conversely, experimental correlations are used for considering the porous structural changes [8, 10, 14, 18, 22, 26, 27]. In this latter approach, the problem is addressed by feeding the model with the anode mechanical properties or other experimental data. These models explicitly mention the solid microstructure changes during the reaction and the influence of the microstructure evolution on reactivity, but despite changes in the structure, the particle size during the process remains invariant. The literature abounds with simplified techniques to circumvent mathematical and computational difficulties. Jamshidi and Ale Ebrahim [7, 28, 29] developed a semi-analytical, semi-numerical method, Quantize Method (QM), with simplifying assumptions. Their model leads to acceptable results based on the experimental data, though without mentioning the effect of solid structural changes into the solid volume.

Thus, the particle radius remained fixed during the gasification - that is not truly representing the real gasification conditions.

In a non-catalytic carbon-CO_2 reaction, it is essential to take into account the solid structural changes as the reaction progresses, because the reaction rate is a function of both gas and solid concentrations [14, 18, 19]. From a mathematical point of view, this aspect leads to coupling the gas-solid conservation equations within the model that increases the complexity of the problem. Researchers have extensively studied the computational aspects of these models, but there is only limited research data available on single-particle reactions, considering gas-solid conservation equations [18-22], and it is essential to develop models for such practical systems. An accurate model for a particle reaction could generate valuable insights for modeling the whole anode reaction in the future.

In this contribution, we attempted to reduce the gap between theory and experiment, by providing a model that considers diffusion and pore growth during the reaction of an anode particle. Upon the gasification process, the anode particles are consumed, and the apparent radius of the carbon anode reduces gradually while also the porosity of the particle increases. Hence, the effect of shrinkage and the particle porosity was considered in mathematical modeling. Therefore, suitable numerical methods were implemented in the mathematical model for solving the governing transfer equations. First, the intrinsic kinetics of CO_2 gasification is experimentally investigated by using a thermogravimetric analysis. Then, a global reaction model was developed by considering all the above-mentioned aspects. The suitability of the existing structural reaction models for our global reaction model was examined.

2.2 Experiments

2.2.1 Materials and method

2.2.1.1 Materials

The carbon anode particles were obtained from the Deschambault aluminum smelting plant (Alcoa Corporation). Ball milling was used to mill large particles into the fine fractions. To have various particle sizes of anodes, the particles were crushed and passed through various USA standard sieve trays (from 20 µm to 4380 µm).

The real density of the anode particles was measured using a Helium-pycnometer (Micromeritics, AccuPyc II 1340, USA). Each analyzed sample (2 g) was weighed three times with an analytical balance (MS204S, Mettler Toledo, USA) and placed in a stainless-steel cell in the He-pycnometer. The real density was obtained by dividing the mass of the sample to the volume obtained by the pycnometer.

To obtain the specific surface area, powder samples, with a given size, were first degassed under pure nitrogen (N_2) at 523 K for five hours. Then, the samples were analyzed with a gas adsorption analyzer (Micromeritics, Tristar II 3020, USA). Nitrogen (Praxair, purity: 99.995 %, USA) was used as the adsorbing gas at 97 K. The chemical composition was analyzed for all samples using the X-ray Fluorescence Spectrometer (Panalytical, USA). Characteristics of the anode particles with different sizes are presented in the Table 2.1. The amounts of sulfur, vanadium, nickel and sodium are similar for all particle sizes. The increase in the amount of iron observed with decreasing particle size may be explained by the crushing and grinding of the particles which resulted in potential iron contamination. The variability of silicon and calcium concentrations is difficult to explain.

Table 2.1. Elemental composition and physical properties of anode particles with different particle size.

Properties	(4380±380) µm	(3680 ± 320) µm	(2190 ± 190) µm	(1200 ± 205) µm	(500±60) µm	(200±33) µm	(50±11) µm	(20±1) µm
S (%)	1.87 ± 0.06	1.84 ± 0.06	1.85 ± 0.06	1.86 ± 0.06	1.83 ± 0.06	1.82 ± 0.06	1.81 ± 0.06	1.84 ± 0.06
Si (ppm)	254 ± 36	252 ± 35	257 ± 36	222 ± 37	293 ± 35	453 ± 63	745 ± 34	475 ± 66
Ca (ppm)	174 ± 9	174 ± 9	468 ± 23	335 ± 63	204 ± 10	459 ± 63	1259 ± 63	1059 ± 63
V (ppm)	302 ± 15	302 ± 15	308 ± 15	316 ± 15	312 ± 15	308 ± 15	309 ± 15	311 ± 15
Fe (ppm)	737 ± 37	747 ± 37	696 ± 35	740 ± 37	775 ± 35	895± 45	973 ± 49	1058± 49
Ni (ppm)	182 ± 9	183 ± 9	187 ± 9	197± 10	201 ± 10	188 ± 9	190 ± 10	193 ± 10
Helium density ($kg \cdot m^{-3}$)	1980	1980	1990	2002	2008	2020	2055	2060
BET surface area ($m^2 \cdot g^{-1}$)	4.2	4.5	4.5	5.3	5.0	5.5	6.3	6.9

2.2.2 Gasification tests

A thermo-gravimetric analyzer (Netzsch STA 449 F3 Jupiter) was used for measuring the apparent reaction rate of anode particles at 1233 K by measuring the online weight loss of the samples. To remove moisture content, the samples were placed in an oven at 423 K for 15 h. Only one layer of dried particles was placed in the TGA sample holder (1.82 mm height and 6.45 mm diameter) to ensure the constant composition of the feeding gas near the surface of each particle. The temperature was gradually raised (20 $K \cdot min^{-1}$) to the target reaction temperature (1233 K). Nitrogen (99.995 %, 100 $mL \cdot min^{-1}$) was used as a protecting gas during the heating step. After reaching the target temperature, the system was stabilized for 15 min under flow of N_2. The flow rate of nitrogen was then steadily decreased to 20 $mL \cdot min^{-1}$ while the flow of CO_2 gas (99.9 %) was increased to 100 $mL \cdot min^{-1}$, and the mass loss was recorded. At the end of the experiment, the CO_2 flow was cut off and substituted by N_2 flow, and the furnace was switched off to cool down to ambient temperature. Each experiment was stopped once no further mass loss was occurring, indicating complete gasification of the samples. The reaction time was indeed a function of the particle size. Equation (2.2) states

the gasification conversion (X) of the carbon material to be used for expressing the apparent anode reactivity:

$$X = (1 - \frac{m_t}{m_0}) \quad (2.2)$$

where m_0 , is the initial mass of the anode particle sample and m_t is the instantaneous mass at time.

As part of this report, uncertainties have been calculated to estimate the weight of measurement and / or experimental errors, and the variation between the different repetitions of the analyses. These uncertainties were calculated using Equation 2.3. To account for any possible variability in the results, this expression assumes that the samples analyzed in this study comprise part of a population, allowing the uncertainties to be overestimated.

$$e = \sqrt{\frac{(x - \bar{x})^2}{N-1}} \quad (2.3)$$

where x is value of each sample $\bar{x}$ is mean of samples and N is the number of samples.

2.3 Mathematical Modeling

2.3.1 Gasification models

The primary chemical reaction can be represented by Equation (2.4):

$$aA_{(g)} + bB_{(s)} \rightarrow C_{(g)} \quad (2.4)$$

where A and B are the gas and solid reactants, respectively, and C is the gaseous product while a and b are their corresponding stoichiometric coefficients. Some simplifying assumptions are used in this model as follows: the domain of the anode particle consists of a spherical reactive solid and the intra-particle porosity, which shelters the gaseous reactants and products. On account of the small size of the particles, it is safe to assume that both gas and solid phases are in an isothermal state [15]. For simplicity, we assume the topochemical

particle evolution preserving its sphericity during the gasification process. CO_2 in a spherical anode particle reacts with carbon according to the following reaction:

$$CO_{2(g)} + C_{(s)} \rightarrow 2CO_{(g)} \quad (2.5)$$

The local mass conversation equations for each species assuming spherical particle symmetry can thus be written as:

$$\frac{1}{r^2}\frac{\partial}{\partial r}(r^2 D_{i,e}\frac{\partial C_{CO_2}}{\partial r}) + R_{CO_2} = \frac{\partial(\varepsilon C_{CO_2})}{\partial t} \quad (2.6)$$

$$\frac{1}{r^2}\frac{\partial}{\partial r}(r^2 D_{CO,e}\frac{\partial C_{CO}}{\partial r}) - 2R_{CO_2} = \frac{\partial(\varepsilon C_{CO})}{\partial t} \quad (2.7)$$

$$R_C = -\frac{\partial C_C}{\partial t} = R_{CO_2} \quad (2.8)$$

Equations 2.6 and 2.7 assume that convective mass transfer is not comparable to the diffusion mass transfer. That is, mass transfer occurs through diffusion via the interconnected pores inside the particle. Also, the tortuosity of pores is applied using effective diffusion coefficient.

The boundary and initial conditions are:

$$\text{at } r = r_0 : \; C_{CO_2} = C_{CO_{2,0}}, C_{CO} = 0 \quad (2.9)$$

$$\text{at } r = 0 : \; \frac{\partial C_{CO_2}}{\partial r} = 0, \; \frac{\partial C_{CO}}{\partial r} = 0 \quad (2.10)$$

$$C_{CO_2}\big|_{t=0} = C_{CO_{2,0}}, \; C_{CO}\big|_{t=0} = 0, \; C_C\big|_{t=0} = C_{C_0} \quad (2.11)$$

where: R_{CO_2} is the chemical reaction rate of CO_2, R_C is the rate of anode reactant consumption, C_C is the instantaneous concentration of carbon, C_{C_0} is the initial concentration of carbon, C_{CO_2} is the concentration of the gaseous reactant, $C_{CO_{2,0}}$ is the initial concentration of the gaseous reactant, D_e is the effective molecular diffusivity, r is the local radial position within the anode particle, r_0 is the initial particle radius. According to Equation (2.8), both

rates of gas consumption (R_{CO_2}) and carbon reactant consumption (R_C) are equal during gasification. The void fraction or the local porosity of the anode particle may change during reaction, due to the consumption of solid reactant or the difference between the volume of the solid reactant and product. The variation of local porosity can be modelled by Equation (2.12) [15] as follows:

$$\varepsilon = \varepsilon_0 + (1-\varepsilon_0) X \tag{2.12}$$

where, ε_0, is the initial porosity of the anode. The equation (2.12) can be derived by means of a material balance, based on the assumption that the bulk density of the ash remains constant [30] and the local porosity satisfies a linear relation with conversion [31].

According to Equations (2.13-2.15), first, the partial differential Equations (2.6, 2.7) with boundary and initial conditions (Equations 3.9-3.11) are solved to obtain the instantaneous C_{CO_2}, C_{CO} radial profiles. Then C_C is calculated from the mass balance at each location by:

$$C_C = C_{C_0} + (C_{CO_2} - C_{CO_{2,0}}) \tag{2.13}$$

The carbon conversion has been experimentally acquired and calculated by Equation (2.2). Carbon conversion and porosity, which both are locally dependent, are calculated in the model as follows:

$$X = 1 - \frac{C_C}{C_{C,0}} \tag{2.14}$$

$$\varepsilon = \varepsilon_0 + (1-\varepsilon_0) X = 1 - (1-\varepsilon_0)\left(\frac{C_C}{C_{C,0}}\right) \tag{2.15}$$

For the structural evolution of the particles during the gasification, different models have been proposed in the literature. For instance, RPM assumes that the pore structure of porous particles consists of cylindrical channels having different sizes and that the reaction takes place on the wall surfaces. According to this model, the relationship between the internal surface area of particle and its porosity can be given by [10, 32]:

$$S(X) = S_0(1-X)\sqrt{1-\psi \ln(1-X)} \tag{2.16}$$

where S_0 is the initial surface area, ψ is a dimensionless parameter indicating the nature of pore structure (i.e., RPM structural parameter) was calculated using Equation (2.18) and also other related parameters are determined by the following equations [33]:

$$S_0 = 2\int_0^{\infty} \frac{v_0(r)}{r} dr \tag{2.17}$$

$$\psi = \frac{4\pi L_0(1-\varepsilon_0)}{S_0^2} \tag{2.18}$$

$$\varepsilon = \int_0^{\infty} v_0(r) dr \tag{2.19}$$

$$L_0 = \int_0^{\infty} \frac{v_0(r)}{\pi r^2} dr \tag{2.20}$$

where L_0, ε, ρ_s, and $v_0(r)$ are the pore length, the porosity, the density of the anode particle, and pore radii distribution, respectively.

Gas diffusion in a porous solid is affected by the porosity and the pore structure. Therefore, an effective diffusion coefficient is considered. The effective molecular diffusivity (D_e) of the gas in a porous particle is obtained by [24]:

$$D_{i,e} = D_{ij} \frac{\varepsilon}{\tau} \tag{2.21}$$

where $D_{i,e}$, and D_{ij} are the effective diffusion coefficient of gaseous species and - molecular diffusion coefficient of the gaseous species, τ is the tortuosity factor, and ε is the particle porosity. The binary diffusion coefficient of component (D_{IJ}) at each temperature, for species I in reaction J, is estimated by correlation of Hirschfelder [34].

$$D_{IJ} = \frac{0.001858 T^{1.5} \left[\frac{1}{M_I} + \frac{1}{M_J}\right]^{0.5}}{P_{abs}\sigma_{IJ}^2 \Omega_D} \tag{2.22}$$

where, P_{abs} is Absolute pressure in atmospheres, M_I and M_J Molecular weights of I and J, respectively. σ_{IJ} is Lennard-Jones collision diameter in Angstroms, and Ω_D is Collision integral for molecular diffusion.

Both chemical reaction rate and diffusion rate may contribute to the overall reaction rate. At high diffusion rates, the chemical reaction could be a limiting factor, and reciprocally. Thiele modulus is a dimensionless parameter that informs which phenomenon has the leading characteristic time [35]. Here, a modified Thiele modulus (λ) is developed to account for the structural change undergone due to the consumption of the material during the particle's gasification. For a first-order chemical reaction, a modified Thiele modulus is defined as [15]:

$$\lambda^2 = \varphi^2 \sqrt{1+\psi \ln(1-\varepsilon_0) - \psi \ln(1-\varepsilon)} \times (1-\varepsilon)/\varepsilon^2 \tag{2.23}$$

in which φ is the Thiele modulus [15], defined as:

$$\varphi = r_0 (k \rho_s S_0 D_e)^{1/2} \tag{2.24}$$

where k is the reaction-rate constant, r_0 is the initial particle radius, ρ_s is the density of the anode particle, S_0 is the initial surface area, and D_e is the effective diffusivity.

The effectiveness factor η can be calculated using the modified Thiele modulus by the following equation:

$$\eta = \frac{1}{\lambda}\left(\frac{1}{\tanh(3\lambda)} - \frac{1}{3\lambda}\right) \tag{2.25}$$

As the largest characteristic length scale of the pore structure is much smaller than the characteristic length associated with the concentration gradients, the reaction rate term in Equations (2.6-2.8) should be adequately defined. So, from a particle point of view, the reaction rate per unit volume must be formulated in a "structural" form. Thus, a function that summarizes the available reaction sites at a given time should be introduced. To incorporate

this feature explicitly, we assume the following intrinsic kinetics at any location within the particle as:

$$R = -r(C_{CO_2}) \cdot F(X) \tag{2.26}$$

This reaction rate consists of two parts, $r(C_g)$ and $F(X)$. The first part stands for the influence of the gas phase components on the reaction rate, whereas the second part depicts the structural change brought by the reaction in the porous solid phase [31].

In this work, to model CO_2 gasification of the anode particles, two types of equations are used to describe the gas phase reaction, $r(C_A)$, a simple first-order form, and a Langmuir-Hinshelwood (L-H) form. The latter is preferred due to its ability to account for the species adsorption/desorption. In the L-H formulation, the adsorption coefficients of CO and CO_2 are assumed to be constant (k_1 , k_2 , and k_3), and the following pathway is proposed for this process:

$$C_f + CO_2 \xrightarrow{k_1} C(O) + CO \tag{2.27}$$

$$C(O) + CO \xrightarrow{k_2} C_f + CO_2 \tag{2.28}$$

$$C(O) \xrightarrow{k_3} CO + C_f \tag{2.29}$$

where C_f is the active carbon site, k_1 , k_2 , and k_3 are the reaction rate constants, and $C(O)$ represents the carbon-oxygen surface. The presence of CO results in lowering the steady-state concentration of $C(O)$ by an inhibiting effect $r(C_g)$ as described by Equation (2.30):

$$r_{c_g} = \frac{k_1 P_{co_2}}{1 + k_2 P_{co_2} + k_3 P_{co}} \tag{2.30}$$

Equation (2.26) becomes Equation (2.31) by substitution of $-r(Cg)$ (Equation 2.30):

$$R = \frac{k_1 P_{co_2}}{1 + k_2 P_{co_2} + k_3 P_{co}} F(X) \tag{2.31}$$

An Arrhenius-type of temperature dependence is assumed for k:

$$k = k_0 \exp(-\frac{E}{R_m T}) \quad (2.32)$$

where, E is activation energy, k_0 is the preexponential factor ($atm^{-n} \cdot s^{-1}$) and R_m is the universal gas constant ($kJ \cdot mol^{-1} \cdot K^{-1}$).

There are also various models to cast the kinetics of gasification reaction for the porous solid phase *F(X)*. In general, different kinetic models can be applied to the structure part of Equation (2.26), among which, the shrinking core model, the volumetric reaction model, the modified volumetric model, and the random pore model are widely used by researchers [9, 14, 15, 17, 18, 36, 37] (Table 2.2). To evaluate these different models, a set of experimental data is used. The carbon conversion is calculated by using various kinetic models and the solved set of equations is compared with the experimental data. Models that account for particle shrinking-core behavior usually assume that the external layer of the particles is removed with time, which is referred to the exposed shrinking-core model (CM). Therefore, in these models, the external mass transfer and intrinsic kinetics in the external surface are considered. Besides, reacting particles are assumed to preserve their spherical shape during gasification, as stated earlier. The reaction between particle and gas reactants is started on the interface of particle and gas. As the external surface is consumed, the reaction front moves gradually to the particle's interior. This results in decreasing the particle's radius during the gasification reaction progress. However, this model cannot capture the structural changes inside the particle since the gasification takes place only on the external surface of the particle.

On the other hand, in the volumetric model (VM), it is assumed that a homogeneous reaction occurs [10, 14, 15, 32]. It results in a linear decrease of the surface area with conversion during the reaction. In the RPM model, from a practical standpoint, while S_0 and ε_0 are accessible experimentally, L_0 cannot be measured [14, 15]. ψ is a free parameter that is adjusted using experimental data. The value of ψ is related to the solid material and the formation condition [26, 38, 39]. Moreover, modified random pore model (MRPM) is the improved pore structure model to simulate the evolution of superficial area of carbon

particles during CO_2 reaction. Different forms of MRPM have been proposed in the literature by introducing a new conversion term and a time function with two or three dimensionless parameters into the original random pore model [14, 40-43]. We used the equation which is proposed by Gómez-Barea [14] in which, the new conversion term and time function have a linear relation with time. It simplifies the equations and let us to find the analytical solution with reasonable results. The influencing factors, such as pore characteristics and the superficial area of porous particles during gasification are taking into account [40, 44, 45]. *t* in MRPM represents the gasification time, and ψ and, ω are the structural parameter and the power-law constant, respectively. ω is the power-law constant that can be positive or negative that shows the effects of time on *ks* that is defined by $[1+(\omega+1)(\alpha t)]$. The negative value of ω means that the reaction rate is constant. The higher value of ω (> 5) shows the higher impact of time on the reaction rate. In this case, MRPM can deliver reliable results comparing to RPM. α is a discreteness parameter. When α goes to zero, the results of RPM and MRPM are the same. The parameter α is related to the structural parameters of particles such as initial porosity and specific surface area. With an increase in α, the value of the surface area is reduced.

Table 2.2. Main structural reaction models for gasification rate [14, 31, 46].

Model	Equation $(F(X))$
Volumetric model (VM)	$(1-X)$
Shrinking core model (CM)	$(1-X)^{2/3}$
Random pore model (RPM)	$(1-X)\sqrt{1-\psi\ln(1-X)}$
Modified Random pore model (MRPM)*	$[1+(\omega+1)(\alpha t)](1-X)\sqrt{1-\psi\ln(1-X)}$
Traditional (TM)	$(1-X)^{n}$

* α: modified random pore model constant, (s^{-1}), ω : power-law constant, (-)

Several equations were applied to obtain the effective diffusion coefficient, which depends on both porosity and tortuosity (Equation (3.21)). Comiti and Renaud [16, 47, 48] defined the tortuosity of spheres based on the theoretical tortuosity-porosity relations. Their equations are used by numerous researchers, especially for porous carbon materials [49, 50]. Akkani and Evans investigated different practical equations to calculate tortuosity value, and their results showed that the effective diffusion could be related to the particle size, shrinkage, and the pore size of the particle [50]. In this work, we applied various tortuosity equations proposed in the literature to obtain the one best representing the anode particle behavior. To do so, the model was run using different models, and the calculated results using the MATLAB software were compared to the experimental gasification tests. The experiments were carried out at different particle sizes of 0.05, 1, and 3 mm to cover the diffusion effect from low to high, respectively. The errors were derived for R=1 mm from experimental validation and for other particle sizes (0.05 mm and 3 mm) by comparing experimental data with predicted model results. The results, summarized in Table 2.3, reveal that using the tortuosity expression in the first row is the most suitable one for anode particles ranging between 0.05 mm to 3 mm for which the fitted tortuosity led to the least error among all the tested tortuosity models.

Table 2.3 Summarized model results for different tortuosity equations for three anode particle sizes [50, 51].

Theoretical tortuosity–porosity relations				**Remarks**
	Error			
	R = 0.05 mm	R = 1 mm	R = 3 mm	
$\tau = (3-\varepsilon)/2$	0.04	0.01	0.05	Packing[50]
$\tau = 0.8(1-\varepsilon)+1$	0.08	0.03	0.07	Laboratory contaminant diffusion[51]
$\tau = \varepsilon^{-1/2}$	0.07	0.20	0.06	Spherical particle[51]
$\tau = 1-0.5\ln\varepsilon$	0.09	0.03	0.11	Sand-spherical particle[50]
$\tau = \varepsilon^{-2}$	0.04	0.03	0.05	Overlapping spheres[50]

2.3.2 Particle shrinkage

Understanding the structural features of anode particles and their evolution during gasification provides useful information for the development of gasification-based systems. During the gasification process, the anode particle starts to shrink, and the apparent radius of the anode particle (r_{ap}) decreases gradually. In this step, the outer layer of the solid is fragmented [32]. In the developed model, the fragmentation occurs when 100 % of an imaginary external layer is consumed. This imaginary external layer may have a finite thickness, which could be defined depending on the resolution of the calculations. In our model, the apparent radius is kept unchanged until the conversion at the outer surface layer reaches 100 %. On the other hand, at this step the thin outer layer of particle, reaches to conversion of $X(r_{ap})=1$. After consuming the outer layer, a new updated outer layer is defined, and the radius of the particle is now smaller by the thickness of the removed outer layer [32]. According to this description, the change in the anode particle radius during the process can mathematically be represented employing a moving boundary condition as follows:

$$\frac{\partial r_{ap}}{\partial t}=\begin{cases}0 & X(r_{ap})_{\text{outer layer}}<1\\ \dfrac{\partial X/\partial t}{\partial X/\partial r} & X(r_{ap})_{\text{outer layer}}=1\end{cases} \tag{2.33}$$

when 100 % of an imaginary external layer is consumed, the start point shrinkage conversion (X_{sh}) will be obtained by solving the second condition term of equation (2.33). Schematic of gasification inside an anode particle is illustrated in Figure 2.1. At the center of the particle, apparent radius equals 0, and at the outer layer of the particle, apparent radius and related anode conversion, equal r_{ap}, and $X(r_{ap})$, respectively.

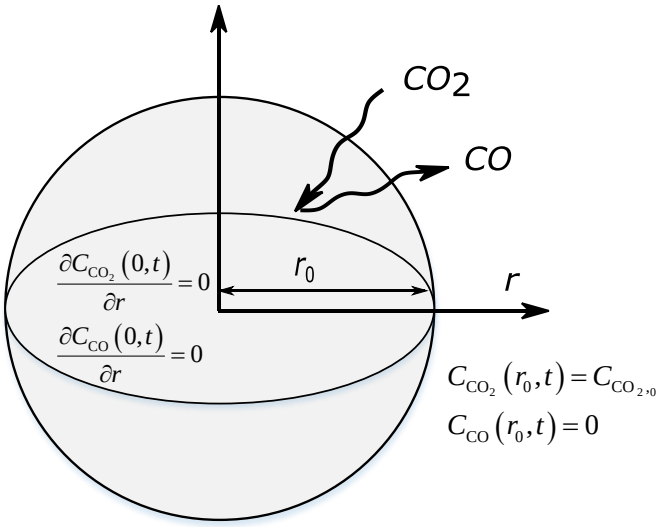

Figure 2.1 Conditions and conceptual gasification of a single particle.

2.3.3 Numerical method

In the developed model, the anode conversion (*X*) is the target variable to be computed. In this model, after reaching a critical carbon conversion rate, the apparent radius of the anode particle decreases until it eventually leads to particle vanishment (depending on the ash content of the particle, complete disappearance of this latter may not occur experimentally). Thus, it is essential to consider the moving boundary condition method for solving the proposed model. The model includes certain nonlinear partial differential equations (PDEs), which are also time-dependent equations. Since the numerical method of lines is a proper technique for solving the time dependent partial differential equations, the sets of PDEs of this model can be solved using this method [52]. In the method of lines, all the derivatives are substituted by the finite difference method, but the time derivatives remain with no change. It is assumed that the variables *C* and *X* are related to (r_i , t_j) but are independent on (r_{i-1} , t_j) or (r_i , t_{j-1}). Here, "*i*" and "*j*" indicate the indices of a computational grid node, index "*i*" defines the position and "*j*" the time instant. The grid number in the *r* direction equals 10 for a particle with 1 mm radius. The model is an explicit time step of a finite

difference algorithm, in which the time step is automatically defined, and it is compatible with the ODE solver. Therefore, PDEs are converted into a system of ordinary differential equation (ODEs). This package is written in MATLAB software in three-layers of calculations. All the input data are imported to the first layer; an appropriate model is defined; at the end of calculations, the results are returned to this layer. The second layer is a transporter layer in which all the required data are transported to the solver of the model. Besides, the results of the modeling are reflected from the calculation core to the upper layer by this part. The third layer (calculation core) is the ODE solver. In this package, the ODE solver consists of ode23s that accurately calculates rigid systems using raw error tolerances. This solver is an Implicit Runge-Kutta method. All unknown variables must be solved simultaneously in one system of ODEs. The model outputs are the carbon conversion (X) versus time. The model constants can be regressed using the experimental data of carbon conversion versus time.

Originally, X is a local value, but to compare it with the experimental value, X must be averaged over the particle volume at each time instant as follows:

$$X_{\text{ave}}(t) = \frac{3}{r_0^3}\int_0^{r_0} X(r,t)\, r^2 dr \tag{2.34}$$

We defined Equation (2.35) as an objective function for identification of the model constants, including the chemical reaction rate constant and adjustable parameters in the function of $F(X)$ such as ψ for RPM, w, and α for MRPM and n for TM equation.

$$\text{OF} = \sum_{j=1}^{H} (X_{\text{ave},j}(t) - X_{\text{exp},j}(t))^2 \tag{2.35}$$

where H is the number of experimental time points. The Values of OF are given in Table 2.3. The optimization procedure was done using fminsearch of MATLAB software [53]. That is, a set of ODEs are solve using ode23s of MATLAB software at different time points, then the calculated $X_{\text{ave}}(t)$ are inserted into equation 2.35 to calculate the objective function (OF). A termination tolerance equal to 10^{-4} was set both on the regressed parameters (Tolx) and OF values (TolFun). The fminsearch function stops when it satisfies both TolFun and TolX.

2.4 Results and Discussion

Figure 2.2 shows the conversion of the anode particle as a function of time both in terms of model predictions and experimentally determined one. Particles with an average size of 1 mm were used to generate experimental data, and the spherical particles of diameter 1 mm were used for simulation. In the model, we integrated different structural kinetic models presented in Table 2.3 to verify their suitability for the gasification of anode particles. The results exhibited good agreement between experiments and three models (RPM, MRPM, CM). The errors between experimental and simulated results are presented in Table 2.4. As the RPM model showed the reasonable outcome with the low error and number of parameters, thus, we used hereafter the RPM model to simulate the gasification of anode particles under varying conditions.

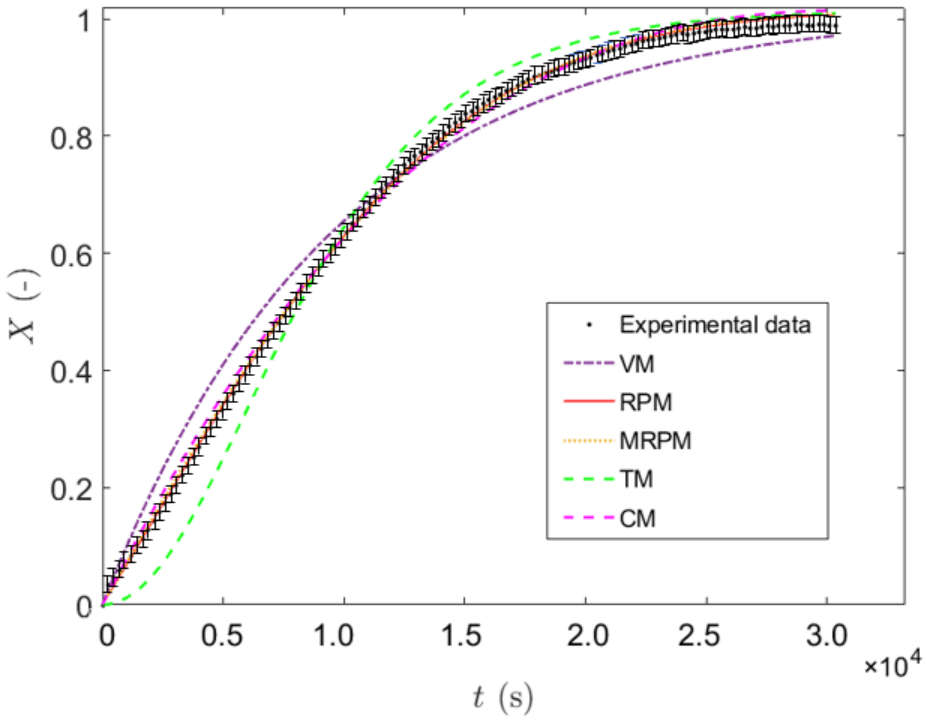

Figure 2.2 Anode particle conversion versus time using different kinetic models (experimental data comes from the gasification of the carbon particles with the size of 1 mm, T = 1233 K).

Figure 2.3 demonstrates the time required for full consumption of the particles with different sizes as a function of their initial radius. The results revealed that a good agreement exists between predicted (continuous red line) and measured (solid circles) data. As expected, the smaller particles are consumed faster due to both a higher specific external area and smaller quantity of material to be consumed.

Table 2.4 Model parameters for various structural kinetic models, where *r(C)* is the first-order equation.

Reaction Model	Model Parameters	OF
VM	k = 1.7064 (s^{-1})	1.7E-03
CM	k = 3.5873 (s^{-1})	2.4E-4
RPM	k = 1.0935 (s^{-1}) ψ = 2.7687	5.60E-05
MRPM	k = 0.3959 (s^{-1}) ψ = 2.9811 ω = -1.0076 (s^{-1}) α = 0.0031	5.59E-05
TM	k = 1.3178 (s^{-1}) n = 1.1790	6.6E-03

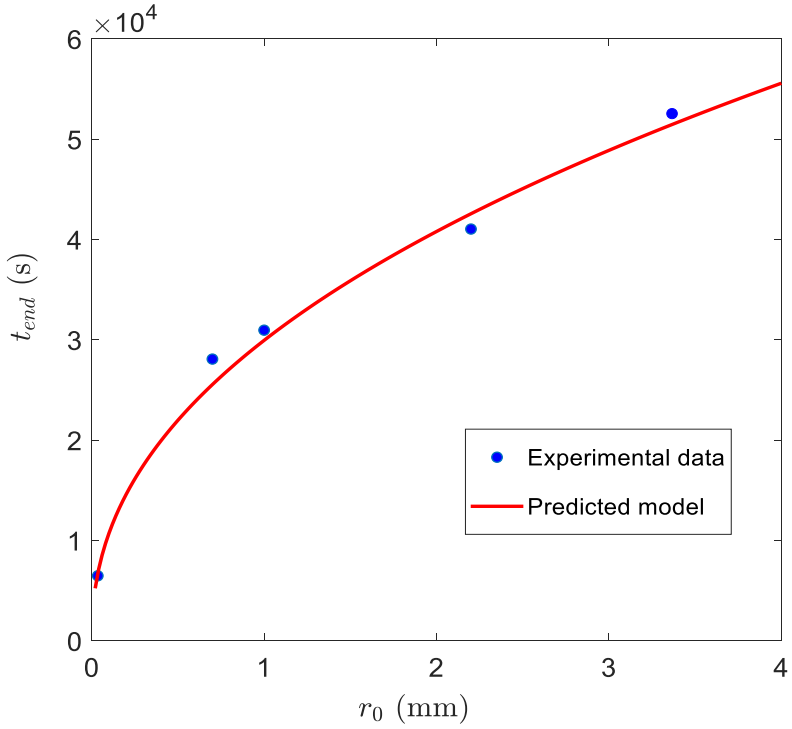

Figure 2.3 Time for full consumption versus initial particle radius (T = 1233 K).

Figure 2.4 shows the simulated plots of anode particle conversion versus time for different particle sizes. The experimental data points for the particle size of 1 mm were also presented for comparison. Figure reveal that the model validated by one set of experiment data (particle size = 1 mm) and other particle sizes were obtained by model prediction not just validation and data fitting. The results suggest that the particle size significantly affects the reaction rate of the particle gasification (as reflected by the slope of the curves). As the particle size decreases, the reaction rate increases, and full consumption is reached in a shorter time. Particles with a radius larger than 1 mm did not achieve total consumption after 10 hours of reaction. This could be attributed to the larger external surface area of the fine particles compared to that of the coarser ones. This also indicates the diffusion-inhibited reaction rate for the coarser particles [23], the same as the observations reported by Gómez [14]. As expected, the conversion rate holds a direct relationship with the reaction time, but an inverse relationship with the particle size.

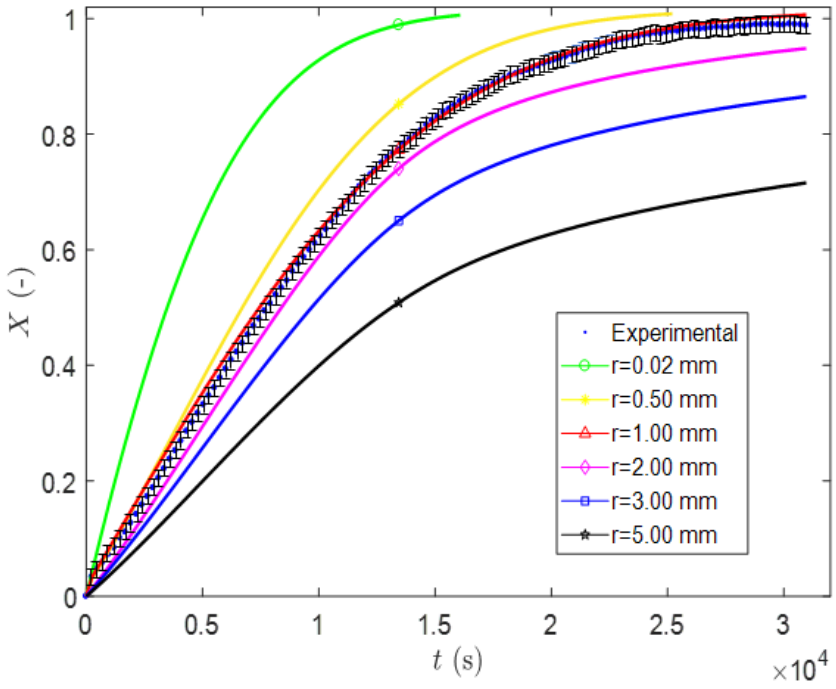

Figure 2.4 Conversion versus time for different particle sizes of anode particle (experimental data for the particle size 1 mm, T = 1233 K).

CO_2 mole fraction inside a reacting particle (the concentration of component i is defined as $Y=n_i/V$)., predicted by the model during the gasification time, is shown in Figure 2.5 for Equations 3.6-3.7 solved for the central position (r = 0) of the anode particle for different particle sizes. Initially, CO_2 reactive gas is introduced into the pores. Therefore, the CO_2 mole fraction is near one within the pores and at the surface of the particles (Figure 2.5 a). When the reactions start, CO_2 is consumed and CO is generated, resulting in a gradual increase of CO concentration at the expense of that of CO_2. The graph (Figure 2.5 b) shows that the CO_2 concentration at the center of the particle decreases first to reach a minimum at ($t = 1\times10^4$ s), then it increases gradually until the particle is fully consumed. This peak of CO_2 is attributed to the quick consumption of active carbon at the beginning of the reaction. In fact, not all carbon sites have the same activity with respect to CO_2, and some of them are more reactive, as reported earlier [36]. In these areas, carbon is consumed quickly when they come in contact with CO_2. Therefore, in the beginning (Figure 2.5 a), the rate of reaction is high due to the presence of active carbon sites, resulting in a quick depletion of CO_2 concentration over the first 25 s. Then, the rate of CO_2 reaction with carbon decreases as the active sites are consumed. At the same time, the presence of CO results also in a decrease of CO_2 reaction with carbon. These two phenomena result in a balance between the consumption rate of CO_2 and its diffusion rate from the surface at around $t= 1\times10^4$ s. By progressing the reaction, the porosity of the particle increases, so as its permeability, leading to the increase of the CO_2 diffusion from the surface and its mole fraction at the center of the particle. The reaction rate with CO_2 for all particle sizes follows the same trends. Another observation is that the CO_2 fraction at the center of large particles is always smaller than that of the fine particles, mainly due to higher diffusion distance.

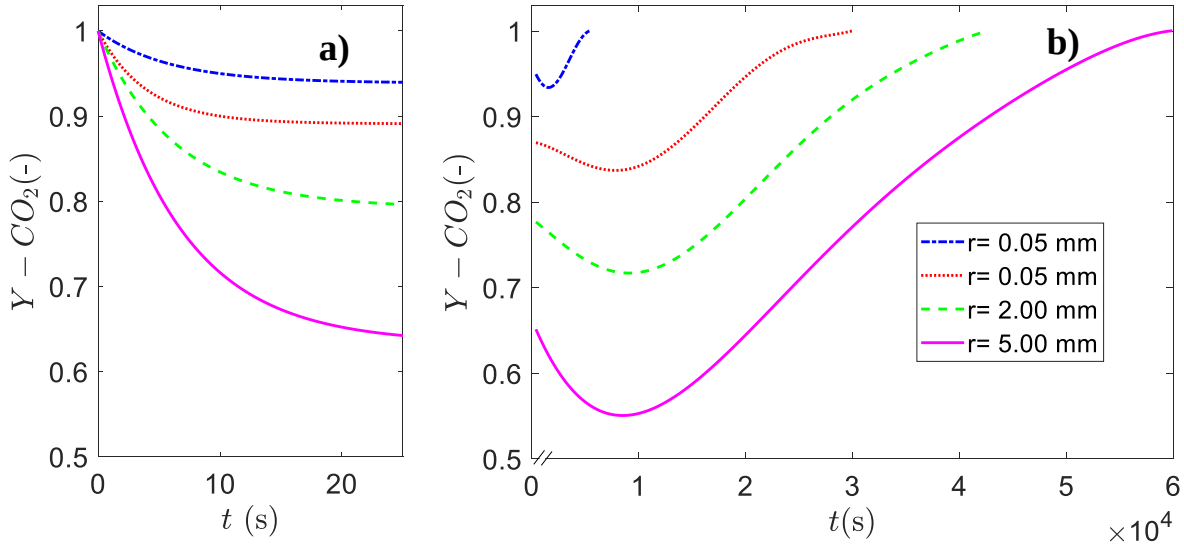

Figure 2.5 Mole fractions of CO_2 inside reacting anode particle (at r = 0) versus time for various initial particle sizes and T = 1233 K and different time scales, a) the first 25 s, b) the rest of the process time.

2.4.1 Structural evolution of anode particle during gasification

Figure 2.6 is demonstrating RPM predictions of carbon consumption as a function of time for particles with a radius of 1 mm for different initial porosity. The rate of solid consumption (slope of curves in Figure) in the first stage of the reaction is steep, and then it reduces gradually at a later stage. The monotonic reduction of reaction rate is presumably ascribed to the lesser amount of residual solid to react as reaction progresses. Therefore, the porous samples will vanish in a shorter process time. The difference between slopes increases by increasing the porosity. As expected, for the samples with higher porosity (ε >= 0.5 and more), the slope of the curves at the first stage is steeper since the diffusion rate is higher at high porosity levels and conversely for the sample with lower porosity (ε <= 0.2 and less) the difference between two stages is not significant.

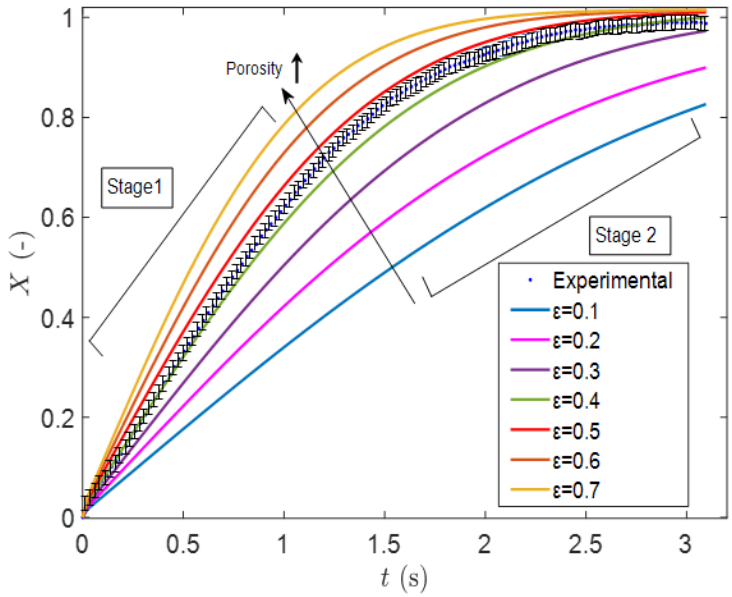

Figure 2.6 The effects of initial porosity on the conversion of carbon versus time, initial particle radius is 1 mm, T = 1233 K.

Experimentally, Figure 2.7 shows the pore volume distributions measured by mercury intrusion (Auto Pore IV, Micromeritics, Norcross, GA, USA) as a function of the pore size for anode particles gasified under CO_2 at 1233 K and at gasification levels of 0, and 50 wt % for two particle sizes (1 mm and 2 mm). As can be seen in Figure the pore interval (0.1 - 40 μm) has the largest pore volume for both particle sizes, and these pore sizes increase strongly with the increase in the percentage of gasification. A broader peak for the pore size range larger than approximately 80 μm is observed that is associated with the voids between the particles.

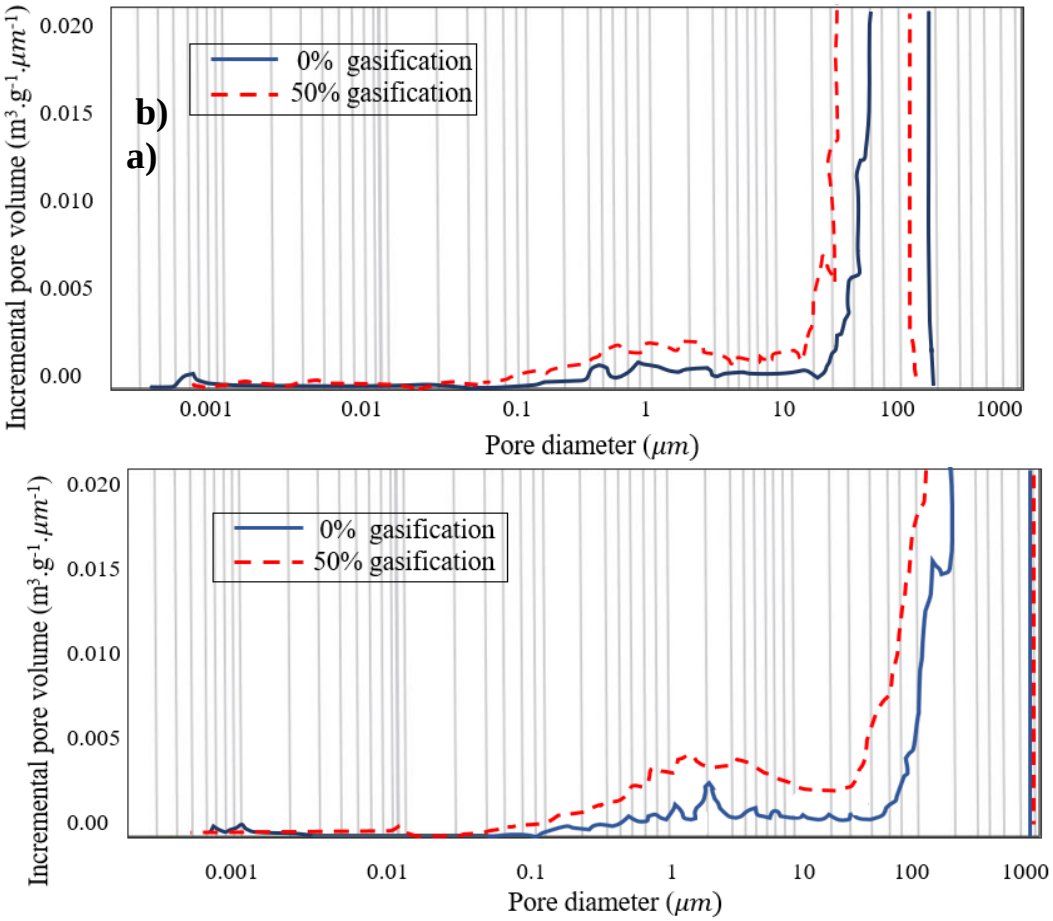

Figure 2.7 Pore volume distribution versus the pore size for anode particles gasified in two particle sizes a) 1 mm, and b) 2 mm, gasified at two percentages (0 and 50 %) under CO_2 at T = 1233 K by intrusion of mercury

Over the gasification process, the model includes both effects of transport of gaseous species and intrinsic reaction rates. Due to the diffusion resistance, it is expected that the reaction on the particle surface be faster than that inside the particle. This description conforms to simulation outcomes for the anode particle gasification at 1233 K, as shown in Figure 2.8.This figure presents the consumption of carbon (mole fraction) as a function of time at three different locations of the particles: at the external layer, at the middle radial position, and at the center of the particle. As Figure 2.8 show, the anode particle on the external surface layer will be consumed faster than on other positions within the anode particle. This difference is getting larger when the size of the particle increases. The shorter consumption time at the surface confirms the particle shrinkage over the gasification process.

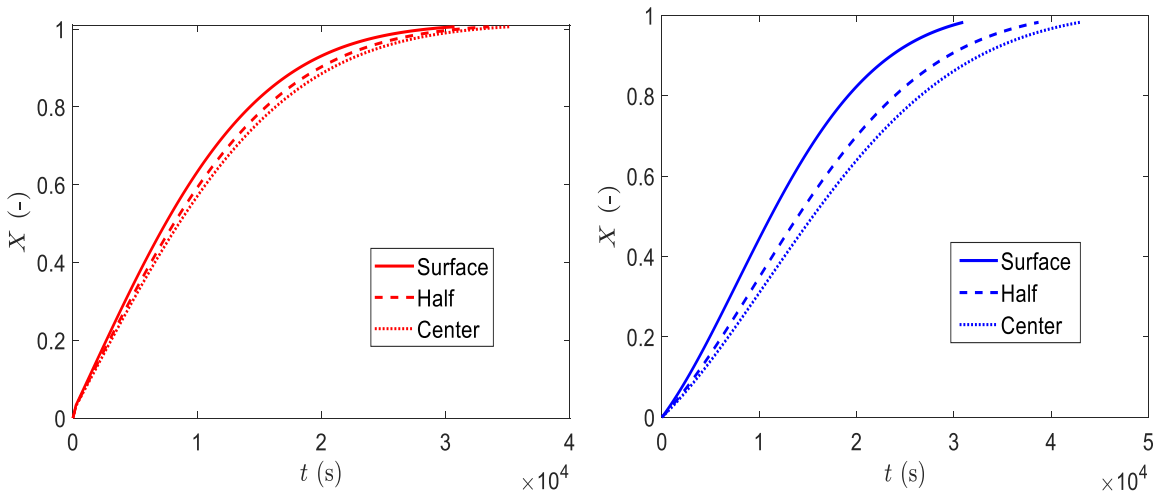

Figure 2.8 The mole fraction of the consumption anode particle during process time for three positions (surface, middle, and center of the particle). Initial particle size a) r_0 = 1 mm, b) r_0 = 2 mm.

Figure 2.9 a shows the change of the relative particle radius (r/r_0) as a function of reaction time. It can be seen that the relative radius of all samples remains unchanged within the first 1×10^4 s of reaction. After this period, the particles start to shrink. According to Figure , this reaction time corresponds to almost full consumption of small particles (r = 0.05 mm) and 33 % of consumption for the largest particles (r = 5 mm). It is interesting to see which fraction of a particle is consumed when it starts to shrink. Thus, we plotted the shrinkage conversion, corresponding to the conversion of the partcile at a shrinkage starting point (X_{sh}), as a function of particle radius (Figure 2.9 b). We can see that Xsh decreases sharply with increasing particle size. In other words, as the particle radius increases, inception of shrinkage occurs at the smaller conversions, X_{sh}, e.g., 45, 33, 25, 18, and 12 % for r_0 = 1, 2, 3, and 5 mm, respectively.

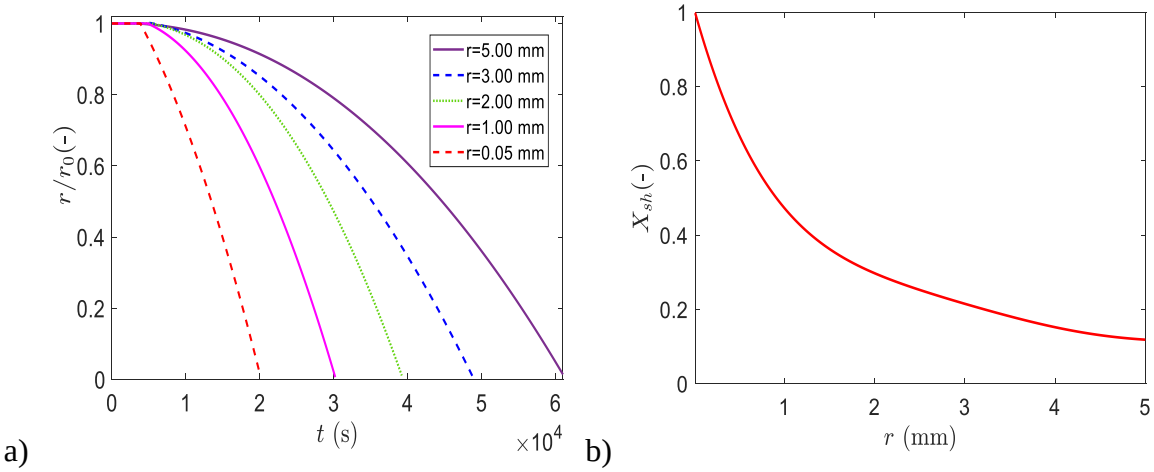

Figure 2.9 a) Relative radius (r/r_0) versus processing time for different anode particle radii, b) X_{sh} versus initial particle radius.

2.4.2 Modified Thiele module and effectiveness factor

The modified Thiele modulus, λ, describes the relationship between diffusion and reaction rate in porous particles with no mass transfer limitations [35] (Equation 2.23). The effectiveness factor, η, is a measure indicating that the diffusion resistance neutralizes the intrinsic reaction rate (Equation 2.25). An effectiveness factor approaching unity indicates that the reaction controls the process. The results of the kinetic model show that, depending on particle size and the mass conversion of the anode, the intrinsic reaction and diffusion can be significant parameters in determining the overall gasification process. Achieved by RPM expression at multiple carbon conversions, the effectiveness factors,η, and modified Thiele module, λ, are shown in Table 2.5 for both first-order and L-H kinetic models. By increasing the particle size, modified Thiele modulus increases whereas the effectiveness factor decreases. It means that, as expected, the diffusion resistance increases with the particle size, resulting in a reduction in the effectiveness factor [23].

For all samples, the effectiveness factor increases by conversion, approaching 1 at 80 % of conversion. When the carbon conversion does not exceed 60 %, the results reveal that both reaction and diffusion control the reaction. By further increasing in the anode conversion, the

reaction becomes more dominant; due to the particle shrinkage during the gasification process.

For small particles (r = 0.035 mm) the low values of Modified Thiele modulus (< 2) demonstrate that reactant is homogeneous distributed inside of the anode, and therefore, diffusion resistance is negligible. Inversely, for the larger particles (2.2 mm), especially for the initial conversion, high values of modified Thiele modulus (> 3) confirm that the diffusion significantly resists against the gasification for large particles. By starting the gasification process and anode particle conversion, modified Thiele modulus decreases and approached one at 80 % of conversion. Because at the early stages, the reactant gas cannot easily penetrate inside the particle and the diffusion is dominant for larger particles [11].

Table 2.5 Modified Thiele moduli and Effectiveness factor for different particle sizes and carbon conversions.

radius (mm)	Reaction rate	Definition	Carbon conversion %				
			0	20	40	60	80
0.035	First order	Effectiveness factor	0.81	0.85	0.89	0.94	0.98
		Modified Thieles	1.89	1.75	1.41	1.11	0.40
	L-H	Effectiveness factor	0.75	0.79	0.86	0.93	0.97
		Modified Thieles	1.94	1.82	1.45	1.15	0.43
0.7	First order	Effectiveness factor	0.49	0.64	0.79	0.88	0.94
		Modified Thieles	4.98	3.22	2.37	1.50	1.01
	L-H	Effectiveness factor	0.44	0.60	0.75	0.86	0.93
		Modified Thieles	5.41	3.41	2.56	1.59	1.06
1.0	First order	Effectiveness factor	0.45	0.63	0.77	0.87	0.93
		Modified Thieles	5.47	3.25	2.46	1.54	1.04
	L-H	Effectiveness factor	0.38	0.57	0.71	0.81	0.90
		Modified Thieles	5.74	3.45	2.57	1.67	1.18
2.2	First order	Effectiveness factor	0.43	0.59	0.74	0.86	0.92
		Modified Thieles	5.71	4.80	2.5	1.68	1.07
	L-H	Effectiveness factor	0.36	0.53	0.68	0.81	0.89
		Modified Thieles	6.19	5.06	2.81	1.79	1.16

2.4.3 Specific surface area

The model allows capturing the evolution of the specific surface area during the gasification process. Figure 2.20 a shows the evolution of the surface area versus the gasification conversion for four different particle sizes. For ease of comparison in a single graph, we used the relative specific surface area, obtained by dividing the actual specific surface area of the sample (S) into its initial specific surface area (S_0) to make a dimensionless parameter for the specific surface area. It can be seen that the specific surface area increases at the early stages of the gasification, reaching a maximum, and then declining until vanishing. By computing the derivative of the curves and plotting it against the gasification conversion (X), the maximum of the curves can be better visualized. These maxima can be seen in Figure b, where the curves cross the zero line. We can see that the maximum specific surface area for the smallest sample (r = 0.05 mm) occurs after 25 % of gasification. By increasing the particle size, the maximum is shifted towards lower gasification levels. For instance, this maximum occurs at 4 % gasification for the largest sample (r = 3 mm). In other words, the conversion at which the maximum surface area occurs depends on the particle size and it decreases drastically by increasing the particle size. For all particle sizes, the specific surface area increases at the early stage of conversion. This is attributed to pore enlargement. However, with the progress of gasification, the overlapping of the multiple capillaries [22] and the coalescence of neighboring pores [26, 54] take place (mostly through disappearing inter-walls), thus decreasing the specific surface area. For the small particles, there is not a big difference between the reaction rates at the internal and external layers (Figure 2.10 a); however, this difference becomes significant as the particle size increases (Figure 2.10 b). The delay of the reaction in the internal layers mitigates the increase of the specific surface area. That is, when the internal layer reaches its maximum specific surface area, the surface area of the external layers is already in a declining phase. Therefore, the maximum is barely seen for the largest particle.

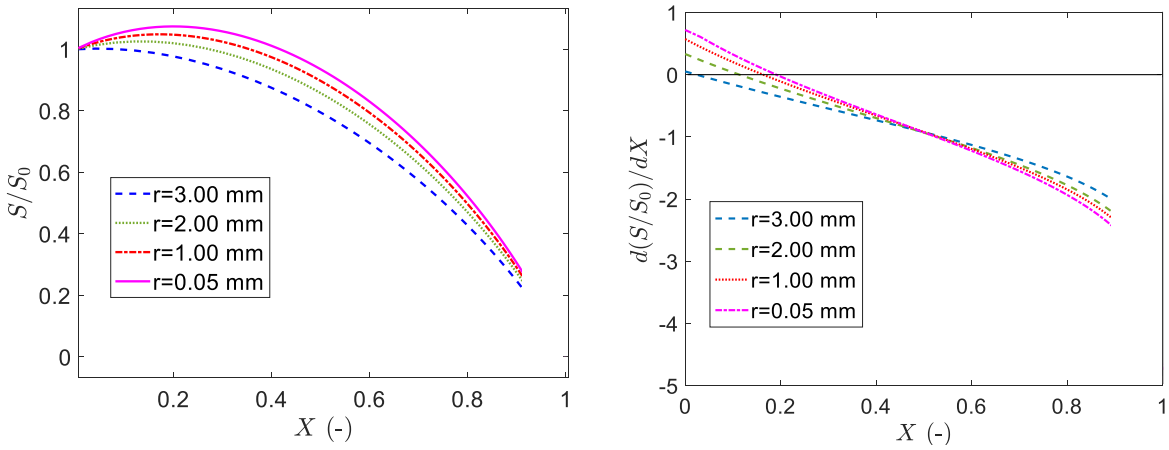

a) b)

Figure 2.10 a) Prediction of the surface area of the particle during the gasification. b) Differentiation of surface area versus carbon conversion (T = 1233 K, r = 3.0, 2, 1.0 and 0.05 mm).

2.4.4 Inhibition effect of CO in anode gasification

The presence of CO in the internal anode pores can play an inhibition role on the carbon gasification reaction which could explain the lower observed reaction rate compared to the expected one. To describe these observations, the inhibition effect caused by CO should be modelled by a reasonable kinetic expression to understand its effect. A Langmuir-Hinshelwood model can adequately separate the inhibition effect of CO (chemical limitation) from purely diffusional effects (physical limitation). It is believed that adsorption of CO_2 on the surface of the anode followed by desorption of CO are the main steps determining the gasification rate (Equations 2.27-2.29). Adsorption of CO on the carbon sites may decrease the rate of adsorption of CO_2 by occupying the active sites, thus inhibiting the reaction rate. To assess this effect, we ran the reaction with three different CO concentrations in the inlet gas. Figure 2.11 shows the conversion in mole fraction at the center of a particle (r = 1 mm) as a function of time for three different inlet gas compositions. Table 2.6 shows the experimental data and the corresponding values obtained from the model for the parameters of k_1, k_2, and k_3 (L-H Equation), for different values of initial P_{CO}, as well as their temperature

dependence by means of its Arrhenius coefficients. The results show good agreement between calculated data and experimental data for k_1 and k_3 but there is a high level of uncertainty and discrepancy for k_2, particularly at the start and the end partial pressure ratio ranges (P_{CO}/P_{CO_2} = 0 and 1). These values confirm stronger CO inhibition effect in the anode-CO_2 gasification in comparison with that obtained with pure CO_2 in the inlet gas. As a result of this mechanism, any increase in CO amount at the inlet gas causes a decrease in the conversion of anode particles during the gasification process.

Figure 2.12 shows the rate of gasification reaction as a function of time for three different gas compositions in the inlet gas. It can be seen that the rate of reaction at the beginning of the reaction is much smaller for higher CO concentrations. As discussed above, all reactions reach a maximum rate after a while, which is due to the fast reaction of the more active carbon sites. However, this maximum occurs earlier for pure CO_2. The inhibition effect of CO delays the occurrence of this maximum and decreases the maximum value of the reaction rate. After about 1×10^4 s, it seems that the reaction rate for the samples with pure CO_2 becomes smaller than those with CO in the inlet gas. This is basically due to the lower amount of remaining solid carbon in the former case at the same reaction time. For instance, at $t = 1\times10^4$ s 60 % of the sample is consumed under pure CO_2 while only 42 % is consumed under 50 % CO_2.

Table 2.6 Reaction-rate parameters k of the L–H model for anode-CO_2 gasification in different temperatures and CO concentrations in the inlet gas

		Model results				Experiment result		
Temperature (K)	$\frac{P_{CO}}{P_{CO_2}}$	k_1 ($g\cdot cm^{-2}\cdot atm^{-1}\cdot s^{-1}$)	$k_2\times10^5$ ($atm^{-1}\cdot s^{-1}$)	$k_3\times10^5$ ($atm^{-1}\cdot s^{-1}$)	R^2	k_1 ($g\cdot cm^{-2}\cdot atm^{-1}\cdot s^{-1}$)	$k_2\times10^5$ ($atm^{-1}\cdot s^{-1}$)	$k_3\times10^5$ ($atm^{-1}\cdot s^{-1}$)
1233	0.00	100.6	105	66	96.8	101.5	101	66
1233	0.25	96.6	101	64	98.6	97.9	101	65
1233	0.50	95.3	102	63	99.4	95.8	102	64
1233	0.75	91.2	102	64	98.8	90.8	102	63
1233	1.00	84.9	97	63	96.5	84.4	103	62
1193	1.00	82.8	94	62	97.9	85.0	95	63
1273	1.00	86.7	98	64	98.4	85.7	99	64

According to the L-H mechanism, it is possible to use the values of activation energies (E_1, E_2 and E_3) respectively corresponding to k_1, k_2 and k_3 to illustrate how the various activation energies are involved in the C-CO_2 reaction. The amount of activation energy was calculated by Arrhenius-type of temperature dependence (Equation 2.32) for each L-H mechanism step. The activation energies of 59 kJ·mol^{-1}, 17 kJ·mol^{-1} and 187 kJ·mol^{-1}, were obtained for three steps of the reaction, respectively. Higher partial pressure of carbon monoxide leads to a decreasing gasification rate, which is reflected by the k_3 reaction rate constant of L-H Equation (2.30) [9-11, 25, 55]. Results are in accordance with those obtained in most studies and showing that the activation energy of step 3 (E_3) is higher than that of step 1 (E_1). This means that the third step (Equation 2.29) is the limiting step of the reaction rate [56].

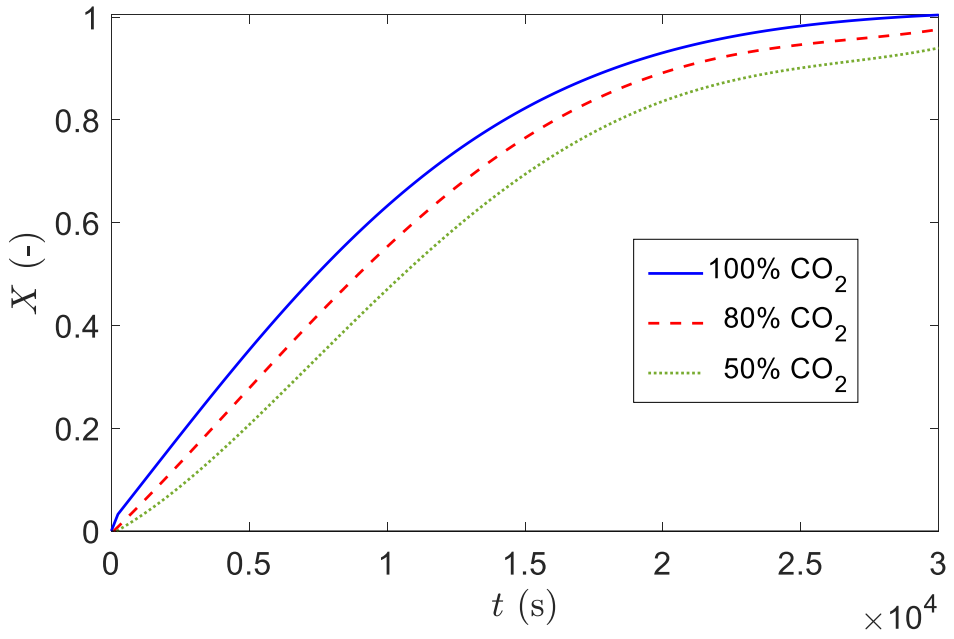

Figure 2.11 Anode particle conversion versus process time at the different ratios of the partial pressure of CO_2 and CO in the inlet gas (T = 1233 K, r_0 = 1.0 mm).

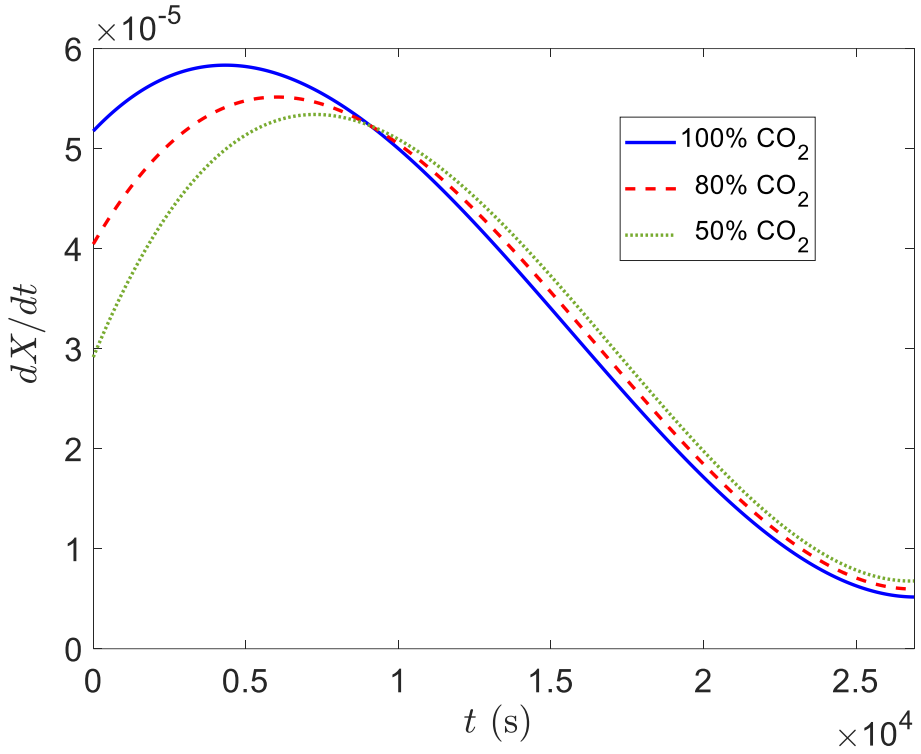

Figure 2.12 Simulation of anode particle gasification rate at the different ratios of the partial pressure of CO_2 and CO in the inlet gas (T = 1233 K, r_0 = 1.0 mm).

2.5 Conclusion

A diffusion-reaction model was developed for the gasification reaction of aluminum-industry anode particles, involving different kinetic models. The model assumed spherical symmetry and included the most notable chemical reactions, e.g., Boudouard reaction, intra-particle mass transfer resistance, mass conservation and anode structural characteristics such as porosity, permeability and shrinkage. The heat transfer was not included since the size of the anode particles was small enough to assume insignificant temperature gradient across the particle. A numerical method was used to solve the model. Model parameters were obtained experimentally by reacting monolayer anode particles in TGA. According to the experimental and simulated results, we concluded that the random pore model (RPM) is best describing the anode reaction behavior. Thus, this model was chosen among 5 models tested in this study.

The model outputs allow tracking the particle consumption rate and the distribution of gas composition inside the reacting particle. In addition, due to the moving boundary condition for the external gasification, it is also possible to track the shrinkage and structural evolution of the particle during the gasification process. These data, mostly impossible to obtain experimentally, allow better interpretation of the reaction behavior. As such, the evolution of different parameters such as particle size, processing time, porosity, and surface area of the anode particles during gasification are revealed and their effect on the gasification process are discussed. The simulation results demonstrated that the anode structure (specific surface area and porosity) has a significant effect on both the intrinsic reaction rate and the intra-particle mass transport. The relative importance of intrinsic reaction and diffusion on the overall gasification process are quantified by calculating the Thieles modulus and effectiveness factor. Analyzing these factors reveals that their contribution on gasification rate may evolve at different stages of reaction, i.e., diffusion is more important at the beginning and chemical reaction becomes dominant towards the end of gasification. The L-H type reaction, integrated in the model, allowed revealing the inhibition effect CO on the gasification reaction. Although the inhibition effect of CO on carbon gasification is a well-known feature, our model allows quantifying this effect along the whole gasification process. The effect of three different concentrations of CO in the inlet gas were given as examples. In summary, the model predicts well the gasification rate of anode particles, considering structural and diffusion parameters, thus offering a useful tool for optimization of gasification of anode particles.

Acknowledgments

The authors would like to acknowledge the financial support of Natural Sciences and Engineering Research Council of Canada, Fonds de Recherche du Québec - Nature et Technologies, Alcoa Canada Inc. and the Aluminium Research Centre – REGAL. The authors would like to express their appreciation to Mr. Guillaume Gauvin and Hugues Ferland for their technical support.

References

1. Azari, K., *Investigation of the materials and paste relationships to improve forming process and anode quality*, in *Material and Metallogy Department* 2013, Ph.D. dissertation, Laval Uinversity: Canada.
2. Chevarin, F., et al., *Active pore sizes during the CO_2 gasification of carbon anode at 960°C.* Fuel, 2016. **178**: p. 93-102.
3. Tabatabaee Ghomshe, S.M., R. Aminzadeh, and M. Abarzani, *Use of response surface methodology to study the combined effect of various parameters on hexavalent chromium adsorption.* Chemical Engineering Communications, 2014. **201**(2): p. 191-208.
4. Azari, K., et al., *Compaction properties of carbon materials used for prebaked anodes in aluminum production plants.* Powder Technology, 2013. **246**(C): p. 650-657.
5. Azari, K., et al., *Influence of coke particle characteristics on the compaction properties of carbon paste material.* Powder Technology, 2014. **257**: p. 132-140.
6. Keller, F., U. Mannweiler, and E. Knall, *Anode for the aluminum industry.* Constructing and Operating Anode Plants: What Top Management Needs to Know; R & D Carbon Ltd.: Sierre, Switzerland, 1995: p. 217-224.
7. Jamshidi, E. and H. Ale Ebrahim, *An incremental analytical solution for gas-solid reactions, application to the grain model.* Chemical Engineering Science, 1996. **51**(18): p. 4253-4257.
8. G.S., L., et al., *Modeling of Infra-Particle C-CO_2 Reaction: An Application of the Random Pore Model.* Developments in Chemical Engineering and Mineral Processing, 1999. **7**(5-6): p. 525-536.
9. Kajitani, S., et al., *CO_2 gasification rate analysis of coal char in entrained flow coal gasifier.* Fuel, 2006. **85**(2): p. 163-169.
10. Mandapati, R.N., et al., *Experiments and Kinetic Modeling for CO_2 Gasification of Indian Coal Chars in the Context of Underground Coal Gasification.* Industrial & Engineering Chemistry Research, 2012. **51**(46): p. 15041-15052.
11. Mani, T., N. Mahinpey, and P. Murugan, *Reaction kinetics and mass transfer studies of biomass char gasification with CO_2.* Chemical Engineering Science, 2011. **66**(1): p. 36-41.
12. Chevarin, F., et al., *Characterization of carbon anode constituents under CO_2 gasification: A try to understand the dusting phenomenon.* Fuel, 2015. **156**: p. 198-210.
13. Kovacik, G., A. Chambers, and B. Özüm, *CO_2 gasification kinetics of two Alberta coal chars.* The Canadian Journal of chemical engineering, 1991. **69**(3): p. 811-815.
14. Gómez-Barea, A. and P. Ollero, *An approximate method for solving gas–solid non-catalytic reactions.* Chemical Engineering Science, 2006. **61**(11): p. 3725-3735.
15. Fei, H., et al., *A New Mathematical Model Study on CO_2 Gasification Reaction of Typical Agricultural Residues.* Industrial & Engineering Chemistry Research, 2012. **51**(42): p. 13619-13626.
16. Comiti, J. and M. Renaud, *A new model for determining mean structure parameters of fixed beds from pressure drop measurements: application to beds packed with parallelepipedal particles.* Chemical Engineering Science, 1989. **44**(7): p. 1539-1545.
17. Zhang, J.-L., et al., *A Modified Random Pore Model for the Kinetics of Char Gasification.* BioResources, 2014. **9**(2): p. 11.
18. Zou, J.H., et al., *Modeling reaction kinetics of petroleum coke gasification with CO_2.* Chemical Engineering and Processing: Process Intensification, 2007. **46**(7): p. 630-636.
19. Rafsanjani, H.H. and E. Jamshidi, *Kinetic study and mathematical modeling of coal char activation.* Chemical Engineering Journal, 2008. **140**(1): p. 1-5.

20. Wu, Y., S. Wu, and J. Gao, *A Study on the Applicability of Kinetic Models for Shenfu Coal Char Gasification with CO_2 at Elevated Temperatures.* Energies, 2009. **2**(3): p. 545.
21. Zhang, Y., et al., *Modeling of catalytic gasification kinetics of coal char and carbon.* Fuel, 2010. **89**(1): p. 152-157.
22. Tomaszewicz, M., et al., *The kinetics of CO_2 gasification of coal chars.* Journal of Thermal Analysis and Calorimetry, 2013. **113**(3): p. 1327-1335.
23. Huo, W., et al., *Mechanism analysis and experimental verification of pore diffusion on coke and coal char gasification with CO_2.* Chemical Engineering Journal, 2014. **244**: p. 227-233.
24. Prabhakar, A., et al., *Modeling and Experimental Studies on CO_2 Gasification of Coarse Coal Char Particle.* Energy & Fuels, 2017. **31**(3): p. 2652-2662.
25. Keller, F., F. Küster, and B. Meyer, *Determination of coal gasification kinetics from integral drop tube furnace experiments with steam and CO_2.* Fuel, 2018. **218**: p. 425-438.
26. Matsumoto, K., et al., *Gasification reaction kinetics on biomass char obtained as a by-product of gasification in an entrained-flow gasifier with steam and oxygen at 900–1000°C.* Fuel, 2009. **88**(3): p. 519-527.
27. Reyes, S. and K.F. Jensen, *Percolation concepts in modelling of gas-solid reactions—II. Application to char gasification in the diffusion regime.* Chemical Engineering Science, 1986. **41**(2): p. 345-354.
28. Jamshidi, E. and H. Ale Ebrahim, *A new solution technique of moving boundary problems for gas-solid reactions; application to half-order volume reaction model.* The Chemical Engineering Journal and the Biochemical Engineering Journal, 1996. **63**(2): p. 79-83.
29. Jamshidi, E. and A.A. Ebrahim, *Erratum to 'A quantized solution for the nucleation model in gas—solid reactions' [Chemical Engineering Journal 68 (1997) 1–6].* Chemical Engineering Journal, 1998. **70**(3): p. 245.
30. Everson, R.C., H.W.J.P. Neomagus, and R. Kaitano, *The random pore model with intraparticle diffusion for the description of combustion of char particles derived from mineral- and inertinite rich coal.* Fuel, 2011. **90**(7): p. 2347-2352.
31. Gómez-Barea, A., P. Ollero, and R. Arjona, *Reaction-diffusion model of TGA gasification experiments for estimating diffusional effects.* Fuel, 2005. **84**(12): p. 1695-1704.
32. Xu, Q., S. Pang, and T. Levi, *Reaction kinetics and producer gas compositions of steam gasification of coal and biomass blend chars, part 2: Mathematical modelling and model validation.* Chemical Engineering Science, 2011. **66**(10): p. 2232-2240.
33. Bhatia, S.K. and D.D. Perlmutter, *A random pore model for fluid-solid reactions: I. Isothermal, kinetic control.* AIChE Journal, 1980. **26**(3): p. 379-386.
34. Welty, J.R., *Fundamentals of momentum, heat, and mass transfer*. 5th ed. 2008, Hoboken, N.J. ; Chichester: Wiley. xiii, 711 p.
35. Levenspiel, O., *Chemical reaction engineering*. 3rd ed. 1999, New York: Wiley. xvi, 668 p.
36. Xu, Q., S. Pang, and T. Levi, *Reaction kinetics and producer gas compositions of steam gasification of coal and biomass blend chars, part 1: Experimental investigation.* Chemical Engineering Science, 2011. **66**(10): p. 2141-2148.
37. Ollero, P., et al., *Diffusional effects in TGA gasification experiments for kinetic determination.* Fuel, 2002. **81**(15): p. 1989-2000.
38. Sadhukhan, A.K., P. Gupta, and R.K. Saha, *Characterization of porous structure of coal char from a single devolatilized coal particle: Coal combustion in a fluidized bed.* Fuel Processing Technology, 2009. **90**(5): p. 692-700.
39. Ochoa, J., et al., *CO2 gasification of Argentinean coal chars: a kinetic characterization.* Fuel Processing Technology, 2001. **74**(3): p. 161-176.
40. Zhang, Y., et al., *Proposal of a semi-empirical kinetic model to reconcile with gasification reactivity profiles of biomass chars.* Fuel, 2008. **87**(4): p. 475-481.

41. Bhatia, S.K. and B.J. Vartak, *Reaction of microporous solids: The discrete random pore model.* Carbon, 1996. **34**(11): p. 1383-1391.
42. Struis, R.P.W.J., et al., *Gasification reactivity of charcoal with CO_2. Part I: Conversion and structural phenomena.* Chemical Engineering Science, 2002. **57**(17): p. 3581-3592.
43. Betancur, M., et al., *CO_2 gasification of char derived from waste tire pyrolysis: Kinetic models comparison.* Fuel, 2020. **273**: p. 117745.
44. Fei, H., et al., *Modified Discrete Random Pore Model Considering Pore Structure Evolution to Depict Coal Chars Combustion in O2/CO2.* Energy & Fuels, 2017. **31**(12): p. 14280-14287.
45. Cortazar, M., et al., *Experimental study and modeling of biomass char gasification kinetics in a novel thermogravimetric flow reactor.* Chemical Engineering Journal, 2020. **396**: p. 125200.
46. Umemoto, S., S. Kajitani, and S. Hara, *Modeling of coal char gasification in coexistence of CO_2 and H_2O considering sharing of active sites.* Fuel, 2013. **103**: p. 14-21.
47. Seguin, D., et al., *Liquid—solid mass transfer in packed beds of variously shaped particles at low Reynolds numbers: experiments and model.* The Chemical Engineering Journal and the Biochemical Engineering Journal, 1996. **63**(1): p. 1-9.
48. Miller, P.A. and N.L. Clesceri, *Waste sites as biological reactors: characterization and modeling*. 2002: CRC Press.
49. Ho, F.-G. and W. Striender, *A variational calculation of the effective surface diffusion coefficient and tortuosity.* Chemical Engineering Science, 1981. **36**(2): p. 253-258.
50. Akanni, K.A., J.W. Evans, and I.S. Abramson, *Effective transport coefficients in heterogeneous media.* Chemical Engineering Science, 1987. **42**(8): p. 1945-1954.
51. Hamad, H.T., D.W. Abbood, and A.S. Mustafa. *Strength Tortuosity-Porosity Relation in Locally Types of Porous Media (Experimental Model)*. in *IOP Conference Series: Materials Science and Engineering*. 2018. IOP Publishing.
52. Kavand, M., et al., *An improved film–pore–surface diffusion model in the fixed-bed column adsorption for heavy metal ions: Single and multi-component systems.* Process Safety and Environmental Protection, 2018. **113**: p. 330-342.
53. Lagarias, J.C., et al., *Convergence Properties of the Nelder--Mead Simplex Method in Low Dimensions.* SIAM Journal on Optimization, 1998. **9**(1): p. 112-147.
54. Feng, B. and S.K. Bhatia, *Variation of the pore structure of coal chars during gasification.* Carbon, 2003. **41**(3): p. 507-523.
55. Massoudi Farid, M., M.S. Kang, and J. Hwang, *The effect of CO on coal–biomass co-gasification with CO_2.* Fuel, 2017. **188**: p. 98-101.
56. Ollero, P., et al., *The CO_2 gasification kinetics of olive residue.* Biomass and Bioenergy, 2003. **24**(2): p. 151-161.

Chapter 3

Multiscale CFD-DEM model for the CO_2 gasification reaction of carbon anode

Mohammad Kavand

Aluminum Research Centre REGAL, Université Laval, 1065 avenue de la Médecine, Québec, Québec, G1V 0A6

Abstract

The reactivity of carbon anodes with CO_2 is one of the main concerns in aluminum smelters using the Hall–Héroult process. Such reactivity is undesirable because it increases the net carbon consumption and thus shortens anode lifetime. Anode overconsumption is affected by anode intrinsic reactivity and mass-transport phenomena. Herein, as a first step toward the simulation of anode gasification with CO_2, an anode particle bed was considered. Numerical multiscale computational fluid dynamics–discrete-element method (DEM) model was developed based on an Eulerian-Lagrangian concept. The model includes an Eulerian finite-element method for the gas and solid particles and a Lagrangian DEM for the particle phase. It was intended to capture the particle-shrinkage effect (movement of particles during gasification). The physical (e.g., porosity and specific surface area) and thermochemical (e.g., the heat of reaction) properties of particles are ultimately tracked. Geometric changes in particles, heat and mass transfer, particle shrinkage, and chemical reactions are considered during anode gasification with CO_2. The dynamic concentration and temperature profiles of the reactant and product gases and the solid conversion were modeled in the voids between the particles and the pores inside each particle. The validation of the model was performed using a bed of particles.

Résumé

La réactivité des anodes de carbone avec le CO_2 est l'une des principales préoccupations des alumineries utilisant le procédé Hall – Héroult. Une telle réactivité est indésirable car elle augmente la consommation nette de carbone et raccourcit ainsi la durée de vie de l'anode. La surconsommation d'anode est affectée par la réactivité intrinsèque de l'anode et les phénomènes de transport de masse. Ici, comme première étape vers la simulation de la gazéification d'anode avec du CO_2, un lit de particules d'anode a été considéré. Un modèle numérique multi-échelles de calcul dynamique des fluides – méthode des éléments discrets (DEM) a été développé sur la base d'un concept eulérien – lagrangien. Le modèle comprend une méthode des éléments finis eulériens pour le gaz et les particules solides, et un MNA lagrangien pour la phase particulaire. L'objectif était de capturer l'effet de retrait des particules (mouvement des particules lors de la gazéification). Les propriétés physiques (par exemple, la porosité et la surface spécifique) et thermochimiques (par exemple, la chaleur de réaction) des particules sont finalement suivies. Les changements géométriques des particules, le transfert de chaleur et de masse, le retrait des particules et les réactions chimiques sont pris en compte lors de la gazéification de l'anode avec du CO_2. Les profils dynamiques de concentration et de température du réactif et des gaz produits, ainsi que la conversion solide, ont été modélisés dans les vides entre les particules et les pores à l'intérieur de chaque particule. Pour valider le modèle, des tests expérimentaux ont été réalisés à l'aide d'un lit de particules anodiques.

Keywords: CO_2 gasification; carbon anode particle; multiscale model; mass-transport phenomena; shrinkage; CFD

Nomenclature

C_C	concentration of anode reactant, (mol·m^{-3})
C	concentration of gaseous species, (mol·m^{-3})
$C(O)$	surface of carbon-oxygen complex, (mol·m^{-2})

CL	contact list of particle *i*, (-)
D	diffusion coefficient, ($m^2 \cdot s^{-1}$)
D	bed diameter, (m)
d_P	particle diameter, (m)
H	convective heat transfer, ($W \cdot m^{-1} \cdot K^{-1}$)
h_D	convective mass transfer coefficient ($m \cdot s^{-1}$)
L	bed height, (m)
J	mass flux, ($mol \cdot s^{-1} \cdot m^{-2}$)
K	reaction rate constant, $(mol \cdot m^{-3})^{(1-n)} \cdot s^{-1}$
L_0	pore length, ($m \cdot kg^{-1}$)
L	height of the bed reactor, (m)
M	torque, ($kg \cdot m^2 \cdot s^{-2}$)
$\vec{M}_{ij}^{\,r}$	rotation of particles, ($kg \cdot m^2 \cdot s^{-2}$)
$\vec{M}_{ij}^{\,t}$	tangential torque, ($kg \cdot m^2 \cdot s^{-2}$)
m	mass of anode particle, (kg)
N	partial reaction order, (-)
N	number of experimental data
Nu	Nusselt number, (-)
P	partial pressure, ($kg \cdot m^{-1} \cdot s^{-2}$)
Pr	Prandtl number, (-)

R_{pe}	particle radius, (m)
R	radius of the bed reactor, (m)
Re	Reynolds number, (-)
Re_e	effective Reynolds number, (-)
S	specific surface area, ($m^2 \cdot kg^{-1}$)
S_p	surface area of the anode per unit volume of the bed, ($m^2 \cdot m^{-3}$)
Sc	Schmidt number, (-)
Sh	Sherwood number, (-)
T	reaction time, (s)
T	temperature, (K)
Q	flow rate, ($L \cdot min^{-1}$)
Q	heat flux, ($W \cdot m^{-2}$)
U	flow velocity, ($m \cdot s^{-1}$)
W	chemical reaction rate, ($mol \cdot s^{-1} \cdot m^{-3}$)
X	gasification conversion of anode particle, (-)
Greek symbols	
B	permeability, (m^2)
ΔH	enthalpy of reaction, ($kJ \cdot mol^{-1}$)
ε_b	bed void fraction, (-)
ε_{pe}	particles void fraction, (-)
φ	angular position, ($rad \cdot s^{-2}$)

H	effectiveness factor, (-)
μ	viscosity, (Pa·s)
$\vec{v}$	translational velocity
ρ	density, ($kg \cdot m^{-3}$)
τ	tortuosity, (-)
ψ	structural parameter, (-)
$\vec{\omega}$	rotational velocity, ($rad \cdot s^{-1}$)

Subscripts

Ap	apparent
Ave	average
B	bulk
C	carbon
CO	carbon monoxide
CO_2	carbon dioxide
Diss	dissolved
E	effective
F	active carbon site
G	gas phase
Gs	gas-solid interface
M	molten
Mix	mixed gases

P	particle
S	solid phase
t	instantaneous
0	initial
Superscripts	
ext	external
f-p	fluid-particle interaction forces
p-p	particle-particle interaction

3.1 Introduction

The Hall–Héroult process is a common industrial process of producing aluminum where alumina is fed to electrolysis cells (also called pots) containing carbon anodes [1-5]. A pot, representing an electrolysis cell, consists of molten cryolite, prebaked carbon anodes, and a liquid layer of aluminum, which lies over the cathode carbon blocks [1]. The electrolysis reaction can be written as

$$2Al_2O_3\,(diss) + 3\,C\,(s) \rightarrow 4\,Al\,(m) + 3\,CO_2\,(g) \qquad (3.1)$$

where molten aluminum is the main product of Equation (3.1). During this process, the carbon anode is consumed and replaced by a new anode approximately every 25 days.

The least amount of theoretically combusted carbon is equal to 0.33 kg C/kg Al produced. However, the actual electrolytic consumption of carbon is approximately 0.41 kg C/kg Al produced because cell efficiency does not usually reach 100%. The overconsumption of one kg anode per one tonne produced aluminum is around 2 US$ [2]. The overconsumption of a midsize smelter (producing 300 000 tons of aluminum per year and using 150 000 anodes per year) is approximately 40 kg per anode [2, 6]. Thus, the estimated extra cost could be about 12 MUS$ per year [2, 6]. The overconsumption could be related to two main factors:

gasification by air and CO_2 and the anode properties [6, 7], which may lead to carbon dust. Carbon dust is principally defined by selective burning of the anode components in contact with air or CO_2 and the detachment of carbon particles from the anode surface [8]. The anode-gasification rate depends on the surface structure, temperature, permeability, and reactivity of anode constituents [3]. The effect of air reactivity is relatively well mitigated by covering the anode with alumina, which reduces air diffusion toward the anode surface. However, this solution is not possible for CO_2 reactivity because it primarily occurs in the part of the anode immersed in molten salt. Providing a solution for CO_2 reactivity requires a deep understanding of the effect of different parameters on reaction rates. Accordingly, the present work aims to provide a model to predict and quantify the effect of such parameters on the CO_2 gasification of carbon anodes.

$$C(s)+CO_2(g)\leftrightarrows 2CO\ (g) \qquad \Delta G^\circ = 40800-41.7T\ \text{cal} \tag{3.2}$$

The reaction, described by equation (3.2), occurs in the presence of CO_2 [1]. A gas-bubble layer forms underneath the bottom surface of the carbon anode, which prevents the reaction of the anode with electrolyte and increases the cell voltage [1, 2]. CO_2 also diffuses into the anode pores and reacts with carbon on the active surfaces of the anode, generating CO. The diffusion of CO_2 in anode pores is enhanced under the hydraulic pressure of the bath. Thus, chemical reaction and mass-transport phenomena are essential factors for this reaction.

To develop a mathematical model for anode-reaction simulation, the anode structure is simplified. We consider the anode as a fixed bed of particles, exhibiting two types of porosities, i.e., porosity inside each particle, representing the interparticle porosity of the coke aggregates in the anode which are not filled with pitch, and the voids between the particles, representing the pores within the binder matrix, generated during compaction or baking process. Reaction 2 is a function of temperature and partial pressure of the gas species in the pores, and both are affected by the flow patterns and mass transport in the fixed-bed reactor.

Different mathematical approaches can simulate reactions in fixed-bed reactors depending on system complexity, i.e., pseudo homogeneous or pseudo heterogeneous models in steady-state or transient regimes. Pseudo homogeneous models assume that the surface of the solid phase is fully exposed to the gas phase, with no gas-to-solid mass and heat-transfer

resistances. The heterogeneous approach assumes conservation equations for both phases separately.

Over the past decade, several researchers have modeled fixed-bed reactors based on radial, axial, and circumferential profiles [9-13]. However, few studies have coupled the macro-and microscales of fluid dynamics and particle reactions in fixed beds. Moreover, most previous research has been performed for catalytic reactions, where the bed's size and structural characteristics remained unaltered during the process [9-15]. Larachi [16, 17] investigated a reactor design by applying a parallel modeling structure in which the scales of particle and reactor are considered. To study the deposition of fine in packed beds, a computational fluid dynamics (CFD) approach [18] has been used by Valkov et al.[19]. Partopour and Dixon [20] proposed a multiscale model of steam methane reforming with reactive catalytic particles by applying the interactions between local pellet-scale dynamic responses and the bed-scale global fields through CFD. Non-catalytic reactions in fixed-bed reactors have also been reported; however, the kinetics are often limited to a specific range of process parameters [19, 21-26], but all assume the solid phase Non-catalytic change during the process. Besides, owing to computational hardware limitations, researchers are restricted to a small number of solid particles (<50) forming a random fixed bed.

Improvements in computer performance can enable studies on a larger number of particles. These numerical methods capture the properties of a material, so the accuracy and robustness of material properties tracking are insufficiently high to conduct the modeling of time-history variables. Meanwhile, Eulerian methods do not predict accurate results in case of material response to loading and damage. Lagrangian methods are more precise for the solid phase than Eulerian methods that are preferable for the fluid phase. It demonstrates the importance of coupling these two methods for the calculation of solid-fluid interactions. An Eulerian-Lagrangian approach has recently been used to simulate porous particles [20, 23, 27-32]. However, an Eulerian-Lagrangian model of entrained-flow solid gasification and its validation are unavailable to the best of our knowledge.

In the present study, a multiscale model with non-catalytic reaction was developed to investigate fixed-bed reactors and apply a new approach to consider solid structural changes

during gasification. In this method, the solid particles were considered a non-catalytic part, and the space between the particles' flow was considered a continuum phase. An Eulerian finite-element method (FEM) served as the basis of the proposed mathematical method to model the fluid phase, coupled with a discrete-element method (DEM) applied to model the anode particles' dynamics and particle shrinkage, which enabled the tracking of the particles' motion and the fluid phase's dynamics. Communication between the two length scales was achieved through an interpolation strategy, and the dual-grid multiscale scheme was originally proposed to combine DEM and FEM. To facilitate data conversion between continuum models derived from FEM and DEM, an interface was defined. This process was the key point to model gasification and enable the investigation of particle–fluid interaction without missing the particles' information.

To validate the model, a set of experiments was needed. A fixed-bed design was used to determine the effect of operating parameters, such as flow rate, bed height, particle size examined, and unknown parameters (e.g., chemical-reaction constants). The model output included the distribution of concentration, pressure, flow rate, and temperature of gas components inside and outside of particles. Structural parameters such as particle porosity, permeability, and specific surface area were also determined. The model was also applied to particle shrinkage during the process, and particle tracking was available for all anode particles.

3.2 Mathematical Modeling

3.2.1 Methodology

The mathematical model in the present work is developed with the following assumptions.

- Conform to anode microstructure; a simplified structure may be applicable by considering a bed of particles assuming that the porosity inside a particle represents small pores and the voids between particles represent large pores. The active sites on

the anode particles are susceptible to letting the reaction occur, which is a strong function of the particle temperature and species partial pressures, affected by the flow patterns and mass transport in the fixed-bed reactor.

- Mass transfer occurs through convection and diffusion at the macroscale (fluid phase) and diffusion within the anode-particle domain.
- Non-isothermal conditions prevail in the fixed-bed domain.
- Chemical reactions (Boudourad reaction) occur in the solid phase as non-catalytic reactions.
- All particles are spherical.
- The Langmuir–Hinshelwood (L-H) mechanism and random-pore model (RPM) equation are used to define the chemical reaction term.

Anode-gasification reactions are sensitive to mass-transfer effects. The gasification-rate schematic illustrated in Figure and may occur by physical and chemical processes through the following steps: 1) mass transfer (by diffusion) of gaseous reactant(s) from the bulk gas phase to the carbon surface; 2) adsorption of reactant(s) on the carbon surface; 3–5) chemical rearrangements (reactions) on the surface, mobility, and formation of adsorbed product(s); 6) desorption of product(s), and 7) mass transport (by diffusion) of the gaseous reaction product(s).

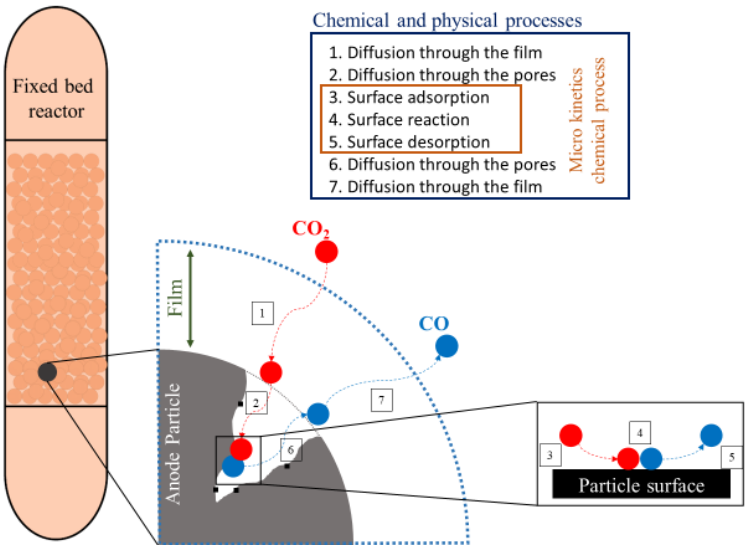

Figure 3.1 Chemical and physical processes of each particle in a fixed-bed reactor

As Figure 3.2 shows, the bed is a 3D cylinder which has axisymmetric. In addition, there are 3D porous spherical particles inside the bed. The extra dimension is the added radial (r) microscale dimension inside each particle. The system has two types of porosities: porosity due to void in particles and between particles. The 3D model was used in the simulations.

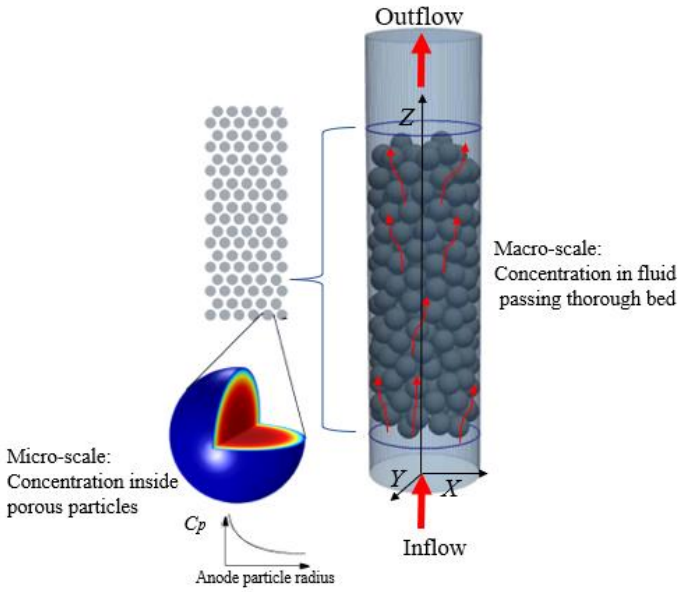

Figure 3.2 Fluid–particle flow field for a 3D cylinder axisymmetric model

3.2.2 Simulation

Euler- Lagrange approaches are used to simulate the fluid–particle flows in this work to consider a combination of CFD and DEM, referred to as CFD-DEM. Including constitutive equations related to fluids and solids and proper coupling strategy in CFD-DEM allows us to study momentum, heat and mass transports, and chemical reactions in almost any detail on the particle scale.

3.2.2.1 CFD

Due to the bed's porosity, Darcy's Law as a simplified of Navier-Stokes and continuity equations is used to simulate fluid flow through interstices in a porous medium. It can be used to model low-velocity flows or media where the permeability and porosity are very small. The pressure gradient is the major driving force, and the frictional resistance within the pores mostly influences the flow. In addition, DEM was coupled with the CFD equation to provide higher accuracy than the two-fluid model TFM [33].

3.2.2.1.1 Mass equations

A mass-balance-based reaction-transport model is developed to simulate the dynamics of anode CO_2 reactivity by applying heat-transfer equations and momentum equations to describe the gasification process. CO is the product of the Boudouard reaction. Because of the inhibition effect of CO on gasification (by adsorption and desorption), it should be applied in the model for each step to achieve accurate modeling. This model facilitates the incorporation of a nonlinear chemical-reaction rate, *w*, the conversion-induced transformations in the porous structure by the pertinent Equation, and the reaction-induced changes in the effective diffusivity through the input of conversion (*X*) [34-36]. The concentration profile within particles can be obtained for a particle position (*r*) and specific time (*t*) by solving the set of equations in the bed:

$$\frac{\partial(\varepsilon_b C_i)}{\partial t} + u.\nabla C_i = \varepsilon_b D_i \nabla^2 C_i - h_{D,i} S_p (C_i - C_{pe,i}), \quad i = CO_2, CO \qquad (3.3)$$

where C_{CO_2} and C_{CO} are the reactant and product gas concentrations (mol / m3) of the bed, respectively. u (m/s) is the velocity of the fluid, ε_b is the porosity of the bed, $h_{D,i}$ (m/s) is the convective mass-transfer coefficient around the particle, and S_p (m^2 particles/m^3 bed) is the surface area of particles the per unit volume of the bed. The first right-hand term represents species diffusion in the gas phase obtained by Fick's law [37] (Equation 3.3). The second left-hand term describes the convective mass flux of species related to the velocity of fluid

gases. The last right-land term represents the convective mass flux owing to the concentration driving force between the surfaces of particles and the gas bulk.

The boundary conditions in the z direction for Equations (3.3) - at the reactor inlet and outlet for each component '*i*' are as follows:

$$C_i\left(r,z,t\geq 0\right)\Big|_{z=0} = C_{in,i} \tag{3.4}$$

$$\left.\frac{\partial C_i\left(r,z,t\geq 0\right)}{\partial z}\right|_{z=L} = 0 \tag{3.5}$$

The concentration of species is finite at the center and also there is no mass flux from the wall of the bed. Equations (3.6) and (3.7) describe these two conditions:

$$\left.\frac{\partial C_i\left(r,z,t\geq 0\right)}{\partial z}\right|_{r=0} = 0 \tag{3.6}$$

$$\left.\frac{\partial C_i\left(r,z,t\geq 0\right)}{\partial z}\right|_{r=R} = 0 \tag{3.7}$$

Initially, the bed is clean, and carbon dioxide is not present such that the fluid concentrations are zero everywhere within the bed:

$$C_i\left(r,z,t\right)\Big|_{t=0} = 0,\ \ i = \mathrm{CO}_2, \mathrm{CO} \tag{3.8}$$

$$C_{\mathrm{C}}\left(r,z,t\right)\Big|_{t=0} = C_{\mathrm{C}_0} \tag{3.9}$$

where C_C is the concentration of carbon, this initial condition applies to the bulk fluid concentration and the concentration in the particles.

Due to the axisymmetric, there is no concentration variation in the θ direction. The reaction inside the particles is included as a sink term in the intraparticle mass balances for the transport of dilute species interfaces with reactive particle features. Looking inside a pellet: Assuming no concentration variations in the space-angle (θ, φ) direction, but only in the spherical particle's radial (rpe) direction allows a spherically symmetric reaction-diffusion

transport equation inside the pellet. A shell mole balance across a spherical shell at radius r_{pe} of the particle gives:

$$4\pi N\left[\frac{\partial\left(\varepsilon_{pe}C_{pe,i}\right)}{\partial t}+\frac{1}{r_{pe}^{2}}\frac{\partial}{\partial r_{pe}}\left(-r_{pe}^{2}D_{pe,i}\frac{\partial C_{pe,i}}{\partial r_{pe}}\right)=w_{pe,i}\right] \tag{3.10}$$

where N is the number of particles per unit volume of bed, ε_{pe} is the pellet (microscale) porosity, $C_{pe,i}$ is the interstitial (physical) species concentration in moles/m^3 of fluid volume element inside the pore channel, $w_{pe,i}$ is the particle reaction rate, where corresponds to reactions taking place inside the particles (per unit volume of pellet.). $D_{pe,i}$ is the effective diffusion coefficient of component i inside the particle. The effective diffusion coefficient, which is dependent on the porosity ε_{pe}, tortuosity τ, and physical gas diffusivity D_i, can be calculated as follows:

$$D_{pe,i}=\frac{\varepsilon_{pe}D_i}{\tau} \tag{3.11}$$

The number of particles per unit volume of bed is calculated from the porosity of the bed and volume of a pellet as:

$$N=\frac{1-\varepsilon_b}{V_{pe}} \tag{3.12}$$

The boundary condition at the center and the radius of the particles (R_{pe}) is:

$$\frac{\partial C_{pe,i}\left(0,t\geq 0\right)}{\partial r}=0 \tag{3.13}$$

$$\frac{1}{R_{pe}}\left(D_{pe,i}\frac{\partial C_i\left(R_{pe}\right)}{\partial r}\right)=h_{D,i}\left(C_i-C_{pe,i}\right) \tag{3.14}$$

Equation (3.14) is the Neumann boundary condition that specifies the normal derivative of the function on a surface. In this process, an assumption lies in the claim that the gas components' external convective mass-transfer rate to the surface has to be equal to the

transport rate via the particle surface. The bed and particle equations are linked through the mass transfer on the surface according to the boundary conditions appearing in the mass-balance Equation.

For the case of randomly packed spherical particles, the specific surface area exposed to the free fluid is[38]:

$$S_{\mathrm{b}} = \frac{3}{R_{\mathrm{pe}}}\left(1-\varepsilon_{\mathrm{b}}\right) \tag{3.15}$$

Equation (3.15) is used in Equation (3.3). The mass transfer coefficient in Equations (3.3) and (3.14) can be computed from the fluid properties and flow characteristics within the porous media. For this, the Sherwood, Sh, number defined as the ratio between the convective mass transfer coefficient and the diffusive mass transfer coefficient is used [39]:

$$Sh_i = \frac{h_{D,i}L}{D_i} \tag{3.16}$$

where L is a characteristic length (for particles, typically the radius), and D_i is the diffusion coefficient of component *i* in the fluid. From the Sherwood number, the mass transfer coefficient can be computed. The Frössling relation [38] was used as an empirical expression for the calculation of the Sherwood number as:

$$Sh = 2 + 0.552\,\mathrm{Re}^{\frac{1}{2}}\,Sc^{\frac{1}{3}} \tag{3.17}$$

Where *Re*, and *Sc* are the Reynolds, and Schmidt, numbers as:

$$\mathrm{Re} = \frac{\rho_f u L}{\mu_f} \tag{3.18}$$

$$Sc = \frac{\mu_f}{\rho_f D_i} \tag{3.19}$$

Here L is the characteristics length of the particles, ρ_f, u, μ_f are the density of the fluid, the velocity of the fluid, and viscosity of fluid between particles.

Various models can explain the kinetics of the CO_2 gasification reaction. The reaction rate per unit of particle volume is essential to formulate in a "structural" format [35] inside a particle. Thus, an equation is introduced to outline the reaction for the available particle sites at a given processing time. To explicitly combine this feature, the following intrinsic kinetics is assumed to be established for all locations in the particle:

$$w_{\mathrm{pe,CO_2}} = -r_{\mathrm{CO_2}} \cdot F(X) \tag{3.20}$$

$$r_{\mathrm{CO_2}} = r_{\mathrm{C}} = -\frac{\partial C}{\partial t} \tag{3.21}$$

$$r_{\mathrm{CO}} = -2r_{\mathrm{CO_2}} \tag{3.22}$$

In Equation (3.20), the reaction rate can be divided into two parts [40]. In the first part $r_{\mathrm{CO_2}}$, the effect of CO_2 concentration on the reaction rate is considered. The second part, *F(X)*, depicts changes in the available reacting surface. The description of this Equation is detailed in previous work [41]. In general, the L-H rate equation is considered for $r_{\mathrm{CO_2}}$. This mechanism is proposed based on the adsorption and desorption of CO and CO_2 to yield expressions for calculating the reaction rates of anode gasification. The RPM [42] is applied to the structural part of the chemical-reaction Equation. Therefore, the chemical-reaction term is as follows:

$$\frac{dX}{dt} = \frac{k_1 P_{\mathrm{co_2}}}{1 + k_2 P_{\mathrm{co_2}} + k_3 P_{\mathrm{co}}} S_0 (1 - X)\sqrt{1 - \psi \ln(1 - X)} \tag{3.23}$$

Here X is the carbon conversion, and S_0 and ψ are the initial specific surface area and the structural parameters of the RPM equation, respectively.k_1, k_2, and k_3 are the chemical-reaction rate constants.

3.2.2.1.2 Movement equations

The momentum balance that governs the fluid flow is built upon the Navier–Stokes and continuity equations. The conservation of mass is the generic Equation used, and the following continuity equation is written for a porous medium with an effective term of the chemical reaction on the flow [37]:

$$\frac{\partial(\varepsilon_b \rho_f)}{\partial t} + \nabla.(\rho u) = Q_m \tag{3.24}$$

$$u = -\frac{\beta}{\mu L} \nabla P \tag{3.25}$$

where Q_m (kg/m^3.s) is the - mass source or sink; this term accounts for mass deposit and/or mass creation in the inter-particles domain. ρ_f is the density of the fluid and β is the permeability. When gas flow inter to the bed, gas goes up through the particle bed; therefore, flow leads to a pressure drop during the reactor, to be able add this effect on the motion equation, the Ergun equation has been defined, and it can be written as [37]:

$$\frac{\Delta P}{L} = \frac{150 \mu_f u (1-\varepsilon_b)^2}{R_{pe}^2 \varepsilon_b^{\,3}} + 1.75 \frac{\rho_f u^2 (1-\varepsilon_b)}{R_{pe} \varepsilon_b^{\,3}} \tag{3.26}$$

where ε_b is the bed porosity, μ_f (Pa.s) stands for the viscosity of the fluid, ρ_f *is* the fluid density (kg.m^{-3}), L is the bed length (m), u is the fluid velocity (m.s^{-1}). The Ergun equation combines both the laminar and turbulent components of the pressure loss across a packed bed. In laminar flow, the first term is predominant. Under turbulent flow, the second term is dominant. The pressure drop is related to the square of the superficial velocity and linearly depends on the density of the fluid passing through the anode. Darcy's law is derived because the viscous resisting force in the Navier-Stokes equation is linear with the velocity (equation 3.25).

3.2.2.1.3 Energy equations

The bulk energy balance for a fixed-bed reactor can be written as follows:

$$\rho_f C_{\mathrm{P},f}\left[\frac{\partial\left(\varepsilon_{\mathrm{b}} T_f\right)}{\partial t}+u.\nabla T_f\right]=\varepsilon_{\mathrm{b}} k_f \nabla^2 T_f-h_f S_{\mathrm{p}}(T_f-T_{\mathrm{pe}}\big|_{r_{\mathrm{pe}}=R_{\mathrm{pe}}}) \tag{3.27}$$

where $-C_{P,f}$ is the heat capacity ($\mathrm{J\cdot mol^{-1}\cdot K^{-1}}$), T_f is the bulk fluid temperature, and h_f is the convective heat transfer coefficient between the fluid and the surface of the particles. The $u.\nabla T_f$ represents the energy transfer owing to the convection of fluid, the $\varepsilon_{\mathrm{b}} k_f \nabla^2 T_f$ term demonstrates the conduction heat flux of the gas phase, and the last term describes the convective heat flux from the particle's surface to the fluid bulk. The boundary conditions in the *z*-direction of the bed are:

$$T_f\left(r,z,t\geq 0\right)\big|_{z=0}=T_{in} \tag{3.28}$$

$$\left.\frac{\partial T_f\left(r,z,t\geq 0\right)}{\partial z}\right|_{z=L}=0 \tag{3.29}$$

In addition, the temperature in the center of bed is finite and around the walls is fixed using a heater.

$$\left.\frac{\partial T\left(r,z,t\geq 0\right)}{\partial r}\right|_{r=0}=0 \tag{3.30}$$

$$T\left(r,z,t\geq 0\right)\big|_{r=R}=T_{\mathrm{wall}} \tag{3.31}$$

where R is the radius of bed, and T_{wall} is the fixed temperature at the wall. The relation to the particle-energy balance is:

$$\frac{\partial[(\rho C_P)_{\mathrm{eff}} T_{\mathrm{pe}}]}{\partial t}=k_{\mathrm{eff}}\nabla^2 T_{\mathrm{pe}}+r_{\mathrm{CO_2}}\Delta H_{\mathrm{CO_2}} \tag{3.32}$$

$$\left(\rho C_P\right)_{eff}=\left(1-\varepsilon_{\mathrm{pe}}\right)\rho_C C_{P,C}+\varepsilon_{\mathrm{pe}}\rho_f C_{P,f} \tag{3.33}$$

$$k_{eff}=\left(1-\varepsilon_{\mathrm{pe}}\right)k_C+\left(\varepsilon_{\mathrm{pe}}\right)k_f \tag{3.34}$$

where ρ_C ($\mathrm{kg/m^3}$), $C_{P,C}$ (J/kg.K), and k_C (W./m.K) stand for the density, heat capacity, and conductive heat transfer coefficient of carbon. $\Delta H_{\mathrm{CO_2}}$ (J/kg) is the heat of the reaction. It

should be noted that it is assumed that the total volume of the particles is reactive instead of the pore volume.

The following - boundary conditions are used to solve Equations (3.32):

$$\left.\frac{\partial T_{\mathrm{pe}}\left(r_{\mathrm{pe}}, t \geq 0\right)}{\partial r_{\mathrm{pe}}}\right|_{r_{\mathrm{pe}}=0} = 0 \tag{3.35}$$

$$\frac{1}{R_{\mathrm{pe}}}\left(D_{\mathrm{pe},i}\frac{\partial T_{\mathrm{pe}}\left(R_{\mathrm{pe}}\right)}{\partial r}\right) = h_f\left(T_f - T_{\mathrm{pe}}\big|_{r_{\mathrm{pe}}=R_{\mathrm{pe}}}\right) \tag{3.36}$$

Equation (3.36) represents that no accumulation of heat takes place on the particle's surfaces. In other words, heat is carried by the fluid outside the particles. According to Equation (3.36), the bed equation and particle equation are linked through heat transfer on the surface of the particles.

The value of convective heat flux is calculated as [43]:

$$Nu = \frac{h_f L}{k_f} \tag{3.37}$$

where k_f is the conductive heat transfer coefficient of the fluid. Nu is the Nusselt number, which is the convective-to-conductive heat-transfer ratio across the boundary, in which the convection covers advection and diffusion mechanisms. For a single particle, this number is obtained for the fluid as follows:

$$Nu = 2 + \left(0.4\,Re^{\frac{1}{2}} + 0.06\,Re^{\frac{2}{3}}\right) Pr^{0.4}\left(\frac{\mu_{f,\infty}}{\mu_{f,w}}\right)^{\frac{1}{4}} \tag{3.38}$$

where $\mu_{f,\infty}$, and $\mu_{f,w}$ are the viscosity of fluid far from the surface of the particles and near the surface of the particles. Pr is the Prandtl number and calculated as:

$$\mathrm{Pr} = \frac{C_{P,f}\,\mu_f}{k_f} \tag{3.39}$$

Initially, the bed and particles are at the same temperature:

$$T_f\left(r,z,t\right)\Big|_{t=0} = T_0 \tag{3.40}$$

$$T\left(r_{\mathrm{pe}},t\right)\Big|_{t=0} = T_0 \tag{3.41}$$

For a bed of spherical particles, the following equations have been obtained by Gunn et al. [44]:

$$\mathrm{Re_e} = \frac{1}{(1-\varepsilon_b)}\mathrm{Re} \tag{3.42}$$

$$\mathrm{Nu_b} = 1+1.5(1-\varepsilon_b)\mathrm{Nu_p} \tag{3.43}$$

3.2.2.1.4 Particle shrinkage

Anode-gas chemistry causes solid particle shrinkage because of the reaction with the gas phase. In addition to influencing gasification, particle shrinkage robustly affects the particle direction on the way out of the reactor [45]. The absence of particle shrinkage causes particle entrainment to be highly overpredicted. The change in the anode particle radius during the process can mathematically be explained by a moving boundary condition obtained by Kavand et al. [41] as follows:

$$\frac{\partial r_{ap}}{\partial t} = \begin{cases} 0 & X(a)<1, X(100\%)_{\textit{outer layer}} \\ \dfrac{\partial X/\partial t}{\partial X/\partial r} & X\ \ a\ =1, X\ \ 100\%\ _{\textit{outer layer}} \end{cases} \tag{3.44}$$

when 100% of an imaginary external layer is consumed, shrinkage conversion is obtained by solving the second-condition term of Equation (3.44).

3.2.2.2 DEM

To add a particle's motion and the effect of interaction between particle-particle and particle–fluid to the model, a DEM needs to be applied. Gas flow through an anode particle bed has been examined conventionally in a continuum model that can successfully capture some essential points of the porous solid-phase behavior. Nevertheless, some phenomena and structural exchanges, such as shrinkage effects at the particle scale and particle-particle interactions, cannot be explained by macro-partial differential equations (PDEs) [29, 33]. Therefore, these phenomena should be modeled by a DEM.

According to the DEM, the deformation of the material is simulated by successively solving the law of motion for each element and the force-displacement law for each contact [23, 29, 30]. In this dynamic process, a centered finite-difference scheme solves the equations through a time-stepping algorithm, assuming that the time step is sufficiently small such that the velocities and accelerations are constant within each time step. The algorithm tries to detect the contacts according to the known positions of the elements, so the magnitude of the possible overlaps among elements is detected. Then, by applying the force-displacement law, the propagated contact forces are calculated. After the forces are inserted into the law of motion, the velocity and acceleration of the particles are calculated. According to the obtained values, the updated positions of all particles in the current time step are determined. This cycle of calculations is repeated and solved at each time step, so the flow or deformation of the material is simulated.

Elements in DEM are rigid bodies in the form of circles (in 2D). However, they can overlap with one another owing to applied forces, and the magnitude of the overlaps is related to the contact force via the predefined contact model [33].

Newton's equation of motion for N spherical particles in the system is as follows:

$$m_i \frac{d\vec{v}_i}{dt} = m_i \frac{d^2\vec{x}_i}{dt^2} = \sum_{j\vec{I}CL_i} \vec{f}_{i,j}^{\,p\text{-}p} + \vec{f}_i^{\,f\text{-}p} + \vec{f}_i^{\,ext} \tag{3.45}$$

$$I_i \frac{d\vec{\omega}_j}{dt} = I_i \frac{d^2\vec{\varphi}_j}{dt^2} = \sum_{j \in CL_i} (\vec{M}^t_{ij} + \vec{M}^r_{ij}) \tag{3.46}$$

where *fi* and M_i are the sums of the different forces and torques that act on particle *i*, respectively. They are complex functions of variables such as the particle position x_i, angular position$_{\vec{\varphi}_j}$, translational velocity of the center of mass v_i, and rotational velocity around the center of mass $\vec{\omega}_j$. We call these four variables the state variables of the particle. We use the subscript *j* for the input parameters of the forces and torque functions to denote that the state variables of particle *i* and other particles in the system affect the resultant interactions. The first term on the right-hand side of Equation (3.45) is the sum of particle-particle interaction forces acting on the particle, and *i* may involve collisional or interparticle forces. This summation is implemented for all particles existing in the contact list of particle *i*, CL_i. The second term represents the fluid-particle interaction forces; when the fluid effects are insignificant, this term is assumed to be zero. The third term describes the external forces acting on particle *i* owing to uniform or non-uniform external fields. Two types of contacts between particles exist, namely, physical and nonphysical. Physical contact covers a condition where the surfaces of two particles are contiguous; By contrast, a condition in which particles are not necessarily contiguous but are still interactive is referred to as nonphysical contact. Calculating the collision force between two physical contact-sharing particles is performed according to the force-displacement laws and the interaction force between two particles with nonphysical connections according to interparticle interactions. In Equation (3.46), the first term in the summation represents the tangential torque $\vec{M}^t_{ij}$ produced by the particle-particle collision. Considering that the particle-particle collision force acts on the contact point (particle surface), it causes a torque that is the origin of the rotation of particles. $\vec{M}^r_{ij}$ represents rolling friction, which is considered to be another torque applied onto particle i because it lies almost opposite of the particle's rotation; accordingly, it is recognized as the rolling-resistance torque. To resolve the particle-wall and interparticle collisions, a soft sphere DEM was used. The forces for interparticle contact are computed using equivalent simple mechanical elements, such as a spring, slider, and dashpot. However, particles can lightly overlap, and the normal force that tends to repel the particles can then be

subtracted from this spatial overlap and the normal relative velocity at the contact point. The spring stiffness can be calculated by Hertzian contact theory by knowing physical properties such as Young's modulus and Poisson's ratio. The soft sphere model's characteristic features that detail the implementation issues of the DEM are available in the literature [23, 33].

The physical properties adopted in the current study for the collision model include the following: Poisson's ratio of 0.3; Young's modulus of 5×10^6 Pa; and restitution and friction coefficients of 0.9 and 0.3, respectively [23, 33].

3.2.2.2.1 Generation of DEM sample

Several methods exist for solving sphere placement, including dynamic compression [46, 47], radius growth, and solving geometrical equations [48, 49]. It is necessary to specify the porosity and define the sphere overlap to obtain the desired specimen. In this work, the YADE software, an open-source 3D simulation program, was used to generate fixed-bed structures. Yade can implement computational algorithms using the discrete element method (DEM) in a stable and uniform environment. As a result of the soft-body model, rigid particle surfaces can penetrate each other during collisions. It is assumed that particles are rigid bodies, but interparticle deformation is allowed by a simple force-displacement law to overlap between particles. A specified number of spheres Np with diameter dp are placed within a cylinder at random positions by allowing particles to penetrate one another through interpenetration available in the YADE software and allowed to fall due to gravity (Figure. 3.3). A total of three column diameter (D) to particle diameter (d) with D/d = 6, 12, 24 are used. A maximum particle overlap of 1% of the particle diameter is obtained from the DEM-code. A 2D mesh with 1.0 mm holes was produced by Gmsh, a finite element mesh generator [50] (Geuzaine and Remacle, 2009). After the pellets have settled in the container, information about the simulated packings, particularly bulk porosity, is generated using a post-processing mesh-based analysis [51].

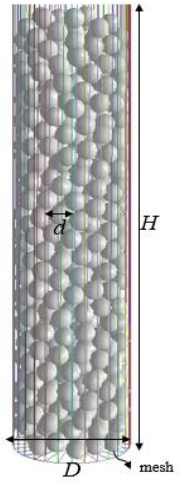

Figure. 3.3 Random packing of spherical particles obtained from DEM simulations for D/d = 6

3.2.3 Numerical method for solving the developed model

The developed model considers the gas species concentration (C) and anode-conversion rate (X) as the objective variables that should be computed. As the apparent radius of an anode particle starts decreasing after the critical anode-conversion rate [3] and finally approaches zero, the proposed model uses the moving-boundary method to solve the equations. The model incorporates a series of nonlinear PDEs, and it can use a proper numerical technique to solve these equations. Communication between the two grids and length scales can be ensured through an interpolation strategy. The dual-grid multiscale scheme is originally proposed to couple DEM and FEM. From a software viewpoint, implementing the dual-grid multiscale approach needs two computational grids and a routine for interpolating between them. The DEM platform has been used to evolve a set of discrete spherical-anode particles that move as long as a gas-phase flow exists. At every step, the positions and orientations of the particles are updated, and the program's outputs represent the gas concentration (C) versus time. The mesh grids are shown in Figure 3.4. The left picture shows the macroscale mesh in two dimensions. The right picture illustrates one particle with the micromesh and the heat and mass fluxes, establishing the connection between the two scales. By matching the simulation and experimental data, unknown variables such as reaction-rate constants can be calculated. The best-fit curve is obtained by minimizing the f function, given as [52]:

$$f(\min) = \sum_{j=1}^{n} (C_j - C_{\exp,j})^2 \tag{3.47}$$

where *n* is the number of experimental points.

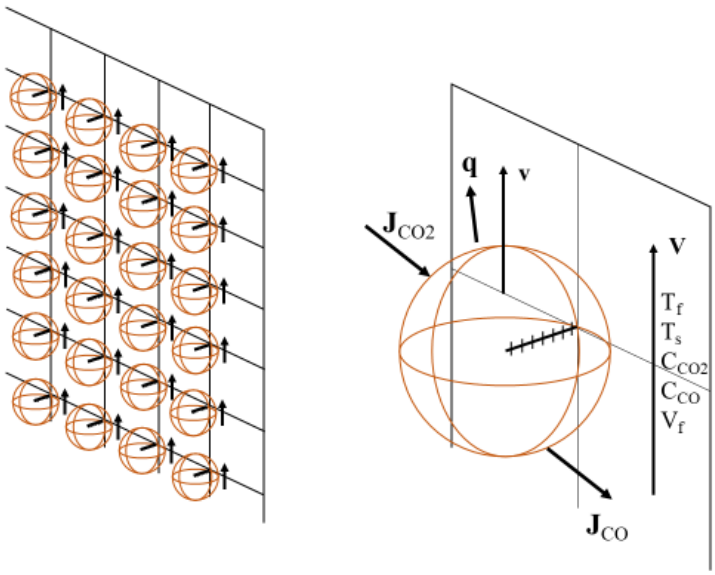

Figure 3.4 Schematic of two-scale simulation for gasification in a fixed-bed reactor

This paper defines an interface to convert the data between continuum models derived from the FEM mechanism and the DEM model. A partially coupled framework is involved in the interface between the FEM and DEM mechanisms [53]. Figure 3.5 presents the algorithm used for this process. "n" is the number of simulations; so, it makes the simulation time, simulation time = time step (dt) × number of simulations (n). In the beginning, all components of simulation will be initialized; DEM, CFD, and coupling. Based on the position of particles and fluid mesh information, the coupling calculates the fluid porosity. The particles' velocity and fluid velocity are then used to calculate the fluid-particle interaction force acting on each particle. The next step involves iterating the DEM. During the coupling step, the fluid-particle force is calculated and used in the Equation of motion of each particle. For the DEM iteration loop, the time step is dt, and the iteration loop for the Equation of motion is n. All particles' new positions and translational and rotational velocities are calculated following the DEM loop for the next fluid time step. Calculated porosity and

volumetric fluid-particle interactions in each fluid cell are used to solve mass and momentum conservation equations for the fluid phase.

Finally, to change the initial conditions for each time step, the data are sent to the FEM mechanism to set the values of the parameters obtained from the DEM and run the simulation. The unknown variables are calculated in the next step by comparing them with the simulation and experimental data.

A sensitivity study of the model compared to the size of the mesh has been carried out to know the optimal size of the chosen mesh. Accordingly, seven levels of mesh, including extremely coarse, extra course, coarser, coarse, normal, fine, and finer, were used. At the finer level, 75800 prisms, 3032 triangles, 4400 quads, 488 edge elements, and 10 vertex elements were used. The average mesh quality is equal to 0.889. As the mesh quality at this level is suitable, finer mesh level was used to study the model. In addition, the extra fine and extremely finer mesh were used to investigate the smaller mesh. The results showed that only the computation time increases, but the results do not change. The velocity of the fluid, the temperature of the fluid, the concentration of species in fluid, temperature of particles, concentration of species inside the particles, porosity of the bed, the porosity of particles, radius, and position of particles are the dependent variables. Equations (3.3), (3.10), (3.23)-(3.27), (3.32), (3.42)-(3.44) as PDEs and ODEs are solved simultaneously via coupling COMSOL and YADE. A constant damped version of Newton's method (damped factor=0.8) was used to solve the fully coupled phenomena. Backward differentiation formula (BDF) with an order of accuracy varying from one (backward Euler) to two was used as time steps. BDF methods have been used for a long time and are known for their stability. Node information can be modified by MATLAB scripts. YADE software, an open-source C++ framework, was applied as a DEM engine that can solve Newton's second law of motion for each anode particle. Relative tolerance of 0.001 was used as stopping criteria. To validate the model with experimental data, an algorithm genetic is applied using MATLAB.

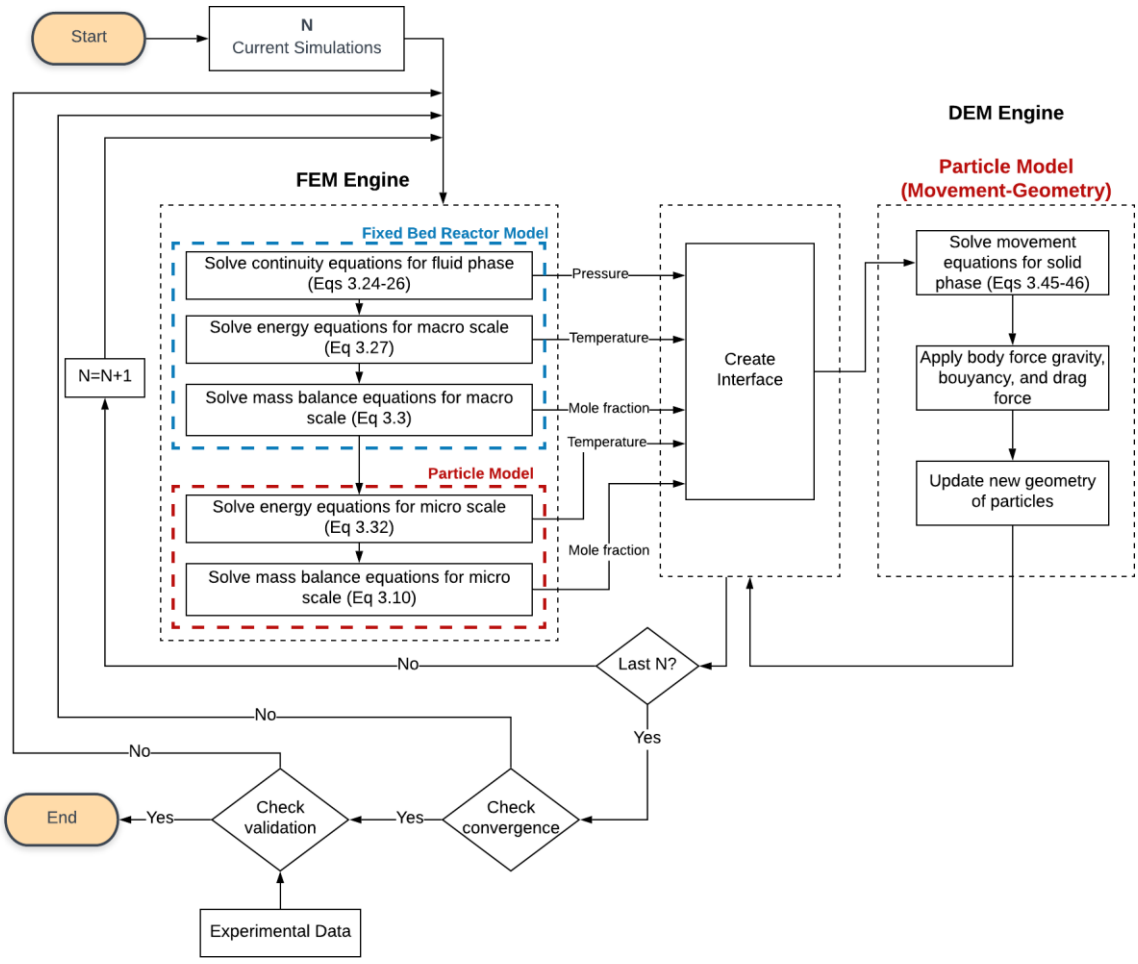

Figure 3.5 Algorithm of the mathematical model

3.3 Experiments

Several sets of experiments are needed to establish an accurate model to determine solid and gas phases' physical and chemical properties during gasification.

3.3.1 Materials

3.3.1.1 Anode particle

Raw carbon anode particles were provided by the Deschambault aluminum smelting plant (Alcoa Corporation). An anode was made from a mixture of 50%–65% petroleum coke, 14%–17% coal tar pitch binder, and 15%–30% recycled anode butts [1, 4, 5]. The raw material was first crushed and sieved in various USA standard mesh sizes (16, 30, 50, and 100). Ball milling was used to mill large particles (>1 mm) into finer ones (Blaine Number 2300). Some experimental tests were conducted to obtain the physical properties of the anode particles. The real density of the anode particles was measured using a helium pycnometer (Micromeritics, AccuPyc II 1340, USA) at different particle sizes (0.5, 1, and 2 mm). Each sample was weighed three times with an analytical balance (MS204S, Mettler Toledo, USA) and placed in a stainless-steel cell in a helium pycnometer. Real density was obtained by dividing the mass of the sample by the volume obtained with the pycnometer. To obtain the specific surface area, powder samples containing 0.02 g to 3.00 g of particles with a given size were degassed under pure nitrogen (N_2) at 523 K for 5 h [3]. Then, the samples were analyzed with a gas-adsorption analyzer (Micromeritics, Tristar II 3020, USA). The gas used for surface measurements was N_2 (purity = 99.995%; Praxair, USA) at 77 K. The chemical composition of all samples was analyzed with an X-ray fluorescence spectroscopy system (Axios max, Panalytical, USA). The particle properties of anodes with different particle sizes are presented in Table 3.1.

Table 3.1 Elemental composition and physical properties of anode particles with different particle sizes

Properties	Particle size			
	2.190 ± 0.190 (mm)	1.200 ± 0.205 (mm)	0.500 ± 0.060 (mm)	0.200 ± 0.033 (mm)
S (%)	1.85 ± 0.06	1.86 ± 0.06	1.83 ± 0.06	1.82 ± 0.06
Si (ppm)	257 ± 36	222 ± 37	293 ± 35	453 ± 63
Ca (ppm)	468 ± 23	335 ± 63	204 ± 10	459 ± 63
V (ppm)	308 ± 15	316 ± 15	312 ± 15	308 ± 15
Fe (ppm)	696 ± 35	740 ± 37	775 ± 35	895 ± 45
Ni (ppm)	187 ± 9	197 ± 10	201 ± 10	188 ± 9
Helium density ($g \cdot cm^{-3}$)	1.990	2.002	2.008	2.020
BET surface area ($m^2 \cdot g^{-1}$)	4.5	5.3	5.0	5.5

3.3.2 Gasification tests

Figure 3.6 shows a schematic of the experimental gasification process. A fixed-bed reactor (MTI; GSL-1600X50) with a 1.2 cm inner diameter and 40 cm-long glass column was used. The properties of the fixed bed reactor has been gathered in table 3.2. Temperature probes (K-type thermocouples) were placed along the bed to measure the temperature. Before entering the reactor, the gas phase was mixed in an inert fixed bed to homogenize the temperature equilibrium. The outlet-gas concentrations were measured with a gas analyzer (E-1500, E Instruments, USA). First, the fixed-bed reactor was loaded with a predetermined amount of anode particles (samples containing 1 g to 4.00 g, depending on bed height), and then the reactor was placed in a furnace at a high temperature (1233 K). Subsequently, a condenser was attached to either the exit of the reactor or a gas collector. Furthermore, nitrogen was used as a carrier gas. The temperature controller was configured according to the considered value (1233 K) for each test. Experiments were conducted for different gas-flow rates (0.5, 1, and 2 $L \cdot s^{-1}$), bed heights (2, 3, and 5 cm), and particle radii (0.5, 1, 2, and 3 mm). The particles were heated with an inert gas (99.995% N_2 at 200 ml/min) from room

temperature to 1233 K at 8 K/min heating rate. The setup was maintained for 20 min under N_2 to stabilize at 1233 K. The sample was then gasified under CO_2 (99.9%). After a specific duration of carbon conversion, the furnace was switched off, and the anode particles were cooled down in an inert atmosphere. The monitored data during each experiment included the measured inlet and outlet temperatures, masses of anode particles, pressure drop, the specific surface area of samples, and reactor-exit gas concentrations at different time intervals. The reaction time depended on the sample particle size and varied between 3 and 15 h. The outlet-gas flow was directed to the oil tank to avoid emissions to the atmosphere.

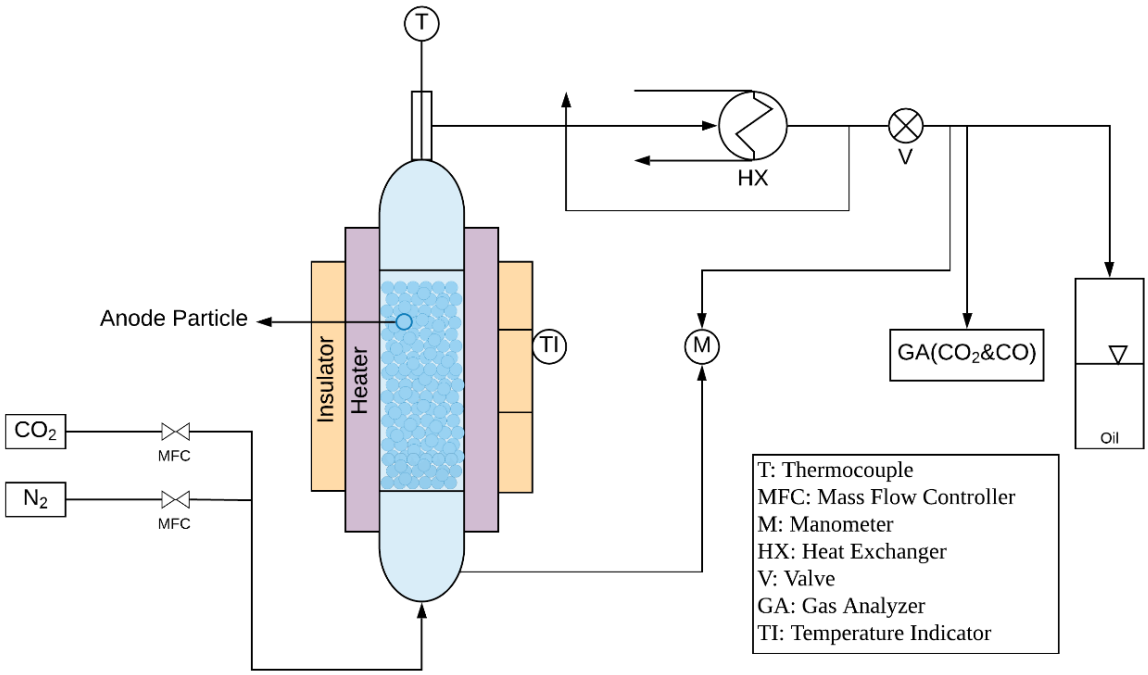

Figure 3.6 Schematic of the experimental setup (fixed-bed reactor)

Table 3.2 Summary of experimental conditions used for modeling.

Property	Description	Values for different particle sizes		
		0.5 mm	1mm	2 mm
L (m)	Height of the bed reactor		0.05	
d (m)	Diameter of the bed reactor		0.012	
ρ_b (kg · m^{-3})	Density of bed		1.238	
ρ_p (kg · m^{-3})	Real density	1.989	1.985	1.983
ε_b	Macroscale porosity (of bed)		0.38	
ε_p	Microscale porosity (of particle)	0.33	0.35	0.37
S (m^2 · kg^{-1})	Initial specific surface area particle bed		4.57	
β (m^2)	Permeability of bed		2×10^{-12}	
D_i (m^2 · s^{-1})	Diffusion coefficient of particle		5.67×10^{-5}	
μ_{Mix} (kg · s^{-1} · m^{-1})	Viscosity of gas phase		4.35×10^{-5}	

3.4 Results and discussion

The outputs of CFD-DEM include the velocity of fluid, temperature, pressure drop, and species concentration for the fluid phase, as well as particle position (The particles do not carry by the gas, but due to their consumption, they fall down, and the height of the bed decreases over time. The second law of mechanics was used to find a new position of the particles in the bed. The YADE software implemented the numerical procedure), velocity, temperature, and interparticle forces of particles, changes in structural parameters (e,g, porosity, permeability, and specific surface area at any time interval of the process). These parameters are unachievable through experimental works.

3.4.1 Pressure drops

The pressure drop across the carbon anode is one of the critical parameters for designing a plan related to the operational conditions and flow distribution. It leads to the formation of convection term and increased consumption of anode. The concentration and pressure profiles in line with the reactor's radial and axial coordinates are provided using the numerical model presented in this research. The reactor's wall temperature remains fixed at 1233 K, favoring the Boudouard reaction [3]. The manometer monitors the pressure drop along the anode particle bed. The pressure drop 3.4.1 results from the model are compared with the experimental ones by using those plotted against gas velocity in three ratios of the bed diameter per particle diameter (d/dp), as depicted in Figure 3.7a. Results from the figure and the calculated ones confirm the good agreement between the experimental data of the model (R^2 = 98.95). With increased particle size, less pressure drop occurs for an identical gas velocity. This status may be due to the lower gas velocity in the distance between the anode's particles with an equal flow rate over the larger particles, where the local void fractions remain larger than the smaller ones. Additionally, the pressure drop rises with increased superficial gas velocity for all ratios (d/dp). A decrease in the ratio can stem from a non-uniform flow that exerts a bypass effect throughout the bed of particles because the wall effects stay paramount at a low gas-flow rate [54, 55]. By contrast, for a high ratio d/dp of 24, the near-wall non-uniform effect can be found at larger gas velocities (v > 0.3 m $\cdot$ s^{-1}), satisfying the conditions linked to the bed's turbulent-flow regime [56]. To better design large-scale anode particles, these behaviors seem excessively practical. However, the impact of porosity remains dominant at high flow rates. A lower porosity confers difficulty in fluid penetration into the bed, so a higher pressure drop occurs.

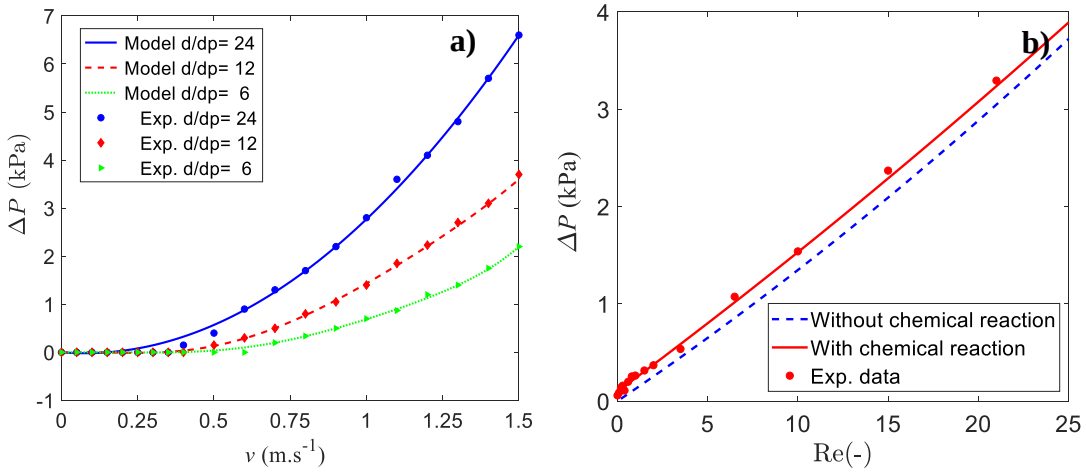

Figure 3.7 a) Pressure drops of the model compared with experiments against gas for three ratios of *D/dp*. b) Pressure drop as a function of effective Reynolds numbers for simulations with and without chemical reactions (R = 6 mm, H = 5 cm, T = 1233 K).

Figure 3.7 b shows that the pressure drop as a function of the Reynolds number (Equation - 3.42) decreases for simulations containing and lacking chemical reactions. According to the result, the pressure drop increases by applying the chemical reaction for all ranges of Re. Considering that gasification is an exothermic reaction, gas properties change with increased temperature and affect the Re. The transition Re_e number between the laminar and turbulent regimes Re_e is based on the average interstitial velocity and the characteristic length scale of the pores, so the limitation of laminar flow for a porous fixed-bed reactor is relatively low. Proper fitting between the experimental and model data in the laminar regime occurs ($Re_e \leq 1$). For larger Reynolds numbers ($Re_e > 5$), a slight overestimate of the pressure drop is shown by the model for turbulent regimes [54, 57]. This effect can be due to the flow channeling in the bed and increases with increased flow rate [56].

3.4.2 Diffusion-coefficient dependence on mass transfer

To determine the dependence of the CO_2 outlet concentration on the gas velocity with/without mass-transfer limitation, Figure 3.8 is plotted in the outlet gas. Figure shows

the mass-transfer limitations in the outlet gas according to the model results. A notable difference exists between C_{CO_2} conversion with and without mass-transfer limitations. With mass-transfer limitations, the velocity dependence on the outlet concentration of C_{CO_2} remains weak. The thin gas film surrounding the anode particles decreases with increased velocity, making the mass-transfer limitations less important. Eventually, the two plots approach each other as the velocity increases, and the outlet concentration becomes less dependent on the mass-transfer limitations.

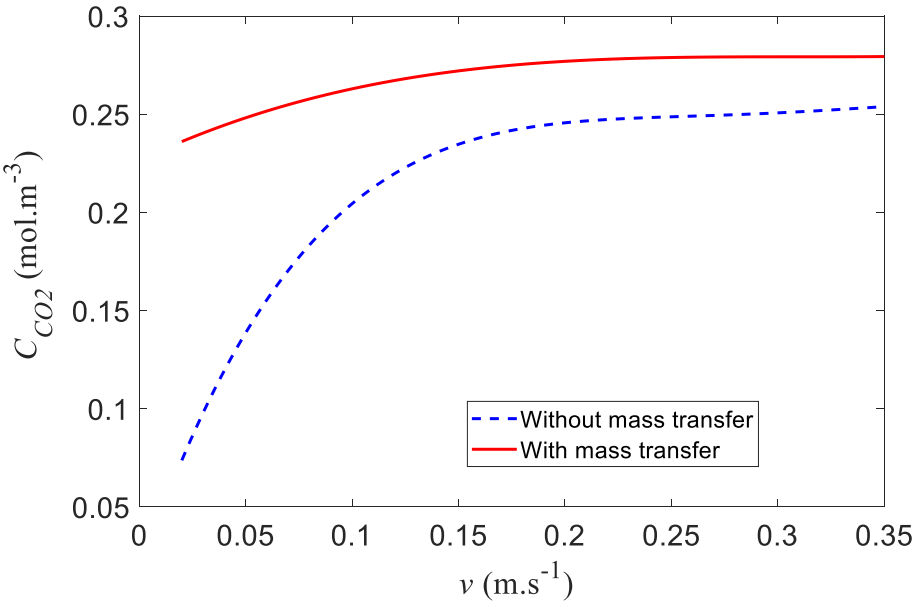

Figure 3.8 Mass-transfer limitations in the outlet gas (r = 1 mm, R = 6 mm, H = 5 cm, T = 1233 K)

Figure 3.9 depicts simulation results of the outlet C_{CO_2} dependence on the mass-transfer coefficient for a 0.2 m·s^{-1} entrance velocity. i.e., a medium-velocity level in the laminar flow in the fixed-bed reactor. With an increased mass transfer coefficient, the outlet C_{CO_2} decreases. This situation underlies the rationale that a higher C_{CO_2} bulk concentration approaches the surfaces of anode particles and reacts. With an increased mass-transfer

coefficient, the concentration advances from the bulk toward the surface and becomes the reaction's driving force.

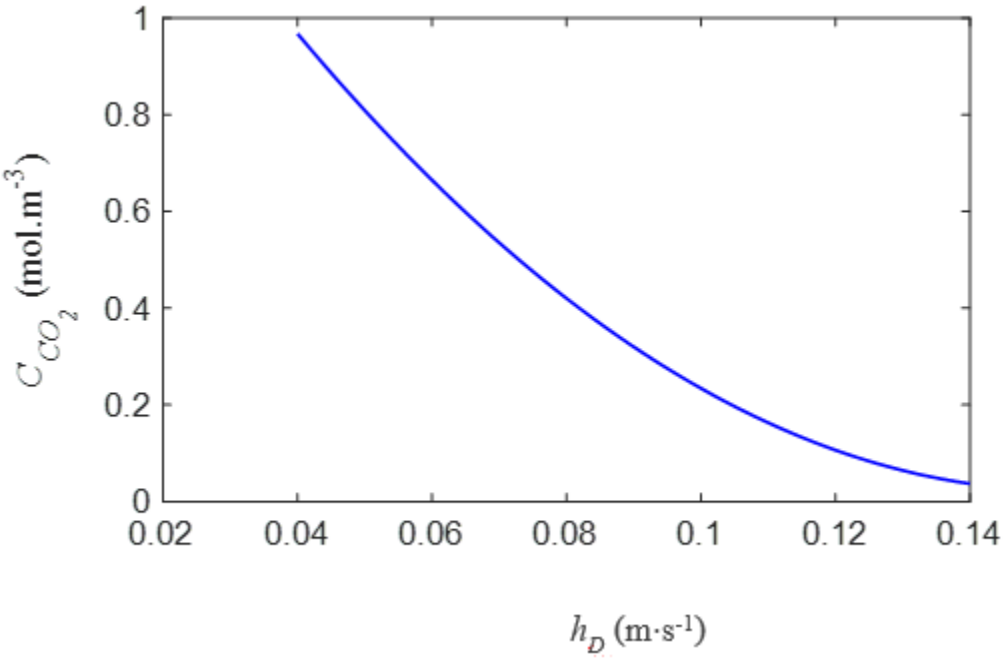

Figure 3.9 Outlet C_{CO_2} dependence on the mass-transfer coefficient for 0.2 m·s^{-1} velocity (r = 1 mm, R = 6 mm, H = 5 cm, T = 1233 K).

4.4.3 Concentration distribution

After model verification, one of the significant applications is used to predict the concentration distribution in the carbon anode. The superiority of this model is the prediction of gas-component concentration in the particle size (microscale) and between the particle (macroscale) in the fixed-bed reactor simultaneously at each time and position. Figure 3.8 shows the simulation results of the molar concentrations of the gas species with CO_2 (Figure 3.10a) and CO conversion (Figure 3.10b) along the reactor length. With decreased CO_2 concentration, CO drastically increases at an extremely close distance to the reactor entrance. These results demonstrate that CO_2 and CO are distributed inside a particle in the middle of

the bed and their concentration plots within the particle. Evidently, the concentration close to the center of the particle is higher for CO, where products form and diffuse into the bulk gas from this specified location.

In contrast to the reactant gas, the CO_2 concentration is small at the center and approaches the bulk concentration on the surface. Figure 3.8 verifies the general trends observed in the reactor. The CO_2 molar concentration progressively decreases as the gas stream passes through the bed, whereas the CO concentration increases through the Boudouard reaction. It should be noted that the anode bed has axisymmetric so that a cut plan in 3D can be done, which in turn results in a 2D plan (*yz*-plan). Figure 3.10 is a 2D plan from the simulated 3D bed.

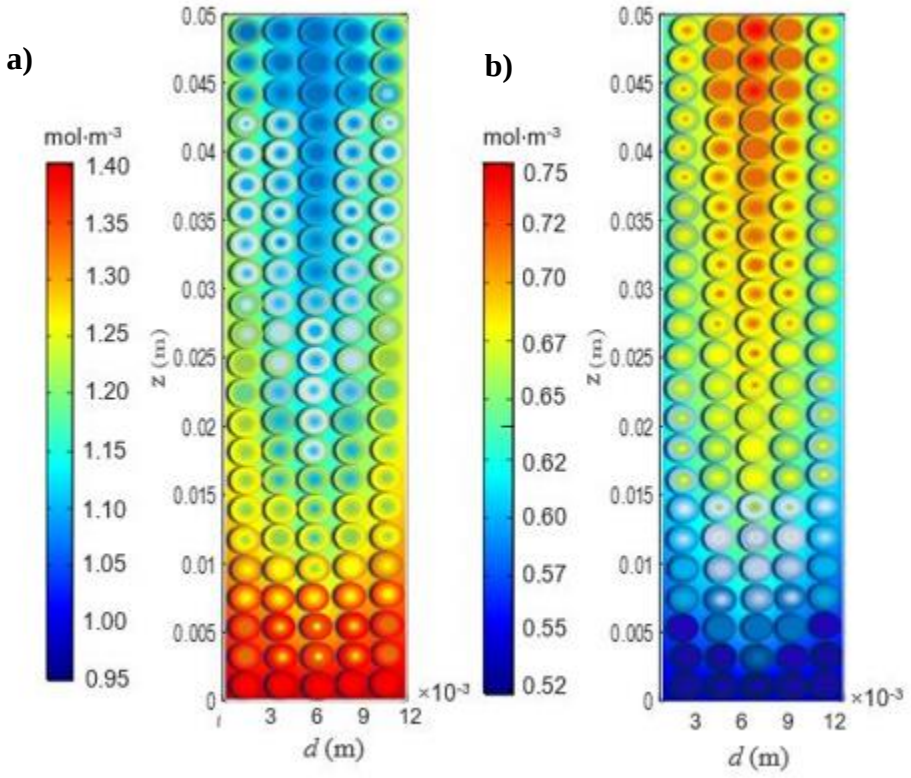

Figure 3.10 Molar concentrations of gas species in the vertical fixed-bed reactor (inlet gas input from the bottom of the reactor: a) CO_2 and b) CO conversion along the reactor length (r = 1 mm, Q = 1 l·min^{-1}, H = 5 cm, T = 1233 K).

Figure 3.11 shows the simulation results of CO_2 concentrations inside the particle at various reactor positions. The CO_2 concentration is lower at the particle's center than at all reactor positions. In other words, the performance of the reactor is constrained by diffusion inside the particle, and the active porous material in the center of the particle is not consumed. Decreasing the particle diameter can avert this limitation. For a particle radius of 1 mm, the intraparticle diffusion limits the reactor because the active sites in the particle interior are not used to their fullest potential, as shown by the slope of the solid lines. The lines level out more quickly with decreased particle size (0.5 mm), implying more significant reaction-rate-limited regions.

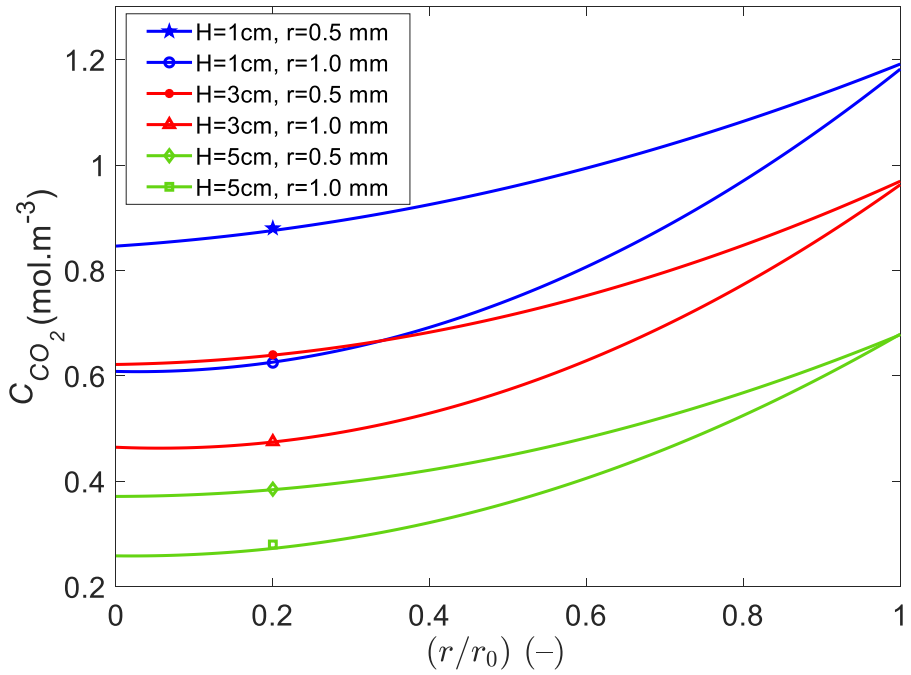

Figure 3.11 CO_2 concentration (inside the particle) at various reactor positions (Q = 1, R = 6 mm L·min^{-1}, H = 5 cm, T = 1233 K).

Figure 3.12 compares the computed results with the experimental ones for the outlet gases. The experimental results were measured by placing the gas analyzer in the outlet stream. The

profiles show that the degree of conversion dramatically increases from the start of the reaction until it reaches approximately 0.60 and 0.4 for CO_2 at 1 $L \cdot min^{-1}$ flow rate. Accordingly, the reaction advances very slowly until full conversion. Initially, the fast-increasing conversion can be directly attributed to the rapid evolution of the surface area until the pores collapse. In this status, either the reaction surface or the reaction rate decreases. The dashed line shows the distribution concentrations after 8 h. The particles have shrunk, so the total bed height decreases to 3 cm. The slopes are steeper because of the reactive particles' surfaces. The results indicate good agreement between the calculated and experimental data ($R^2 = 0.9921$), and the model can provide highly reliable estimates of experiments.

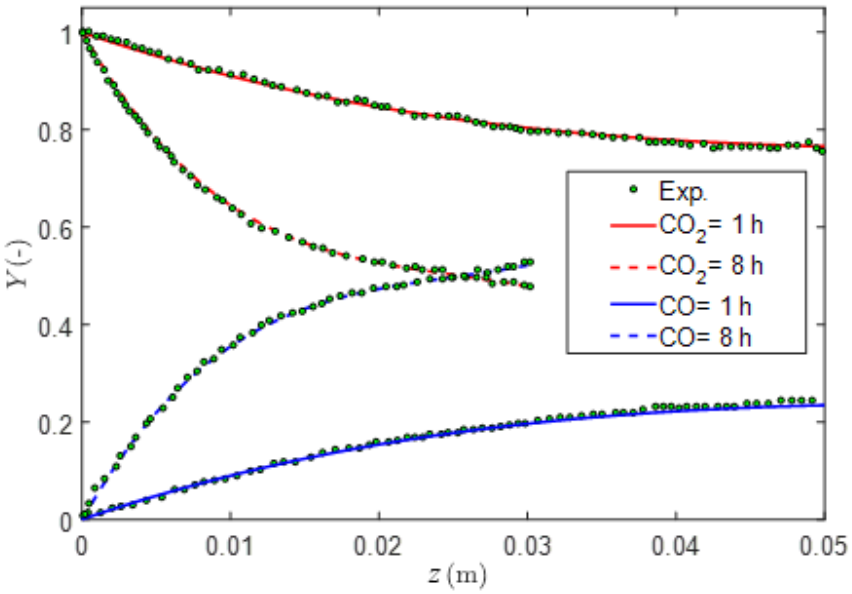

Figure 3.12 Comparison of the model to the experimental data along the reactor length at different processing times (r = 1 mm, flow rate = 1 $L \cdot min^{-1}$, bed height = 5 cm, temperature = 1233 K).

3.4.4 Specific surface area and porosity

The model allows the tracking of the evolution of the specific surface area throughout gasification at each time and position of the fixed-bed reactor. Figure 3.13 shows the variations in the surface area versus the bed position for four anode particles (1 mm particle

size) in the different process periods. As indicated in the figure, the surface increases rapidly at the beginning during gasification and approaches the highest point (1, 2, and 4 h). The anode particle surface remarkably rises to 10% of the initial surface area after 1 h. The maximum surface point proceeds from top to bottom after 4 h and then starts to decrease. Different zones exist in the reactor with different values of chemical-reaction rate and mass transfer, so the structural parameters of the particles remain unchanged throughout the process. In this model, the evolution of specific surface area is performed by the RPM equation in the chemical reaction term because RPM can indicate the nature of pore structure and pore-volume distribution. At the first time step, the increase in the surface area may be due to surface reactions [33, 58, 59]. As the reaction proceeds, the specific surface area initially increases with increased pore radii and pores smaller than 1 nm open gradually. Conversely, they decrease at the next step, possibly because of the appearance and coalescence of pores [60, 61].

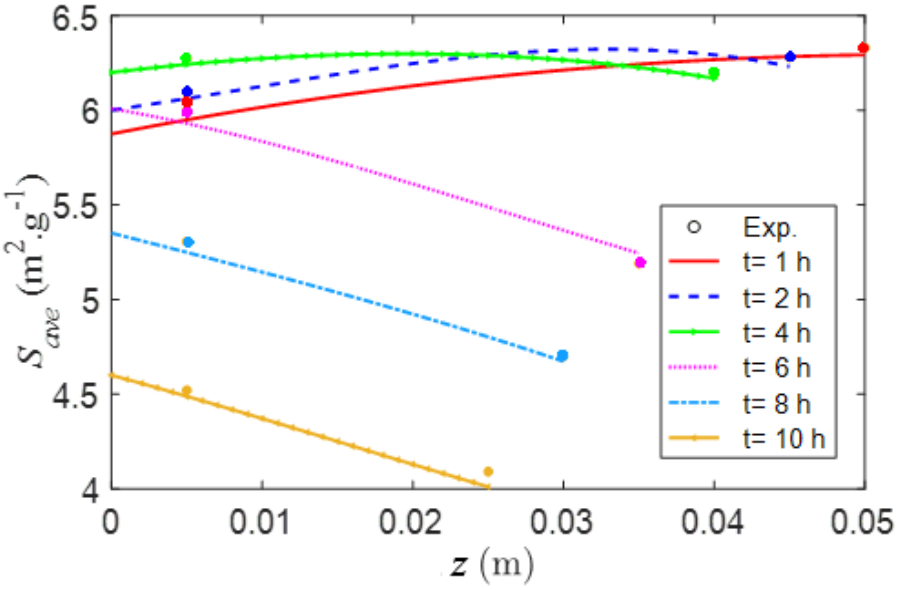

Figure 3.13 Variations in the surface area versus bed position of four anode particles (r = 1 mm, Q = 1 L·min^{-1}, H = 5 cm, T = 1233 K) throughout the different process periods.

Porosity is found to change with particle position in the fixed-bed reactor, as shown in Figure . To avoid edge effects, the first and last layers of particles are not taken into

consideration.The figure shows the volume fraction at each cross-section of the particle bed at various periods along with the bed height. In the first-time steps, no notable porosity change occurs with bed height. After a while, porosity increases with time at each position. Additionally, the porosity in each time step evidently has a maximum amount at the bottom of the reactor, which can be related to more available active sites for the reaction at the bottom of the reactor. Therefore, the slope of the porosity changes dramatically in this zone and decreases at the top of the particle bed. These results demonstrate that after a 12 h gasification reaction, more than 90% of the solid particle is consumed. This consumption includes internal and external gasification, leading to the shrinkage of particles and bed height. The bed height reaches 0.01 after 12 h.

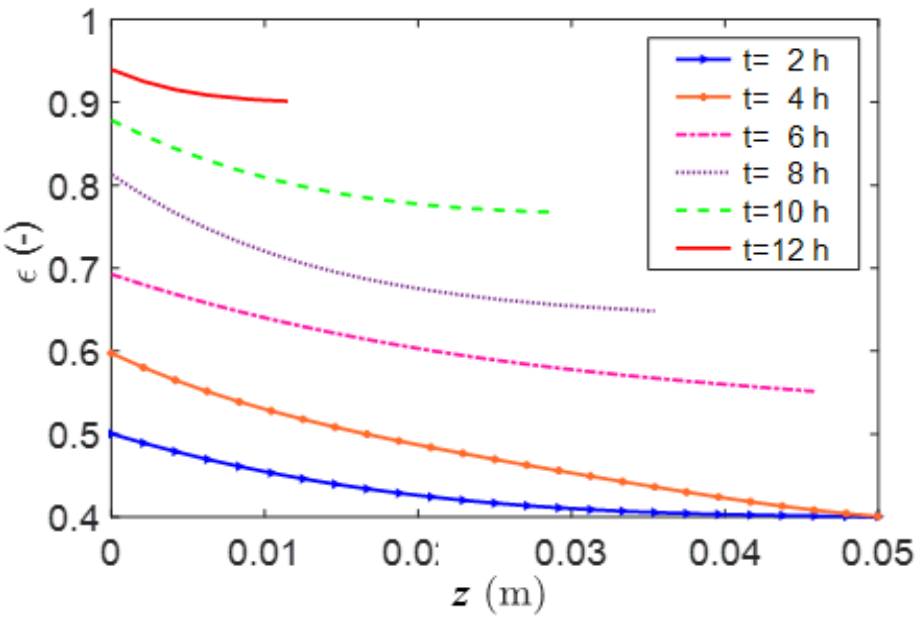

Figure 3.14 Porosity changes with particle position (r = 1 mm, Q = 1 L·min^{-1}, H = 5 cm, T = 1233 K)

Figure 3.15 shows the distribution of external and internal gasification for different particle sizes during gasification. Simulation results show that internal gasification is dominant for all particle sizes in the initial steps, but over time, the sizes decrease rapidly as the reaction progresses. Increasing the external gasification can be related to improving the outer surface of the anode particle by reaction progress. F. Chevarin et al. [3] reported that the external surface increases because of two factors. First, after gasification progresses, the particles

shrink, increasing the ratio of the external surface to the particle volume. Second, the enlargement of pores near the external surface after a certain processing step is evaluated as the external surface, leading to increased external gasification.

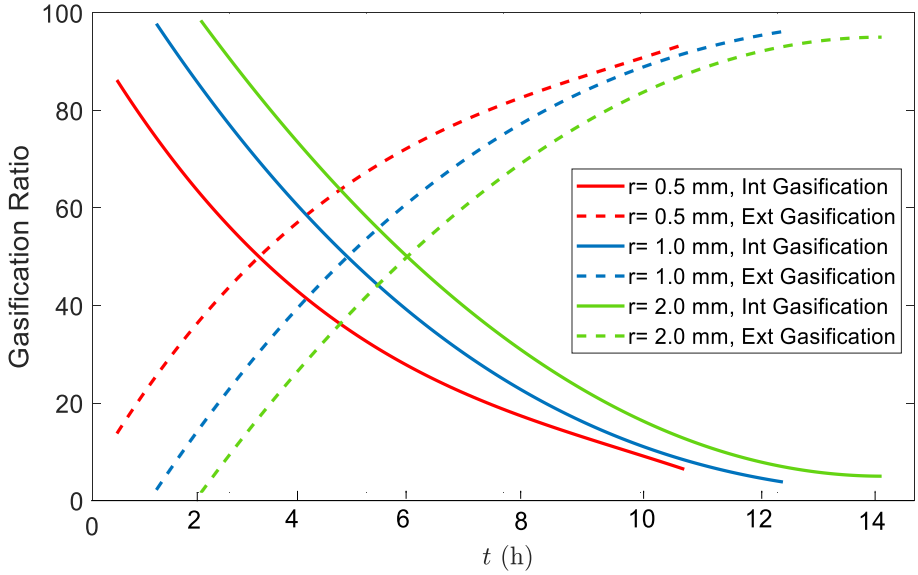

Figure 3.15 Ratios of internal and external gasification versus the processing time for three different particle sizes (Q = 1 l. min^{-1}, H = 5 cm, T = 1233 K).

3.4.5 Effectiveness factor

Effectiveness factor is a measure used to compute the minimum ratio of the reaction rate owing to the particles' pore-diffusion resistance [62]. The kinetic model results reveal that anode-particle gasification depends on anode conversion. The effectiveness factor is almost 0.95 for particle sizes less than 0.05 mm, with X = 0.60 at the reactor center and upwards, but lower for greater particle sizes (Table 3.3). The diffusion rate is recommended to be equal to the reaction rate. A significant difference exists for large size particles (2.0 mm) than for small ones.

The distributions of the effectiveness factor in a fixed-bed reactor at multiple heights are presented in Figure 3.1. The factor fluctuates at around 0.900–0.959. The first and second steps gradually increase from the wall to 0.001 m distance and decrease from 0.001 m to the

reactor center, where the lowest value emerges. According to the definition of the effectiveness factor, the control of gasification follows the reactants' mass-fraction distributions because the temperature gradient inside the particles is not included. A relatively low reaction remains when the comparatively small temperature near the wall at the fixed-bed reactor's center. By distancing the fluid from the wall and increasing the temperature gradually, the temperature that positively affects the intraparticle transfer exceeds the value shown for the reaction rate. The concentration gradient within the anode particles is weakened by continuing this process, so the effectiveness factor increases with increased distance from the wall [27]. However, nearer to the reactor's center, a higher temperature increases the reaction rate. At 0.001 m distance from the reactor's wall, the reaction rate is positively affected by temperature exceeding that for intraparticle transfer, which in turn causes the enhancement in concentration gradient within the particles. Hence, the effectiveness factor decreases when approaching the center of the reactor. As a result, Figure 3.16 shows the reverse trend of the effectiveness factor. Additionally, at the height of 0.030 m, the maximum temperature causes the effectiveness factor to be minimized at the center of the reactor.

Table 3.3 Effectiveness factor for different particle sizes and anode conversions.

Radius (mm)	Reaction rate	Carbon conversion %				
		0	20	40	60	80
0.05	First order	0.81	0.85	0.89	0.94	0.98
	L-H	0.75	0.79	0.86	0.93	0.97
0.5	First order	0.49	0.64	0.79	0.88	0.94
	L-H	0.44	0.60	0.75	0.86	0.93
1.0	First order	0.45	0.63	0.77	0.87	0.93
	L-H	0.38	0.57	0.71	0.81	0.90
2.0	First order	0.43	0.59	0.74	0.86	0.92
	L-H	0.36	0.53	0.68	0.81	0.89

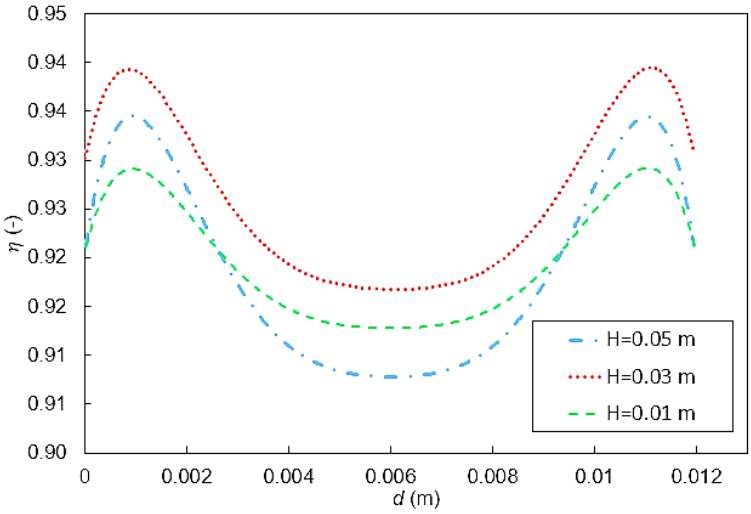

Figure 3.16 Effectiveness factor distribution in the radial-bed direction for different bed heights. (r = 1 mm, R = 6 mm, Q = L·min^{-1}, T = 1233 K).

3.4.6 Temperature profiles

Figure 3.17 and Figure 3.18 exhibit the temperature distributions at various positions and directions (axial and radial). Figure 3.17 demonstrates that the hotspot is located close to the reactor exit. The solid temperature is higher than that of the gas because of the exothermic reaction within the particles [21, 56, 59, 63]. Based on Figure 3.18, the temperature increases at the center and decreases on both sides in a parabolic manner because of the wall heat sinks. This temperature difference results from a competition between the rates of interfacial heat and mass exchange. In this particular case slight resistances to heat transfer to and from the solid particles cause a higher temperature in the particle. The solid temperature is higher than the gas temperature [64]. In practical applications, the above temperature variations are due to the much higher thermal-conductivity performance and heat capacity of the solid phase than those of the gas phase.

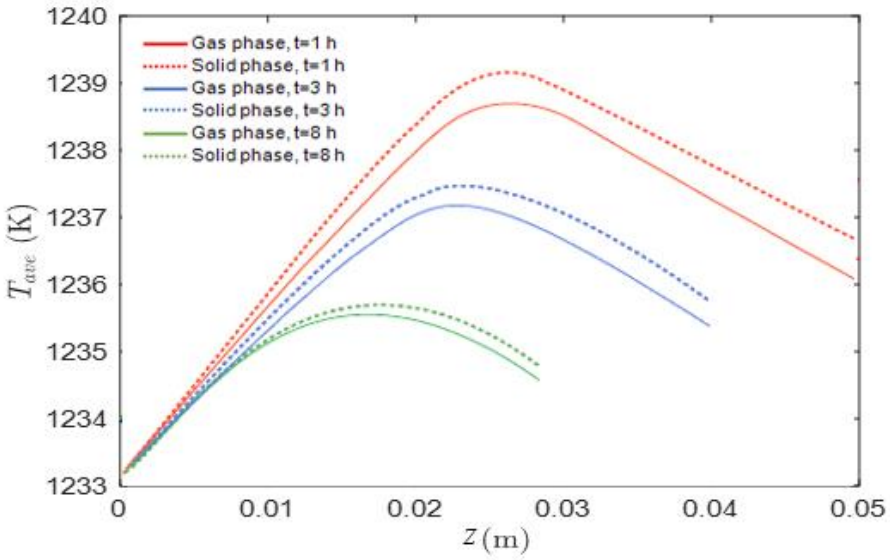

Figure 3.17 Temperature profiles in the reactor. Temperature distributions along the axial direction of the reactor (r = 1 mm, Q = 1 L·min^{-1}, H = 5 cm, T = 1233 K)

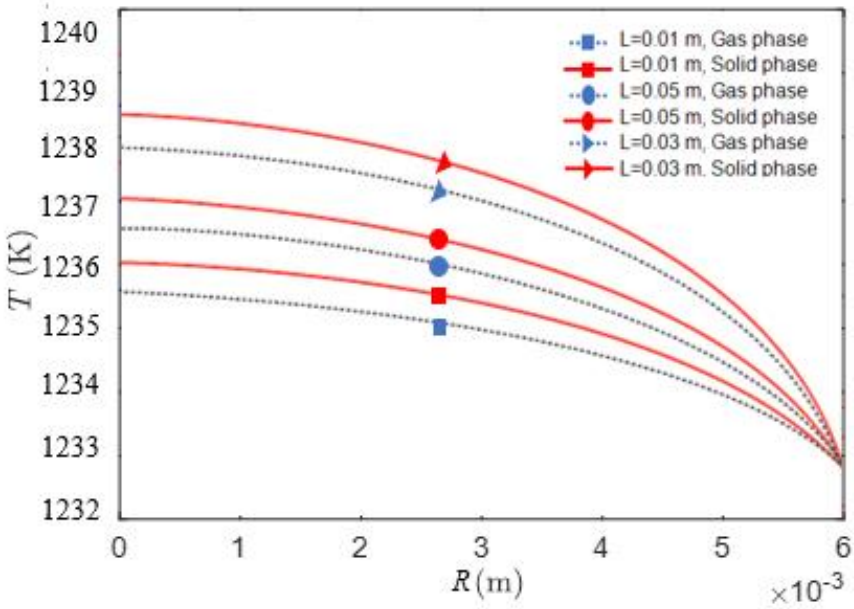

Figure 3.18 Temperature profiles in the reactor. Temperature distributions along the radial direction of the reactor (r = 1 mm, Q = 1 L·min^{-1}, H = 5 cm, T = 1233 K)

Figure 3.19a-c demonstrates the simulation outcomes at multiple flow rates. The hotspot temperature rises as flow rates increase. Moreover, the outlet temperature increases slightly.

Whenever the volume flow rate of the material increases, the Reynolds number in the bed significantly increases. Consequently, the axial and radial heat-transfer rates increase, whereas the radial-temperature difference and hotspot temperature decrease to their original value.

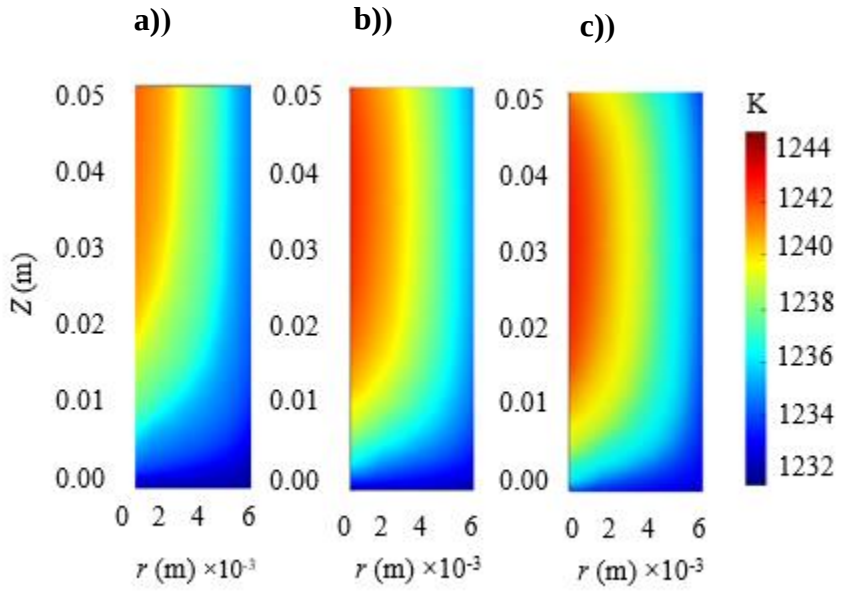

Figure 3.19 Temperature distribution of the hotspot at multiple flow rates: a) 0.5 L·min^{-1}, b) L·min^{-1} and c) 2 L·min^{-1} (r = 1 mm, R = 6 mm, hotspot·min^{-1}, H = 5 cm, T = 1233 K)

3.4.7 Particle shrinkage

Figure 3.20 illustrates the evolving particle size during the process through the shrinkage effect. As expected, the particle size is fixed and identical to the initial value at any point inside the domain when no shrinking exists. By contrast, the particle size decreases with gasification progress. Similar to the apparent density, the particle shrinkage's greatest gradient is observed near the inlet area where the reactions primarily occur. The simulation reveals that the mean particle diameters decrease to 3 mm after 10 h at the reactor's bottom side. As a consequence of particle shrinkage, they fall, and the height of the bed begins to decrease throughout gasification.

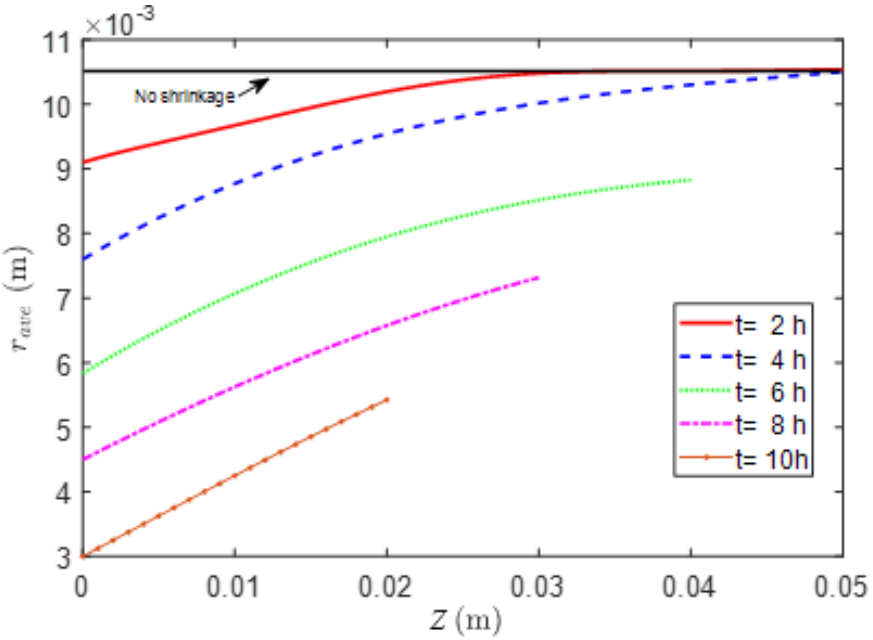

Figure 3.20 Evolving particle size for the shrinking pattern (Q = 1 l. min^{-1}, H = 5 cm, T = 1233 K)

3.4.8 Particle tracking

The movement trajectory for selected particles is shown in Figure 3.21. The moving direction of the particle changes and falls into the bed because of gas-particle interactions, particle-particle collisions, and boundary effects in the vicinity of the bed top [23]. Figure 3. compares the tracking at multiple flow rates. The figures show that for a smaller particle size r = 0.5 mm (Figure 3.21 a and 3.21b), either the passing direction or processing time remains lower than those of other tests (9 h). Clearly, with increased flow rate, the passing direction, and processing time decrease (Figure 3.21c and 3.21d). In each figure, particle tracking is simulated in three different bed positions. The particles in the reactor's central position vanish in less time, and the tracing pad may stem from a higher chemical reaction in such regions.

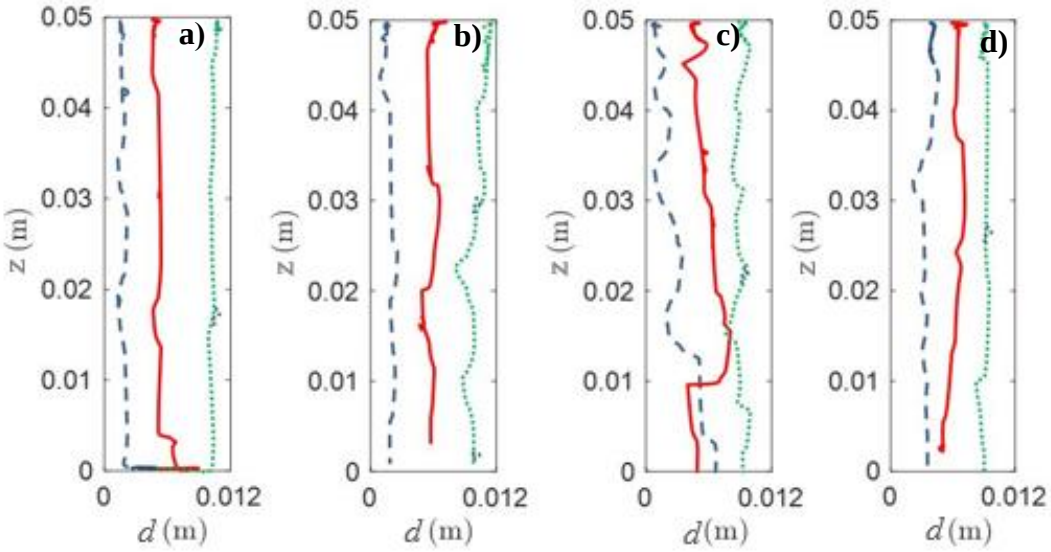

Figure 3.21 Comparison of particle trajectories in the bed of particles at a) 0.5 L·min^{-1}, r = 1 mm, b) 0.5 L·min^{-1}, r = 0.5 mm, c) 1.0 L·min^{-1}, r = 1 mm, and d) 2 L·min^{-1}, r = 1 mm

3.5 Conclusion

This research addresses the development of a reaction-transport model to simulate anode CO_2-reactivity dynamics using the FEM-DEM model. The gasification process of anode particles was explained using mass transfer, heat transfer, and momentum equations. A particle-shrinkage pattern was rigorously applied to determine how density and size variation affect the main performance parameters, such as specific surface area, particle porosity, carbon anode conversion, and process time of the fixed bed. CO_2 and CO concentration distributions inside particles and throughout the bed were analyzed, and gas velocity and pressure simulations were conducted. With an increased flow rate, gasification time decreased. Results revealed that conversion drastically increased in the reaction's early stages. The gas distribution showed that the maximum change occurred in the first steps, and this change was primarily due to the existing surface reactions. Accordingly, the distribution decreased owing to pore merges. Anode consumption during the process included internal and external gasification and consequently led to the shrinkage of particles and bed height. Internal gasification was predominant in the initial stages, but external gasification increased

as the reaction progressed. The results indicated that the CFD–DEM model could predict the particle's bed scale and the complete microscale. An inventive particle-tracking technology based on the CFD-DEM approach was illustrated in this work to quantitatively evaluate the actual process time and the passing direction of particles.

Acknowledgments

The authors acknowledge the financial support of Alcoa and the Aluminium Research Centre–REGAL. The authors would like to express their appreciation to Guillaume Gauvin for his technical support.

References

1. Azari, K., *Investigation of the materials and paste relationships to improve forming process and anode quality*. 2013, Laval Uinversity: Canada.
2. Chevarin, F., *Relation entre les propriétés physico-chimiques de l'anode en carbone et sa vitesse de réaction sous CO_2,* in *in Metallurgy and Materials Department*. 2015, Laval University:: Quebec, CANADA.
3. Chevarin, F., et al., *Active pore sizes during the CO_2 gasification of carbon anode at 960°C.* Fuel, 2016. **178**: p. 93-102.
4. Chevarin, F., et al., *Substrate effect of coke particles on the structure and reactivity of coke/pitch mixtures in carbon anodes.* Fuel, 2016. **183**: p. 123-131.
5. Chevarin, F., et al., *Air and CO_2 reactivity of carbon anode and its constituents: an attempt to understand dusting phenomenon,* in *Light Metals 2015*. 2015, Springer. p. 1147-1152.
6. Engvoll, M.A., *Reactivity of Anode Raw Materials And Anodes For Production of Aluminium, Dissertation*, in *sceince and engineering*. 2001, the Norwegian University of science and technology (NTNU): Norvay.
7. Houston, G. and H. Øye, *Consumption of anode carbon during aluminium electrolysis.* Aluminium, 1985. **61**(5): p. 346-349.
8. Sadler, B.A. and S.H. Algie, *Porosimetric study of sub-surface carboxy oxidation in anodes,* in *TMS*. 1991, Minerals, Metals & Materials Soc New Orleans, LA, USA.
9. Fedkiw, R.P., *Coupling an Eulerian fluid calculation to a Lagrangian solid calculation with the ghost fluid method.* Journal of Computational Physics, 2002. **175**(1): p. 200-224.
10. Jiang, Y., et al., *CFD modeling of multiphase flow distribution in catalytic packed bed reactors: scale down issues.* Catalysis Today, 2001. **66**(2): p. 209-218.
11. Potapov, A.V., M.L. Hunt, and C.S. Campbell, *Liquid–solid flows using smoothed particle hydrodynamics and the discrete element method.* Powder Technology, 2001. **116**(2-3): p. 204-213.

12. Salmi, T. and J. Warma, *Modelling of catalytic packed-bed reactors—comparison of different diffusion models.* Computers & Chemical Engineering, 1991. **15**(10): p. 715-727.
13. Thomas, J.R. and F. Fucher, *Thermal Modeling of Microwave Heated Packed and Fluidized Bed Catalytic Reactors.* Journal of Microwave Power and Electromagnetic Energy, 2000. **35**(3): p. 165-174.
14. Wehinger, G., T. Eppinger, and M. Kraume, *Detailed numerical simulations of catalytic fixed-bed reactors: Heterogeneous dry reforming of methane. Chemical Engineering Science*, 2015. **122**: p. 197-209.
15. Singhal, A., et al., *Multiscale modeling of a packed bed chemical looping reforming (pbclr) reactor.* Energies, 2017. **10**(12): p. 2056.
16. Larachi, F.ç., I. Iliuta, and K. Belkacemi, *Catalytic wet air oxidation with a deactivating catalyst analysis of fixed and sparged three-phase reactors.* Catalysis Today, 2001. **64**(3): p. 309-320.
17. Larachi, F.ç., et al., *gas–liquid interfacial areas in three-phase fixed bed reactors1Paper presented by André Laurent at the 12th International Congress of Chemical and Process Engineering CHISA 1996, Praha, Czech Republic, 25–30 August, 1996.1.* Chemical Engineering and Processing: Process Intensification, 1997. **36**(6): p. 497-504.
18. Ortiz-Arroyo, A., et al., *CFD modeling and simulation of clogging in packed beds with nonaqueous media.* AIChE Journal, 2002. **48**(8): p. 1596-1609.
19. Valkov, B., C.H. Rycroft, and K. Kamrin, *Eulerian method for multiphase interactions of soft solid bodies in fluids.* Journal of Applied Mechanics, 2015. **82**(4): p. 041011.
20. Partopour, B. and A.G. Dixon, *Integrated multiscale modeling of fixed bed reactors: Studying the reactor under dynamic reaction conditions.* Chemical Engineering Journal, 2018.
21. Gao, X., Y.-P. Zhu, and Z.-H. Luo, *CFD modeling of gas flow in porous medium and catalytic coupling reaction from carbon monoxide to diethyl oxalate in fixed-bed reactors.* Chemical Engineering Science, 2011. **66**(23): p. 6028-6038.
22. Hou, Q., D. E, and A. Yu, *Discrete particle modeling of lateral jets into a packed bed and micromechanical analysis of the stability of raceways.* AIChE Journal, 2016. **62**(12): p. 4240-4250.
23. Ku, X., T. Li, and T. Lovas, *CFD–DEM simulation of biomass gasification with steam in a fluidized bed reactor.* Chemical Engineering Science, 2015. **122**: p. 270-283.
24. Rabbani, S., M. Sassi, and T. Shamim, *Modeling of hydrodynamics of fine particles deposition in packed-bed reactors.* 2017. **9**(4): p. 157-168.
25. Wolfrum, C., A. Josten, and P. Götz, *Optimization and scale-up of oligonucleotide synthesis in packed bed reactors using computational fluid dynamics modeling.* 2014. **30**(5): p. 1048-1056.
26. Wang, L., C. Wu, and W. Ge, *Effect of particle clusters on mass transfer between gas and particles in gas-solid flows.* Powder Technology, 2017. **319**: p. 221-227.
27. Huang, K., et al., *Numerical evaluation on the intraparticle transfer in butylene oxidative dehydrogenation fixed-bed reactor over ferrite catalysts.* Journal of Industrial and Engineering Chemistry, 2015. **29**: p. 172-184.
28. Petera, J., L. Nowicki, and S. Ledakowicz, *New numerical algorithm for solving multidimensional heterogeneous model of the fixed bed reactor. Chemical Engineering Journal*, 2013. **214**: p. 237-246.
29. Pozzetti, G., et al., *A parallel dual-grid multiscale approach to CFD–DEM couplings.* Journal of Computational Physics, 2019. **378**: p. 708-722.
30. Santana, E.R., G. Pozzetti, and B. Peters, *Application of a dual-grid multiscale CFD-DEM coupling method to model the raceway dynamics in packed bed reactors.* Chemical Engineering Science, 2019. **205**: p. 46-57.

31. Zhu, Y.-P., G.-Q. Chen, and Z.-H. Luo, *Iterative Multiscale Computational Fluid Dynamics–Single-Particle Model for Intraparticle Transfer and Catalytic Hydrogenation Reaction of Dimethyl Oxalate in a Fluidized-Bed Reactor*. *Industrial & Engineering Chemistry Research*, 2013. **53**(1): p. 110-122.
32. Ziarati, M., M.A. Ghafouri Roozbahani, and N. Khandan, *New Method of Rigorous Modeling and CFD Simulation for Methanol—Steam Reforming in Packed-Bed Reactors.* Chemical Engineering Communications, 2016. **203**(10): p. 1359-1373.
33. Norouzi, H.R., et al., *Coupled CFD-DEM modeling: formulation, implementation and application to multiphase flows*. 2016: John Wiley & Sons.
34. Dixon, A.G., et al., *CFD Method To Couple Three-Dimensional Transport and Reaction inside Catalyst Particles to the Fixed Bed Flow Field.* Industrial & Engineering Chemistry Research, 2010. **49**(19): p. 9012-9025.
35. Gómez-Barea, A. and P. Ollero, *An approximate method for solving gas–solid non-catalytic reactions.* Chemical Engineering Science, 2006. **61**(11): p. 3725-3735.
36. Gudekar, K.G., *, Modeling, control, and optimization of fixed bed reactors*, in *chemical engineering*. 2002, Texas Tech University.
37. Bird, R.B., W.E. Stewart, and E.N. Lightfoot, *Transport Phenomena*. 2006: Wiley.
38. JM Coulson, a.J.R., *CHEMICAL ENGINEERING: Fluid Flow, Heat Transfer and Mass Transfer* 4th ed. Chemical Engineering Education. Vol. 1. 1991, Oxford, U.K.: Pergamon Press. 182-183.
39. Garner, F.H. and R.W. Grafton, *Mass Transfer in Fluid Flow from a Solid Sphere.* Proceedings of the Royal Society of London. Series A, Mathematical and Physical Sciences (1934-1990), 1954. **224**(1156): p. 64-82.
40. Gómez-Barea, A., P. Ollero, and R. Arjona, *Reaction-diffusion model of TGA gasification experiments for estimating diffusional effects.* Fuel, 2005. **84**(12-13): p. 1695-1704.
41. Kavand, M., et al., *Reaction−Diffusion Model for Gasification of a Shrinking Single Carbon-Anode Particle.* ACS Omega, 2021.
42. Xu, Q., S. Pang, and T. Levi, *Reaction kinetics and producer gas compositions of steam gasification of coal and biomass blend chars, part 2: Mathematical modelling and model validation. Chemical Engineering Science*, 2011. **66**(10): p. 2232-2240.
43. Aissa, A., et al., *Ranz and Marshall correlations limits on heat flow between a sphere and its surrounding gas at high temperature.* Thermal Science, 2015. **19**(5): p. 1521-1528.
44. Gunn, D. and J. De Souza, *Heat transfer and axial dispersion in packed beds.* Chemical Engineering Science, 1974. **29**(6): p. 1363-1371.
45. Tamer, C., et al., *Effect of Drying on Porous Characteristics of Orange Peel.* International Journal of Food Engineering, 2016. **12**(9): p. 921-928.
46. Frédéric, D. and S.-A. Magnier, *Formulation of a 3-D numerical model of brittle behavior.* Geophysical Journal International, 1995. **122**(3): p. 790-802.
47. Donzé, F.V., et al., *Numerical Study of Compressive Behavior of Concrete at High Formulation.* Journal of Engineering Mechanics, 1999. **125**(10): p. 1154-1163.
48. Jerier, J.F., Donze, F.V., Imbault, D. and Doremus, P, *A geometric algorithm for discrete element method to generate composite materials* in *Discrete Element Group for Hazard Mitigation, annual report*, 2008. p. pp. A1-8.
49. Jerier, J.F., Donze, F.V. and Imbault, D., *An algorithm to generate random dense arrangements discs based on the triangulation, Discrete Element Group for Hazard Mitigation, annual report*. 2007. p. D1-7.
50. Geuzaine, C. and J.-F. Remacle, *Gmsh: A 3-D finite element mesh generator with built-in pre-and post-processing facilities.* International Journal for Numerical Methods in Engineering, 2009. **79**(11): p. 1309-1331.

51. Moghaddam, E.M., et al., *Rigid Body Dynamics Algorithm for Modeling Random Packing Structures of Nonspherical and Nonconvex Pellets.* Industrial & Engineering Chemistry Research, 2018. **57**(44): p. 14988-15007.
52. Kavand, M., et al., *An improved film–pore–surface diffusion model in the fixed-bed column adsorption for heavy metal ions: Single and multi-component systems.* Process Safety and Environmental Protection, 2018. **113**: p. 330-342.
53. Pirnia, P., et al., *ICY: An interface between COMSOL multiphysics and discrete element code YADE for the modeling of porous media.* Computers & Geosciences, 2019. **123**: p. 38-46.
54. Abdulmohsin, R.S. and M.H. Al-Dahhan, *Pressure Drop and Fluid Flow Characteristics in a Packed Pebble Bed Reactor.* Nuclear Technology, 2017. **198**(1): p. 17-25.
55. Ahmadi, S. and F. Sefidvash, *Study of Pressure Drop in Fixed Bed Reactor Using a Computational Fluid Dynamics (CFD) Code.* Chem Engineering, 2018. **2**(2): p. 14.
56. Miroliaei, A.R., F. Shahraki, and H. Atashi, *Computational fluid dynamics simulations of pressure drop and heat transfer in fixed bed reactor with spherical particles. Korean Journal of Chemical Engineering*, 2011. **28**(6): p. 1474-1479.
57. Jafari, A., et al., *Modeling and CFD simulation of flow behavior and dispersivity through randomly packed bed reactors.* Chemical Engineering Journal, 2008. **144**(3): p. 476-482.
58. Taskin, M.E., et al., *CFD Study of the Influence of Catalyst Particle Design on Steam Reforming Reaction Heat Effects in Narrow Packed Tubes.* Ind. Eng. Chem. Res., 2008. **47**: p. 5966.
59. Singhal, A., et al., *Verification of Heat and Mass Transfer Closures in Industrial Scale Packed Bed Reactor Simulations.* Energies, 2018. **11**(4): p. 805.
60. Feng, B. and S.K. Bhatia, *Variation of the pore structure of coal chars during gasification.* Carbon, 2003. **41**(3): p. 507-523.
61. Matsumoto, K., et al., *Gasification reaction kinetics on biomass char obtained as a by-product of gasification in an entrained-flow gasifier with steam and oxygen at 900–1000 C. Fuel*, 2009. **88**(3): p. 519-527.
62. Mani, T., N. Mahinpey, and P. Murugan, *Reaction kinetics and mass transfer studies of biomass char gasification with CO_2. Chemical Engineering Science*, 2011. **66**(1): p. 36-41.
63. Behnam, M., et al., *A new approach to fixed bed radial heat transfer modeling using velocity fields from computational fluid dynamics simulations.* Industrial & Engineering Chemistry Research, 2013. **52**(44): p. 15244-15261.
64. Sadooghi, P. and R. Rauch, *Experimental and modeling study of catalytic steam reforming of methane mixture with propylene in a packed bed reactor.* International Journal of Heat and Mass Transfer, 2014. **78**: p. 515-521.

Conclusions and Recommendations

Conclusions

First Part (Single Particle)- A diffusion-reaction model was developed for the gasification reaction of aluminum-industry anode particles, involving different kinetic models. The model assumed spherical symmetry and included the most notable chemical reactions, e.g., Boudouard reaction, intra-particle mass transfer resistance, mass conservation, and anode structural characteristics such as porosity, permeability, and shrinkage. The heat transfer was not included since the size of the anode particles was small enough to assume insignificant temperature gradient across the particle. A numerical method was used to solve the model. Model parameters were obtained experimentally by reacting monolayer anode particles in TGA. According to the experimental and simulated results, we concluded that the random pore model (RPM) is best describing the anode reaction behavior. Thus, this model was chosen among 5 models tested in this study. The model outputs allow tracking the particle consumption rate and the distribution of gas composition inside the reacting particle. In addition, due to the moving boundary condition for the external gasification, it is also possible to track the shrinkage and structural evolution of the particle during the gasification process. These data, mostly impossible to obtain experimentally, allow better interpretation of the reaction behavior. As such, the evolution of different parameters such as particle size, processing time, porosity, and surface area of the anode particles during gasification are revealed and their effect on the gasification process are discussed. The simulation results demonstrated that the anode structure (specific surface area and porosity) has a significant effect on both the intrinsic reaction rate and the intra-particle mass transport. The relative importance of intrinsic reaction and diffusion on the overall gasification process are quantified by calculating the Thieles modulus and effectiveness factor. Analyzing these factors reveals that their contribution on gasification rate may evolve at different stages of reaction, i.e., diffusion is more important at the beginning and chemical reaction becomes dominant towards the end of gasification. The L-H type reaction, integrated in the model, allowed revealing the inhibition effect CO on the gasification reaction. Although the

inhibition effect of CO on carbon gasification is a well-known feature, our model allows quantifying this effect along the whole gasification process. The effect of three different concentrations of CO in the inlet gas were given as examples. In summary, the model predicts well the gasification rate of anode particles, considering structural and diffusion parameters, thus offering a useful tool for optimization of gasification of anode particles.

Second Part (Bed of Particles)- This research addressed the development of a reaction-transport model to simulate anode CO_2 reactivity dynamics using the FEM-DEM model. To explain the gasification process of anode particles within a fixed-bed gasifier, mass, heat transfer, and momentum equations were used. A particle shrinkage pattern was applied rigorously to determine how density and size variation affect the main performance parameters such as specific surface area, particle porosity, carbon anode conversion, process time of the fixed bed. CO_2 and CO concentration distributions inside particles and throughout the bed, and simulations of gas velocity and pressure were conducted. An increased flow rate gave rise to decreasing the gasification time. The results revealed that the conversion drastically rises in the reaction's early stages. The distribution of gases showed that a maximum change exists in the first steps, and this change is mainly caused by the existing surface reactions. Accordingly, the distribution decreases due to pore merges. Anode consumption during the process includes both internal and external gasification and consequently leads to shrinkage of particles and bed height. In the initial steps, the internal gasification was prominent, and as the reaction progressed, the external gasification increased. The model results depict that CFD–DEM model can predict not only the bed scale but also complete micro-scale inside the particle. An inventive particle tracking technology based on the CFD-DEM approach is illustrated in this work to quantitatively evaluate the real process time and the passing direction of particles.

Third Part (Anode Slab)- The simulation of carbon anode reaction with CO_2, gasification, at the Hall-Héroult process, was studied for anode slab. Such gasification is not desirable because it increases net carbon consumption. The gasification process is including anode intrinsic reactivity and mass transport phenomena. In this part, a numerical model was developed for a large-scale anode slab. The model includes a finite element method (FEM) for the gas and solid phases (anode). The distribution of physical properties of solid phases,

such as porosity and specific surface area are ultimately tracked. In order to modify geometric changes in the anode slab, a moving boundary condition was applied during the process. Mass transfer phenomena and chemical reactions are considered during anode gasification with CO2. The results demonstrated that both are important and limitation term depends on operation condition, kind of materials and structural properties of carbon anode.

Recommendations

This study looked at the development of mathematics model of carbon anode gasification through various approaches and geometries including single particles, bed of particles, and simulation of anode slab. Further research can focus on the effects of catalytic material on the anodes that it will make a complicated model. The particle shapes of anodes can be assumed in different shapes. Experimental tests of anode slab to validation of simulation well be assist.

In addition, to be closer in the industrial condition, wettability, and joule effect respectively in the mass and heat balance equations will be helpfull.

Appendix A

Modeling of CO_2 gasification reaction of carbon anode slab

Abstract

The reactivity of carbon anodes with CO_2 is one of the main concerns in aluminum smelters that use the Hall-Héroult process. This reactivity is not desirable because it increases the net carbon consumption and thus shortens the lifetime of the anodes. Anode overconsumption is affected by anode intrinsic reactivity and mass transport phenomena. As a first step toward the simulation of the gasification process of the anode with CO_2, the use of an anode particle bed was first considered. A Mathematical model was developed for large-scale modeling of the anode slab. The model includes a finite element method (FEM) for the gas and solid phases (anode). The physical properties of the solid phase, such as porosity and specific surface area, and the thermochemical properties of particles like the reaction heat, were ultimately tracked. Geometric changes in the anode slab, heat and mass transfer, and chemical reactions were considered during anode gasification with CO_2. The dynamic concentration and temperature profiles of the anode were modeled.

Résumé

La réactivité des anodes de carbone avec le CO_2 est l'une des principales préoccupations des alumineries utilisant le procédé Hall-Héroult. Une telle réactivité n'est pas souhaitable car elle augmente la consommation nette de carbone et raccourcit ainsi la durée de vie des anodes. La surconsommation d'anode est affectée par la réactivité intrinsèque de l'anode et les phénomènes de transport de masse. Comme première étape vers la simulation du processus de gazéification de l'anode avec du CO_2, un lit de particules d'anode a d'abord été envisagé. Un modèle numérique a été développé pour une dalle à grande échelle qui représente l'anode en carbone. Le modèle est basé sur la méthode des éléments finis (FEM) pour les phases gazeuse et solide (anode). Les propriétés physiques de la phase solide, comme la porosité et la surface spécifique, ainsi que les propriétés thermochimiques des particules, telles que la chaleur de réaction, sont finalement suivies. Les changements géométriques dans la dalle anodique, le transfert de chaleur et de masse, et les réactions chimiques sont pris en compte lors de la gazéification anodique avec du CO_2. Les profils dynamiques de concentration et de température de l'anode ont été modélisés.

Keywords: Anode slab, CO_2 gasification; carbon anode particle; transport phenomena

Nomenclature

a_s	surface area of the anode per unit volume of the bed, ($m^2 \cdot m^{-3}$)
C_C	concentration of anode reactant, ($mol \cdot m^{-3}$)
C	concentration of gaseous species, ($mol \cdot m^{-3}$)
C(O)	surface of carbon-oxygen complex, ($mol \cdot m^{-2}$)
C_P	specific heat capacity, ($J \cdot kg^{-1} \cdot K^{-1}$)
D	diffusion coefficient, ($m^2 \cdot s^{-1}$)
E	apparent activation energy, ($J \cdot mol^{-1}$)
h	thermal conductivity, ($W \cdot m^{-1} \cdot K^{-1}$)
J	mass flux, ($mol \cdot s^{-1} \cdot m^{-2}$)
K	reaction rate constant, $(mol \cdot m^{-3})^{(1-n)} \cdot s^{-1}$
k	convective mass transfer coefficient, ($m \cdot s^{-1}$)
L_0	pore length, ($m \cdot kg^{-1}$)
n	partial reaction order, (-)
P	partial pressure, ($kg \cdot m^{-1} \cdot s^{-2}$)
R_g	gas constant, ($J \cdot mol^{-1} \cdot K^{-1}$)
r	Chemical reaction rate, ($kg \cdot m^{-3} \cdot s^{-1}$)
S	specific surface area, ($m^2 \cdot kg^{-1}$)
t	reaction time, (s)
T	temperature, (K)
q	heat flux, ($W \cdot m^{-2}$)
u	flow velocity, ($m \cdot s^{-1}$)
X	gasification conversion of anode particle, (-)
Greek symbols	
β	permeability, (m^2)
ΔH	enthalpy of reaction, ($kJ \cdot mol^{-1}$)

ε	void fraction, (-)
θ	solid volume fraction, (-)
κ	thermal conductivity, ($W \cdot m^{-1} \cdot K^{-1}$)
μ	viscosity, (Pa·s)
Φ	Wilke's coefficient, (-)
ρ	density, ($kg \cdot m^{-3}$)
σ	potential characteristic length, (m)
τ	tortuosity, (-)
ψ	structural parameter, (-)
Subscripts	
b	Bulk
C	Carbon
CO	carbon monoxide
CO_2	carbon dioxide
diss	Dissolved
e	Effective
f	active carbon site
g	gas phase
m	Molten
mix	mixed gases
s	solid phase
t	Instantaneous
0	Initial

Introduction

In this study, the gasification of carbon anode with CO_2 was modeled. In this process, anodes are partially submerged into the electrolyte solution, which is made up of molten cryolite. Molten aluminum is produced by reducing dissolved alumina in the cryolite, and the anode is oxidized electrochemically, generating CO_2 [1]. The stoichiometry of this overall

electrolysis reaction is shown as Equation (a.1). The CO_2 generated on the anode surface flows directly to the electrolysis cell headspace. However, part of the generated CO_2 diffuses into the porous structure of the carbon anode due to the electrolyte hydrostatic head and the concentration gradient (according to reports by Sadler & Zeigler).

Consequently, it reacts with the solid carbon through the Boudouard reaction [2]. The Boudouard reaction is not desirable because it increases net carbon consumption and may contribute to the generation of carbon dust in the pots, which is an operational problem [3, 4]. The carbon dust is principally generated by the selective reaction of the anode components in contact with air or CO_2. For instance, it has been suggested that the binder matrix within the anode preferentially burns, causing detachment of the carbon particles from the anode surface, which then fall into the electrolyte bath [5].

$$2Al_2O_{3(diss)} + 3C_{(s)} \rightarrow 4Al_{(m)} + 3CO_{2(g)} \qquad (a.1)$$

The combustion reactions occur either at the anode surface or within the anode bulk. For a given anode formulation, the reaction rate is a function of temperature, pore structure, permeability, and intrinsic reactivity of the anode constituents [5-7]. The minimum theoretical carbon consumption for aluminum electrolysis is 0.334 kg/ kg of Al produced. However, since the cell efficiency is usually less than 100%, the real electrolytic consumption of carbon is around 0.41 kg per kg of Al produced.

Gasification of the anode by air and CO_2 greatly contributes to this carbon overconsumption. Several researchers/works/reports [8-12] have discussed the influence of anode properties on its reactivity with air and CO_2 and the net carbon consumption. The present work will mainly focus on the quantification of the structural changes of anode slab during CO_2 gasification and its effect on the gasification reactions.

The electrolysis cell (*pot*) is composed of prebaked carbon anodes, molten cryolite, and a liquid layer of aluminum lying on cathode carbon blocks. The carbon anode is consumed during the process, and it should be replaced by a new one approximately every 25 days. The anodes in the electrolysis cell are in contact with CO_2 at high temperatures (typically 960 °C). At temperatures higher than 800 °C, the apparent rate of carbon-CO_2 gasification reaction becomes more significant due to the combined chemical reaction and the mass transfer effects. It is worth mentioning that diffusion is the main part of the mass transfer [13, 14] and its effect on the gasification rate becomes more significant for particles larger than 0.1 mm [14, 15].

The mass of generated carbon monoxide is 7.1% of that of CO_2. In addition to the electrolytic reactions, the anode can also react with air and produce CO_2 (Figure a.1). On the top and bottom of the anode, CO_2 and O_2 concentration gradients cause mass transfer by diffusion. The hydraulic pressure gradient at the bottom of the anode causes mass transfer by convection of CO_2. These reactions are not desirable because they result in an increase in net carbon consumption.

Air reactivity is based on the oxidation of carbon by the oxygen within the air:

$$C_{(s)} + O_{2(g)} \rightarrow CO_{2(g)} \quad \text{(a.2)}$$

and

$$2C_{(s)} + O_{2(g)} \rightarrow 2CO_{(g)} \quad \text{(a.3)}$$

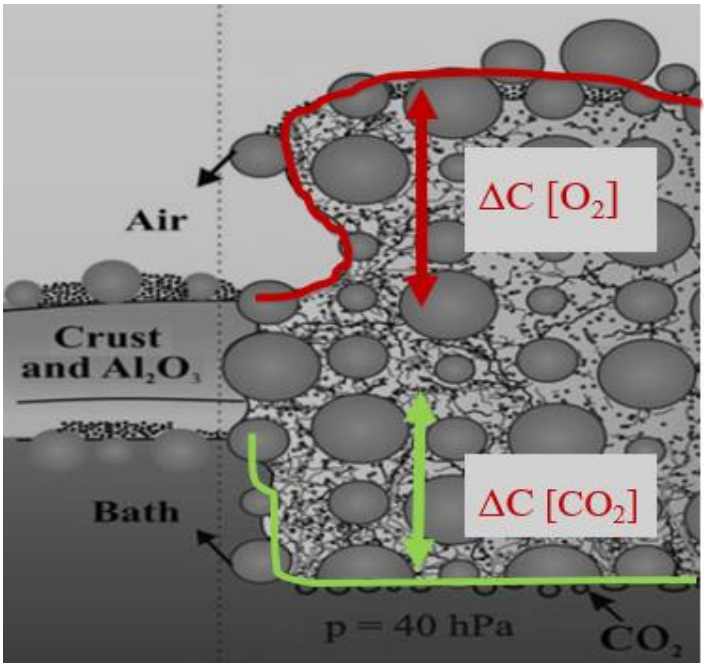

Figure a.1 Definition of gas reactivity in the anode slab [2]

CO_2 molecules generated by the electrochemical reaction at the anode's bottom react with the anode's surface. Besides, diffusion of CO_2 may occur through the porous structure and consume the anode's interior [5-7].

$$C_{(s)} + CO_{2(g)} \leftrightarrows 2CO_{(g)} \quad \text{(a.4)}$$

This reaction is beneficial over 930 °C [1, 9]. CO_2 diffuses through the anode and then reacts at the chemically active surface, thereby generating CO. Thus, both the chemical reaction and the mass transport are significant in the anode's mass loss.

The overall gasification rate of an anode is determined by combining the intrinsic chemical reaction rate with mass transport limitation. Rafsanjani et al. [16] assume that the gasification reaction of char particles is the first order of gas reaction. When presenting their model, they introduce a term to consider the variation in the activation energy as the reaction proceeds. Simple modeling approaches are mostly applicable to isothermal conditions and usually limited for the following reasons: (i) they are only applicable to first-order kinetics on gas or solid reactants, and (ii) they do not explicitly make allowance for structural changes with reaction. Qixiang Xu et al. [17] apply a mathematical method for solving gas-solid non-

catalytic reactions to predict char activation processes. The model also includes mass transfer through convection and diffusion within the char particle. They solve a set of non-linear differential equations to predict gas production rate, gas composition, and carbon consumption rate during gasification. To this end, they use the Quantize Method (QM). Jamshidi and Ale-Ebrahim [10, 18-20] have developed a semi-analytical, semi-numerical method and employed new tactics for solving coupled partial differential equations, where considerably reduces the mathematical difficulties commonly present in gas-solid problems. These authors illustrate the QM potential by applying it to several gas-solid reaction models--including the grain model--half-order model, and modified grain model. More recently, Gómez-Barea [21] has applied this method and has suggested a new mathematical solution for predicting char activation reactions. He has proposed a simplified model for gas-solid reactions in the fluidized bed (FB). The model has been formulated under a local volumetric approach, using non-linear chemical kinetics. They have reported a change in the porous structure during gasification.

Although some research has been done on particle gasification, few works have been carried out on slab anode modeling; most studies have focused on practical ways to improve properties and efficiency of anodes. Ziegler [22] has used a transport-reaction model to describe the dusting phenomena in the anode slab. His model calculates porosity as a function of the slab height while observing the simultaneous flow of carbon dioxide under the influence of a pressure gradient and its diffusion under a concentration gradient. Although the results accurately describe the reaction localization on the submerged sides of the anode, permeability is not considered.

In this work, we have expounded on a mathematic model based on an experiment addressing the gasification of the anode slab from the starting time to when only one-third of the anode remains. This whole process took 21 days. The anode that disappeared has been calculated in the model by adding the burning rate of the anode and the moving boundary condition in the model.

Mathematical model

A homogeneous model for the fluid phase and the solid phase was applied to model an anode slab. According to this model, all of the anode slab is considered as one porous control volume, so that we can imagine a uniform porosity (ε), contained in a long column of length L along which the gas flows at a superficial velocity u and an initial concentration equal to C_0. Figure a.2 shows a schematic representation of an anode slab under CO_2 and O_2 reactivity at the bottom and top, respectively [2]. The anode gasification reactions are sensitive to mass-transfer effects. The gasification rate diagram is illustrated in Figure a.2 It may take place through physical as well as chemical processes in the following steps: 1. mass transfer (by diffusion) of gaseous reactant(s) from the bulk gas phase to the carbon surface; 2. adsorption of reactant(s) on the carbon surface; 3, 4, and 5. chemical rearrangements (reactions) on the surface, mobility, and formation of adsorbed product(s); 6. desorption of product(s); and 7. mass transport (by diffusion) of the gaseous reaction product(s).

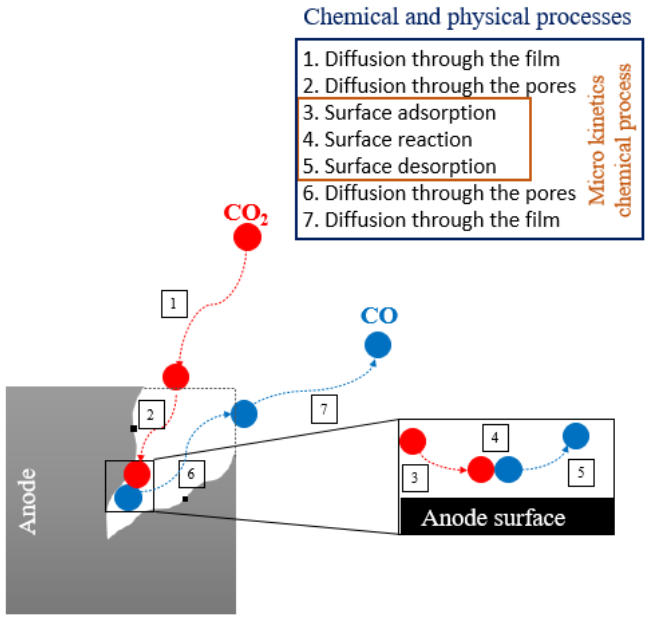

Figure a.2 Chemical and physical processes of each particle in an anode slab

With a very long history of the Hall-Héroult process (over 125 years), the orientation of specialists and experts in aluminum production makes it possible to rely on this hypothesis that the overall reactivity of carbonaceous materials is controlled by their microstructures and by physicochemical phenomena, including the diffusion and convection of gases in solids. Industrial parameters such as joule effect interferences in the determination of anode reactivity were avoided by Sadler and Zeigler [22, 23]. Therefore, as the current work relay on Sadler's study, the Jule effect has been avoided. The mathematical model described in the present work is founded on the following assumptions:

- The mass transfer occurs through convection and diffusion within the anode.
- A non-isothermal condition in the anode is established through solving heat balance PDE with the initial and boundary conditions.
- The gas exiting the anode would be in equilibrium with the carbon.
- Chemical reactions (Boudourad reaction) occur in the solid phase as non-catalytic reactions.
- The Langmuir-Hinshelwood (L-H) mechanism and the random pore model (RPM) equation are used to define the chemical reaction term.

Mass transfer equations

Equation (a.5) provides a conceptual mass balance used for each component in the anode slab.

Input-output + generation – consumption = accumulation (a.5)

It is possible to incorporate a non-linear chemical reaction rate, expressed by *R*, and the changes in porous structure during conversion by an appropriate equation into the mass balance. Mass balance also allows for changes in the effective diffusivity with reaction through the input of conversion (*X*). For a given time *t* and the particle position, it can predict the concentration profiles within the particle and the slab. Equations (a.6) and (a.7) describe the mass balance of CO and CO_2 in the slab.

$$\frac{\partial C_{CO2}\varepsilon}{\partial t} + \nabla.(C_{CO2}u) = \nabla.(D_{CO2}.\nabla C_{CO2}) - R_{CO2} \quad \text{(a.6)}$$

$$\frac{\partial C_{CO}\varepsilon}{\partial t} + \nabla.(C_{CO}u) = \nabla.(D_{CO}.\nabla C_{CO}) + 2R_{CO2} \quad \text{(a.7)}$$

where C_{CO_2} and C_{CO} are the concentrations of reactant and product gases of the anode, respectively. The first left-hand term shows the accumulation rate, while the second term describes the convective mass flux related to the velocity of fluid gases. The first right-hand term represents the diffusion of fluid gas onto the anode slab obtained by Fick's law [24]. Finally, the last term represents the chemical reaction of CO_2 within the carbon anode.

Sadler and Algie [23] have proposed that mass transport of carbon dioxide occurs by viscous flow and is related to anode permeability. The driving force comes from a hydrostatic pressure of around 200 mm water. The electrolytic face of the anode will apply.

Heat Transfer Between the Phases

To model heat transfer in a porous matrix that possibly consists of several solids and is filled with a mobile fluid, equation (a.8) is used.

$$(\rho C_P)_{eff}\frac{\partial T}{\partial t} + \rho_f C_{P,f} u.\nabla T + \nabla.\left(-h_{eff}\nabla T\right) + \theta_s \sum_i \Delta H_{r,i} R_i \quad \text{(a.8)}$$

$$\left(\rho C_P\right)_{eff} = \theta_s \rho_s C_{P,s} + \left(1-\theta_s\right)\rho_f C_{P,f} \quad \text{(a.9)}$$

$$h_{eff} = \theta_s h_s + \left(1-\theta_s\right)h_f \quad \text{(a.10)}$$

In the above equations, θ_s stands for the solid volume fraction of the matrix. Here, ρ_f (kg/m^3) is the density of the mobile fluid; $C_{P,f}$ (J/(kg·K)) is the heat capacity at a constant pressure of the mobile fluid, $(\rho C_P)_{eff}$ (J/(m^3·K)) is the effective volumetric heat capacity at constant pressure, defined by an average volume model to take into account both the solid matrix and fluid properties; and u (m/s) stands for the velocity field of the mobile fluid, either an analytic expression or the velocity field from a fluid flow. It is noteworthy that u should be interpreted as the Darcy velocity, that is, the volume flow rate per unit cross-sectional area. The average linear velocity (the velocity within the pores) can be calculated as $u_L=u/\varepsilon_p$, where ε_p is the porosity and equal to 1-θ_s; h_{eff} (W/(m·K)) is the effective thermal conductivity, defined by a volume average model (equation a.9) to take into account both solid matrix and fluid properties; and $\Delta H_{r,i}$ is the enthalpy of the reaction I which is calculated using equation (a.11).

$$\Delta H_{r,i} = \sum_j \upsilon_{j,i} H_j(T) \tag{a.11}$$

Here, $\upsilon_{j,i}$ is the stoichiometric coefficient of the component j in the reaction i, positive for products and negative for reactants. $H_i(T)$ is the enthalpy of component j and is calculated as:

$$H_j(T) = \Delta H_j^f(298.15) + \int_{298.15}^{T} C_{P,j}(T)\,dT \tag{a.12}$$

where $\Delta H_j^f(298.15)$ and $C_{P,j}(T)$ stands for the enthalpy of formation of component j at 298.15 K and heat capacity of component j. $H_j(T)$ can also be calculated from NASA relations.

Movement equations

The momentum balance that governs the fluid flow is built upon the momentum equation and continuity equations. The conservation of mass is the generic equation used, and the following continuity equation is formulated for a porous medium with a term that effectively represents the chemical reaction on the flow [24]:

$$\frac{\partial(\varepsilon_b \rho_f)}{\partial t} + \nabla.(\rho u) = W \tag{a.13}$$

$$u = -\frac{k}{\mu L}\nabla P \tag{a.14}$$

where W (kg/m^3.s) is the mass source or sink, which accounts for mass deposit and/or mass creation in porous domains; and ρ_f is the fluid density. When gas flow enters the reactor, gas climbs through the particle bed. The flow leads to a pressure drop in the reactor. This effect is integrated into the motion equation, leading to the formulation of the Ergun equation, which can be written as follows [24]:

$$\frac{\nabla P}{L} = \frac{150\mu_{mix}u(1-\varepsilon_b)^2}{d_p^2\varepsilon_b^3} + 1.75\frac{\rho_f u^2(1-\varepsilon_b)}{d_p\varepsilon_b^3} \quad \text{(a.15)}$$

where ε_b is the bed porosity, μ_{mix} (Pa·s) denotes the viscosity of the mixed-gas, ρ_f *is* the gas density (kg·m^{-3}), L is the anode length coordinate (m), u is the gas flow velocity (m·s^{-1}), and k is the sphericity of the particles. The Ergun equation combines both the laminar and turbulent components of the pressure loss across a packed bed. In laminar flow, the first term is predominant. Under turbulent flow, the second term is dominant. The pressure drop is related to the square of the superficial velocity and linearly depends on the density of the fluid passing through the anode. Darcy's law is derived because the viscous resisting force in the Navier-Stokes equation is linear with the velocity (equation a.14).

Reaction rate

The random pore model developed by Bhatia et al. [25] was applied to intra-particle gasification reactivity of carbon with carbon dioxide in the present study. The reaction is mechanistically considered as an adsorption-desorption two-step reaction, with the product gas, CO, having an inhibiting effect on the reaction--something that is not present in the n-th order equation. In the L-H formulation, the adsorption coefficients of CO and CO_2 are assumed to be constant (k_1, k_2, andk_3), and the following pathway is proposed for this process:

$$C_f + CO_2 \xrightarrow{k_1} C(O) + CO \quad \text{(a.16)}$$

$$C(O) + CO \xrightarrow{k_2} C_f + CO_2 \quad \text{(a.17)}$$

$$C(O) \xrightarrow{k_3} CO + C_f \quad \text{(a.18)}$$

where C_f is the active carbon site; k_1 , k_2, and k_3 are the reaction rate constants; and $C(O)$ represents the carbon-oxygen surface. The presence of CO results in the lowering of the steady-state concentration of $C(O)$ by an inhibiting effect. $r(C_g)$ as described by Equation (a.19):

$$r_{c_g} = \frac{k_1 P_{co_2}}{1 + k_2 P_{co_2} + k_3 P_{co}} \quad \text{(a.19)}$$

where P_{CO2} and P_{CO} are the partial pressure of CO_2 and CO. When the CO concentration is small and/or the inhibiting effect exerted by this species is not considered, a simple global model can be applied.

The intrinsic rates of the gasification reaction are a function of three variables: temperature, the concentration of the bulk gas, and the activated reaction surface of the solid. In general, kinetic models for intrinsic rates of heterogeneous reactions can be expressed as the product of three contributing parameters.

$$R_i = k(T) f(C) S(X) \quad \text{(a.20)}$$

$$S(X) = S_0(1-X)\sqrt{1-\psi \ln(1-X)} \quad \text{(a.21)}$$

where S_0 is the specific surface area and ψ is the dimensionless parameter indicating the nature of pore structure:

$$\psi = \frac{4\pi L_0(1-\varepsilon_0)}{S_0^2} \quad \text{(a.22)}$$

In this equation, L_0, S_0, and ε_0 are the initial pore length, pore surface, and solid particle porosity.

The *k* function can be calculated by the Arrhenius equation as [17]:

$$k(T) = k_o e^{\frac{-Eg}{RT}} \quad \text{(a.23)}$$

Here, E is the apparent activation energy, R_g is the gas constant (J/mol.K), and T is the reaction temperature (K).

In the present study, the L-H rate equation is considered for $f(C)$. This mechanism is proposed based on the adsorption and desorption of CO and CO_2 to yield expressions for calculating the reaction rates of anode gasification. The RPM [17] is applied to the structural part of the chemical reaction equation. Therefore, the chemical-reaction term is as follows:

$$\frac{dx}{dt} = k_i.S = \frac{k_1 P_{CO2}}{1 + k_2 P_{CO2} + k_3 P_{CO}} . \frac{S_0(1-x)\sqrt{1-\psi_0 \ln(1-x)}}{1-\varepsilon_0} \quad \text{(a.24)}$$

This set of Equations defines a boundary value problem involving a pair of partial differential equations coupled through CO and CO_2 components such as the following L-H reaction mechanism Equations. The values of the parameters, namely, k_1, k_2, and k_3, are determined by regression of the total experimental carbon conversion to the calculated carbon conversion using the minimization of the relevant objective function. The details of the optimization procedure are provided by *Kavand* et al. [26]

Gas properties:

The following equation obtains thermal conductivity, molecular diffusion, viscosity, and heat capacity in the model [17].

$$h_i = 2.699\times10^{-6} \frac{\sqrt{T\left(M_i \times 10^3\right)}}{\sigma_i^2} \times \frac{1.15C_{P_i} + 0.88R_g}{M_i} \quad \text{(a.25)}$$

where Ω_D is the dimensionless collision integral, σ is the potential characteristic length value, T is the temperature (K), and M_i is the molecular weight of component I, and C_P denotes the heat capacity.

The binary diffusion coefficient of component (D_{ij}) for species i in reaction j is estimated by correlation of Hirschfelder as [27]

$$D_{i,j} = 2.628\times10^{-22}\frac{\sqrt{T^3(M_i+M_j)/(2\times10^3 M_i M_j)}}{P\Omega_D\sigma_i\sigma_j} \tag{a.26}$$

Here, D_{ij} (m^2/s) is the binary diffusion coefficient, M (kg/mol) equals the molecular weight, T (K) represents the temperature, P (Pa) is the pressure, and σ (m) equals the characteristic length of the Lennard-Jones/Stockmayer potential.

The viscosity of the gas mixture can be evaluated by Wilke's correlation as follows [17].

$$\mu = \sum_{i=1}^{n}\frac{y_i\mu_i}{\sum y_i\Phi_{ij}} \tag{a.27}$$

$$\Phi_{ij} = \frac{1}{\sqrt{8}}(1+\frac{M_i}{M_j})^{-1/2}\left[1+(\frac{\mu_i}{\mu_j})^{1/2}(\frac{M_i}{M_j})^{1/4}\right]^2 \tag{a.28}$$

In order to calculate heat capacity and enthalpy of the components in the reaction, NASA correlation is applied [28] as:

$$C_P = R_g(a_1+a_2T+a_3T^2+a_4T^3+a_5T^4) \tag{a.29}$$

$$H = R_g(a_1T+\frac{a_2}{2}T^2+\frac{a_3}{3}T^3+\frac{a_4}{4}T^4+\frac{a_5}{5}T^5+a_6) \tag{a.30}$$

The apparent and real densities of the anode are set to 1600 and 2100 $kg\cdot m^{-3}$, respectively, which gives a void fraction equal to 0.238 at the initial condition. As the carbon is consumed, the porosity of the bed increases. The porosity of the bed in the y-direction is calculated as[22]:

$$\frac{d\varepsilon}{dy} = \frac{\varepsilon M_{wc}}{1000\rho_{real}\upsilon_{burn}}R \tag{a.31}$$

$$\upsilon_{burn} = j\frac{M_{WC}}{4F1000\rho_{app}} \tag{a.32}$$

where R is the reaction rate based on the CO_2, j (A/m^2) is the current density, F (C/eq) represents Faraday constant, M_{WC} is the molecular weight of the carbon anode, and υ_{burn} is anode's consumption velocity. The current density, used for the anode consumption at the bottom, is set to 9000 $A\cdot m^{-2}$. Together with these parameters, equation (a.32) give a

burn rate or descent velocity of the anode of 1.75×10^{-7} $m\cdot s^{-1}$. Equation (a.31) couples the transport phenomena with the porosity of the anode bed. In this way, the porosity of the anode slab appears in both models.

Geometry and Boundary Conditions

The geometry of the anode slab is shown in Figure a.3. Domain width is 0.3 m, which corresponds to a 0.6 m anode width with symmetry in the middle. A circular arc of 0.04 m radius surrounds the immersed corner of the anode. A bath of density 2100 kg/m^3 is immersed at the bottom of the anode for 0.12 m [22].

By setting atmospheric pressure at 10^5 Pa, the CO_2 pressure at the bottom of the anode equals 102470. Pa. We assume that the gas is 100% CO_2, and we calculate the gas concentration using the ideal gas law. The CO2 concentration of zero is set at the top of the 0.60 m thick anode, and CO concentration equals 1-atmosphere total pressure. An electrolytic process at the anode generates a hydrostatic pressure of around 200 mm water gauge, driving this flow. Above the anode working face, the hydrostatic head is most likely to dominate internal mass transport.

A fixed temperature equal to 1233.15 K was applied to the immersed part of the slab, and also heat flux ($q=h\times(T_w-T)$) was applied as B.C. of the un-immersed part of the slab. Also, owing to high temperature, surface to surface radiation was applied.

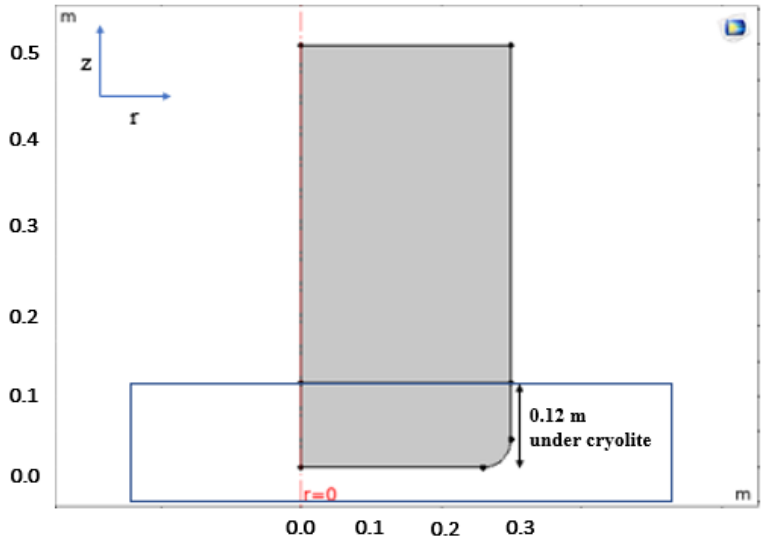

Figure a.3. Geometry of anode slab immersed under cryolite solution

Mesh creation

Depending on the detail of mesh refinement required, the simulation geometry can be meshed at three different levels, edges, surfaces, and volumes. When a global uniform mesh suffices, the meshing can take place on the volume level. At this point, one uniform control volume size is determined, and the entire simulation geometry is meshed with this standard control volume size, creating a uniform mesh density. When local refinement is required, e.g., in sensitive regions of the geometry, different mesh densities can be defined to surfaces or edges specifically. For example, to get a converging flow solution, the mesh needs to be finer near contact point areas, between particles in the geometry, or between particles and the externally bounding column wall, than in larger void areas in the geometry. To be able to adjust the mesh locally, mesh densities must be defined on edges along with these contact points. A sensitivity study of the model compared to the size of the mesh was carried out to find out the optimal size to choose. Accordingly, five levels of meshes, namely extremely coarse, extra coarse, coarser, coarse, and normal, were used. At the normal level, 378 triangles, 62 edge elements, and 7 vertex elements were used. The average mesh quality is equal to 0.87. As the mesh quality at this level is suitable, the normal mesh level was used to study the model. Figure a.4 displays the used mesh and its quality. In addition, the fine and finer mesh was used to investigate the smaller mesh. The results showed that except for the computation time, which increases, the results would not change.

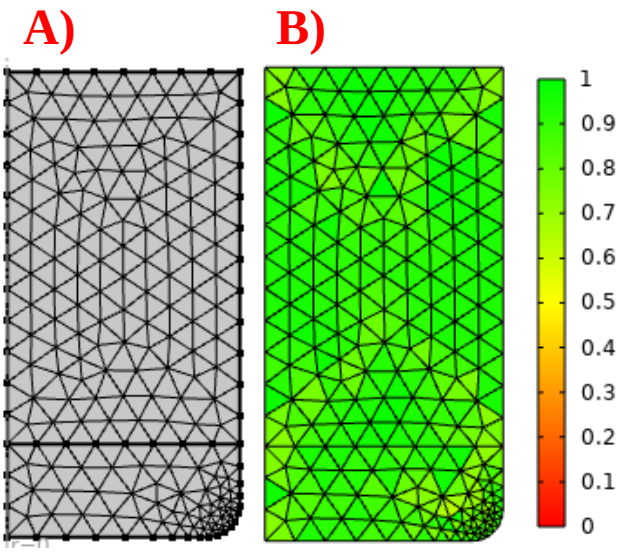

Figure a.4. A) The used mesh in the simulation, B) the quality of the used mesh.

As the anode slab is consumed, the geometry is deformed in the y-direction. Therefore, automatic remeshing was activated in the COMSOL software to update the mesh of the geometry. It should be noted that the anode is a three-dimension, and owing to its axial symmetry; the anode was simulated using 2D axisymmetric in the COMSOL software.

Numerical Solution

In this model, gas species concentration (C), the temperature of the anode slab, the velocity, the gas pressure, porosity of the anode slab, and anode conversion rate (X) are the variables to be calculated. Because of a series of non-linear partial differential equations (PDEs), the COMSOL software uses an appropriate numerical technique to obtain the mentioned variables. A commercial FEM (finite-element method) software, COMSOL Multiphysics, is used to simulate the problem. The software appears with various modules in its library for special purposes. The Chemical Engineering Module contains tools for modeling fluid, heat, and mass transfer, as well as for chemical reactions. These tools can be used for both steady-state and transient analysis[29].

Results and Discussion

A constant damped version of Newton's method (damped factor = 1) was used to solve the fully coupled phenomena. Backward differentiation formula (BDF) with an order of accuracy varying from one (backward Euler) to two was used as time stepping. BDF methods have been used for a long time and are known for their stability. The simulation was run for 26.5 days.

Pressure drops

One of the critical parameters on CO_2 gasification of the anode is the pressure drop across the carbon anode related to the operational conditions and the flow distribution. It can lead to the formation of convection terms and more consumption of anode. The fluid moves from the high-pressure zone to the low-pressure zone, resulting in convection that results in the movement of carbon dioxide from the bottom to the top of the anode. The presence of carbon dioxide causes the carbon grains to consume. Pressure profiles in line with the anode slab are provided, using the numerical model presented in Figure a.5. The results reveal that the pressure is higher at the working face of the anode. The pressure drop causes an increase in carbon consumption because it causes more carbon dioxide transfer and consequently more reaction. Figure a.5 a depicts the pressure contours on the first day of the process, and Figure a.5 b shows the pressure contours of the part of the anode remaining after 18 days.

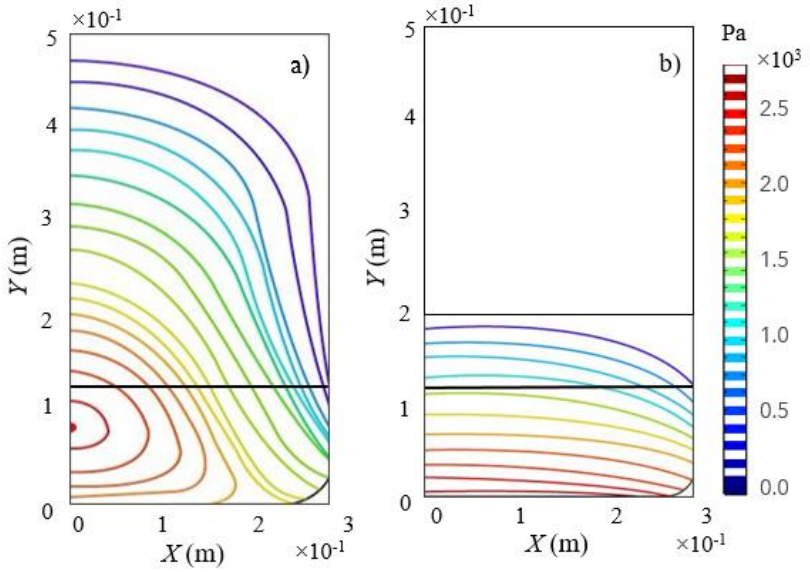

Figure a.5. Contour of pressure after a) 1 day (a), and 18 days (b) of the gasification process

Porosity distribution

Figure a.6 a and 6b show that the porosity is higher at the vertex of the anode than on the working face. This evidence depicts that this mechanism causes an increase in the carbon dust, particularly on the vertexes of the anode; Under the same operation conditions, the porosity of the vertex of anode remaining in the cryolite solution increased over 18 days from 0.23 to 0.27.

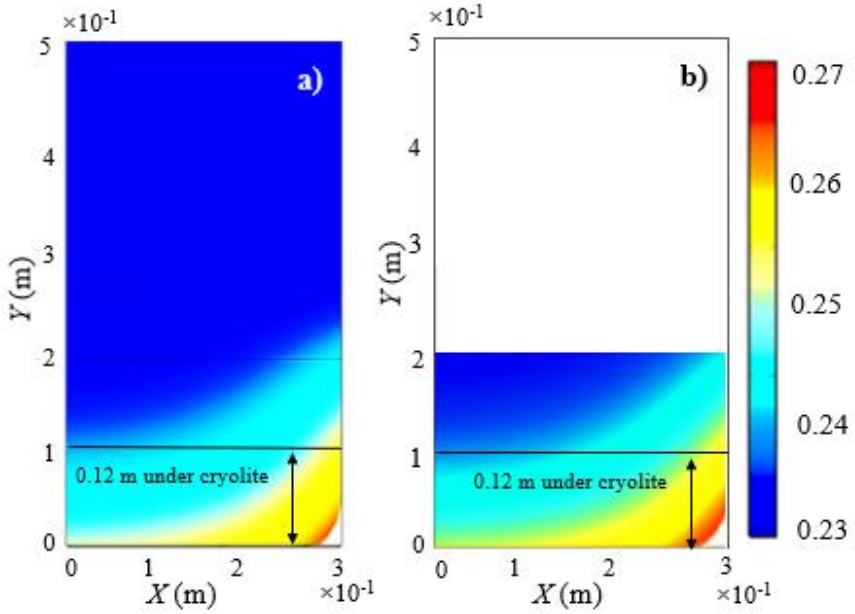

Figure a.6. Distribution of Porosity after a) 1 day (a) 18 days (b) of the gasification process

Temperature profiles

Figure a.7a,b exhibits the temperature distributions at various anode positions after 1 day and 18 days of the gasification process, respectively. The maximum temperature took place at the bottom and the side, which are in direct contact with 960 °C electrolyte. The figure shows that in the same y position, the temperature would not remain constant but was affected by structural changes such as porosity and permeability, which in turn lead to changes in mass transport and in the intensity of chemical reaction intensity.

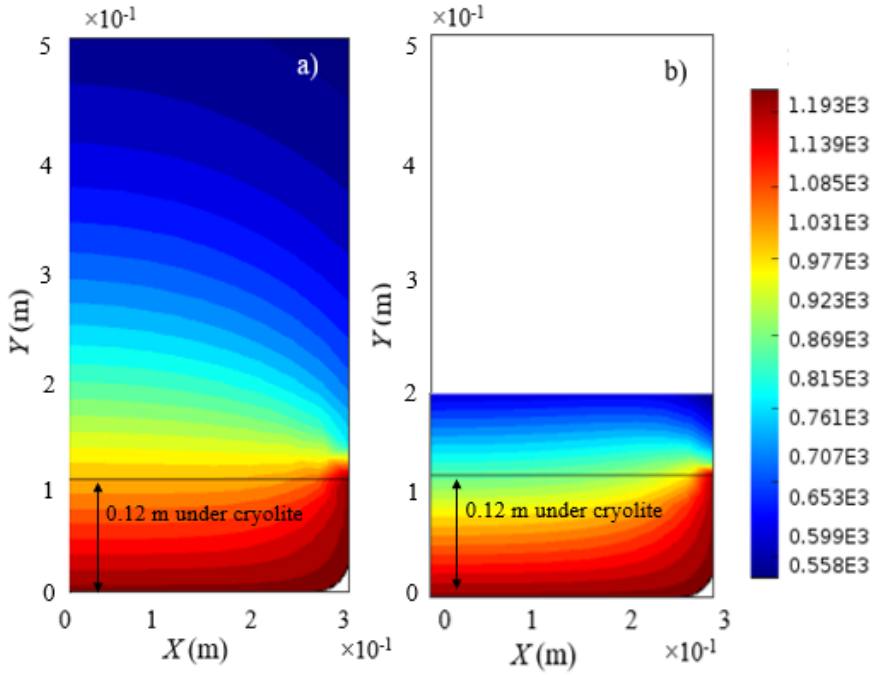

Figure a.7. Temperature profiles of anode slab after 1 day (a) and 18 days (b) of gasification

Chemical reaction rate

The distribution of chemical reaction rates at various positions is depicted in Figure a,8. The rate is higher on the vertex of the anode than on its working face. This finding, like in the case of porosity, supports the hypothesis about the formation of carbon dust on the vertex of the anode. Besides, as the process advanced, the porosity of the carbon anode increased, which led to an increase in the specific surface area and the chemical reaction rate. For instance, in the middle of the working face, the chemical reaction rate approached 8×10^{-3} after 18 days, which, compared to the chemical reaction rata at the same place after 1 day, is more than two times as much.

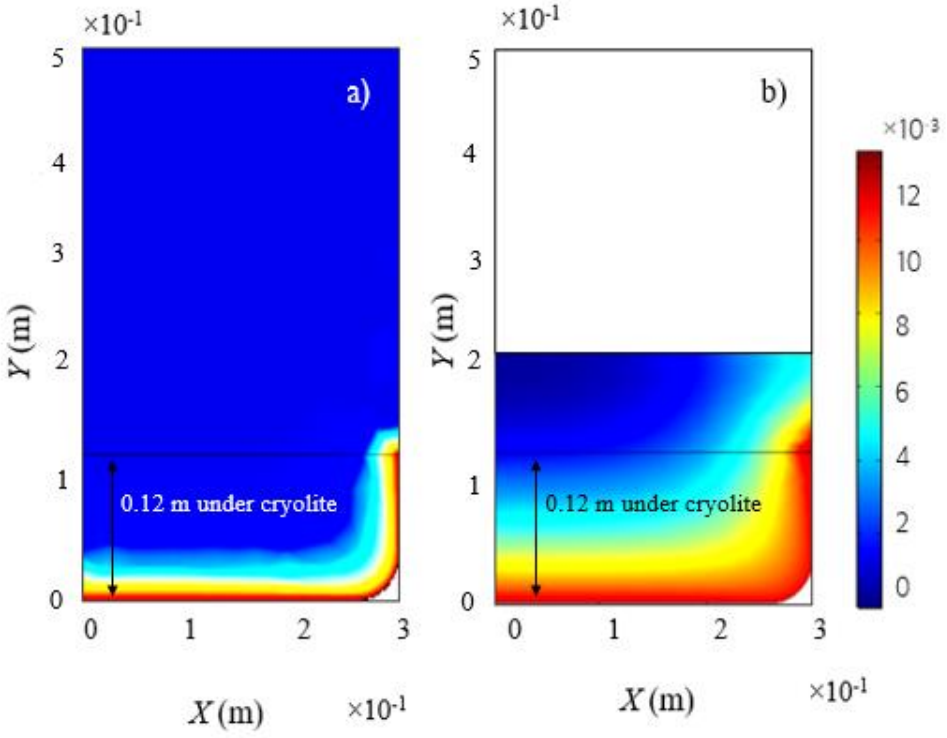

Figure a.8. Distribution of Chemical reaction rate after 1 day (a) and 18 days (b) of gasification

Mass transfer study

To find out how the presence or absence of mass transfer limitations would affect the relationship between CO2 concentration and gas velocity, Figure a.9 is plotted to show CO_2 concentration at the center of the anode slab. The figure shows the mass transfer limitations in the outlet gas according to the model results. As can be seen, there is a notable difference between C_{CO_2} conversion with and without mass transfer limitations. With mass transfer limitations, the velocity's dependence on the generated concentration of C_{CO_2} remains weak. As velocity increases, mass transfer limitations become less significant. The reaction will cause a convective flow out of the reaction zone. In this way, the reaction is sustained by fresh CO_2, which must diffuse upwind, that is, against the convective flow outward. The convective flow itself is relatively insensitive to the permeability; if the permeability decreases, the pressure gradient can increase to provide the same flow rate, which is ultimately determined by the diffusion rate. There are secondary effects due to changes in permeability, which account for minor differences in calculations. As the velocity increases, the two plots eventually approach each other, with the outlet concentration becoming less dependent on the mass transfer limitations.

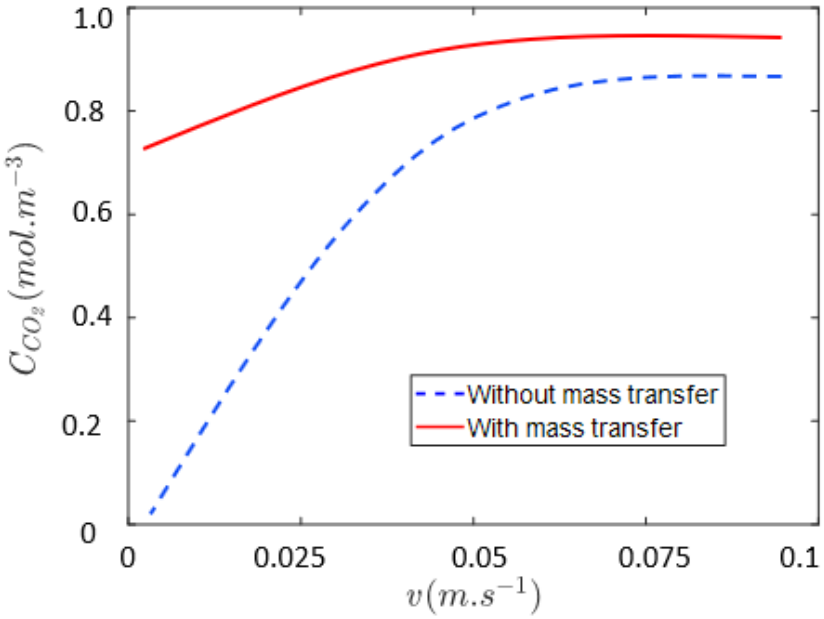

Figure a.9. Mass transfer limitations in the center of anode working face

Conclusion

In this chapter, a simulation of the anode slab was carried out as a large geometry using the homogenous model. The results accurately describe the reaction localization on the submerged sides of the anode. The model takes account of the mass and heat transfer equations for the gas components and the solid carbon anode. It results in a set of non-linear partial differential equations, which can be solved using a finite element method. The model has the capability to predict the gas generation rate, the gas compositions, the carbon consumption rate, the pressure drop, and temperature distribution during the gasification process. Besides, the values for structural parameters including porosity, permeability, and surface area were obtained. Results confirm an unsteady state process with an increasing trend in the values for structural parameters. Diffusion and convection are important terms during gasification. The controlling term depends on a variety of parameters, including pressure gradient, the porosity of carbon material, and the velocity of reactant gas.

References

1. Azari, K., *Investigation of the materials and paste relationships to improve forming process and anode quality*. 2013, Laval Uinversity: Canada.

2. Chevarin, F., *Relation entre les propriétés physico-chimiques de l'anode en carbone et sa vitesse de réaction sous CO_2*, in *in Metallurgy and Materials Department*. 2015, Laval University:: Quebec, CANADA.
3. Azari, K., *Investigation of the materials and paste relationships to improve forming process and anode quality*, in *Material and Metallogy Department* 2013, Ph.D. dissertation, Laval Uinversity: Canada.
4. Chevarin, F., et al., *Active pore sizes during the CO_2 gasification of carbon anode at 960°C.* Fuel, 2016. **178**: p. 93-102.
5. Tabatabaee Ghomshe, S.M., R. Aminzadeh, and M. Abarzani, *Use of response surface methodology to study the combined effect of various parameters on hexavalent chromium adsorption.* Chemical Engineering Communications, 2014. **201**(2): p. 191-208.
6. Azari, K., et al., *Compaction properties of carbon materials used for prebaked anodes in aluminum production plants.* Powder Technology, 2013. **246**(C): p. 650-657.
7. Azari, K., et al., *Influence of coke particle characteristics on the compaction properties of carbon paste material.* Powder Technology, 2014. **257**: p. 132-140.
8. G.S., L., et al., *Modeling of Infra-Particle C-CO_2 Reaction: An Application of the Random Pore Model.* Developments in Chemical Engineering and Mineral Processing, 1999. **7**(5-6): p. 525-536.
9. Gómez-Barea, A., P. Ollero, and C. Fernández-Baco, *Diffusional Effects in CO2 Gasification Experiments with Single Biomass Char Particles. 1. Experimental Investigation.* Energy & Fuels, 2006. **20**(5): p. 2202-2210.
10. Jamshidi, E. and H. Ale Ebrahim, *An incremental analytical solution for gas-solid reactions, application to the grain model.* Chemical Engineering Science, 1996. **51**(18): p. 4253-4257.
11. Kajitani, S., et al., *CO_2 gasification rate analysis of coal char in entrained flow coal gasifier.* Fuel, 2006. **85**(2): p. 163-169.
12. Mandapati, R.N., et al., *Experiments and Kinetic Modeling for CO2 Gasification of Indian Coal Chars in the Context of Underground Coal Gasification.* Industrial & Engineering Chemistry Research, 2012. **51**(46): p. 15041-15052.
13. Mani, T., N. Mahinpey, and P. Murugan, *Reaction kinetics and mass transfer studies of biomass char gasification with CO_2.* Chemical Engineering Science, 2011. **66**(1): p. 36-41.
14. Chevarin, F., et al., *Characterization of carbon anode constituents under CO_2 gasification: A try to understand the dusting phenomenon.* Fuel, 2015. **156**: p. 198-210.
15. Kovacik, G., A. Chambers, and B. Özüm, *CO_2 gasification kinetics of two Alberta coal chars.* The Canadian Journal of chemical engineering, 1991. **69**(3): p. 811-815.
16. Rafsanjani, H.H. and E. Jamshidi, *Kinetic study and mathematical modeling of coal char activation.* Chemical Engineering Journal, 2008. **140**(1-3): p. 1-5.
17. Xu, Q., S. Pang, and T. Levi, *Reaction kinetics and producer gas compositions of steam gasification of coal and biomass blend chars, part 2: Mathematical modelling and model validation.* Chemical Engineering Science, 2011. **66**(10): p. 2232-2240.
18. Jamshidi, E. and H. Ale Ebrahim, *A new solution technique of moving boundary problems for gas-solid reactions; application to half-order volume reaction model.* The Chemical Engineering Journal and the Biochemical Engineering Journal, 1996. **63**(2): p. 79-83.
19. Jamshidi, E. and H.A. Ebrahim, *A quantized solution for the nucleation model in gas-solid reactions.* Chemical Engineering Journal, 1997. **68**(1): p. 1-6.
20. Jamshidi, E. and H. Ale Ebrahim, *A new solution technique for gas–solid reactions with structural changes.* Chemical Engineering Science, 1999. **54**(7): p. 859-864.
21. Gómez-Barea, A. and P. Ollero, *An approximate method for solving gas–solid non-catalytic reactions.* Chemical Engineering Science, 2006. **61**(11): p. 3725-3735.

22. Ziegler, D.P., *Sub-surface carbon dioxide reaction in anodes,* in *Light Metals 2011*. 2011, Springer. p. 901-906.
23. Sadler, B.A. and S.H. Algie, *Porosimetric study of sub-surface carboxy oxidation in anodes*, in *TMS*. 1991, Minerals, Metals & Materials Soc New Orleans, LA, USA.
24. Bird, R.B., W.E. Stewart, and E.N. Lightfoot, *Transport Phenomena*. 2006: Wiley.
25. Bhatia, S.K. and D.D. Perlmutter, *A random pore model for fluid-solid reactions: I. Isothermal, kinetic control.* AIChE Journal, 1980. **26**(3): p. 379-386.
26. Kavand, M., et al., *Reaction-Diffusion Model for Gasification of a Shrinking Single Carbon-Anode Particle.* ACS Omega, 2021. **6**(12): p. 8002-8015.
27. *Fundamentals of momentum, heat, and mass transfer*, J.R. Welty, Editor. 2008, Wiley: Hoboken, NJ :.
28. McBride, B.J., *NASA Glenn coefficients for calculating thermodynamic properties of individual species*. 2002: National Aeronautics and Space Administration, John H. Glenn Research Center ….
29. https://www.comsol.com/chemical-reaction-engineering-module.

Appendix B

Corrections and supplementary documents of chapter 3

As Figure b.1 shows, the bed is a 3D cylinder which has axisymmetric. In addition, there are 3D porous spherical particles inside the bed. The extra dimension is the added radial (r) microscale dimension inside each particle. The system has two types of the porosities including porosity due to void in particles and due to void between particles. The 3D of the model was used in the simulations.

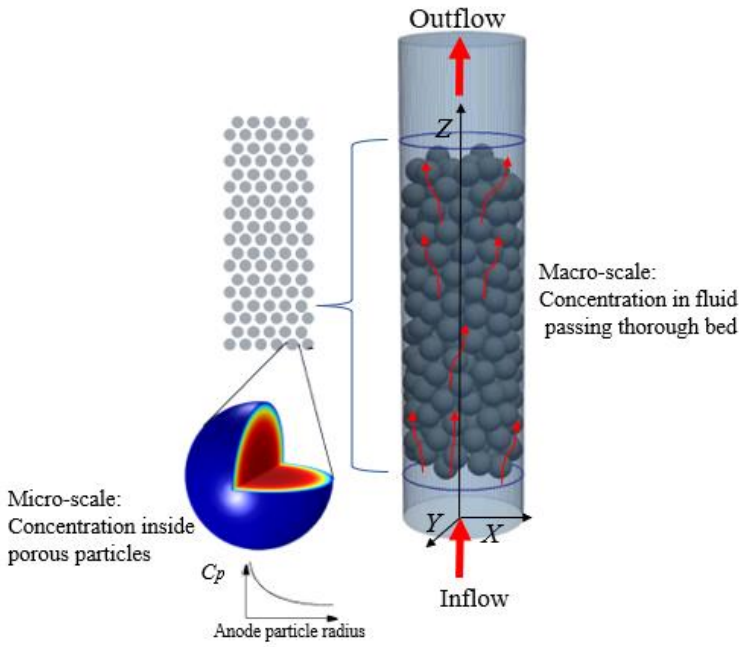

Figure b.1 Fluid–particle flow field for a 3D cylinder axisymmetric model.

Mass equations

A mass-balance-based reaction-transport model is developed to simulate the dynamics of anode CO_2 reactivity by applying heat-transfer equations, as well as momentum equations, to describe the gasification process. CO is the product of the Boudouard reaction, and because of the inhibition effect of CO on gasification (by adsorption and desorption), it should be applied in the model for each step to achieve accurate modeling. This model facilitates the incorporation of a nonlinear chemical-reaction rate, w, the conversion-induced transformations in the porous structure by the pertinent equation, and the reaction-induced changes in the effective diffusivity through the input of conversion (X) [2-4]. The

concentration profile within particles can be obtained for a particle position (r) and certain time (t) by solving the set of equations in the bed:

$$\frac{\partial(\varepsilon_b C_i)}{\partial t} + \varepsilon_b u.\nabla C_i = \varepsilon_b D_i \nabla^2 C_i - h_{D,i} S_b (C_i - C_{pe,i}), \quad i = CO_2, CO \tag{b.1}$$

where - C_{CO_2} and - C_{CO} are the concentrations (mol/m^3) of reactant and product gases of the bed, respectively;-u (m/s) is the - velocity of the fluid; ε_b is the porosity of the bed, $h_{D,i}$ (m/s) is the convective mass-transfer coefficient around the particle; and S_p (m^2 particles/m^3 bed) is the surface area of particles the per unit volume of the bed. The first right-hand term represents the diffusion of species - in the gas phase obtained by Fick's law [5] (Equation b.1) . The second left-hand term describes the convective mass flux of species related to the velocity of fluid gases. The last right-land term represents the convective mass flux owing to the concentration driving force between the surfaces of particles and the gas bulk.

The boundary conditions in the z direction for Equations (b.1) - at the reactor inlet and outlet for each component 'i' are as follows:

$$C_i(r, z, t \geq 0)\Big|_{z=0} = C_{in,i} \tag{b.2}$$

$$\left.\frac{\partial C_i(r, z, t \geq 0)}{\partial z}\right|_{z=L} = 0 \tag{b.3}$$

The concentration of species is finite at the center and also there is no mass flux from the wall of the bed. Equations (b.4) and (b.5) describe these two conditions:

$$\left.\frac{\partial C_i(r, z, t \geq 0)}{\partial z}\right|_{r=0} = 0 \tag{b.4}$$

$$\left.\frac{\partial C_i(r, z, t \geq 0)}{\partial z}\right|_{r=R} = 0 \tag{b.5}$$

Initially, the bed is clean and carbon dioxide is not present such that the fluid concentrations are zero everywhere within the bed:

$$C_i(r, z, t)\Big|_{t=0} = 0, \ i = CO_2, CO \tag{b.6}$$

$$C_C(r, z, t)\Big|_{t=0} = C_{C_0} \tag{b.7}$$

where C_C is the concentration of carbon. This initial condition applies for the bulk fluid concentration as well as the concentration in the particles.

Due to the axisymmetric, there is no concentration variation in the θ direction. The reaction inside the particles is included as a sink term in the intraparticle mass balances for the

transport of dilute species interfaces with reactive particle features. Looking inside a pellet: Assuming no concentration variations in the space-angle (θ, φ) direction, but only in the radial (r_{pe}) direction of the spherical pellet allows a spherically symmetric reaction-diffusion transport equation inside the pellet. A shell mole balance across a spherical shell at radius r_{pe} of the pellet gives:

$$4\pi N\left[\frac{\partial\left(\varepsilon_{\mathrm{pe}}C_{\mathrm{pe},i}\right)}{\partial t}+\frac{1}{r_{\mathrm{pe}}^{2}}\frac{\partial}{\partial r_{\mathrm{pe}}}\left(-r_{\mathrm{pe}}^{2}D_{\mathrm{pe},i}\frac{\partial C_{\mathrm{pe},i}}{\partial r_{\mathrm{pe}}}\right)=w_{\mathrm{pe},i}\right] \tag{b.8}$$

where N is the number of particles per unit volume of bed, $\varepsilon_{\mathrm{pe}}$ is the pellet (microscale) porosity, $C_{\mathrm{pe},i}$ is the interstitial (physical) species concentration in moles/m^3 of fluid volume element inside the pore channel, $w_{\mathrm{pe},i}$ is the pellet reaction rate. This corresponds to reactions taking place inside the particles (per unit volume of pellet.). $D_{\mathrm{pe,i}}$ is the effective diffusion coefficient of component i inside the pellect. The effective diffusion coefficient in the depends on the porosity $\varepsilon_{\mathrm{pe}}$, tortuosity τ, and physical gas diffusivity D_i in the manner of:

$$D_{\mathrm{pe},i}=\frac{\varepsilon_{\mathrm{pe}}D_{i}}{\tau} \tag{b.9}$$

The number of particles per unit volume of bed is calculated from the porosity of the bed and volume of a pellet as:

$$N=\frac{1-\varepsilon_{b}}{V_{\mathrm{pe}}} \tag{b.10}$$

The boundary condition at the center and the radius of the particles (R_{pe}) is:

$$\frac{\partial C_{\mathrm{pe},i}\left(0,t\geq 0\right)}{\partial r}=0 \tag{b.11}$$

$$\frac{1}{R_{\mathrm{pe}}}\left(D_{\mathrm{pe},i}\frac{\partial C_{i}\left(R_{\mathrm{pe}}\right)}{\partial r}\right)=h_{D,i}\left(C_{i}-C_{\mathrm{pe},i}\right) \tag{b.12}$$

Equation (b.12) is the Neumann boundary conditions that specifies the normal derivative of the function on a surface. In this process, an assumption lies in the claim that the gas components' external convective mass-transfer rate to the surface has to be equal to the transport rate via the particle surface. The bed and particle equations are linked through the mass transfer on the surface according to the boundary conditions appearing in the mass-balance equation.

For the case of randomly packed spherical particles, the specific surface area exposed to the free fluid is[6]:

$$S_{\mathrm{b}}=\frac{3}{R_{\mathrm{pe}}}\left(1-\varepsilon_{\mathrm{b}}\right) \tag{b.13}$$

Equation (b.13) is used in equation (b.1). The mass transfer coefficient in Equations (b.1) and (b.12) can be computed from the fluid properties and flow characteristics within the porous media. For this, the Sherwood, Sh, number defined as the ratio between the convective mass transfer coefficient and the diffusive mass transfer coefficient is used [7]:

$$Sh_i = \frac{h_{D,i} L}{D_i} \tag{b.14}$$

where L is a characteristic length (for particles, typically the radius), and D_i is the diffusion coefficient of component i in the fluid. From the Sherwood number, the mass transfer coefficient can be computed. The Frössling relation [6] was used as an empirical expression for the calculation of the Sherwood number as:

$$Sh = 2 + 0.552\,\mathrm{Re}^{\frac{1}{2}}\, Sc^{\frac{1}{3}} \tag{b.15}$$

Where *Re*, and *Sc* are the Reynolds, and Schmidt, numbers as:

$$\mathrm{Re} = \frac{\rho_f u L}{\mu_f} \tag{b.16}$$

$$Sc = \frac{\mu_f}{\rho_f D_i} \tag{b.17}$$

Here L is the characteristics length of the particles, ρ_f, u, μ_f are the density of the fluid, velocity of the fluid, and viscosity of fluid between particles.

Various models can explain the kinetics of the CO_2 gasification reaction. The reaction rate per unit of volume of particle is essential to formulate in a "structural" format [3] inside a particle. Thus, an equation is introduced to outline the reaction for the available particle sites at a given processing time. To explicitly combine this feature, the following intrinsic kinetics is assumed to be established for all locations in the particle:

$$w_{\mathrm{pe,CO_2}} = -r_{\mathrm{CO_2}} \cdot F(X) \tag{b.18}$$

$$r_{\mathrm{CO_2}} = r_{\mathrm{C}} = -\frac{\partial C}{\partial t} \tag{b.19}$$

$$r_{\mathrm{CO}} = -2 r_{\mathrm{CO_2}} \tag{b.20}$$

In equation (b.18), the reaction rate can be divided into two parts [8]. In the first part, $r_{\mathrm{CO_2}}$, the effect of CO_2 concentration on the reaction rate is considered. In the second part, *F(X)*, depicts the effect of changes in the available reacting surface. The description of this equation is detailed in a previous work [9]. In general, the L-H rate equation is considered for $r_{\mathrm{CO_2}}$. This mechanism is proposed based on the adsorption and desorption of CO and CO_2 to yield expressions for calculating the reaction rates of anode gasification. The RPM [10] is applied

to the structural part of the chemical-reaction equation. Therefore, the chemical-reaction term is as follows:

$$\frac{dX}{dt} = \frac{k_1 P_{co_2}}{1 + k_2 P_{co_2} + k_3 P_{co}} S_0 (1 - X)\sqrt{1 - \psi \ln(1 - X)} \quad \text{(b.21)}$$

Here X is the carbon conversion, and S_0 and ψ are the initial specific surface area and the structural parameters of the RPM equation, respectively. k_1, k_2, and k_3 are the chemical-reaction rate-constants.

Movement equation

The momentum balance that governs the fluid flow is built upon the Navier–Stokes and continuity equations. The conservation of mass is the generic equation used, and the following continuity equation is written for a porous medium with an effective term of the chemical reaction on the flow [5]:

$$\frac{\partial(\varepsilon_b \rho_f)}{\partial t} + \nabla.(\rho u) = Q_m \quad \text{(b.22)}$$

$$u = -\frac{k}{\mu L}\Delta P \quad \text{(b.23)}$$

where Q_m (kg/m^3.s) is the - mass source or sink, this term accounts for mass deposit and/or mass creation in inter-particles domain. ρ_f is the density of the fluid. When gas flow inter to the bed, gas is going up through the particle bed, therefore, flow leads to a pressure drop during the reactor, to be able to add this effect on the motion equation, the Ergun equation has been defined, and it can be written as [5]:

$$\frac{\Delta P}{L} = \frac{150\mu_f u(1-\varepsilon_b)^2}{R_{pe}^2 \varepsilon_b^{\,3}} + 1.75\frac{\rho_f u^2 (1-\varepsilon_b)}{R_{pe}\varepsilon_b^{\,3}} \quad \text{(b.24)}$$

where ε_b is the bed porosity, μ_f (Pa.s) stands for the viscosity of the fluid, ρ_f *is* the fluid density (kg.m^{-3}), L is the bed length (m), u is the fluid velocity (m.s^{-1}). The Ergun equation combines both the laminar and turbulent components of the pressure loss across a packed bed. In laminar flow, the first term is predominant. Under turbulent flow, the second term is dominant, and the pressure drop is related to the square of the superficial velocity and linearly depends on the density of the fluid passing through the anode. Assuming the viscous resisting force in Navier-Stokes equation is linear with the velocity, and then the Darcy's law is derived (equation b.23).

Energy equations

The bulk energy balance for a fixed-bed reactor can be written as follows:

$$\rho_f C_{\mathrm{P},f}\left[\frac{\partial\left(\varepsilon_{\mathrm{b}} T_f\right)}{\partial t}+u.\nabla T_f\right]=\varepsilon_{\mathrm{b}} k_f \nabla^2 T_f-h_f S_{\mathrm{p}}(T_f-T_{\mathrm{pe}}\big|_{r_{\mathrm{pe}}=R_{\mathrm{pe}}}) \tag{b.25}$$

where $-C_{P,f}$ is the heat capacity ($\mathrm{J\cdot mol^{-1}\cdot K^{-1}}$), T_f is the bulk fluid temperature, and h_f is the convective heat transfer coefficient between the fluid and the particles surface. The $u.\nabla T_f$ represents the energy transfer owing to the convection of fluid, the $\varepsilon_{\mathrm{b}} k_f \nabla^2 T_f$ term demonstrates the conduction heat flux of the gas phase, and the last term describes the convective heat flux from the surface of the particle to the fluid bulk. The boundary conditions in the *z* direction of bed are:

$$T_f\left(r,z,t\geq 0\right)\big|_{z=0}=T_{in} \tag{b.26}$$

$$\left.\frac{\partial T_f\left(r,z,t\geq 0\right)}{\partial z}\right|_{z=L}=0 \tag{b.27}$$

In addition, the temperature in the center of bed is finite and around the walls is fixed using a heater.

$$\left.\frac{\partial T\left(r,z,t\geq 0\right)}{\partial r}\right|_{r=0}=0 \tag{b.28}$$

$$T\left(r,z,t\geq 0\right)\big|_{r=R}=T_{\mathrm{wall}} \tag{b.29}$$

where R is the radius of bed, and T_{wall} is the fixed temperature at the wall. The relation to the particle-energy balance is:

$$\frac{\partial[(\rho C_P)_{\mathrm{eff}} T_{\mathrm{pe}}]}{\partial t}=k_{\mathrm{eff}}\nabla^2 T_{\mathrm{pe}}+r_{\mathrm{CO_2}}\Delta H_{\mathrm{CO_2}} \tag{b.30}$$

$$\left(\rho C_P\right)_{eff}=\left(1-\varepsilon_{\mathrm{pe}}\right)\rho_C C_{P,C}+\varepsilon_{\mathrm{pe}}\rho_f C_{P,f} \tag{b.31}$$

$$k_{eff}=\left(1-\varepsilon_{\mathrm{pe}}\right)k_C+\left(\varepsilon_{\mathrm{pe}}\right)k_f \tag{b.32}$$

where ρ_C ($\mathrm{kg/m^3}$), $C_{P,C}$ (J/kg.K), and k_C (W./m.K) stand for the density, heat capacity, and conductive heat transfer coefficient of carbon. $\Delta H_{\mathrm{CO_2}}$ (J/kg) is the heat of the reaction. It should be noted that it is assumed that total volume of the particles are reactive instead of pore volume.

The following - boundary conditions are used to solve Equations (b.30):

$$\left.\frac{\partial T_{\mathrm{pe}}\left(r_{\mathrm{pe}}, t \geq 0\right)}{\partial r_{\mathrm{pe}}}\right|_{r_{\mathrm{pe}}=0}=0 \tag{b.33}$$

$$\frac{1}{R_{\mathrm{pe}}}\left(D_{\mathrm{pe},i} \frac{\partial T_{\mathrm{pe}}\left(R_{\mathrm{pe}}\right)}{\partial r}\right)=h_f\left(T_f-T_{\mathrm{pe}}\left|_{r_{\mathrm{pe}}=R_{\mathrm{pe}}}\right.\right) \tag{b.34}$$

Equation (b.34) represents that the no accumulation of heat take place on the particle's surfaces. In other words, heat is carried by the fluid outside the particles. That is, the bed and particle equations are linked through the heat transfer on the surface of the particles according to equation (3.36).

The value of convective heat flux is calculated as [11]:

$$Nu=\frac{h_f L}{k_f} \tag{b.35}$$

where k_f is the conductive heat transfer coefficient of the fluid. *Nu* is the Nusselt number, which is the convective-to-conductive heat-transfer ratio across the boundary, in which the convection covers advection and diffusion mechanisms. For a single particle, this number is obtained for the fluid as follows:

$$Nu=2+\left(0.4 Re^{\frac{1}{2}}+0.06 Re^{\frac{2}{3}}\right) Pr^{0.4}\left(\frac{\mu_{f,\infty}}{\mu_{f,w}}\right)^{\frac{1}{4}} \tag{b.36}$$

where $\mu_{f,\infty}$, and $\mu_{f,w}$ are the viscosity of fluid far from the surface of the particles and near the surface of the particles. *Pr* is the Prandtl number and calculated as:

$$\mathrm{Pr}=\frac{C_{P,f}\mu_f}{k_f} \tag{b.37}$$

Initially, the bed and particles are at the same temperature:

$$T_f\left(r, z, t\right)\big|_{t=0}=T_0 \tag{b.38}$$

$$T\left(r_{\mathrm{pe}}, t\right)\Big|_{t=0}=T_0 \tag{b.39}$$

For a bed of spherical particles, the following equations have been obtained by Gunn et al. [12]:

$$\mathrm{Re}_{\mathrm{e}}=\frac{1}{(1-\varepsilon_b)}\mathrm{Re} \tag{b.40}$$

$$Nu_b = 1 + 1.5(1 - \varepsilon_b) Nu_p \quad \text{(b.41)}$$

Numerical sulotion

Generation of DEM sample

Several methods exist for solving sphere placement, including dynamic compression [14, 15], radius growth, and solving geometrical equations [16, 17]. To achieve the desired specimen, it is necessary to specify the porosity and define the sphere overlap. In this work, the YADE software, an open-source, 3D simulation program, was used to generate fixed-bed structures. Yade, can implement computational algorithms using the discrete element method (DEM) in a stable and uniform environment. As a result of the soft-body model, rigid particle surfaces can penetrate each other during collisions. It is assumed that particles are rigid bodies, but interparticle deformation is allowed by using a simple force displacement law to overlap between particles. Within a cylinder, a specified number of spheres Np with diameter dp are placed at random positions by allowing particles to penetrate one another through interpenetration available in the YADE software and allowed to fall due to gravity(Figure b,2). A total of three column diameter (D) to particle diameter (d) with D/d = 6, 12, 24 are used. A maximum particle overlaps of 1% of the particle diameter is obtained from the DEM-code. A 2D mesh with 1.0 mm holes was produced by Gmsh, a finite element mesh generator [18] (Geuzaine and Remacle, 2009). After the pellets have settled in the container, information about the simulated packings, in particular bulk porosity, is generated using a post-processing mesh-based analysis [19].

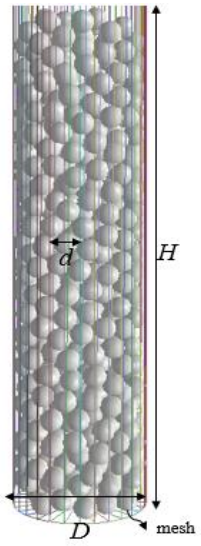

Figure.b.2 . Random packing of spherical particles obtained from DEM simulations for D/d = 6

This paper defines an interface to allow the data to be converted between continuum models derived from the FEM mechanism and the DEM model. A partially coupled framework is involved in the interface between the FEM and DEM mechanisms [20]. Figure b.3 presents the algorithm used for this process. "n" is the number of simulations; so, it makes the simulation time, simulation time = time step (dt) × number of simulations (n). In the beginning, all components of simulation will be initialized; DEM, CFD, and coupling. Based on the position of particles and fluid mesh information, the coupling calculates the fluid porosity. Following that, velocity of particles and velocity of fluid are used to calculate the fluid-particle interaction force acting on each particle. The next step involves iterating the DEM. During the coupling step, the fluid-particle force is calculated and used in the equation of motion of each particle. For the DEM iteration loop, the time step is dt and the iteration loop for the equation of motion is n. Following the DEM loop, all particles' new positions and translational and rotational velocities are calculated for the next fluid time step. Calculated porosity and volumetric fluid-particle interactions in each fluid cell are used to solve mass and momentum conservation equations for the fluid phase.

Finally, to change the initial conditions for each time step, the data are sent to the FEM mechanism to set the values of the parameters obtained from the DEM and to run the simulation. In the next step, the unknown variables are calculated by comparing with the simulation and experimental data.

A sensitivity study of the model compared to the size of the mesh been carried out to know the optimal size of the chosen mesh. Accordingly, seven levels of mesh including extremely coarse, extra course, coarser, coarse, normal, fine, and finer were used. At the finer level 75800 prisms, 3032 triangles, 4400 quads, 488 edge elements, and 10 vertex element were used. The average mesh quality is equal to 0.889. As the mesh quality at this level is suitable, finer mesh level was used to study the model. In addition, the extra fine, and extremely finer mesh was used to investigate the smaller mesh. The results showed that only the computation time increases but the results do not change. Velocity of fluid, temperature of fluid, concentration of species in fluid, temperature of particles, concentration of species inside the particles, porosity of the bed, porosity of particles, radius and position of particles are the dependent variables. Equations (3.3), (3.10), (3.23)-(3.27), (3.32), (3.42)-(3.44) as PDEs and ODEs are solved simultaneously via coupling COMSOL and YADE. A constant damped version of Newton’s method (damped factor=0.8) was used to solve the fully coupled phenomena. Backward differentiation formula (BDF) with an order of accuracy varying from one (that is, backward Euler) to two was used as time stepping. BDF methods have been used for a long time and are known for their stability. Node information can be modified by MATLAB scripts. YADE software, an open-source C++ framework, was applied to work as a DEM engine that can solve Newton’s second law of motion for each anode particle. A relative tolerance of 0.001 was used as stopping criteria. To validate the model with experimental data, an algorithm genetic is applied using MATLAB.

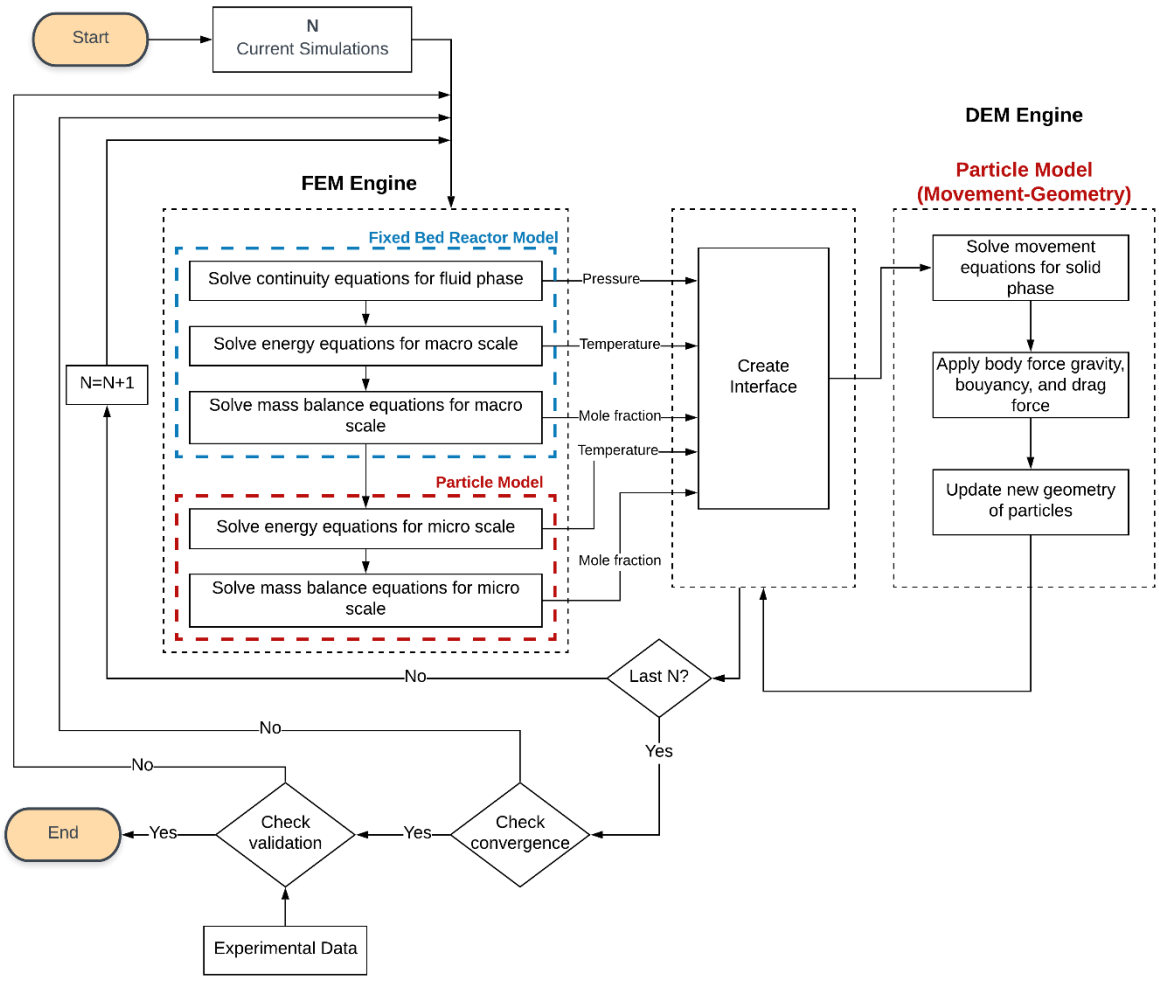

Figure b.3 Algorithm of the mathematical model

Temperature profiles

Figure b.4 and Figure b.5 exhibit the temperature distributions at various positions and directions (axial and radial). Figure b.4 that the hotspot is located close to the reactor exit. The solid temperature is higher than that of the gas because of the exothermic reaction within the particles [21-24]. Based on Figure b.5, the temperature increases at the center and decreases on both sides in a parabolic manner because of the wall heat sinks. This temperature difference results from a competition between the rates of interfacial heat and mass exchange. In this particular case slight resistances to heat transfer to and from the solid particles cause a higher temperature in the particle. The solid temperature is higher than the gas temperature [25]. In practical applications, the above temperature variations are due to the much higher thermal-conductivity performance and heat capacity of the solid phase than those of the gas phase.

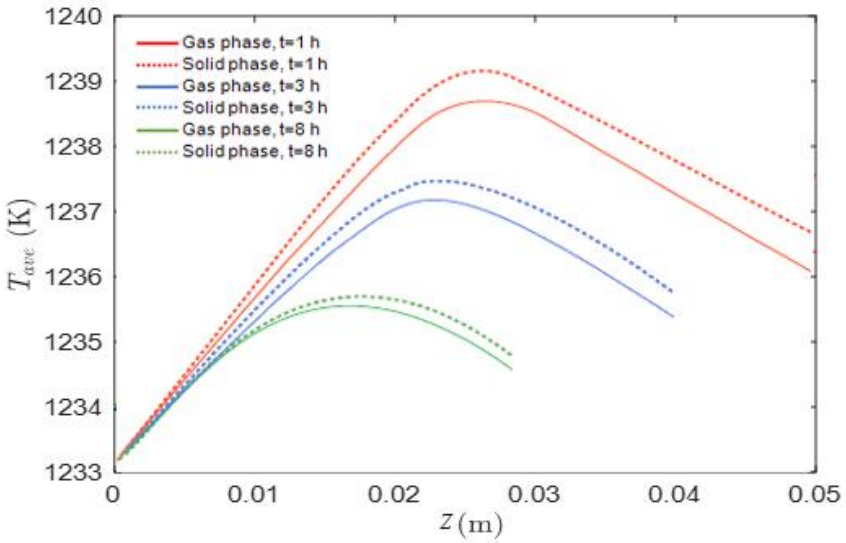

Figure b.4 Temperature profiles in the reactor. Temperature distributions along the axial direction of the reactor (r = 1 mm, Q = 1 L·min^{-1}, H = 5 cm, T = 1233 K)

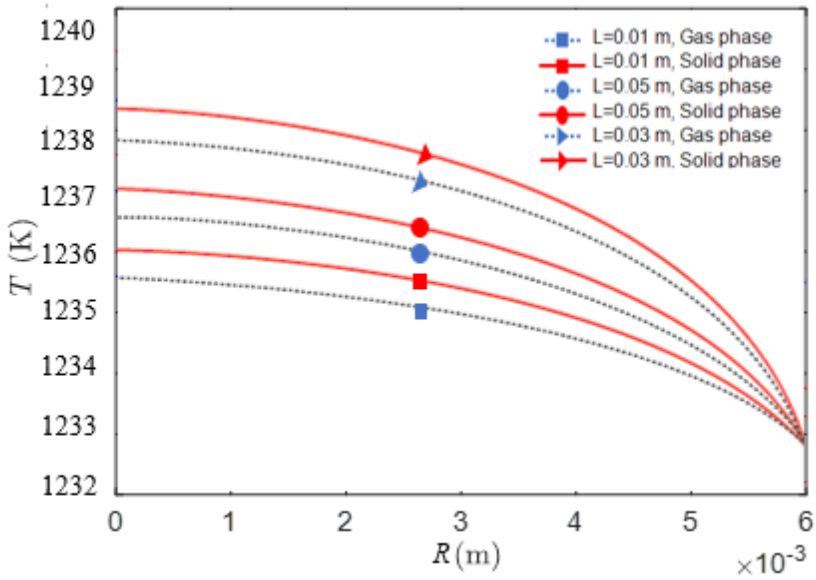

Figure b.5 Temperature profiles in the reactor. Temperature distributions along the radial direction of the reactor (r = 1 mm, Q = 1 L·min^{-1}, H = 5 cm, T = 1233 K)

Figure b.6)a-c demonstrates the simulation outcomes at multiple flow rates. The hotspot temperature rises as flow rates increase. Moreover, the outlet temperature increases slightly. Whenever the volume flow rate of the material increases, the Reynolds number in the bed

significantly increases. Consequently, the axial and radial heat-transfer rates to increase, whereas the radial-temperature difference and hot-spot temperature decrease to their original value

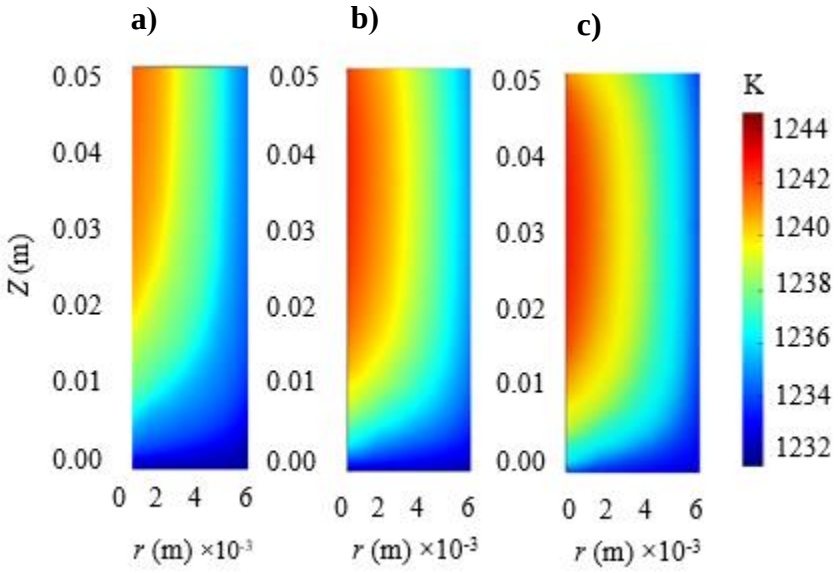

Figure b.6 Temperature distribution of the hotspot at multiple flow rates: a) 0.5 L·min^{-1}, b) L·min^{-1} and c) 2 L·min^{-1} (r = 1 mm, R = 6 mm, Q = 1 L·min^{-1}, H = 5 cm, T = 1233 K)

References

1. Norouzi, H.R., et al., *Coupled CFD-DEM modeling: formulation, implementation and application to multiphase flows*. 2016: John Wiley & Sons.
2. Dixon, A.G., et al., *CFD Method To Couple Three-Dimensional Transport and Reaction inside Catalyst Particles to the Fixed Bed Flow Field.* Industrial & Engineering Chemistry Research, 2010. **49**(19): p. 9012-9025.
3. Gómez-Barea, A. and P. Ollero, *An approximate method for solving gas–solid non-catalytic reactions.* Chemical Engineering Science, 2006. **61**(11): p. 3725-3735.
4. Gudekar, K.G., , *Modeling, control, and optimization of fixed bed reactors*, , in *chemical engineering*. 2002, Texas Tech University.
5. Bird, R.B., W.E. Stewart, and E.N. Lightfoot, *Transport Phenomena*. 2006: Wiley.
6. JM Coulson, a.J.R., *CHEMICAL ENGINEERING: Fluid Flow, Heat Transfer and Mass Transfer* 4th ed. Chemical Engineering Education. Vol. 1. 1991, Oxford, U.K.: Pergamon Press. 182-183.
7. Garner, F.H. and R.W. Grafton, *Mass Transfer in Fluid Flow from a Solid Sphere.* Proceedings of the Royal Society of London. Series A, Mathematical and Physical Sciences (1934-1990), 1954. **224**(1156): p. 64-82.

8. Gómez-Barea, A., P. Ollero, and R. Arjona, *Reaction-diffusion model of TGA gasification experiments for estimating diffusional effects.* Fuel, 2005. **84**(12-13): p. 1695-1704.
9. Kavand, M., et al., *Reaction−Diffusion Model for Gasification of a Shrinking Single Carbon-Anode Particle.* ACS Omega, 2021.
10. Xu, Q., S. Pang, and T. Levi, *Reaction kinetics and producer gas compositions of steam gasification of coal and biomass blend chars, part 2: Mathematical modelling and model validation. Chemical Engineering Science*, 2011. **66**(10): p. 2232-2240.
11. Aissa, A., et al., *Ranz and Marshall correlations limits on heat flow between a sphere and its surrounding gas at high temperature.* Thermal Science, 2015. **19**(5): p. 1521-1528.
12. Gunn, D. and J. De Souza, *Heat transfer and axial dispersion in packed beds.* Chemical Engineering Science, 1974. **29**(6): p. 1363-1371.
13. Tamer, C., et al., *Effect of Drying on Porous Characteristics of Orange Peel.* International Journal of Food Engineering, 2016. **12**(9): p. 921-928.
14. Frédéric, D. and S.-A. Magnier, *Formulation of a 3-D numerical model of brittle behaviour.* Geophysical Journal International, 1995. **122**(3): p. 790-802.
15. Donzé, F.V., et al., *Numerical Study of Compressive Behavior of Concrete at High Strain Rates.* Journal of Engineering Mechanics, 1999. **125**(10): p. 1154-1163.
16. Jerier, J.F., Donze, F.V., Imbault, D. and Doremus, P, *A geometric algorithm for discrete element method to generate composite materials* in *Discrete Element Group for Hazard Mitigation, annual report, .* 2008. p. pp. A1-8.
17. Jerier, J.F., Donze, F.V. and Imbault, D. , *An algorithm to generate random dense arrangements discs based on the triangulation, Discrete Element Group for Hazard Mitigation, annual report*. 2007. p. D1-7.
18. Geuzaine, C. and J.-F. Remacle, *Gmsh: A 3-D finite element mesh generator with built-in pre- and post-processing facilities.* International Journal for Numerical Methods in Engineering, 2009. **79**(11): p. 1309-1331.
19. Moghaddam, E.M., et al., *Rigid Body Dynamics Algorithm for Modeling Random Packing Structures of Nonspherical and Nonconvex Pellets.* Industrial & Engineering Chemistry Research, 2018. **57**(44): p. 14988-15007.
20. Pirnia, P., et al., *ICY: An interface between COMSOL multiphysics and discrete element code YADE for the modelling of porous media*. Computers & Geosciences, 2019. **123**: p. 38-46.
21. Behnam, M., et al., *A new approach to fixed bed radial heat transfer modeling using velocity fields from computational fluid dynamics simulations.* Industrial & Engineering Chemistry Research, 2013. **52**(44): p. 15244-15261.
22. Gao, X., Y.-P. Zhu, and Z.-H. Luo, *CFD modeling of gas flow in porous medium and catalytic coupling reaction from carbon monoxide to diethyl oxalate in fixed-bed reactors.* Chemical Engineering Science, 2011. **66**(23): p. 6028-6038.
23. Miroliaei, A.R., F. Shahraki, and H. Atashi, *Computational fluid dynamics simulations of pressure drop and heat transfer in fixed bed reactor with spherical particles. Korean Journal of Chemical Engineering*, 2011. **28**(6): p. 1474-1479.
24. Singhal, A., et al., *Verification of Heat and Mass Transfer Closures in Industrial Scale Packed Bed Reactor Simulations.* Energies, 2018. **11**(4): p. 805.
25. Sadooghi, P. and R. Rauch, *Experimental and modeling study of catalytic steam reforming of methane mixture with propylene in a packed bed reactor.* International Journal of Heat and Mass Transfer, 2014. **78**: p. 515-521.

Appendix C

ACS OMEGA

http://pubs.acs.org/journal/acsodf

Article

Reaction–Diffusion Model for Gasification of a Shrinking Single Carbon-Anode Particle

Mohammad Kavand, Roozbeh Mollaabbasi, Donald Ziegler, Faïçal Larachi, Donald Picard, and Houshang Alamdari*

Cite This: ACS Omega 2021, 6, 8002−8015

Read Online

ACCESS | Metrics & More | Article Recommendations

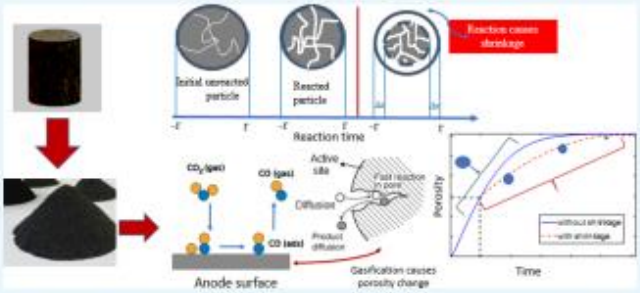

ABSTRACT: The present work focuses on the gasification of a single carbon-anode particle with CO_2, using a detailed reaction-transport model based on the reaction intrinsic kinetics and transport of gaseous species. The model includes the mass conservation equations for the gas components and solid carbon particles, resulting in a set of nonlinear partial differential equations, being solved using numerical techniques. The model may predict the gas generation rate, the gas compositions, and the carbon consumption rate during the gasification of a carbon particle. Five kinetic models were compared to describe the gasification behavior of carbon particles. It was found that the random pore model (RPM) provided the best description of the reactivity of anode particles. The model also predicted the particle shrinkage during the gasification process. The model was validated using experimental results obtained with different particle size ranges, being gasified with CO_2 at 1233 K. The experiments were performed in a thermogravimetric analyzer (TGA). Good agreement between the model results and the experimental data showed that this approach could quantify with success the gasification kinetics and the gas distribution within the anode particle. In addition, the Langmuir−Hinshelwood (L−H) model is used in order to capture the inhibition effect of carbon monoxide on the gasification reaction. The effectiveness factor and Thiele modulus simulated for various particle sizes helped assess the evolution of the relative dominance of diffusion and chemical reactions during the gasification process.

1. INTRODUCTION

Carbon anode reactivity is of considerable concern for most aluminum smelters using the Hall−Héroult electrolysis process. In this process, anodes are partially submerged into the electrolyte solution, which is made up of molten cryolite. Molten aluminum is produced by the reduction of dissolved alumina in the cryolite, and the anode is electrochemically oxidized, generating CO_2. The stoichiometry of this overall electrolysis reaction is shown as eq 1. The generated CO_2 at the anode surface directly escapes to the electrolysis cell headspace. However, part of the generated CO_2 diffuses into the porous structure of the carbon anode due to the electrolyte hydrostatic head and the concentration gradient. Consequently, it reacts with the solid carbon through the Boudouard reaction.[1] The Boudouard reaction is not desirable because it results in an increase in the net carbon consumption and may contribute to the generation of carbon dust in the pots, which is an operational problem.[1,2] The carbon dust is principally generated by selective burning of the anode components that are in contact with air or CO_2. For instance, it is believed that the binder matrix within the anode is preferentially burnt, causing detachment of the carbon particles from the anode surface, which then fall into the electrolyte bath.[3]

Received: October 30, 2020
Accepted: December 22, 2020
Published: March 22, 2021

https://doi.org/10.1021/acsomega.0c05297
ACS Omega 2021, 6, 8002−8015

$$2Al_2O_{3(diss)} + 3C_{(s)} \rightarrow 4Al_{(m)} + 3CO_{2(g)} \quad (1)$$

The combustion reactions occur either at the anode surface or within the anode bulk. For a given anode formulation, the reaction rate is a function of temperature, pore structure, permeability, and intrinsic reactivity of the anode constituents.[3−5] The minimum theoretical carbon consumption for aluminum electrolysis is 0.334 kg per kg of Al produced. However, since the cell efficiency is usually less than 100%, the real electrolytic consumption of carbon is around 0.41 kg per kg of Al produced. Keller et al. reported that the extra cost associated with the overconsumption of 1 kg anode per one ton of produced aluminum is around US$ 2. The overconsumption of a midsize smelter (producing 300,000 tons of aluminum per year, and needing 150,000 anodes per year), is approximately 40 kg per anode. Therefore, the estimated extra cost could be about US$ 12 million per year.[6,2] Gasification of the anode by air and CO_2 greatly contributes to this carbon overconsumption. Several authors[7−10] discussed the influence of anode properties on its air and CO_2 reactivity and the net carbon consumption. The present work will mainly emphasize the quantification of the structural changes of anode particles during CO_2 gasification and its effect on the gasification reactions.

The electrolysis cell (which is called *pot*) is composed of prebaked carbon anodes, molten cryolite, and a liquid layer of aluminum lying on cathode carbon blocks. The carbon anode is consumed during the process, and it should be replaced by a new one approximately every 25 days. The anodes in the electrolysis cell are in contact with CO_2 at high temperatures (typically 1233 K). At temperatures higher than 1073 K, the apparent rate of carbon−CO_2 gasification reaction becomes more significant due to the combined chemical reaction and the mass transfer effects. It is worth mentioning that the diffusion is the main part of the mass transfer,[11,12] and its effect on the gasification rate becomes more significant for particles larger than 0.1 mm.[12,13]

In order to estimate the anode consumption rate, numerous mathematical models have been introduced in the literature such as the grain model (GM),[14,15] the volume reaction model (VM),[8,10,15] the nucleation model, the single-pore model (SPM),[8] the modified grain model (MGM),[16] and the random pore model (RPM).[8,9,15,17] Broadly, these models can be divided into two main categories: structural and volumetric models. The structural models account for the changes in the structure of carbon in the process. During the reaction, the internal pore structure is changing over time.[11,15,18−25] In the volumetric models, conversely, experimental correlations are used for considering the porous structural changes.[8,10,14,18,22,26,27] In this latter approach, the problem is addressed by feeding the model with the anode mechanical properties or other experimental data. These models explicitly mention the solid microstructure changes during the reaction and the influence of the microstructure evolution on reactivity, but despite changes in the structure, the particle size during the process remains invariant. The literature abounds with simplified techniques to circumvent mathematical and computational difficulties. Jamshidi and Ale Ebrahim[7,28,29] developed a semi-analytical, semi-numerical method, the Quantize Method (QM), with simplifying assumptions. Their model leads to acceptable results based on the experimental data, though without mentioning the effect of solid structural changes into the solid volume. Thus, the particle radius remained fixed during the gasification, that is, not truly representing the real gasification conditions.

In a non-catalytic carbon−CO_2 reaction, it is essential to take into account the solid structural changes as the reaction progresses because the reaction rate is a function of both gas and solid concentrations.[14,18,19] From a mathematical point of view, this aspect leads to coupling the gas−solid conservation equations within the model that increases the complexity of the problem. Researchers have extensively studied the computational aspects of these models, but there is only limited research data available on single-particle reactions, considering gas−solid conservation equations,[18−22] and it is essential to develop models for such practical systems. An accurate model for a particle reaction could generate valuable insights for modeling the whole anode reaction in the future.

In this contribution, we attempted to reduce the gap between theory and experiment by providing a model that considers diffusion and pore growth during the reaction of an anode particle. Upon the gasification process, the anode particles are consumed, and the apparent radius of the carbon anode reduces gradually while the porosity of the particle also increases. Hence, the effect of shrinkage and particle porosity was considered in mathematical modeling. Therefore, suitable numerical methods were implemented in the mathematical model for solving the governing transfer equations. First, the intrinsic kinetics of CO_2 gasification is experimentally investigated by using a thermogravimetric analysis. Then, a global reaction model was developed by considering all the abovementioned aspects. The suitability of the existing structural reaction models for our global reaction model was examined.

2. EXPERIMENTS

2.1. Materials and Method. *2.1.1. Materials.* The carbon anode particles were obtained from the Deschambault aluminum smelting plant (Alcoa Corporation). Ball milling was used to mill large particles into fine fractions. To have various particle sizes of anodes, the particles were crushed and passed through various USA standard sieve trays (from 20 to 4380 μm).

The real density of the anode particles was measured using a Helium-pycnometer (Micromeritics, AccuPyc II 1340, USA). Each analyzed sample (2 g) was weighed three times with an analytical balance (MS204S, Mettler Toledo, USA) and placed in a stainless-steel cell in the He pycnometer. The real density was obtained by dividing the mass of the sample to the volume obtained by the pycnometer.

To obtain the specific surface area, powder samples, with a given size, were first degassed under pure nitrogen (N_2) at 523 K for 5 h. Then, the samples were analyzed with a gas adsorption analyzer (Micromeritics, Tristar II 3020, USA). Nitrogen (Praxair, purity: 99.995%, USA) was used as the adsorbing gas at 97 K. The chemical composition was analyzed for all samples using an X-ray fluorescence spectrometer (Panalytical, USA). Characteristics of the anode particles with different sizes are presented by Chevarin et al.[2] The amounts of sulfur, vanadium, nickel, and sodium are similar for all particle sizes. The increase in the amount of iron observed with decreasing particle size may be explained by the crushing and grinding of the particles, which resulted in potential iron contamination. The variability of silicon and calcium concentrations is difficult to explain.

https://doi.org/10.1021/acsomega.0c05297
ACS Omega 2021, 6, 8002−8015

2.1.2. Gasification Tests. A thermogravimetric analyzer (Netzsch STA 449 F3 Jupiter) was used for measuring the apparent reaction rate of anode particles at 1233 K by measuring the online weight loss of the samples. To remove moisture content, the samples were placed in an oven at 423 K for 15 h. Only one layer of dried particles was placed in the TGA sample holder (1.82 mm height and 6.45 mm diameter) to ensure the constant composition of the feeding gas near the surface of each particle. The temperature was gradually raised (20 K·min^{-1}) to the target reaction temperature (1233 K). Nitrogen (99.995%, 100 mL·min^{-1}) was used as a protecting gas during the heating step. After reaching the target temperature, the system was stabilized for 15 min under the flow of N_2. The flow rate of nitrogen was then steadily decreased to 20 mL·min^{-1}, while the flow of CO_2 gas (99.9%) was increased to 100 mL·min^{-1}, and the mass loss was recorded. At the end of the experiment, the CO_2 flow was cut off and substituted by N_2 flow, and the furnace was switched off to cool down to ambient temperature. Each experiment was stopped once no further mass loss was occurring, indicating complete gasification of the samples. The reaction time was indeed a function of the particle size. Equation 2 states the gasification conversion (X) of the carbon material to be used for expressing the apparent anode reactivity:

$$X = \left(1 - \frac{m_t}{m_0}\right) \tag{2}$$

where m_0 is the initial mass of the anode particle sample and m_t is the instantaneous mass at time.

3. MATHEMATICAL MODELING

3.1. Gasification Models. The primary chemical reaction can be represented by eq 3:

$$aA_{(g)} + bB_{(s)} \rightarrow C_{(g)} \tag{3}$$

where A and B are the gas and solid reactants, respectively, and C is the gaseous product while a and b are their corresponding stoichiometric coefficients. Some simplifying assumptions are used in this model as follows: the domain of the anode particle consists of a spherical reactive solid and the intra-particle porosity, which shelters the gaseous reactants and products. On account of the small size of the particles, it is safe to assume that both gas and solid phases are in an isothermal state.[15] For simplicity, we assume the topochemical particle evolution preserving its sphericity during the gasification process. CO_2 in a spherical anode particle reacts with carbon according to the following reaction:

$$CO_{2(g)} + C_{(s)} \rightarrow 2CO_{(g)} \tag{4}$$

The local mass conversation equations for each species assuming spherical particle symmetry can thus be written as:

$$\frac{1}{r^2}\frac{\partial}{\partial r}\left(r^2 D_e \frac{\partial C_{CO_2}}{\partial r}\right) + R_{CO_2} = \frac{\partial(\varepsilon C_{CO_2})}{\partial t} \tag{5}$$

$$\frac{1}{r^2}\frac{\partial}{\partial r}\left(r^2 D_e \frac{\partial C_{CO}}{\partial r}\right) - 2R_{CO_2} = \frac{\partial(\varepsilon C_{CO})}{\partial t} \tag{6}$$

$$R_C = -\frac{\partial C_C}{\partial t} = R_{CO_2} \tag{7}$$

The boundary and initial conditions are:at

$$r = r_0;\ C_{CO_2} = C_{CO_{2,0}},\ C_{CO} = 0 \tag{8}$$

at

$$r = 0;\ \frac{\partial C_{CO_2}}{\partial r} = 0,\ \frac{\partial C_{CO}}{\partial r} = 0 \tag{9}$$

$$C_{CO_2}|_{t=0} = C_{CO_{2_0}},\ C_{CO}|_{t=0} = 0,\ C_C|_{t=0} = C_{C_0} \tag{10}$$

where R_{CO_2} is the chemical reaction rate of CO_2 ,R_C is the rate of anode reactant consumption, C_C is the instantaneous concentration of anode, C_{C_0} is the initial concentration of anode, C_{CO_2} is the concentration of the gaseous reactant, $C_{CO_{2,0}}$ is the initial concentration of the gaseous reactant, D_e is the effective molecular diffusivity, r is the local radial position within the anode particle, and r_0 is the initial particle radius. According to eq 7, both rates of gas consumption (R_{CO_2}) and carbon reactant consumption (R_C) are equal during gasification. The void fraction or the local porosity of the anode particle may change during reaction due to the consumption of the solid reactant or the difference between the volume of the solid reactant and product. The variation of local porosity can be modeled by eq 11[15] as follows:

$$\varepsilon = \varepsilon_0 + (1 - \varepsilon_0)X \tag{11}$$

where ε_0 is the initial porosity of the anode. Equation 11 can be derived by means of a material balance based on the assumption that the bulk density of the ash remains constant[30] and the local porosity satisfies a linear relation with conversion.[31]

According to eqs 12−14, first, the partial differential eqs 5 and 6 with boundary and initial conditions (eqs 8−10) are solved to obtain the instantaneous C_{CO_2} and C_{CO} radial profiles. Then, C_C is calculated from the mass balance at each location by:

$$C_C = C_{C_0} + (C_{CO_2} - C_{CO_{2,0}}) \tag{12}$$

The carbon conversion has been experimentally acquired and calculated by eq 2. Carbon conversion and porosity, which both are locally dependent, are calculated in the model as follows:

$$X = 1 - \frac{C_C}{C_{C,0}} \tag{13}$$

$$\varepsilon = \varepsilon_0 + (1 - \varepsilon_0)X = 1 - (1 - \varepsilon_0)\left(\frac{C_C}{C_{C,0}}\right) \tag{14}$$

For the structural evolution of the particles during the gasification, different models have been proposed in the literature. For instance, RPM assumes that the pore structure of porous particles consists of cylindrical channels having different sizes and that the reaction takes place on the wall surfaces. According to this model, the relationship between the internal surface area of particle and its porosity can be given by:[10,32]

$$S(X) = S_0(1 - X)\sqrt{1 - \psi \ln(1 - X)} \tag{15}$$

where S_0 is the initial surface area, ψ is a dimensionless parameter indicating that the nature of the pore structure (i.e., RPM structural parameter) was calculated using equation 17,

https://doi.org/10.1021/acsomega.0c05297
ACS Omega 2021, 6, 8002−8015

and also other related parameters are determined by the following equations;

$$S_0 = \frac{2}{(V_p + 1/\rho_s)} \int_0^\infty \frac{v_0(r)}{r}\,dr \tag{16}$$

$$\psi = \frac{4\pi L_0(1-\varepsilon_0)}{S_0^2} \tag{17}$$

$$\varepsilon_0 = \frac{V_p}{V_p + 1/\rho_s} \tag{18}$$

$$V_p = \int_0^\infty v_0(r)\,dr \tag{19}$$

$$L_0 = \frac{1}{\pi(V_p + 1/\rho_s)} \int_0^\infty \frac{v_0(r)}{r^2}\,dr \tag{20}$$

$$\bar{r} = \frac{1}{V_p} \int_0^\infty v_0(r)\,dr \tag{21}$$

where L_0, ε_0, and ρ_s are the pore length, the porosity, and the density of the anode particle, respectively. The pore volume distribution function $V_p(r)$ is obtained by eq 19. Equations 20 and 21 estimate the total pore length and the average pore radius, respectively.

Gas diffusion in a porous solid is affected by the porosity and the pore structure. Therefore, an effective diffusion coefficient is considered. The effective molecular diffusivity (D_e) of the gas in a porous particle is obtained by:[24]

$$D_e = D\frac{\varepsilon}{\tau} \tag{22}$$

where D is the molecular diffusivity of the gaseous species, τ is the tortuosity factor, and ε is the particle porosity. The binary diffusion coefficient of component (D_{IJ}) at each temperature, for species I in reaction J, is estimated by the correlation of Hirschfelder.[33]

$$D_{IJ} = \frac{0.0018583\,T^{1.5}\left[\frac{1}{M_I} + \frac{1}{M_J}\right]^{0.5}}{P_{abs}\sigma_{IJ}^2\Omega_D} \tag{23}$$

where P_{abs} is the absolute pressure in atmospheres and M_I and M_J are the molecular weights of I and J, respectively. σ_{IJ} is the Lennard–Jones collision diameter in angstrom, and Ω_D is the collision integral for molecular diffusion.

Both the chemical reaction rate and diffusion rate may contribute to the overall reaction rate. At high diffusion rates, the chemical reaction could be a limiting factor, and reciprocally. The Thiele modulus is a dimensionless parameter that informs which phenomenon has the leading characteristic time.[34] Here, a modified Thiele modulus (λ) is developed to account for the structural change undergone due to the consumption of the material during the particle's gasification. For a first-order chemical reaction, a modified Thiele modulus is defined as:[15]

$$\lambda^2 = \varphi^2\sqrt{1 + \psi\ln(1-\varepsilon_0) - \psi\ln(1-\varepsilon)} \times (1-\varepsilon)/\varepsilon^2 \tag{24}$$

in which φ is the Thiele modulus,[15] defined as:

$$\varphi = r_0(k\rho_s S_0 D_e)^{1/2} \tag{25}$$

where k is the reaction-rate constant, r_0 is the initial particle radius, ρ_s is the density of the anode particle, S_0 is the initial surface area, and D_e is the effective diffusivity.

The effectiveness factor η can be calculated using the modified Thiele modulus by the following equation:

$$\eta = \frac{1}{\lambda}\left(\frac{1}{\tanh(3\lambda)} - \frac{1}{3\lambda}\right) \tag{26}$$

As the largest characteristic length scale of the pore structure is much smaller than the characteristic length associated with the concentration gradients, the reaction rate term in eqs 5−7 should be adequately defined. So, from a particle point of view, the reaction rate per unit volume must be formulated in a "structural" form. Thus, a function that summarizes the available reaction sites at a given time should be introduced. To incorporate this feature explicitly, we assume the following intrinsic kinetics at any location within the particle as:

$$R = -r(C_{CO_2})\cdot F(X) \tag{27}$$

This reaction rate consists of two parts, $r(C_g)$ and $F(X)$. The first part stands for the influence of the gas phase components on the reaction rate, whereas the second part depicts the structural change brought by the reaction in the porous solid phase.[31]

In this work, to model CO_2 gasification of the anode particles, two types of equations are used to describe the gas phase reaction, $r(C_A)$, a simple first-order form, and a Langmuir−Hinshelwood (L−H) form. The latter is preferred due to its ability to account for the species adsorption/desorption. In the L−H formulation, the adsorption coefficients of CO and CO_2 are assumed to be constant (k_1, k_2, and k_3), and the following pathway is proposed for this process:

$$C_f + CO_2 \xrightarrow{k_1} C(O) + CO \tag{28}$$

$$C(O) + CO \xrightarrow{k_2} C_f + CO_2 \tag{29}$$

$$C(O) \xrightarrow{k_3} CO + C_f \tag{30}$$

where C_f is the active carbon site, k_1, k_2, and $k_3$are the reaction rate constants, and C(O) represents the carbon−oxygen surface. The presence of CO results in lowering the steady-state concentration of C(O) by an inhibiting effect $r(C_g)$ as described by eq 31:

$$r_{C_f} = \frac{k_1 P_{CO_2}}{1 + k_2 P_{CO_2} + k_3 P_{CO}} \tag{31}$$

Equation 27 becomes eq 32 by substitution of $-r(Cg)$ (eq 31):

$$R = \frac{k_1 P_{CO_2}}{1 + k_2 P_{CO_2} + k_3 P_{CO}} F(X) \tag{32}$$

An Arrhenius-type of temperature dependence is assumed for k:

$$k = k_0 \exp\left(-\frac{E}{R_m T}\right) \tag{33}$$

https://doi.org/10.1021/acsomega.0c05297
ACS Omega 2021, 6, 8002−8015

where E is the activation energy, k_0 is the pre-exponential factor ($atm^{-n}·s^{-1}$), and R_m is the ideal gas constant ($kJ·mol^{-1}·K^{-1}$).

There are also various models to cast the kinetics of the gasification reaction for the porous solid phase $F(X)$. In general, different kinetic models can be applied to the structure part of eq 27, among which, the shrinking core model, the volumetric reaction model, the modified volumetric model, and the random pore model are widely used by researchers[9,14,15,17,18,35,36] (Table 1). To evaluate these different

Table 1. Main Structural Reaction Models for the Gasification Rate[14,31,45]

model	equation ($F(X)$)
volumetric model (VM)	$(1-X)$
shrinking core model (CM)	$(1-X)^{2/3}$
random pore model (RPM)	$(1-X)\sqrt{1-\psi \ln(1-X)}$
modified random pore model (MRPM)[a]	$[1+(\omega+1)(\alpha t)](1-X)\sqrt{1-\psi \ln(1-X)}$
traditional (TM)	$(1-X)^n$

[a]α: modified random pore model constant, (s^{-1}), ω: power-law constant, (−).

models, a set of experimental data is used. The carbon conversion is calculated by using various kinetic models, and the solved set of equations is compared with the experimental data. Models that account for particle shrinking-core behavior usually assume that the external layer of the particles is removed with time, which is referred to the exposed shrinking-core model (CM). Therefore, in these models, the external mass transfer and intrinsic kinetics in the external surface are considered. In addition, the reacting particles are assumed to preserve their spherical shape during gasification, as stated earlier. The reaction between the particle and gas reactants is started on the interface of the particle and gas. As the external surface is consumed, the reaction front moves gradually to the particle's interior. This results in decreasing the particle's radius during the gasification reaction progress. However, this model cannot capture the structural changes inside the particle since the gasification takes place only on the external surface of the particle.

On the other hand, in the volumetric model (VM), it is assumed that a homogeneous reaction occurs.[10,14,15,32] It results in a linear decrease of the surface area with conversion during the reaction. In the RPM model, from a practical standpoint, while S_0 and ε_0 are accessible experimentally, L_0 cannot be measured.[14,15] ψ is a free parameter that is adjusted using experimental data. The value of ψ is related to the solid material and the formation condition.[26,37,38] Moreover, the modified random pore model (MRPM) is the improved pore structure model to simulate the evolution of the superficial area of carbon particles during CO_2 reaction. Different forms of MRPM have been proposed in the literature by introducing a new conversion term and a time function with two or three dimensionless parameters into the original random pore model.[14,39−42] We used the equation, which is proposed by Gómez-Barea and Ollero[14] in which the new conversion term and time function have a linear relation with time. It simplifies the equations and lets us find the analytical solution with reasonable results. The influencing factors, such as pore characteristics and the superficial area of porous particles during gasification are taken into account.[39,43,44] t in MRPM represents the gasification time, and ψ and, ω are the structural parameter and the power-law constant, respectively. ω is the power-law constant that can be positive or negative that shows the effects of time on ks that is defined by $[1+(\omega+1)(\alpha t)]$. The negative value of ω means that the reaction rate is constant. The higher value of ω (>5) shows the higher impact of time on the reaction rate. In this case, MRPM can deliver reliable results comparing to RPM. α is a discreteness parameter. When α goes to zero, the results of RPM and MRPM are the same. The parameter α is related to the structural parameters of particles such as initial porosity and specific surface area. With an increase in α, the value of the surface area is reduced.

Several equations were applied to obtain the effective diffusion coefficient, which depends on both porosity and tortuosity (eq 22). Comiti and co-workers[16,46,47] defined the tortuosity of spheres based on the theoretical tortuosity−porosity relations. Their equations are used by numerous researchers, especially for porous carbon materials.[48,49] Akkani et al. investigated different practical equations to calculate the tortuosity value, and their results showed that the effective diffusion could be related to the particle size, shrinkage, and the pore size of the particle.[49] In this work, we applied various tortuosity equations proposed in the literature to obtain the one best representing the anode particle behavior. To do so, the model was run using different models, and the simulated results were compared to the experimental gasification tests. The experiments were carried out at different particle sizes of 0.05, 1, and 3 mm to cover the diffusion effect from low to high, respectively. The results, summarized in Table 2, reveal

Table 2. Summarized Model Results for Different Tortuosity Equations for Three Anode Particle Sizes[49,50]

theoretical tortuosity−porosity relations	error			
	R = 0.05 mm	R = 1 mm	R = 3 mm	remarks
$\tau = (3-\varepsilon)/2$	0.04	0.01	0.05	packing[49]
$\tau = 0.8(1-\varepsilon)+1$	0.08	0.03	0.07	laboratory contaminant diffusion[50]
$\tau = \varepsilon^{-1/2}$	0.07	0.20	0.06	spherical particle[50]
$\tau = 1-0.5\ln\varepsilon$	0.09	0.03	0.11	sand-spherical particle[49]
$\tau = \varepsilon^{-2}$	0.04	0.03	0.05	overlapping spheres[49]

that using the tortuosity expression in the first row is the most suitable one for anode particles ranging between 0.05 and 3 mm for which the fitted tortuosity led to the least error among all the tested tortuosity models.

3.2. Particle Shrinkage. Understanding the structural features of anode particles and their evolution during gasification provides useful information for the development of gasification-based systems. During the gasification process, the anode particle starts to shrink, and the apparent radius of the anode particle (r_{ap}) decreases gradually. In this step, the outer layer of the solid is fragmented.[32] In the developed model, the fragmentation occurs when 100% of an imaginary external layer is consumed. This imaginary external layer may have a finite thickness, which could be defined depending on the resolution of the calculations. In our model, the apparent radius is kept unchanged until the conversion at the outer surface layer reaches 100%. On the other hand, at this step, the

https://doi.org/10.1021/acsomega.0c05297
ACS Omega 2021, 6, 8002−8015

thin outer layer of particle reaches to a conversion of $X(r_{sp}) = 1$. After consuming the outer layer, a new updated outer layer is defined, and the radius of the particle is now smaller by the thickness of the removed outer layer.[32] According to this description, the change in the anode particle radius during the process can mathematically be represented employing a moving boundary condition as follows:

$$\frac{\partial r_{sp}}{\partial t} = \begin{cases} 0 & X(r_{sp})_{\text{outer layer}} < 1 \\ \frac{\partial X|_{\partial t}}{\partial X|_{\partial r}} & X(r_{sp})_{\text{outer layer}} = 1 \end{cases} \quad (34)$$

When 100% of an imaginary external layer is consumed, the start point shrinkage conversion (X_{sh}) will be obtained by solving the second condition term of eq 34. The schematic of gasification inside an anode particle is illustrated in Figure 1. At

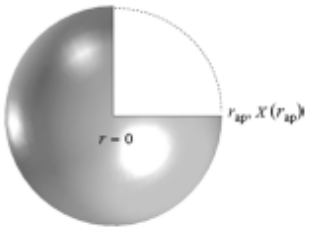

Figure 1. Schematic of the gasification process for a single particle.

the center of the particle, the apparent radius equals 0, and at the outer layer of the particle, the apparent radius and related anode conversion equal r_{sp} and $X(r_{sp})$, respectively.

3.3. Numerical Method. In the developed model, the anode conversion (X) is the target variable to be computed. In this model, after reaching a critical carbon conversion rate, the apparent radius of the anode particle decreases until it eventually leads to particle vanishment (depending on the ash content of the particle, complete disappearance of this latter may not occur experimentally). Thus, it is essential to consider the moving boundary method for solving the proposed model. The model includes certain nonlinear partial differential equations (PDEs), which are also time-dependent equations. Since the numerical method of lines is a proper technique for solving the time-dependent partial differential equations, the sets of PDEs of this model can be solved using this method.[51] In the method of lines, all the derivatives are substituted by the finite difference method, but the time derivatives remain with no change. It is assumed that the variables C and X are related to (z_i, τ_j) but are independent on (z_{i-1}, τ_j) or (z_i, τ_{j-1}). Here, i and j indicate the indices of a computational grid node; index i defines the position and j the time instant. The grid number in the r direction equals 10,000 for a particle with a 1 mm radius. The model is an explicit time step of a finite difference algorithm in which the time step is automatically defined, and it is compatible with the ODE solver. Therefore, PDEs are converted into a system of ODEs. This package is written in MATLAB software in three-layers of calculations. All the input data are imported to the first layer; an appropriate model is defined; at the end of calculations, the results are returned to this layer. The second layer is a transporter layer in which all the required data are transported to the solver of the model. Besides, the results of the modeling are reflected from the calculation core to the upper layer by this part. The third layer (calculation core) is the ODE solver. In this package, the ODE solver consists of ODE23tb that accurately calculates rigid systems using raw error tolerances. This solver is an implicit Runge–Kutta method. All unknown variables must be solved simultaneously in one system of ODEs. The model outputs are the carbon conversion (X) versus time. The model constants can be calculated using the experimental results.

Originally, X is a local value, but to compare it with the experimental value, X must be averaged over the particle volume at each time instant as follows:

$$X_{\text{ave}}(t) = \frac{3}{r_0^3} \int_0^{r_0} X(r, t)\, r^2\, dr \quad (35)$$

We defined eq 36 as a cost function for identification of the model constants, including the chemical reaction rate constant and adjustable parameters in the function of $F(X)$ such as ψ for RPM, w and α for MRPM, and n for the TM equation.

$$\min f = \sum_{j=1}^{H} (X_{\text{ave},j}(t) - X_{\text{exp},j}(t))^2 \quad (36)$$

where H is the number of experimental time points.

4. RESULTS AND DISCUSSION

Figure 2 shows the conversion of the anode particle as a function of time both in terms of model predictions and the

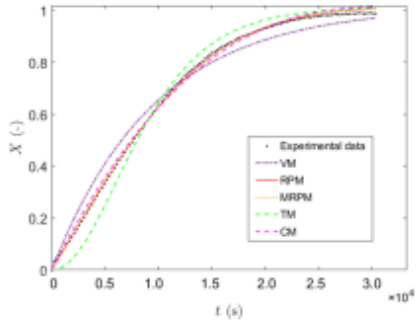

Figure 2. Anode particle conversion versus time using different kinetic models (experimental data comes from the gasification of the carbon particles with the size of 1 mm, T = 1233 K).

experimentally determined one. Particles with an average size of 1 mm were used to generate experimental data, and the spherical particles of diameter 1 mm were used for simulation. In the model, we integrated different structural kinetic models presented in Table 2 to verify their suitability for the gasification of anode particles. The results exhibited good agreement between experiments and three models (RPM, MRPM, CM). The errors between experimental and simulated results are presented in Table 3. As the RPM model showed the reasonable outcome with the low error and number of parameters; thus, we used hereafter the RPM model to simulate the gasification of anode particles under varying conditions.

Figure 3 demonstrates the time required for full consumption of the particles with different sizes as a function of

https://doi.org/10.1021/acsomega.0c05297
ACS Omega 2021, 6, 8002−8015

Table 3. Model Parameters for Various Structural Kinetic Models, where $r(C)$ Is the First-Order Equation

reaction model	model parameters	MSE
VM	$k = 1.7064\ (s^{-1})$	1.7×10^{-3}
CM	$k = 3.5873\ (s^{-1})$	2.4×10^{-4}
RPM	$k = 1.0935\ (s^{-1})$, $\varphi = 2.7687$	5.60×10^{-5}
MRPM	$k = 0.3959\ (s^{-1})$, $\varphi = 2.9811$, $\omega = -1.0076\ (s^{-1})$, $\alpha = 0.0031$	5.59×10^{-5}
TM	$k = 1.3178\ (s^{-1})$, $n = 1.1790$	6.6×10^{-3}

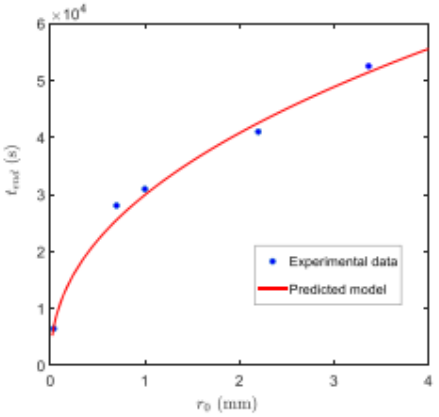

Figure 3. Time for full consumption versus initial particle radius (T = 1233 K).

their initial radius. The results revealed that a good agreement exists between predicted (continuous red line) and measured (solid circles) data. As expected, the smaller particles are consumed faster due to both a higher specific external area and smaller quantity of material to be consumed.

Figure 4 shows the simulated plots of anode particle conversion versus time for different particle sizes. The experimental data points for the particle size of 1 mm were also presented for comparison. Figure 4 reveal that the model validated by one set of experiment data (particle size = 1 mm) and other particle sizes were obtained by model prediction not

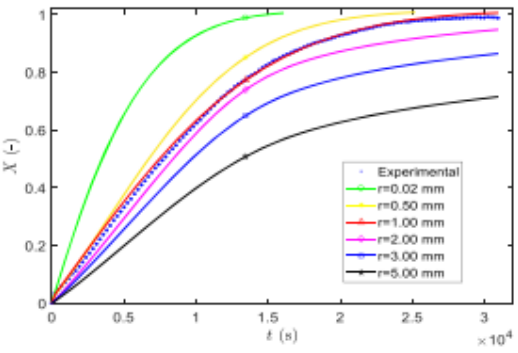

Figure 4. Conversion versus time for different particle sizes of the anode particle (experimental data for the particle size 1 mm, T = 1233 K).

just validation and data fitting. The results suggest that the particle size significantly affects the reaction rate of the particle gasification (as reflected by the slope of the curves). As the particle size decreases, the reaction rate increases, and full consumption is reached in a shorter time. Particles with a radius larger than 1 mm did not achieve total consumption after 10 h of reaction. This could be attributed to the larger external surface area of the fine particles compared to that of the coarser ones. This also indicates the diffusion-inhibited reaction rate for the coarser particles,[23] the same as the observations reported by Gómez-Barea and Ollero.[14] As expected, the conversion rate holds a direct relationship with the reaction time but an inverse relationship with the particle size.

The CO_2 mole fraction inside a reacting particle, predicted by the model during the gasification time, is shown in Figure 5 for eqs 5 and 6 solved for the central position (r = 0) of the anode particle for different particle sizes. Initially, CO_2 reactive gas is introduced into the pores. Therefore, the CO_2 mole fraction is near one within the pores and at the surface of the particles (Figure 5a). When the reactions start, CO_2 is consumed and CO is generated, resulting in a gradual increase of CO concentration at the expense of that of CO_2. The graph (Figure 4b) shows that the CO_2 concentration at the center of the particle decreases first to reach a minimum at ($t = 1 \times 10^4$ s), and then it increases gradually until the particle is fully consumed. This peak of CO_2 is attributed to the quick consumption of active carbon at the beginning of the reaction. In fact, not all carbon sites have the same activity with respect to CO_2, and some of them are more reactive, as reported earlier.[35] In these areas, carbon is consumed quickly when they come in contact with CO_2. Therefore, in the beginning (Figure 5a), the rate of reaction is high due to the presence of active carbon sites, resulting in a quick depletion of CO_2 concentration over the first 25 s. Then, the rate of CO_2 reaction with carbon decreases as the active sites are consumed. At the same time, the presence of CO results also in a decrease of CO_2 reaction with carbon. These two phenomena result in a balance between the consumption rate of CO_2 and its diffusion rate from the surface at around $t = 1 \times 10^4$ s. By progressing the reaction, the porosity of the particle increases, so is its permeability, leading to the increase of the CO_2 diffusion from the surface and its mole fraction at the center of the particle. The reaction rate with CO_2 for all particle sizes follows the same trends. Another observation is that the CO_2 fraction at the center of large particles is always smaller than that of the fine particles, mainly due to higher diffusion distance.

4.1. Structural Evolution of Anode Particle during Gasification. Figure 6 is demonstrating RPM predictions of carbon consumption as a function of time for particles with a radius of 1 mm for different initial porosity. The rate of solid consumption (slope of curves in Figure 6) in the first stage of the reaction is steep, and then it reduces gradually at a later stage. The monotonic reduction of reaction rate is presumably ascribed to the lesser amount of residual solid to react as reaction progresses. Therefore, the porous samples will vanish in a shorter process time. The difference between slopes increases by increasing the porosity. As expected, for the samples with higher porosity ($\varepsilon \geq 0.5$ and more), the slope of the curves at the first stage is steeper since the diffusion rate is higher at high porosity levels and conversely, for the sample

https://doi.org/10.1021/acsomega.0c05297
ACS Omega 2021, 6, 8002−8015

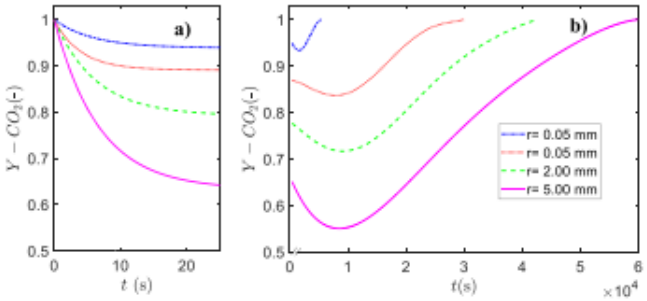

Figure 5. Mole fractions of CO_2 inside the reacting anode particle (at $r = 0$) versus time for various initial particle sizes and $T = 1233$ K and different time scales: (a) the first 25 s and (b) the rest of the process time.

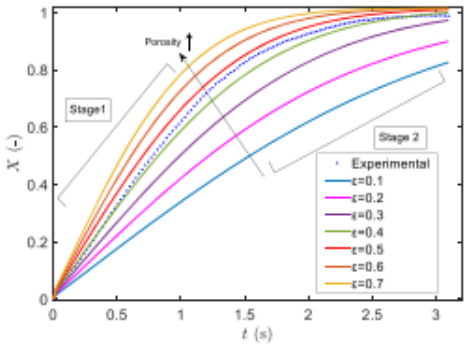

Figure 6. Effects of initial porosity on the conversion of carbon versus time; initial particle radius is 1 mm, $T = 1233$ K.

with lower porosity ($\varepsilon \leq 0.2$ and less), the difference between two stages is not significant.

Experimentally, Figure 7 shows the pore volume distributions measured by mercury intrusion (Auto Pore IV, Micromeritics, Norcross, GA, USA) as a function of the pore size for anode particles gasified under CO_2 at 1233 K and at gasification levels of 0, and 50 wt % for two particle sizes (1 mm and 2 mm). As can be seen in Figure 7 the pore interval (0.1−40 μm) has the largest pore volume for both particle sizes, and these pore sizes increase strongly with the increase in the percentage of gasification. A broader peak for the pore size range larger than approximately 80 μm is observed that is associated with the voids between the particles.

Over the gasification process, the model includes both effects of transport of gaseous species and intrinsic reaction rates. Due to the diffusion resistance, it is expected that the reaction on the particle surface be faster than that inside the particle. This description conforms to simulation outcomes for the anode particle gasification at 1233 K, as shown in Figure 8. This figure presents the consumption of carbon (mole fraction) as a function of time at three different locations of the particles: at the external layer, at the middle radial position, and at the center of the particle. As Figure 8a,b shows, the anode particle on the external surface layer will be consumed faster than on other positions within the anode particle. This difference is getting larger when the size of the particle increases. The shorter consumption time at the surface confirms the particle shrinkage over the gasification process.

Figure 9a shows the change of the relative particle radius (r/r_0) as a function of reaction time. It can be seen that the relative radius of all samples remains unchanged within the first 1×10^4 s of reaction. After this period, the particles start to shrink. According to Figure 4, this reaction time corresponds to almost full consumption of small particles ($r = 0.05$ mm) and 33% of consumption for the largest particles ($r = 5$ mm). It is interesting to see which fraction of a particle is consumed when it starts to shrink. Thus, we plotted the shrinkage conversion, corresponding to the conversion of the particle at a shrinkage starting point (X_{sh}) as a function of particle radius (Figure 9b). We can see that X_{sh} decreases sharply with increasing particle size. In other words, as the particle radius increases, inception of shrinkage occurs at the smaller conversions, X_{sh}, e.g., 45, 33, 25, 18, and 12% for $r_0 = 1$, 2, 3, and 5 mm, respectively.

4.2. Modified Thiele Module and Effectiveness Factor. The modified Thiele modulus, λ, describes the relationship between diffusion and the reaction rate in porous particles with no mass transfer limitations[34] (eq 24). The effectiveness factor, η, is a measure indicating that the diffusion resistance neutralizes the intrinsic reaction rate (eq 26). An effectiveness factor approaching unity indicates that the reaction controls the process. The results of the kinetic model show that, depending on particle size and the mass conversion of the anode, the intrinsic reaction and diffusion can be significant parameters in determining the overall gasification process. Achieved by RPM expression at multiple carbon conversions, the effectiveness factors, η, and modified Thiele module, λ, are shown in Table 4 for both first-order and L−H kinetic models. By increasing the particle size, the modified Thiele modulus increases whereas the effectiveness factor decreases. It means that, as expected, the diffusion resistance increases with the particle size, resulting in a reduction in the effectiveness factor.[23]

For all samples, the effectiveness factor increases by conversion, approaching 1 at 80% of conversion. When the carbon conversion does not exceed 60%, the results reveal that both reaction and diffusion control the reaction. By further increasing in the anode conversion, the reaction becomes more dominant due to the particle shrinkage during the gasification process.

For small particles ($r = 0.035$ mm) the low values of the modified Thiele modulus (<2) demonstrate that reactant is homogeneous distributed inside of the anode, and therefore, the diffusion resistance is negligible. Inversely, for the larger particles (2.2 mm), especially for the initial conversion, high

https://doi.org/10.1021/acsomega.0c05297
ACS Omega 2021, 6, 8002−8015

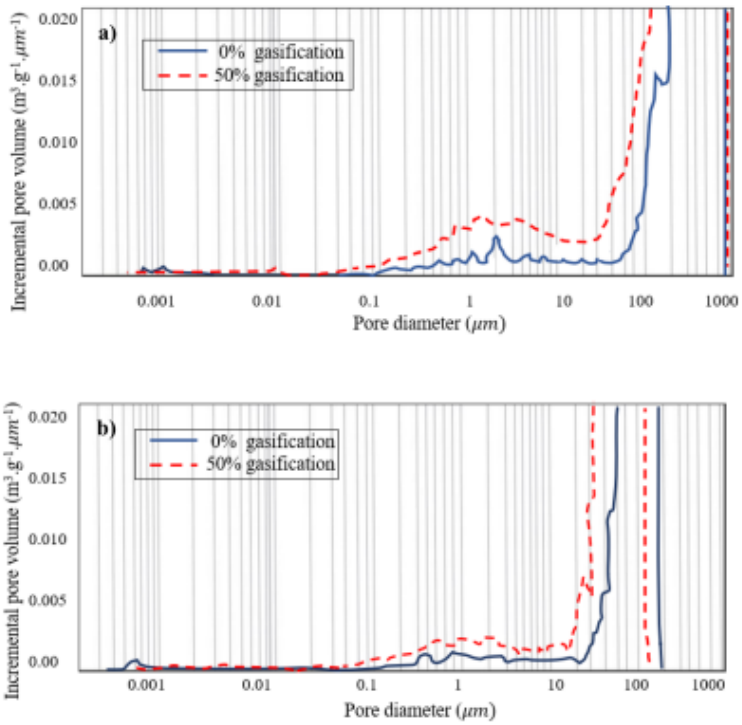

Figure 7. Pore volume distribution versus the pore size for anode particles gasified in two particle sizes: (a) 1 mm and (b) 2 mm, gasified at two percentages (0 and 50%) under CO_2 at T = 1233 K by intrusion of mercury.

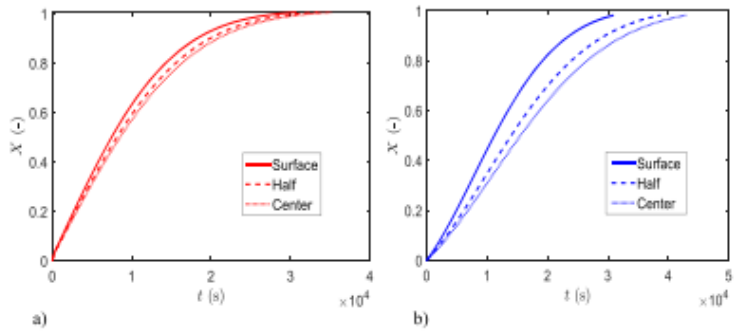

Figure 8. Mole fraction of the consumption anode particle during process time for three positions (surface, middle, and center of the particle). Initial particle size (a) r_0 = 1 mm and (b) r_0 = 2 mm.

values of the modified Thiele modulus (>3) confirm that the diffusion significantly resists against the gasification for large particles. By starting the gasification process and anode particle conversion, the modified Thiele modulus decreases and approached one at 80% of conversion. Because at the early stages, the reactant gas cannot easily penetrate inside the particle and the diffusion is dominant for larger particles.[11]

4.3. Specific Surface Area. The model allows capturing the evolution of the specific surface area during the gasification process. Figure 10a shows the evolution of the surface area versus the gasification conversion for four different particle sizes. For ease of comparison in a single graph, we used the relative specific surface area, obtained by dividing the actual specific surface area of the sample (S) into its initial specific surface area (S_0) to make a dimensionless parameter for the specific surface area. It can be seen that the specific surface area increases at the early stages of the gasification, reaching a maximum, and then declining until vanishing. By computing the derivative of the curves and plotting it against the gasification conversion (X), the maximum of the curves can be better visualized. These maxima can be seen in Figure 10b, where the curves cross the zero line. We can see that the maximum specific surface area for the smallest sample (r = 0.05 mm) occurs after 25% of gasification. By increasing the particle

https://doi.org/10.1021/acsomega.0c05297
ACS Omega 2021, 6, 8002−8015

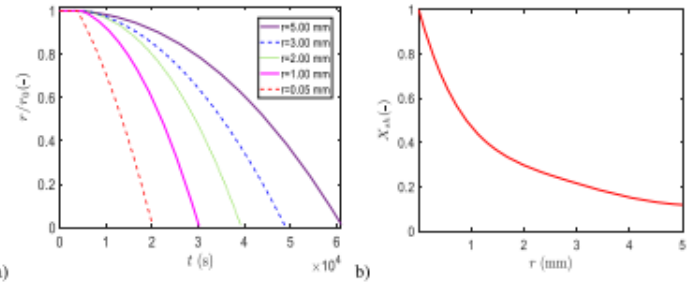

Figure 9. (a) Relative radius (r/r_0) versus processing time for different anode particle radii. (b) X_{s1} versus initial particle radius.

Table 4. Modified Thiele Moduli and Effectiveness Factor for Different Particle Sizes and Carbon Conversions

			carbon conversion %				
radius (mm)	reaction rate	definition	0	20	40	60	80
0.035	first order	effectiveness factor	0.81	0.85	0.89	0.94	0.98
		modified Thieles	1.89	1.75	1.41	1.11	0.40
	L–H	effectiveness factor	0.75	0.79	0.86	0.93	0.97
		modified Thieles	1.94	1.82	1.45	1.15	0.43
0.7	first order	effectiveness factor	0.49	0.64	0.79	0.88	0.94
		modified Thieles	4.98	3.22	2.37	1.50	1.01
	L–H	effectiveness factor	0.44	0.60	0.75	0.86	0.93
		modified Thieles	5.41	3.41	2.56	1.59	1.06
1.0	first order	effectiveness factor	0.45	0.63	0.77	0.87	0.93
		modified Thieles	5.47	3.25	2.46	1.54	1.04
	L–H	effectiveness factor	0.38	0.57	0.71	0.81	0.90
		modified Thieles	5.74	3.45	2.57	1.67	1.18
2.2	first order	effectiveness factor	0.43	0.59	0.74	0.86	0.92
		modified Thieles	5.71	4.80	2.5	1.68	1.07
	L–H	effectiveness factor	0.36	0.53	0.68	0.81	0.89
		modified Thieles	6.19	5.06	2.81	1.79	1.16

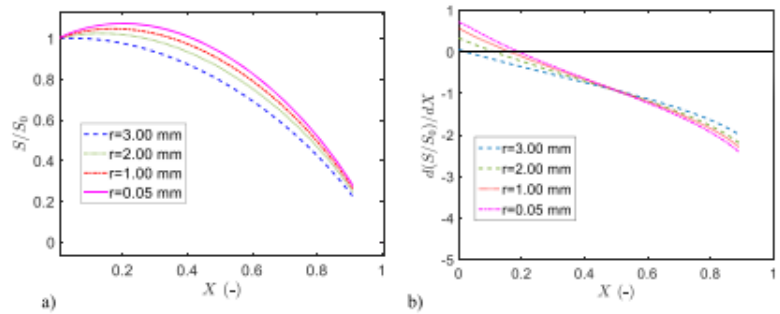

Figure 10. (a) Prediction of the surface area of the particle during the gasification. (b) Differentiation of surface area versus carbon conversion (T = 1233 K, r = 3.0, 2, 1.0, and 0.05 mm).

size, the maximum is shifted toward lower gasification levels. For instance, this maximum occurs at 4% gasification for the largest sample (r = 3 mm). In other words, the conversion at which the maximum surface area occurs depends on the particle size and it decreases drastically by increasing the particle size. For all particle sizes, the specific surface area increases at the early stage of conversion. This is attributed to pore enlargement. However, with the progress of gasification, the overlapping of the multiple capillaries[22] and the coalescence of neighboring pores[26,52] take place (mostly through disappearing inter-walls), thus decreasing the specific surface area. For the small particles, there is not a big difference between the reaction rates at the internal and external layers (Figure 8a); however, this difference becomes significant as the particle size increases (Figure 8b). The delay of the reaction in the internal layers mitigates the increase of the specific surface area. That is, when the internal layer reaches its maximum specific surface area, the surface area of the external layers is already in a declining phase. Therefore, the maximum is barely seen for the largest particle.

https://doi.org/10.1021/acsomega.0c05297
ACS Omega 2021, 6, 8002−8015

4.4. Inhibition Effect of CO in Anode Gasification. The presence of CO in the internal anode pores can play an inhibition role on the carbon gasification reaction, which could explain the lower observed reaction rate compared to the expected one. To describe these observations, the inhibition effect caused by CO should be modeled by a reasonable kinetic expression to understand its effect. A Langmuir−Hinshelwood model can adequately separate the inhibition effect of CO (chemical limitation) from purely diffusional effects (physical limitation). It is believed that adsorption of CO_2 on the surface of the anode followed by desorption of CO are the main steps determining the gasification rate (eqs 28−30). Adsorption of CO on the carbon sites may decrease the rate of adsorption of CO_2 by occupying the active sites, thus inhibiting the reaction rate. To assess this effect, we ran the reaction with three different CO concentrations in the inlet gas. Figure 11 shows

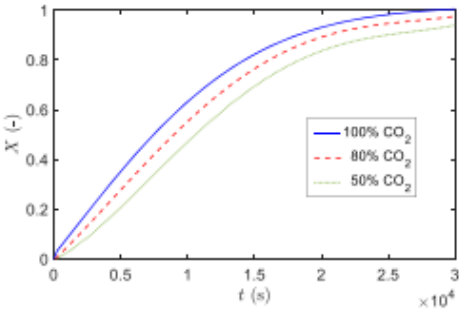

Figure 11. Anode particle conversion versus process time at different ratios of the partial pressure of CO_2 and CO in the inlet gas (T = 1233 K, r_0 = 1.0 mm).

the conversion in mole fraction at the center of a particle (r = 1 mm) as a function of time for three different inlet gas compositions. Table 5 shows the experimental data and the corresponding values obtained from the model for the parameters of k_1, k_2, and k_3 (L−H equation), for different values of initial P_{CO}, as well as their temperature dependence by means of its Arrhenius coefficients. The results show good agreement between calculated data and experimental data for k_1 and k_3, but there is a high level of uncertainty and discrepancy for k_2, particularly at the start and the end partial pressure ratio ranges (P_{CO}/P_{CO_2} = 0 and 1). These values confirm the stronger CO inhibition effect in the anode-CO_2 gasification in comparison with that obtained with pure CO_2 in the inlet gas. As a result of this mechanism, any increase in the CO amount at the inlet gas causes a decrease in the conversion of anode particles during the gasification process.

Figure 12 shows the rate of gasification reaction as a function of time for three different gas compositions in the

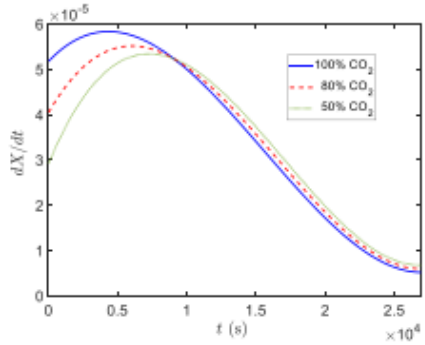

Figure 12. Simulation of the anode particle gasification rate at different ratios of the partial pressure of CO_2 and CO in the inlet gas (T = 1233 K, r_0 = 1.0 mm).

inlet gas. It can be seen that the rate of reaction at the beginning of the reaction is much smaller for higher CO concentrations. As discussed above, all reactions reach a maximum rate after a while, which is due to the fast reaction of the more active carbon sites. However, this maximum occurs earlier for pure CO_2. The inhibition effect of CO delays the occurrence of this maximum and decreases the maximum value of the reaction rate. After about 1×10^4 s, it seems that the reaction rate for the samples with pure CO_2 becomes smaller than those with CO in the inlet gas. This is basically due to the lower amount of remaining solid carbon in the former case at the same reaction time. For instance, at $t = 1 \times 10^4$ s 60% of the sample is consumed under pure CO_2, while only 42% is consumed under 50% CO_2.

According to the L−H mechanism, it is possible to use the values of activation energies (E_1, E_2, and E_3) respectively corresponding to k_1, k_2, and k_3 to illustrate how the various activation energies are involved in the C−CO_2 reaction. The amount of activation energy was calculated by the Arrhenius type of temperature dependence (eq 33) for each L−H mechanism step. The activation energies of 59, 17, and 187 kJ·

Table 5. Reaction-Rate Parameters k of the L−H Model for Anode-CO_2 Gasification in Different Temperatures and CO Concentrations in the Inlet Gas

		model results				experiment result		
		k_1	$k_2 \times 10^5$	$k_3 \times 10^5$		k_1	$k_2 \times 10^5$	$k_3 \times 10^5$
temperature (K)	$\frac{P_{CO}}{P_{CO_2}}$	(g·cm^{-2}·atm^{-1}·s^{-1})	(atm^{-1}·s^{-1})	(atm^{-1}·s^{-1})	R^2	(g·cm^{-2}·atm^{-1}·s^{-1})	(atm^{-1}·s^{-1})	(atm^{-1}·s^{-1})
1233	0.00	100.6	105	66	96.8	101.5	101	66
1233	0.25	96.6	101	64	98.6	97.9	101	65
1233	0.50	95.3	102	63	99.4	95.8	102	64
1233	0.75	91.2	102	64	98.8	90.8	102	63
1233	1.00	84.9	97	63	96.5	84.4	103	62
1193	1.00	82.8	94	62	97.9	85.0	95	63
1273	1.00	86.7	98	64	98.4	85.7	99	64

https://doi.org/10.1021/acsomega.0c05297
ACS Omega 2021, 6, 8002−8015

mol^{-1}, were obtained for three steps of the reaction, respectively. Higher partial pressure of carbon monoxide leads to a decreasing gasification rate, which is reflected by the k_3 reaction rate constant of L−H eq 31.[9−11,25,53] Results are in accordance with those obtained in most studies and showing that the activation energy of step 3 (E_3) is higher than that of step 1 (E_1). This means that the third step (eq 30) is the limiting step of the reaction rate.[54]

5. CONCLUSIONS

A diffusion−reaction model was developed for the gasification reaction of aluminum-industry anode particles, involving different kinetic models. The model assumed spherical symmetry and included the most notable chemical reactions, e.g., Boudouard reaction, intra-particle mass transfer resistance, mass conservation and anode structural characteristics such as porosity, permeability and shrinkage. The heat transfer was not included since the size of the anode particles was small enough to assume insignificant temperature gradient across the particle. A numerical method was used to solve the model. Model parameters were obtained experimentally by reacting monolayer anode particles in TGA. According to the experimental and simulated results, we concluded that the random pore model (RPM) is best describing the anode reaction behavior. Thus, this model was chosen among 5 models tested in this study.

The model outputs allow tracking the particle consumption rate and the distribution of gas composition inside the reacting particle. In addition, due to the moving boundary condition for the external gasification, it is also possible to track the shrinkage and structural evolution of the particle during the gasification process. These data, mostly impossible to obtain experimentally, allow better interpretation of the reaction behavior. As such, the evolution of different parameters such as particle size, processing time, porosity, and surface area of the anode particles during gasification are revealed and their effect on the gasification process are discussed. The simulation results demonstrated that the anode structure (specific surface area and porosity) has a significant effect on both the intrinsic reaction rate and the intra-particle mass transport. The relative importance of intrinsic reaction and diffusion on the overall gasification process are quantified by calculating the Thieles modulus and effectiveness factor. Analyzing these factors reveals that their contribution on gasification rate may evolve at different stages of reaction, i.e., diffusion is more important at the beginning and chemical reaction becomes dominant towards the end of gasification. The L−H type reaction, integrated in the model, allowed revealing the inhibition effect CO on the gasification reaction. Although the inhibition effect of CO on carbon gasification is a well-known feature, our model allows quantifying this effect along the whole gasification process. The effect of three different concentrations of CO in the inlet gas were given as examples. In summary, the model predicts well the gasification rate of anode particles, considering structural and diffusion parameters, thus offering a useful tool for optimization of gasification of anode particles.

AUTHOR INFORMATION

Corresponding Author

Houshang Alamdari − *Aluminum Research Centre REGAL, Université Laval, Québec G1V 0A6, Canada*; orcid.org/0000-0003-3045-2182; Email: houshang.alamdari@gmn.ulaval.ca

Authors

Mohammad Kavand − *Aluminum Research Centre REGAL, Université Laval, Québec G1V 0A6, Canada*

Roozbeh Mollaabbasi − *Aluminum Research Centre REGAL, Université Laval, Québec G1V 0A6, Canada*; orcid.org/0000-0002-9587-6157

Donald Ziegler − *Alcoa corporation, Alcoa Technical Centre, New Kensington, Pennsylvania 15068, United States*

Faïçal Larachi − *Department of Chemical Engineering, Université Laval, Québec G1V 0A6, Canada*; orcid.org/0000-0002-0127-4738

Donald Picard − *Aluminum Research Centre REGAL, Université Laval, Québec G1V 0A6, Canada*; orcid.org/0000-0003-1492-870X

Complete contact information is available at: https://pubs.acs.org/10.1021/acsomega.0c05297

Notes

The authors declare no competing financial interest.

ACKNOWLEDGMENTS

The authors would like to acknowledge the financial support of the Natural Sciences and Engineering Research Council of Canada, Fonds de Recherche du Québec−Nature et Technologies, Alcoa Canada Inc. and the Aluminium Research Centre−REGAL. The authors would like to express their appreciation to Mr. Guillaume Gauvin and Hugues Ferland for their technical support.

NOMENCLATURE

Latin symbols

a	stoichiometric coefficient, (−)
b	stoichiometric coefficient, (−)
C_C	concentration of anode reactant, (mol·m^{-3})
C	concentration of gaseous species, (mol·m^{-3})
C(O)	surface concentration of carbon−oxygen complex, (mol·m^{-2})
D	diffusion coefficient, (m^2·s^{-1})
D_e	effective diffusion coefficient, (m^2·s^{-1})
k	reaction rate constant, (mol · m^{-3})$^{\langle\langle 1-n\rangle\rangle-1}$
k_0	pre-exponential factor, (bar^n·s^{-1})
L_0	pore length, (m·kg^{-1})
H	number of experimental data, (−)
M	molecular weights, (kg·mol^{-1})
m	mass of anode particle, (kg)
n	partial reaction order, (−)
P	pressure, (kg·m^{-2}·s^{-2})
r	particle radius, (m)
R	chemical reaction rate, (mol·s^{-1}·m^{-3})
R_m	gas constant (kJ·mol^{-1}·K^{-1})
S	specific surface area, (m^{-1})
t	reaction time, (s)
T	temperature, (K)
V	pore volume (m^3·kg^{-1})
X	gasification conversion of anode particle, (−)

Greek symbols

α	modified random pore model constant, (s^{-1})
ε	void fraction, (−)
φ	Thiele module, (−)
η	effectiveness factor, (−)
λ	modified Thiele module, (−)
ρ	density, (kg·m^{-3})

σ Lennard-Jones collision diameter, (m)
Ω_D collision integral for molecular diffusion, (−)
τ tortuosity, (−)
ω power-law constant, (−)
ψ structural parameter, (−)

Subscripts

abs absolute
ap apparent
ave average
C carbon
CO carbon monoxide
CO_2 carbon dioxide
diss dissolved
f active carbon site
g gas phase
I gas species
J gas species
m molten
s solid phase
sh shrinkage start point
t instantaneous
0 initial

REFERENCES

(1) Azari, K. Investigation of the materials and paste relationships to improve forming process and anode quality. Ph.D. dissertation, Laval University, Canada, 2013.
(2) Chevarin, F.; Azari, K.; Lemieux, L.; Ziegler, D.; Fafard, M.; Alamdari, H. Active pore sizes during the CO_2 gasification of carbon anode at 960°C. *Fuel* **2016**, *178*, 93−102.
(3) Tabatabaee Ghomshe, S. M.; Aminzadeh, R.; Abarzani, M. Use of response surface methodology to study the combined effect of various parameters on hexavalent chromium adsorption. *Chem. Eng. Commun.* **2014**, *201*, 191−208.
(4) Azari, K.; Alamdari, H.; Aryanpour, G.; Ziegler, D.; Picard, D.; Fafard, M. Compaction properties of carbon materials used for prebaked anodes in aluminum production plants. *Powder Technol.* **2013**, *246*, 650−657.
(5) Azari, K.; Alamdari, H.; Ziegler, D.; Fafard, M. Influence of coke particle characteristics on the compaction properties of carbon paste material. *Powder Technol.* **2014**, *257*, 132−140.
(6) Keller, F.; Mannweiler, U.; Knall, E. Anode for the aluminum industry. *Constructing and Operating Anode Plants: What Top Management Needs to Know*; R & D Carbon Ltd.: Sierre, Switzerland 1995, pp. 217−224.
(7) Jamshidi, E.; Ale Ebrahim, H. An incremental analytical solution for gas-solid reactions, application to the grain model. *Chem. Eng. Sci.* **1996**, *51*, 4253−4257.
(8) Liu, G. S.; Tate, A. G.; Rezaei, H. R.; Beath, A. C.; Wall, T. F. Modeling of Infra-Particle C-CO_2 Reaction: An Application of the Random Pore Model. *Dev. Chem. Eng. Miner. Process.* **1999**, *7*, 525−536.
(9) Kajitani, S.; Suzuki, N.; Ashizawa, M.; Hara, S. CO_2 gasification rate analysis of coal char in entrained flow coal gasifier. *Fuel* **2006**, *85*, 163−169.
(10) Mandapati, R. N.; Daggupati, S.; Mahajani, S. M.; Aghalayam, P.; Sapru, R. K.; Sharma, R. K.; Ganesh, A. Experiments and Kinetic Modeling for CO_2 Gasification of Indian Coal Chars in the Context of Underground Coal Gasification. *Ind. Eng. Chem. Res.* **2012**, *51*, 15041−15052.
(11) Mani, T.; Mahinpey, N.; Murugan, P. Reaction kinetics and mass transfer studies of biomass char gasification with CO_2. *Chem. Eng. Sci.* **2011**, *66*, 36−41.
(12) Chevarin, F.; Lemieux, L.; Picard, D.; Ziegler, D.; Fafard, M.; Alamdari, H. Characterization of carbon anode constituents under CO_2 gasification: A try to understand the dusting phenomenon. *Fuel* **2015**, *156*, 198−210.
(13) Kovacik, G.; Chambers, A.; Özüm, B. CO_2 gasification kinetics of two Alberta coal chars. *Can. J. Chem. Eng.* **1991**, *69*, 811−815.
(14) Gómez-Barea, A.; Ollero, P. An approximate method for solving gas−solid non-catalytic reactions. *Chem. Eng. Sci.* **2006**, *61*, 3725−3735.
(15) Fei, H.; Hu, S.; Shi, F.; Li, Y.; Jiang, D.; Xiang, J. A New Mathematical Model Study on CO_2 Gasification Reaction of Typical Agricultural Residues. *Ind. Eng. Chem. Res.* **2012**, *51*, 13619−13626.
(16) Comiti, J.; Renaud, M. A new model for determining mean structure parameters of fixed beds from pressure drop measurements: application to beds packed with parallelepipedal particles. *Chem. Eng. Sci.* **1989**, *44*, 1539−1545.
(17) Zhang, J.-L.; Wang, G.-W.; Shao, J.-G.; Zuo, H.-B. A Modified Random Pore Model for the Kinetics of Char Gasification. *BioResources* **2014**, *9*, 3497−3507.
(18) Zou, J. H.; Zhou, Z. J.; Wang, F. C.; Zhang, W.; Dai, Z. H.; Liu, H. F.; Yu, Z. H. Modeling reaction kinetics of petroleum coke gasification with CO_2. *Chem. Eng. Process.* **2007**, *46*, 630−636.
(19) Rafsanjani, H. H.; Jamshidi, E. Kinetic study and mathematical modeling of coal char activation. *Chem. Eng. J.* **2008**, *140*, 1−5.
(20) Wu, Y.; Wu, S.; Gao, J. A Study on the Applicability of Kinetic Models for Shenfu Coal Char Gasification with CO_2 at Elevated Temperatures. *Energies* **2009**, *2*, 545.
(21) Zhang, Y.; Hara, S.; Kajitani, S.; Ashizawa, M. Modeling of catalytic gasification kinetics of coal char and carbon. *Fuel* **2010**, *89*, 152−157.
(22) Tomaszewicz, M.; Łabojko, G.; Tomaszewicz, G.; Kotyczka-Morańska, M. The kinetics of CO_2 gasification of coal chars. *J. Therm. Anal. Calorim.* **2013**, *113*, 1327−1335.
(23) Huo, W.; Zhou, Z.; Wang, F.; Yu, G. Mechanism analysis and experimental verification of pore diffusion on coke and coal char gasification with CO_2. *Chem. Eng. J.* **2014**, *244*, 227−233.
(24) Prabhakar, A.; Sadhukhan, A. K.; Kamila, B.; Gupta, P. Modeling and Experimental Studies on CO_2 Gasification of Coarse Coal Char Particle. *Energy Fuels* **2017**, *31*, 2652−2662.
(25) Keller, F.; Küster, F.; Meyer, B. Determination of coal gasification kinetics from integral drop tube furnace experiments with steam and CO_2. *Fuel* **2018**, *218*, 425−438.
(26) Matsumoto, K.; Takeno, K.; Ichinose, T.; Ogi, T.; Nakanishi, M. Gasification reaction kinetics on biomass char obtained as a by-product of gasification in an entrained-flow gasifier with steam and oxygen at 900−1000°C. *Fuel* **2009**, *88*, 519−527.
(27) Reyes, S.; Jensen, K. F. Percolation concepts in modelling of gas-solid reactions—II. Application to char gasification in the diffusion regime. *Chem. Eng. Sci.* **1986**, *41*, 345−354.
(28) Jamshidi, E.; Ale Ebrahim, H. A new solution technique of moving boundary problems for gas-solid reactions; application to half-order volume reaction model. *Chem. Eng J. Biochem. Eng. J.* **1996**, *63*, 79−83.
(29) Jamshidi, E.; Ebrahim, H. A. A quantized solution for the nucleation model in gas-solid reactions. *Chem. Eng. J.* **1997**, *68*, 1−6.
(30) Everson, R. C.; Neomagus, H. W. J. P.; Kaitano, R. The random pore model with intraparticle diffusion for the description of combustion of char particles derived from mineral- and inertinite rich coal. *Fuel* **2011**, *90*, 2347−2352.
(31) Gómez-Barea, A.; Ollero, P.; Arjona, R. Reaction-diffusion model of TGA gasification experiments for estimating diffusional effects. *Fuel* **2005**, *84*, 1695−1704.
(32) Xu, Q.; Pang, S.; Levi, T. Reaction kinetics and producer gas compositions of steam gasification of coal and biomass blend chars, part 2: Mathematical modelling and model validation. *Chem. Eng. Sci.* **2011**, *66*, 2232−2240.
(33) Welty, J. R. *Fundamentals of momentum, heat, and mass transfer*. 5th ed.; Wiley: Hoboken, N.J. ; Chichester, 2008; p xiii, 711 p.
(34) Levenspiel, O. *Chemical reaction engineering*; 3rd ed.; Wiley: New York, 1999; p xvi, 668 p.

https://doi.org/10.1021/acsomega.0c05297

(35) Xu, Q.; Pang, S.; Levi, T. Reaction kinetics and producer gas compositions of steam gasification of coal and biomass blend chars, part 1: Experimental investigation. *Chem. Eng. Sci.* **2011**, *66*, 2141−2148.
(36) Ollero, P.; Serrera, A.; Arjona, R.; Alcantarilla, S. Diffusional effects in TGA gasification experiments for kinetic determination. *Fuel* **2002**, *81*, 1989−2000.
(37) Sadhukhan, A. K.; Gupta, P.; Saha, R. K. Characterization of porous structure of coal char from a single devolatilized coal particle: Coal combustion in a fluidized bed. *Fuel Process. Technol.* **2009**, *90*, 692−700.
(38) Ochoa, J.; Cassanello, M. C.; Bonelli, P. R.; Cukierman, A. L. CO_2 gasification of Argentinean coal chars: a kinetic characterization. *Fuel Process. Technol.* **2001**, *74*, 161−176.
(39) Zhang, Y.; Ashizawa, M.; Kajitani, S.; Miura, K. Proposal of a semi-empirical kinetic model to reconcile with gasification reactivity profiles of biomass chars. *Fuel* **2008**, *87*, 475−481.
(40) Bhatia, S. K.; Vartak, B. J. Reaction of microporous solids: The discrete random pore model. *Carbon* **1996**, *34*, 1383−1391.
(41) Struis, R. P. W. J.; von Scala, C.; Stucki, S.; Prins, R. Gasification reactivity of charcoal with CO_2. Part I: Conversion and structural phenomena. *Chem. Eng. Sci.* **2002**, *57*, 3581−3592.
(42) Betancur, M.; Natalia Arenas, C.; Daniel Martínez, J.; Victoria Navarro, M.; Murillo, R. CO_2 gasification of char derived from waste tire pyrolysis: Kinetic models comparison. *Fuel* **2020**, *273*, 117745.
(43) Fei, H.; Li, P.; Gu, Q. J.; Liu, Y. Modified Discrete Random Pore Model Considering Pore Structure Evolution to Depict Coal Chars Combustion in O_2/CO_2. *Energy Fuels* **2017**, *31*, 14280−14287.
(44) Cortazar, M.; Lopez, G.; Alvarez, J.; Arregi, A.; Amutio, M.; Bilbao, J.; Olazar, M. Experimental study and modeling of biomass char gasification kinetics in a novel thermogravimetric flow reactor. *Chem. Eng. J.* **2020**, *396*, 125200.
(45) Umemoto, S.; Kajitani, S.; Hara, S. Modeling of coal char gasification in coexistence of CO_2 and H_2O considering sharing of active sites. *Fuel* **2013**, *103*, 14−21.
(46) Seguin, D.; Montillet, A.; Brunjail, D.; Comiti, J. Liquid—solid mass transfer in packed beds of variously shaped particles at low Reynolds numbers: experiments and model. *Chem. Eng. J. Biochem. Eng. J.* **1996**, *63*, 1−9.
(47) Miller, P. A.; Clesceri, N. L. *Waste sites as biological reactors: characterization and modeling*; CRC Press: Boca Raton, 2002; pp. 10−80.
(48) Ho, F.-G.; Strieder, W. A variational calculation of the effective surface diffusion coefficient and tortuosity. *Chem. Eng. Sci.* **1981**, *36*, 253−258.
(49) Akanni, K. A.; Evans, J. W.; Abramson, I. S. Effective transport coefficients in heterogeneous media. *Chem. Eng. Sci.* **1987**, *42*, 1945−1954.
(50) Hamad, H. T.; Abbood, D. W.; Mustafa, A. S. *Strength Tortuosity-Porosity Relation in Locally Types of Porous Media (Experimental Model)*, IOP Conference Series: Materials Science and Engineering, 2018; IOP Publishing: 2018; p 012093.
(51) Kavand, M.; Fakoor, E.; Mahzoon, S.; Soleimani, M. An improved film−pore−surface diffusion model in the fixed-bed column adsorption for heavy metal ions: Single and multi-component systems. *Process Saf. Environ. Prot.* **2018**, *113*, 330−342.
(52) Feng, B.; Bhatia, S. K. Variation of the pore structure of coal chars during gasification. *Carbon* **2003**, *41*, 507−523.
(53) Massoudi Farid, M.; Kang, M. S.; Hwang, J. The effect of CO on coal−biomass co-gasification with CO_2. *Fuel* **2017**, *188*, 98−101.
(54) Ollero, P.; Serrera, A.; Arjona, R.; Alcantarilla, S. The CO_2 gasification kinetics of olive residue. *Biomass Bioenergy* **2003**, *24*, 151−161.

https://doi.org/10.1021/acsomega.0c05297
ACS Omega 2021, 6, 8002−8015

Appendix D

Fuel 297 (2021) 120692

Contents lists available at ScienceDirect

Fuel

journal homepage: www.elsevier.com/locate/fuel

Full Length Article

Multiscale CFD-DEM model for the CO_2 gasification reaction of carbon anode

Mohammad Kavand

Aluminium Research Centre REGAL, Université Laval, 1065 Avenue de la Médecine, Québec, Québec G1V 0A6, Canada

ARTICLE INFO

Keywords:
CO_2 gasification
Carbon anode particle
Multiscale model
Mass-transport phenomena
Shrinkage
CFD

ABSTRACT

The reactivity of carbon anodes with CO_2 is one of the main concerns in aluminum smelters using the Hall–Héroult process. Such reactivity is undesirable because it increases the net carbon consumption and thus shortens anode lifetime. Anode overconsumption is affected by anode intrinsic reactivity and mass-transport phenomena. Herein, as a first step toward the simulation of anode gasification with CO_2, an anode particle bed was considered. Numerical multiscale computational fluid dynamics (CFD)–discrete element method (DEM) model was developed based on an Eulerian–Lagrangian concept. The model includes an Eulerian finite-element method for the gas and solid particles, and a Lagrangian DEM for the particle phase. The was intended to capture the particle-shrinkage effect (movement of particles during gasification). The physical (e.g., porosity and specific surface area) and thermochemical (e.g., heat of reaction) properties of particles are ultimately tracked. Geometric changes in particles, heat and mass transfer, particle shrinkage, and chemical reactions are considered during anode gasification with CO_2. The dynamic concentration and temperature profiles of the reactant and product gases, as well as the solid conversion, were modeled in the voids between the particles and the pores inside each particle. To validate the model, experimental tests were performed using a bed of anode particles.

1. Introduction

The Hall–Héroult process is a common industrial process of producing aluminum where alumina is fed to electrolysis cells (also called pots) containing carbon anodes [1–5]. A pot, representing an electrolysis cell, consists of molten cryolite, prebaked carbon anodes, and a liquid layer of aluminum, which lies over the blocks of the cathode carbon [1]. The electrolysis reaction can be written as

$$2Al_2O_3(diss)+3C(s)\rightarrow 4Al(m)+3CO_2(g), \quad (1)$$

where molten aluminum is the main product of Eq. (1). During this process, the carbon anode is consumed and should be replaced by a new anode approximately every 25 days.

The least amount of theoretically combusted carbon is equal to 0.33 kg C/kg Al produced. However, the real electrolytic consumption of carbon is approximately 0.41 kg C/kg Al produced because cell efficiency does not usually reach 100%. The overconsumption of one kg anode per ton of produced aluminum is around 2 US$ [2]. The overconsumption of a midsize smelter (producing 300 000 tons of aluminum per year and using 150 000 anodes per year), is approximately 40 kg per anode [2,6]. Thus, the estimated extra cost could be about 12 MUS$ per year [2,6]. The overconsumption could be related to two main factors, namely, gasification by air and CO_2 and the anode properties [6,7], which may lead to carbon dust. Carbon dust is principally defined by selective burning of the anode components in contact with air or CO_2 and the detachment of carbon particles from the anode surface [8]. The anode-gasification rate depends on the surface structure, temperature, permeability, and reactivity of anode constituents [3]. The effect of air reactivity is fairly well mitigated by covering the anode with alumina, which reduces the diffusion of air toward the anode surface. However, this solution is not possible for CO_2 reactivity because it primarily occurs in the part of the anode immersed in molten salt. Providing a solution for CO_2 reactivity requires a deep understanding of the effect of different parameters on reaction rates. Accordingly, the present work aims to provide a model to predict and quantify the effect of such parameters on the CO_2 gasification of carbon anodes.

$$C(s)+CO_2(g) \rightleftarrows 2CO(g).\Delta G^{\circ}=40800-41.7T \text{ cal} \quad (2)$$

The reaction, described by Eq. (2), occurs in the presence of CO_2 [1]. A gas-bubble layer forms underneath the bottom surface of the carbon anode, which prevents reaction of anode with electrolyte and increases the cell voltage [1,2]. CO_2 also diffuses into the anode pores and reacts with carbon on the active surfaces of anode, generating CO. The diffusion of CO_2 in anode pores is enhanced under the hydraulic pressure of

E-mail address: Mohammad.kavand.1@ulaval.ca.

https://doi.org/10.1016/j.fuel.2021.120692
Received 11 November 2020; Received in revised form 8 March 2021; Accepted 15 March 2021
Available online 6 April 2021
0016-2361/

Nomenclature

a_s	surface area of the anode per unit volume of the bed, ($m^2 \cdot m^{-3}$)
C_C	concentration of anode reactant, ($mol \cdot m^{-3}$)
C	concentration of gaseous species, ($mol \cdot m^{-3}$)
$C(O)$	surface of carbon–oxygen complex, ($mol \cdot m^{-2}$)
CL	contact list of particle i, (–)
D	diffusion coefficient, ($m^2 \cdot s^{-1}$)
D	bed diameter, (m)
d_p	particle diameter, (m)
H	convective heat transfer, ($W \cdot m^{-1} \cdot K^{-1}$)
H	bed height, (m)
J	mass flux, ($mol \cdot s^{-1} \cdot m^{-2}$)
K	reaction rate constant, $(mol \cdot m^{-3})^{(1-n)} \cdot s^{-1}$
K	convective mass transfer coefficient ($m \cdot s^{-1}$)
L_0	pore length, ($m \cdot kg^{-1}$)
L	height of the bed reactor, (m)
M	torque, ($kg \cdot m^2 \cdot s^{-2}$)
$\overrightarrow{M_{ij}^r}$	rotation of particles, ($kg \cdot m^2 \cdot s^{-2}$)
$\overrightarrow{M_{ij}^t}$	tangential torque, ($kg \cdot m^2 \cdot s^{-2}$)
m	mass of anode particle, (kg)
N	partial reaction order, (–)
N	number of experimental data
Nu	Nusselt number, (–)
P	partial pressure, ($kg \cdot m^{-1} \cdot s^{-2}$)
Pr	Prandtl number, (–)
R	particle radius, (m)
R	radius of the bed reactor, (m)
Re	Reynolds number, (–)
Re_e	effective Reynolds number, (–)
S	specific surface area, ($m^2 \cdot kg^{-1}$)
Sc	Schmidt number, (–)
Sh	Sherwood number, (–)
T	reaction time, (s)
T	temperature, (K)
Q	flow rate, ($L \cdot min^{-1}$)
Q	heat flux, ($W \cdot m^{-2}$)
V	flow velocity, ($m \cdot s^{-1}$)
W	chemical reaction rate, ($mol \cdot s^{-1} \cdot m^{-3}$)
X	gasification conversion of anode particle, (–)

Greek symbols

B	permeability, (m^2)
ΔH	enthalpy of reaction, ($kJ \cdot mol^{-1}$)
E	void fraction, (–)
φ	angular position, ($rad \cdot s^{-2}$)
H	effectiveness factor, (–)
κ	sphericity, (–)
Λ	Thiele modulus, (–)
μ	viscosity, ($Pa \cdot s$)
$\overrightarrow{\nu}$	translational velocity
P	density, ($kg \cdot m^{-3}$)
T	tortuosity, (–)
ψ	structural parameter, (–)
$\overrightarrow{\omega}$	rotational velocity, ($rad \cdot s^{-1}$)

Subscripts

Ap	Apparent
Ave	Average
B	Bulk
C	Carbon
CO	carbon monoxide
CO_2	carbon dioxide
Diss	Dissolved
E	Effective
F	active carbon site
G	gas phase
Gs	gas-solid interface
M	Molten
Mix	mixed gases
P	Particle
S	solid phase
T	Instantaneous
0	Initial

Superscripts

Ext	External
f-p	fluid-particle interaction forces
p-p	particle-particle interaction

the bath. Thus, chemical reaction and mass-transport phenomena are important factors for this reaction.

To develop a mathematical model for anode-reaction simulation, the anode structure is simplified. We consider the anode as a fixed bed of particles, exhibiting two types of porosities, i.e., porosity inside each particle, representing the interparticle porosity of the coke aggregates in the anode which are not filled with pitch, and the voids between the particles, representing the pores within the binder matrix, generated during compaction or baking process. Reaction 2 is a function of temperature and partial pressure of the gas species in the pores, and both are affected by the flow patterns and mass transport in the fixed-bed reactor.

Reactions in fixed-bed reactors can be simulated by different mathematical approaches depending on system complexity, i.e., pseudo homogeneous or pseudo heterogeneous models in steady state or transient regimes. Pseudo homogeneous models assume that the surface of the solid phase is fully exposed to the gas phase, with no gas-to-solid mass and heat-transfer resistances. The heterogeneous approach assumes conservation equations for both phases separately.

Over the past decade, several researchers have modeled fixed-bed reactors based on radial, axial, and circumferential profiles [9–13]. However, only a few studies have coupled the macro- and microscales of fluid dynamics and particle reactions in fixed beds. Moreover, most previous research has been performed for catalytic reactions, where the size and the structural characteristics of the bed remained unaltered during the process [9–15]. Larachi [16,17] investigated a reactor design by applying a parallel modeling structure in which the scales of particle and reactor are considered. To study the deposition of fine in packed beds, a computational fluid dynamics (CFD) approach [18] has been used by Valkov et al. [19]. Partopour and Dixon [20] proposed a multiscale model of steam methane reforming with catalytic reactive particles by applying the interactions between local pellet-scale dynamic responses and the bed-scale global fields through CFD. Noncatalytic reactions in fixed-bed reactors have also been reported; however, the kinetics is often limited to a specific range of process parameters [19,21–26], but all of them assume that the solid phase does not change during the process. Besides, owing to computational hardware limitation, researchers are restricted to a small number of solid particles (<50) forming a random fixed bed.

Improvements in computer performance can enable studies on a larger number of particles. These numerical methods capture the properties of a material, so the accuracy and robustness of material properties tracking is insufficiently high to conduct the modeling of time-

history variables. Meanwhile, Eulerian methods do not predict accurate results in case of material response to loading and damage. Lagrangian methods are more accurate for solid phase, in contrast to Eulerian methods that are preferable for fluid phase. It demonstrates the importance of coupling these two methods for the calculation of solid–fluid interactions. An Eulerian–Lagrangian approach has recently been used to simulate porous particles [20,23,27–32]. However, an Eulerian–Lagrangian model of entrained-flow solid gasification and its validation are unavailable to the best of our knowledge.

In the present study, a multiscale model with noncatalytic reaction was developed to investigate fixed-bed reactors and apply a new approach to consider solid structural changes during gasification. In this method, the solid particles were considered as a discrete part, and the flow in the space between the particles was considered as a continuum phase. A Eulerian finite-element method (FEM) served as the basis of the proposed mathematical method to model the fluid phase, coupled with a discrete-element method (DEM) applied to model the anode particles' dynamics and particle shrinkage, which enabled the tracking of the particles' motion and the fluid phase's dynamics. Communication between the two length scales was achieved through an interpolation strategy, and the dual-grid multiscale scheme was originally proposed for the coupling between DEM and FEM. To facilitate data conversion between continuum models derived from FEM and DEM, an interface was defined. This process was the key point to model gasification and enable the investigation of particle–fluid interaction without missing the particles' information.

To validate the model, a set of experiments was needed. A fixed-bed design was used to determine an effect of operating parameters, such as flow rate, bed height, particle size examined, and unknown parameters (e.g., chemical-reaction constants). The model output included the distribution of concentration, pressure, flow rate, and temperature of gas components inside and outside of particles. Structural parameters such as particle porosity, permeability, specific and surface area were also determined. The model was applicable as well to particle shrinkage during the process, and particle tracking was available for all anode particles.

2. Mathematical modeling

2.1. Methodology

The mathematical model in the present work is developed with the following assumptions.

- To conform to a microstructural model of anode, a simplified structure may be applicable by considering a bed of particles assuming that the porosity inside a particle represents small pores and the voids between particles represent large pores. The active sites on the anode particles are susceptible to let the reaction occur, which is a strong function of the particle temperature and species partial pressures, affected by the flow patterns and mass transport in the fixed-bed reactor.
- Mass transfer occurs through convection and diffusion at the macroscale (fluid phase) and diffusion within the anode-particle domain.
- Non-isothermal conditions prevail in the fixed-bed domain.
- Chemical reactions (Boudouard reaction) occur in the solid phase as noncatalytic reactions.
- All particles are spherical.
- The Langmuir–Hinshelwood (L-H) mechanism and random-pore model (RPM) equation are used to define the chemical reaction term.

Anode-gasification reactions are sensitive to mass-transfer effects. The gasification-rate schematic illustrated in Fig. 1, and it may occur by physical and chemical processes through the following steps: 1) mass transfer (by diffusion) of gaseous reactant(s) from the bulk gas phase to the carbon surface; 2) adsorption of reactant(s) on the carbon surface; 3–5) chemical rearrangements (reactions) on the surface, mobility, and formation of adsorbed product(s); 6) desorption of product(s); and 7) mass transport (by diffusion) of the gaseous reaction product(s).

2.2. Simulation

To simulate the fluid–particle flows in this work, Euler–Lagrange approaches are used to consider a combination of CFD and DEM,

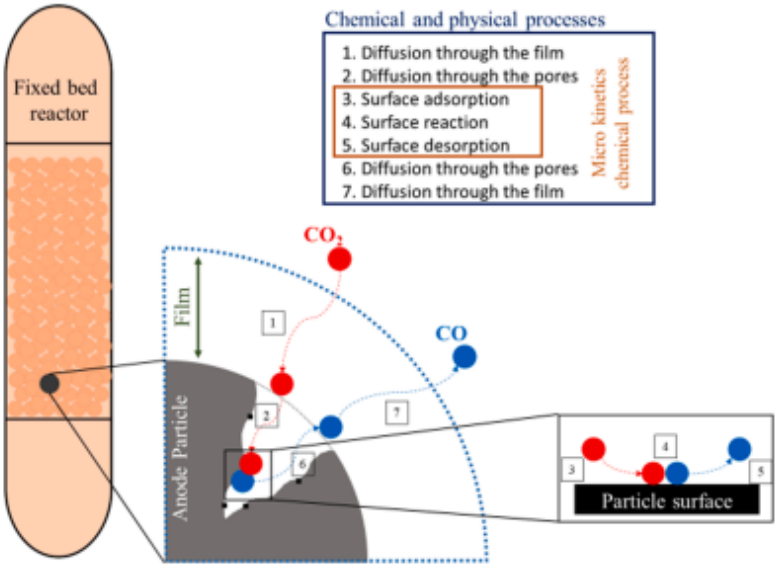

Fig. 1. Chemical and physical processes of each particle in a fixed-bed reactor.

referred to as CFD-DEM. The inclusion of constitutive equations related to fluids and solids and proper coupling strategy in CFD-DEM allows us to study momentum, heat and mass transports, and chemical reactions in almost any detail on the particle scale.

2.2.1. CRd

In this approach, the fluid flow around particles is estimated as a continuum, and its mesoscale motion is described by the volume-averaged Navier–Stokes equation. CFD-DEM increases the computational cost, but it can provide higher accuracy than the two-fluid model TFM [33].

2.2.1.1. Mass equations. A mass-balance-based reaction-transport model is developed to simulate the dynamics of anode CO_2 reactivity by applying heat-transfer equations, as well as momentum equations, to describe the gasification process. CO is the product of the Boudouard reaction, and because of the inhibition effect of CO on gasification (by adsorption and desorption), it should be applied in the model for each step to achieve accurate modeling. This model facilitates the incorporation of a nonlinear chemical-reaction rate, w, the conversion-induced transformations in the porous structure by the pertinent equation, and the reaction-induced changes in the effective diffusivity through the input of conversion (X) [34–36]. The concentration profile within particles can be obtained for a particle position (r) and certain time (t) by solving the set of equations in the bed:

$$\frac{\partial C_{CO_2}\varepsilon_b}{\partial t} = \varepsilon_b\nabla.(D_{CO_2}.\nabla C_{CO_2}) - \varepsilon_b\nabla.(C_{CO_2}v) - k_{gs}a_s(C_{CO_2} - C_{p,CO_2|r=r_b}) \tag{3}$$

$$\frac{\partial C_{CO}\varepsilon_b}{\partial t} = \varepsilon_b\nabla.(D_{CO}.\nabla C_{CO}) - \varepsilon_b\nabla.(C_{CO}v) - k_{gs}a_s(C_{CO} - C_{p,CO|r=r_b}) \tag{4}$$

where C_{CO_2} and C_{CO} are the concentrations of reactant and product gases of the bed, respectively; C_p is the concentration of the reactant gas for the particle considered in the axial position; v is the superficial velocity of the reactant gas; ε_b is the porosity of the bed, k_{gs} is the convective mass-transfer coefficient around the particle; and a_s is the surface area of the per unit volume of the bed. The first right-hand term represents the diffusion of fluid gas onto the solid phase obtained by Fick's law [37] (Eqs. (3) and (4)). The second term describes the convective mass flux related to the velocity of fluid gases. The last term represents the convective mass flux owing to the concentration driving force between the surfaces of particles and the gas bulk.

The boundary conditions for Eqs. (3) and (4) at the reactor inlet and outlet for each component 'i' are as follows:

$$C_{i,0} = C_{i,b|z=0} \tag{5}$$

$$C_{i,b} = C_{i,out|z=L} \tag{6}$$

In addition,

$$\left.\frac{\partial C_{i,b}}{\partial R}\right|_{R=0} = 0 \tag{7}$$

$$\left.\frac{\partial C_{i,b}}{\partial R}\right|_{R=R_b} = 0 \tag{8}$$

The reaction inside the particles is included as a sink term in the intraparticle mass balances for the transport of dilute species interfaces with reactive particle features.

$$\frac{\partial C_{P,i}}{\partial t} = \nabla.(D_{e,i}.\nabla C_{P,i}) - w_P \tag{9}$$

The boundary condition at the center of the particle is

$$\left.\frac{\partial C_{i,p}}{\partial r_p}\right|_{r_p=0} = 0 \tag{10}$$

D_e is an effective diffusion coefficient ($m^2 \cdot s^{-1}$), and w_p is the reaction source term. Various models can explain the kinetics of the CO_2 gasification reaction. The reaction rate per unit of volume is essential to formulate in a "structural" format [35] inside a particle. Thus, an equation is introduced to outline the reaction for the available particle sites at a given processing time. To explicitly combine this feature, the following intrinsic kinetics is assumed to be established for all locations in the particle:

$$W = -r(C_A)\cdot F(X) \tag{11}$$

In Eq. (11), the reaction rate can be divided into two parts [38]. In the first part, $r(C_A)$, the effect of gas concentration on the reaction rate is considered. In the second part, $F(X)$, depicts the effect of changes in the available reacting surface. The description of this equation is detailed in a previous work [39]. In general, the L-H rate equation is considered for $r(C_A)$. This mechanism is proposed based on the adsorption and desorption of CO and CO_2 to yield expressions for calculating the reaction rates of anode gasification. The RPM [40] is applied to the structural part of the chemical-reaction equation. Therefore, the chemical-reaction term is as follows:

$$\frac{dX}{dt} = \frac{k_1 P_{co_2}}{1 + k_2 P_{co_2} + k_3 P_{co}} S_0 (1 - X)\sqrt{1 - \psi ln(1 - X)} \tag{12}$$

where S_0 and ψ are the initial specific surface area and the structural parameters of the RPM equation, respectively, and k_1, k_2, and k_3 are the chemical-reaction rate constants. On the surface, the particle's gas concentration is assessed to provide boundary conditions and solve the proposed model. In this process, an assumption lies in the claim that the gas components' external convective mass-transfer rate to the surface has to be equal to the transport rate via the particle surface. The bed and particle equations are linked through the mass transfer on the surface according to the boundary conditions appearing in the mass-balance equation. Hence,

$$J_i = K_{gs}(C_{i,b} - C_{i,s}) \tag{13}$$

where J_i is the mass flux on the surface of the particle C_b is the component concentration in the bulk gas outside the particle, and K_{gs} is the mass-transfer coefficient specified by correlating the classic Ranz–Marshall forced convection mass transfer for a spherical particle [41]:

$$K_{gs} = \frac{Sh\cdot D}{l} \tag{14}$$

$$Sh = 1 + 1.5(1 - \varepsilon_b)Sh_p \tag{15}$$

$$Sc = \frac{\mu}{\rho D} \tag{16}$$

where l is the characteristic length (m) equal $2r$ in our case, and Sh is the Sherwood number representing the ratio of the convective mass transfer to the diffusive mass-transport rate. This approach can be applied to mass transfer from a single spherical particle to the bulk gas in which Re and Sc represent the Reynolds and Schmidt numbers, respectively. The Sherwood number for a bed of spherical particle can be obtained from Gunn et al. [42] as follows:

$$Sh = 1 + 1.5(1 - \varepsilon_b)Sh_p \tag{17}$$

2.2.1.2. Movement equations. The momentum balance that governs the fluid flow is built upon the Navier–Stokes and continuity equations. The conservation of mass is the generic equation used, and the following continuity equation is written for a porous medium with an effective term of the chemical reaction on the flow [37]:

$$\frac{\partial(\varepsilon_b\rho_{f,i})}{\partial t} + \nabla.(\rho\varepsilon_b U) = W \tag{18}$$

where W is the chemical-reaction rate term, and ρ_f is the density of gas species. When gas flow inter to the reactor, gas is going up through the particle bed, therefore, flow leads to a pressure drop during the reactor, to be able to add this effect on the motion equation, the Ergun equation has been defined, and it can be written as [37]:

$$\frac{\nabla P}{L} = \frac{150\mu_{Mix} v(1-\varepsilon_b)^2}{d_p^2 \kappa \varepsilon_b^3} + 1.75\frac{\rho v^2(1-\varepsilon_b)}{d_p \kappa \varepsilon_b^3} \tag{19}$$

where ε_b is the bed porosity, μ_{Mix} denotes the mixed-gas viscosity (Pa·s), ρ_f is the gas density (kg·m^{-3}), L is the reactor length coordinate (m), v is the reactor flow velocity (m·s^{-1}), and κ is the sphericity of particle. The Ergun equation is valid for laminar and turbulent flows. In laminar flow, the first term is predominant. Under turbulent flow, the second term is dominant, and the pressure drop is related to the square of the superficial velocity and linearly depends on the density of the fluid passing through the bed.

2.2.1.3. Energy equations. The bulk energy balance for a fixed-bed reactor can be written as follows:

$$\rho_f C_f \frac{d\varepsilon_b T_b}{dt} = -\varepsilon_b \rho U.\nabla T_b + \varepsilon_b \nabla.(k_f \nabla T_b) - h_{gs} a (T_b - T_p) \tag{20}$$

where C_p is the heat capacity (J·kg^{-1}·K^{-1}), T_b is the bulk temperature, and k_f is the thermal-conductivity coefficient. The first right-hand term $U.\nabla T_b$ represents the temperature change owing to the convection of fluid, the second term demonstrates the conduction heat flux of the gas phase, and the last term describes the convective heat flux from the surface of the particle to the fluid bulk.

For the surface, the relation to the particle-energy balance is:

$$\langle \rho_p C_{pv} \rangle \frac{\partial(1-\varepsilon_p)T_p}{\partial t} = (1-\varepsilon_p)\nabla.\langle k_s \nabla T_p \rangle + (1-\varepsilon_p)\rho_p \sum \Delta H_i W_i \tag{21}$$

where Cp_s is the heat capacity (J·kg^{-1}·K^{-1}), T_p represents the solid particle temperature, and k is the convective heat transfer, (W·m^{-1}·K^{-1}). All the terms of Eq. (21) is multiplied by $(1-\varepsilon_p)$ to describe the ratio of the volume occupied by the solid to the total volume. The terms of $(K_s \nabla T)$ is the conductive heat flux [37], and (ΔH) is the enthalpy of reaction generated inside the particles.

The following initial and boundary conditions can be used to solve Eqs. (20)–(21):

$$R = 0\left.\frac{\partial T_b}{\partial r_b}\right|_{R_b=0} = 0 \tag{22}$$

$$T_b = T_{s|R=R_b} \tag{23}$$

$$T_b = T_{0|z=0} \tag{24}$$

$$z = IT_b = T_w|_{R=R_b} \tag{25}$$

The gas temperature analogizing the concentration on the particle's surface is assessed to provide heat transfer and temperature equations. An assumption is that the rate of the external convective heat transfer on the surface of the gas components must be identical to that of transport inside the particle surface (no accumulation on the surface) as follows:

$$q = h_{gs}(T_b - T_s) \tag{26}$$

In the above equation, q is the heat flux, and h_{gs} represents the coefficient of heat transfer of a particle determined by correlating a spherical particle's forced convection mass transfer [43].

$$h_{gs} = \frac{Nu\, k}{l} \tag{27}$$

The bed and particle equations are linked through the mass transfer on the surface according to the boundary conditions appearing in the mass-balance equation.

In this equation, Nu is the Nusselt number, which is the convective-to-conductive heat-transfer ratio across the boundary, in which the convection covers advection and diffusion mechanisms. For a single particle, this number is obtained for the fluid as follows

$$Nu_p = 2 + 0.6Re^{1/2}Pr^{1/3} \tag{28}$$

Re and Pr are also obtained by

$$\mathrm{Re} = \frac{\rho U l}{\mu} \tag{29}$$

$$\mathrm{Pr} = \frac{Cp\mu}{k_f} \tag{30}$$

where l is a characteristic linear dimension (m), and k_f is the thermal-conductivity coefficient (W·m^{-1}·K^{-1}).

For a bed of spherical particles, the following equations have been obtained by Gunn et al. [42]:

$$\mathrm{Re}_c = \frac{1}{(1-\varepsilon_b)}\mathrm{Re} \tag{31}$$

$$\mathrm{Nu}_b = 1 + 1.5(1-\varepsilon_b)\mathrm{Nu}_p \tag{32}$$

2.2.1.4. Particle shrinkage. Anode-gas chemistry causes solid particle shrinkage because of the reaction with the gas phase. Particle shrinkage, in addition to influencing gasification, robustly affects the particle direction on the way out of the reactor [44], and the absence of particle shrinkage causes particle entrainment to be highly overpredicted. The change in the anode particle radius during the process can mathematically be explained by a moving boundary condition obtained by Kavand et al. [39] as follows:

$$\frac{dr_{sp}}{dt} = \begin{cases} 0 & X(a) < 1, X(100\%)_{\text{outer layer}} \\ \dfrac{dX_j/dt}{dX_j/dr} & X(a) = 1, X(100\%)_{\text{outer layer}} \end{cases} \tag{33}$$

when 100% of an imaginary external layer is consumed and shrinkage conversion is obtained by solving the second-condition term of Eq. (35).

2.3. DEm

To add a particle's motion and the effect of interaction between particle–particle and particle–fluid to the model, a DEM needs to be applied. Gas flow through an anode particle bed has been examined conventionally in a continuum model that can successfully capture some essential points of the porous solid-phase behavior. Nevertheless, some phenomena and structural exchanges, such as shrinkage effects at the particle scale and particle–particle interactions, cannot be explained by macro-partial differential equations (PDEs) [29,33]. Therefore, these phenomena should be modeled by a DEM.

According to the DEM, the deformation of material is simulated by successively solving the law of motion for each element and the force–displacement law for each contact [23,29,30]. In this dynamic process, a centered finite-difference scheme solves the equations through a time-stepping algorithm, assuming that the time step is sufficiently small such that the velocities and accelerations are constant within each time step. The algorithm tries to detect the contacts according to the known positions of the elements, so the magnitude of the possible overlaps among elements is detected. Then, by applying the force-displacement law, the propagated contact forces are calculated. The forces are then inserted into the law of motion for each particle, and the velocity and acceleration of the particles are calculated. According to the obtained values, the updated positions of all particles in the current time step are determined.

This cycle of calculations is repeated and solved at each time step, so the flow or deformation of the material is simulated.

Elements in DEM are rigid bodies in the form of circles (in 2D). However, they can overlap with one another owing to applied forces, and the magnitude of the overlaps is related to the contact force via the predefined contact model [33].

Newton's equation of motion for N spherical particles in the system is as follows:

$$m_i \frac{d\vec{v}_i}{dt} = m_i \frac{d^2\vec{x}_i}{dt^2} = \sum_{j \in CL_i} \vec{f}_{i,j}^{c-p} + \vec{f}_i^{d-p} + \vec{f}_i^{ext} \tag{34}$$

$$I_i \frac{d\vec{\omega}_i}{dt} = I_i \frac{d^2\vec{\varphi}_i}{dt^2} = \sum_{j \in CL_i} (\vec{M}_{ij}^{t} + \vec{M}_{ij}^{r}) \tag{35}$$

where fi and M_i are the sums of the different forces and torques that act on particle i, respectively. They are complex functions of variables such as the particle position x_i, angular position $\vec{\varphi}_j$, translational velocity of the center of mass v_i, and rotational velocity around the center of mass $\vec{\omega}_j$. We call these four variables the state variables of the particle. We use the subscript j for the input parameters of the forces and torque functions to denote that the state variables of particle i and other particles in the system affect the resultant interactions. The first term on the right-hand side of Eq. (34) is the sum of particle–particle interaction forces acting on the particle, and i may involve collisional or interparticle forces. This summation is implemented for all particles existing in the contact list of particle i, CL_i. The second term represents the fluid–particle interaction forces; when the fluid effects are insignificant, this term is assumed to be zero. The third term describes the external forces acting on particle i owing to uniform or non-uniform external fields. Two types of contacts between particles exist, namely, physical and nonphysical. Physical contact covers a condition where the surfaces of two particles are contiguous; By contrast, a condition in which particles are not necessarily contiguous but are still interactive is referred to as nonphysical contact. Calculating the collision force between two physical contact-sharing particles is performed according to the force–displacement laws and the interaction force between two particles with nonphysical connections according to interparticle interactions. In Eq. (35), the first term in the summation represents the tangential torque $\vec{M}_{ij}^{t}$ produced by the particle–particle collision. Considering that the particle–particle collision force acts on the contact point (particle surface), it causes a torque that is the origin of the rotation of particles. $\vec{M}_{ij}^{r}$ represents rolling friction, which is considered to be another torque applied onto particle i because it lies almost opposite of the particle's rotation; accordingly, it is recognized as the rolling-resistance torque. To resolve the particle-wall and interparticle collisions, a soft sphere DEM was used, in which the forces for interparticle contact are computed with the use of equivalent simple mechanical elements, such as a spring, slider, and dashpot. However, particles can lightly overlap, and the normal force that tends to repel the particles can then be subtracted from this spatial overlap and the normal relative velocity at the contact point. By knowing physical properties such as Young's modulus and Poisson's ratio, the spring stiffness can be calculated by Hertzian contact theory. The soft sphere model's characteristic features that detail the implementation issues of the DEM are available in literature [23,33].

The physical properties adopted in the current study for the collision model include the following: Poisson's ratio of 0.3; Young's modulus of 5×10^6 Pa; and restitution and friction coefficients of 0.9 and 0.3, respectively [23,33].

2.4. Numerical method for solving the developed model

The developed model considers the gas species concentration (C) and anode-conversion rate (X) as the objective variables that should be computed. As the apparent radius of an anode particle starts decreasing after the critical anode-conversion rate [3] and finally approaches zero, the proposed model uses the moving-boundary method to solve the equations. The model incorporates a series of nonlinear PDEs, and it can use a proper numerical technique to solve these equations. Communication between the two grids and length scales can be ensured through an interpolation strategy, and the dual-grid multiscale scheme is originally proposed for the coupling between DEM and FEM. From a software viewpoint, implementing the dual-grid multiscale approach needs two computational grids and a routine for interpolating between them. The DEM platform has been used for the evolution of a set of discrete spherical-anode particles that move as long as a gas-phase flow exists. At every time step, the positions and orientations of the particles are updated, and the outputs of the program represent the gas concentration (C) versus time. The mesh grids are shown in Fig. 2. The left picture shows the macroscale mesh in two dimensions. The right picture illustrates one particle with the micromesh, as well as the heat and mass fluxes establishing the connection between the two scales. By matching the simulation and experimental data, unknown variables such as reaction-rate constants can be calculated. The best-fit curve is obtained by minimizing the f function, given as [45]:

$$f(min) = \sum_{j=1}^{n} (C_j - C_{exp,j})^2 \tag{36}$$

where n is the number of experimental points.

This paper defines an interface to allow the data to be converted between continuum models derived from the FEM mechanism and the DEM model. A partially coupled framework is involved in the interface between the FEM and DEM mechanisms [46]. Fig. 3 presents the algorithm used for this process. The equations of the continuum and discrete elements are solved separately through the partially coupled approach for each time step, and these two models accordingly exchange the results at the end of each time step. Finally, to change the initial conditions for each time step, the data are sent to the FEM mechanism to set the values of the parameters obtained from the DEM and to run the simulation. In the next step, the unknown variables are calculated by comparing with the simulation and experimental data.

To solve PDEs, we use COMSOL Multiphysics as a commercial finite-element engine that can simultaneously solve a huge range of PDEs. COMSOL can create a model with a series of nodes to create the model geometry, apply the property of materials, boundary, and initial conditions, PDEs, solutions, etc. Node information can be modified by MATLAB scripts. YADE software, an open-source C++ framework, is applied to work as a DEM engine that can solve Newton's second law of

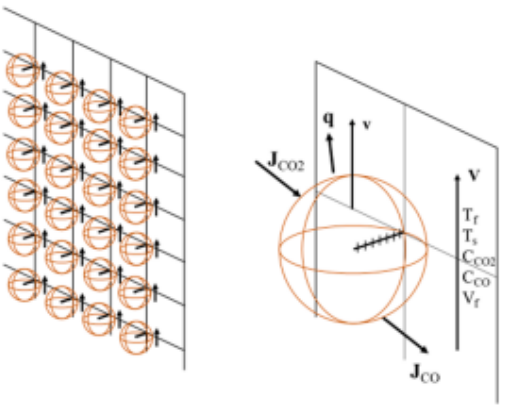

Fig. 2. Schematic of two-scale simulation for gasification in a fixed-bed reactor.

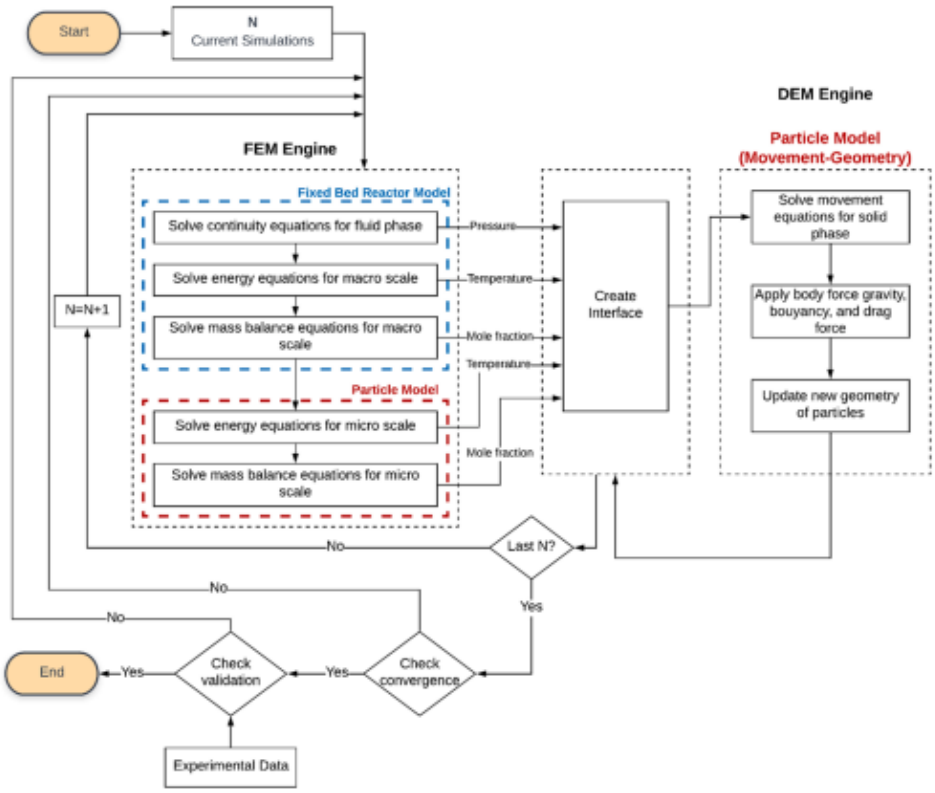

Fig. 3. Algorithm of the mathematical model.

motion for each anode particle. To validate the model with experimental data, an algorithm genetic is applied using MATLAB.

3. Experiments

To establish an accurate model, several sets of experiments are needed to determine the physical and chemical properties of solid and gas phases during gasification (Table 1).

Table 1
Summary of experimental conditions used for modeling.

Property	Description	Values for different particle sizes		
		0.5 mm	1 mm	2 mm
L (m)	Height of the bed reactor		0.05	
d (m)	Diameter of the bed reactor		0.012	
ρ_b (kg·m^{-3})	Density of bed		1.238	
ρ_p (kg·m^{-3})	Real density	1.989	1.985	1.983
ϵ_b	Macroscale porosity (of bed)		0.38	
ϵ_p	Microscale porosity (of particle)	0.33	0.35	0.37
S (m^2·kg^{-1})	Initial specific surface area particle bed		4.57	
δ (m^2)	Permeability of bed		2×10^{-12}	
D_i (m^2·s^{-1})	Diffusion coefficient of particle		5.67×10^{-5}	
μ_{Mix} (kg·s^{-1}·m^{-1})	Viscosity of gas phase		4.35×10^{-5}	

3.1. Materials

3.1.1. Anode particle

Baked Carbon anode was provided by Alcoa Corporation. An anode was made from a mixture of 50%–65% petroleum coke, 14%–17% coal tar pitch binder, and 15%–30% recycled anode butts [1,4,5]. The raw material was first crushed and sieved in various USA standard mesh sizes (16, 30, 50, and 100). Ball milling was used to mill large particle (>1 mm) into finer ones (Blaine Number 2300). Some experimental tests were conducted to obtain the physical properties of the anode particles. The real density of the anode particles was measured using a helium pycnometer (Micromeritics, AccuPyc II 1340, USA) at different particle sizes (0.5, 1, and 2 mm). Each sample was weighed three times with an analytical balance (MS204S, Mettler Toledo, USA) and placed in a stainless-steel cell in a helium pycnometer. Real density was obtained by dividing the mass of the sample by the volume obtained with the pycnometer. To obtain the specific surface area, powder samples containing 0.02 g to 3.00 g of particles with a given size were degassed under pure nitrogen (N_2) at 523 K for 5 h [3]. Then, the samples were analyzed with a gas-adsorption analyzer (Micromeritics, Tristar II 3020, USA). The gas used for surface measurements was N_2 (purity = 99.995%; Praxair, USA) at 77 K (Table 1).

3.2. Gasification tests

Fig. 4 shows a schematic of the experimental gasification process. Fixed-bed reactor (MTI; GSL-1600IX50) with 1.2 cm inner diameter and

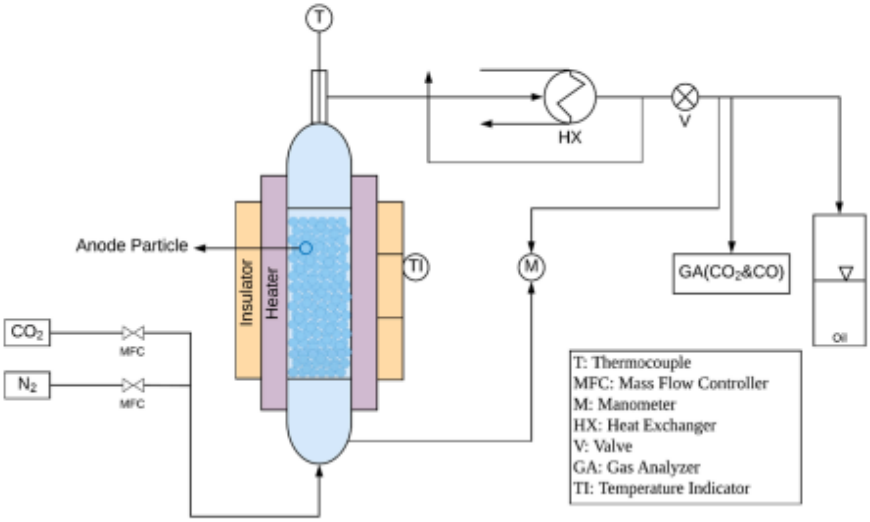

Fig. 4. Schematic of the experimental setup (fixed-bed reactor).

40 cm-long glass column was used. Temperature probes (K-type thermocouples) were placed along the bed to measure the temperature. Before entering the reactor, the gas phase was mixed in an inert fixed bed to homogenize the temperature equilibrium. The outlet-gas concentrations were measured with a gas analyzer (E-1500, E Instruments, USA). First, the fixed-bed reactor was loaded with a predetermined amount of anode particles (samples containing 1 g to 4.00 g, depending on bed height), and then the reactor was placed in a furnace at a high temperature (960 °C). Subsequently, a condenser was attached to either the exit of the reactor or a gas collector. Furthermore, nitrogen was used as a carrier gas. The temperature controller was configured according to the considered value (1233 K) for each test, and experiments were conducted for different gas-flow rates (0.5, 1, and 2 $L{\cdot}s^{-1}$), bed heights (2, 3, and 5 cm), and particle radii (0.5, 1, 2, and 3 mm). The particles were heated with an inert gas (99.995% N_2 at 200 ml/min) from room temperature to 1233 K at 8 K/min heating rate. The set up was maintained for 20 min under N_2 to stabilize at 1233 K. The sample was then gasified under CO_2 (99.9%). After a specific duration of carbon conversion, the furnace was switched off, and the anode particles were cooled down in an inert atmosphere. The monitored data during each experiment included the measured inlet and outlet temperatures, masses of anode particles, pressure drop, specific surface area of samples, and reactor-exit gas concentrations at different time intervals. The reaction time depended on the sample particle size and varied between 3 and 15 h. The outlet-gas flow was directed to the oil tank to avoid emission to the atmosphere.

4. Results and discussion

The outputs of CFD-DEM include the velocity of fluid, temperature, pressure drop, and species concentration for the fluid phase, as well as particle position, velocity, temperature, and interparticle forces of particles, changes in structural parameters (e.g., porosity, permeability, and specific surface area at any time interval of the process). These parameters are obviously unachievable through experimental works.

4.1. Pressure drops

The pressure drop across the carbon anode is one of the critical parameters for the design of a plan related to the operational conditions and flow distribution. It leads to the formation of convection term and increased consumption of anode. The concentration and pressure profiles in line with the reactor's radial and axial coordinates are provided using the numerical model presented in this research. The reactor's wall temperature remains fixed at 1233 K, which favors the Boudouard reaction [3]. The manometer monitors the pressure drop along the anode particle bed, and the pressure-drop results from the model are compared with the experimental ones by using those plotted against gas velocity in three ratios of the bed diameter per particle diameter (d/dp), as depicted in Fig. 5a. Results from the figure and the calculated ones confirm good agreement between the experimental data of the model ($R^2 = 98.95$). With increased particle size, less pressure drop occurs for an identical gas velocity. This status may be due to the lower gas velocity in the distance between the anode's particles with an equal flow rate over the larger particles, where the local void fractions remain larger than the smaller ones. Additionally, the pressure drop rises with increased superficial gas velocity for all ratios (d/dp). A decrease in the ratio can stem from a nonuniform flow that exerts a bypass effect throughout the bed of particles because the wall effects stay paramount at a low gas-flow rate [47,48]. By contrast, for a high ratio d/dp of 24, the near-wall bypass flow effect can be found at larger gas velocities ($v > 0.3$ $m{\cdot}s^{-1}$), satisfying the conditions linked to the bed's turbulent-flow regime [49]. To better design large-scale anode particles, these behaviors seem excessively practical. However, the impact of porosity remains dominant at high flow rates. A lower porosity confers difficulty in fluid penetration into the bed, so a higher pressure drop occurs.

Fig. 5b shows that the pressure drop as a function of the Reynolds number (Eq. (31)) decreases for simulations containing and lacking chemical reactions. According to the result, by applying the chemical reaction, the pressure drop increases for all ranges of Re. Considering that gasification is known as an exothermic reaction, gas properties change with increased temperature and affects the Re. The transition Re_e number between the laminar and turbulent regimes Re_e is based on the average interstitial velocity and on the characteristic length scale of the pores, so the limitation of laminar flow for a porous fixed-bed reactor is relatively low. Proper fitting between the experimental and model data in the laminar regime occurs ($Re_e \leq 1$). For larger Reynolds numbers ($Re_e > 5$), a slight overestimate of the pressure drop is shown by the model for turbulent regimes [47,50] This effect can be due to the flow channeling that occurs in the bed and increases with increased flow rate

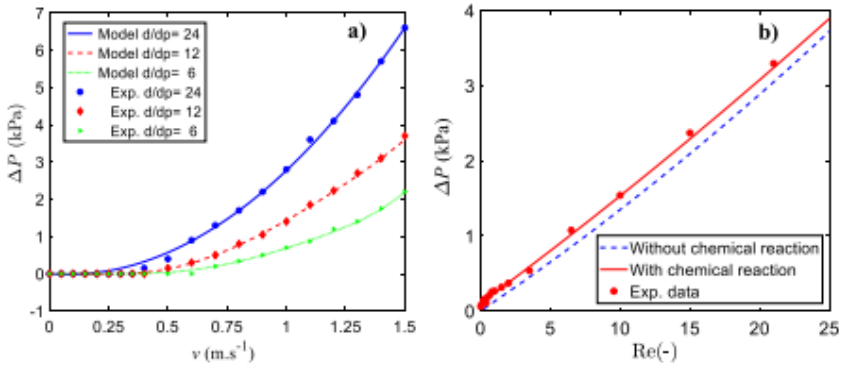

Fig. 5. a) Pressure drops of the model compared with experiments against gas for three ratios of D/dp. b) Pressure drop as a function of effective Reynolds numbers for simulations with and without chemical reactions (R = 6 mm, H = 5 cm, T = 1233 K).

[49].

4.2. Diffusion-coefficient dependence on mass transfer

To determine the dependence of the CO_2 outlet concentration on gas velocity with/without mass-transfer limitation, Fig. 6 is plotted in the outlet gas. Fig. 6 shows the mass-transfer limitations in the outlet gas according to the model results. A notable difference exists between C_{CO_2} conversion with and without mass-transfer limitations. With mass-transfer limitations, the velocity dependence on the outlet concentration of C_{CO_2} remains weak. With increased velocity, the thin gas film surrounding the anode particles decreases, so the mass-transfer limitations become less important. Eventually, the two plots approach each other as the velocity increases, and the outlet concentration becomes less dependent on the mass-transfer limitations.

Fig. 7 depicts simulation results of the outlet C_{CO_2} dependence on the mass-transfer coefficient for a 0.2 $m{\cdot}s^{-1}$ entrance velocity. i.e., a medium-velocity level in the laminar flow in the fixed-bed reactor. With increased mass-transfer coefficient, the outlet C_{CO_2} decreases. This situation underlies the rationale that a higher C_{CO_2} from the bulk concentration approaches the surfaces of anode particles and reacts. With increased mass-transfer coefficient, the concentration advances from the bulk toward the surface and becomes the reaction's driving force.

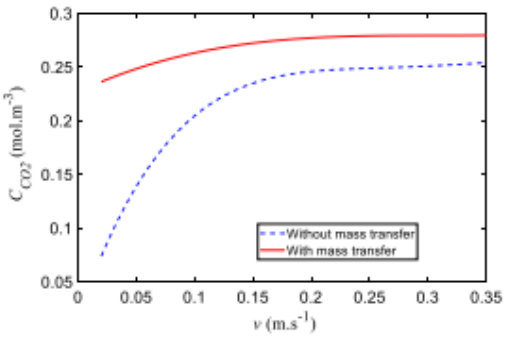

Fig. 6. Mass-transfer limitations in the outlet gas (r = 1 mm, R = 6 mm, H = 5 cm, T = 1233 K).

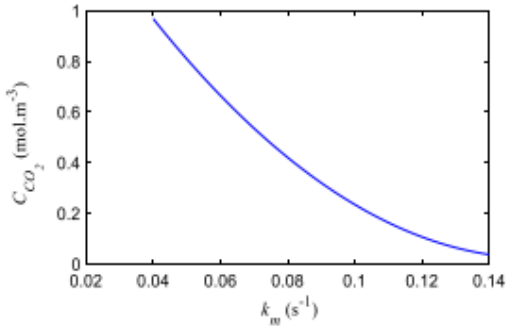

Fig. 7. Outlet C_{CO_2} dependence on the mass-transfer coefficient for 0.2 $m{\cdot}s^{-1}$ velocity (r = 1 mm, R = 6 mm, H = 5 cm, T = 1233 K).

4.3. Concentration distribution

After model verification, one of the major applications is used to predict the concentration distribution in the carbon anode. The superiority of this model is the prediction of gas-component concentration in the particle size (microscale) and between the particle (macroscale) in the fixed-bed reactor simultaneously at each time and position. Fig. 8 shows the simulation results of the molar concentrations of the gas species with CO_2 (Fig. 8a) and CO conversion (Fig. 8b) along the reactor length. With decreased CO_2 concentration, that of CO drastically increases at an extremely close distance to the reactor entrance. These results demonstrate that CO2 and CO are distributed inside a particle in the middle of the bed and their concentration plots within the particle. Evidently, the concentration close to the center of the particle is higher for CO, where products form and diffuse into the bulk gas from this specified location. In contrast to the reactant gas, the CO2 concentration is small at the center and approaches the bulk concentration on the surface. Fig. 8 verifies the general trends observed in the reactor. The CO_2 molar concentration progressively decreases as the gas stream passes through the bed, whereas the CO concentration increases through the Boudouard reaction.

Fig. 9 shows the simulation results of CO_2 concentrations inside the particle at various reactor positions. The CO_2 concentration is lower at the particle's center than at all reactor positions. In other words, the performance of the reactor is constrained by diffusion inside the particle, and the active porous material in the center of the particle is not

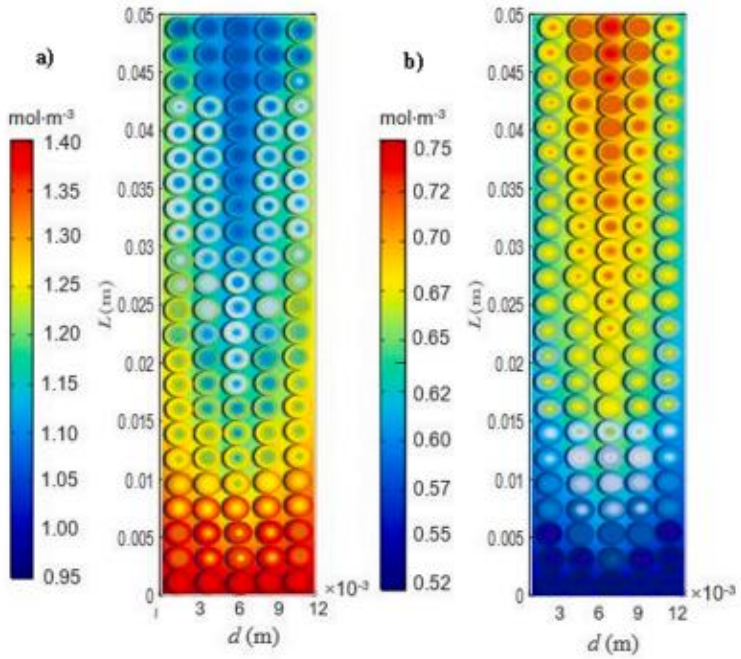

Fig. 8. Molar concentrations of gas species in the vertical fixed-bed reactor (inlet gas input from the bottom of the reactor: a) CO_2 and b) CO conversion along the reactor length (r = 1 mm, Q = 1 L·min^{-1}, H = 5 cm, T = 1233 K).

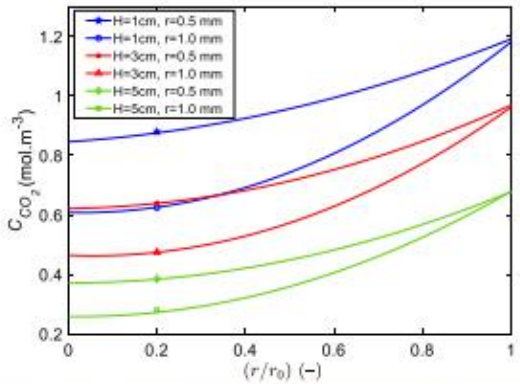

Fig. 9. CO_2 concentration (inside the particle) at various reactor positions. (Q = 1, R = 6 mm L·min^{-1}, H = 5 cm, T = 1233 K).

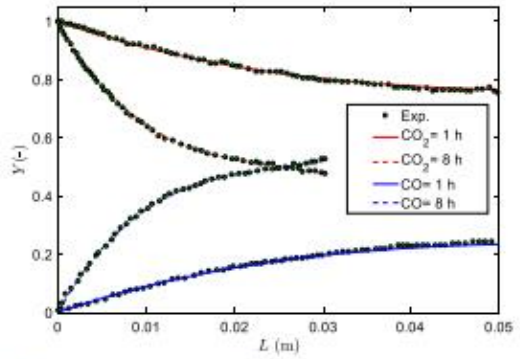

Fig. 10. Comparison of the model to the experimental data along the reactor length at different processing times (r = 1 mm, flow rate = 1 L·min^{-1}, bed height = 5 cm, temperature = 1233 K).

consumed. Decreasing the particle diameter can avert this limitation. For a particle radius of 1 mm, the intraparticle diffusion limits the reactor because the active sites in the particle interior are not used to their fullest potential, as shown by the slope of the solid lines. With decreased particle size (0.5 mm), the lines level out more quickly, implying greater reaction-rate-limited regions.

Fig. 10 compares the computed results with the experimental ones. The profiles show that the degree of conversion dramatically increases from the start of the reaction until it reaches approximately 0.60 and 0.4 for CO_2 at 1 L·min^{-1} flow rate. Accordingly, the reaction advances very slowly until full conversion. Initially, the fast-increasing conversion can be directly attributed to the rapid evolution of the surface area until the pores collapse. In this status, either the reaction surface or the reaction rate decreases. The dash line shows the distribution concentrations after 8 h. The particles have shrunk, so the total bed height decreases to 3 cm. The slopes are steeper because of the reactive particles' surfaces. The results indicate good agreement between the calculated and experimental data (R^2 = 0.9921), and the model can provide highly reliable estimates of experiments.

4.4. Specific surface area and porosity

The model allows the tracking of the evolution of the specific surface area throughout gasification in each time and position of the fixed-bed reactor. Fig. 11 shows the variations in surface area versus the bed position for four anode particles (1 mm particle size) in the different process periods. As indicated in the figure, the surface increases rapidly at the beginning during gasification and approaches the highest point (1, 2, and 4 h). The anode particle surface remarkably rises to 10% of the initial surface area after 1 h. The maximum surface point proceeds from top to bottom after 4 h and then starts to decrease. Different zones exist in the reactor with different values of chemical-reaction rate and mass transfer, so the structural parameters of the particles will not remain unchanged throughout the process. In this model evolution of specific surface area performed by RPM equation in the chemical reaction term because RPM can indicate the nature of pore structure, and pore-volume distribution. At the first time step, the increase in the surface area may be due to surface reactions [33,51,52]. As the reaction proceeds, the specific surface area initially increases with increased pore radii, and pores smaller than 1 nm open gradually. Conversely, they decrease at the next step possibly because of the appearance and coalescence of pores [53,54].

Porosity is found to change with particle position in the fixed-bed reactor, as shown in Fig. 12. To avoid edge effects, the first and last layers of particles are not taken into consideration.

The figure shows the volume fraction at each cross-section of the particle bed at various periods along with the bed height. In the first-time steps, no notable porosity change occurs with bed height. After a while, porosity increases with time at each position. Additionally, the porosity in each time step evidently has a maximum amount at the bottom of the reactor, which can be related to more available active sites for the reaction at the bottom of the reactor. Thus, the slope of the porosity changes drastically in this zone and decreases at the top of the particle bed. These results demonstrate that after a 12 h gasification reaction, >90% of the solid particle is consumed. This consumption includes internal and external gasification, leading to the shrinkage of particles and bed height. The bed height reaches 0.01 after 12 h.

The distributions of external and internal gasification are shown in Fig. 13 for various particle sizes during gasification. Simulation results show that in the initial steps, internal gasification is dominant for all particle sizes, but over time, the sizes decrease rapidly as the reaction progresses. Increasing the external gasification can be related to improving the outer surface of the anode particle by reaction progress. F. Chevarin et al. [3] reported that the external surface increases because of two factors. First, after gasification progresses, the particles shrink, increasing the ratio of the external surface to the particle volume.

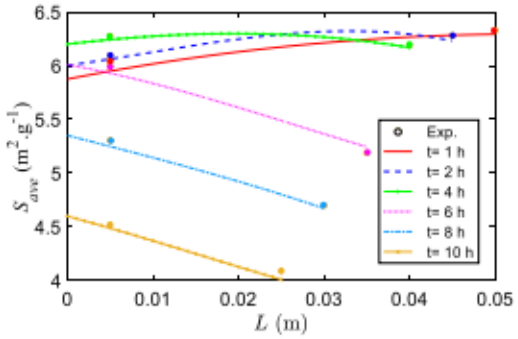

Fig. 11. Variations in surface area versus bed position of four anode particles (r = 1 mm, Q = 1 L·min^{-1}, H = 5 cm, T = 1233 K) throughout the different process periods.

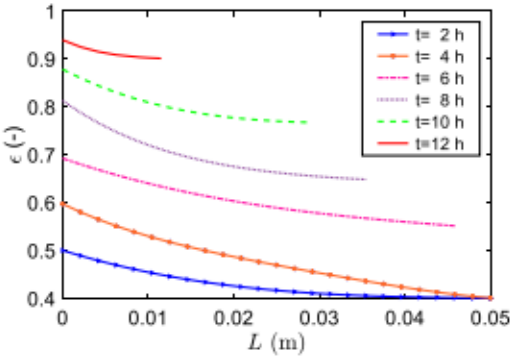

Fig. 12. Porosity changes with particle position (r = 1 mm, Q = 1 L·min^{-1}, H = 5 cm, T = 1233 K).

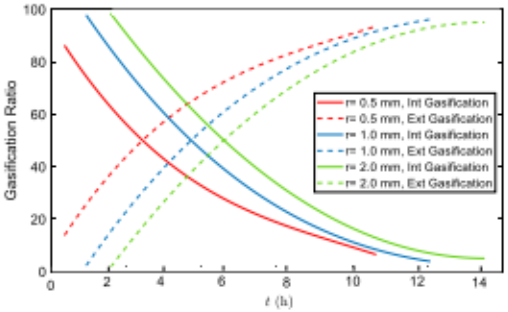

Fig. 13. Ratios of internal and external gasification versus the processing time for three different particle sizes (Q = 1 L. min^{-1}, H = 5 cm, T = 1233 K).

Second, the enlargement of pores near the external surface after a certain processing step is evaluated as the external surface, leading to increased external gasification.

4.5. Effectiveness factor

Effectiveness factor is a measure used to compute the minimum ratio of the reaction rate owing to the particles' pore-diffusion resistance [55]. The kinetic model results reveal that anode-particle gasification depends on anode conversion. The effectiveness factor is almost 0.95 for particle sizes less than 0.05 mm, with X = 0.60 at the reactor center and upwards, but it is lower for greater particle sizes (Table 2). The diffusion rate is recommended to be equal to the reaction rate. A significant difference exists for large size particles (2.0 mm) than for small ones.

Table 2
Effectiveness factor for different particle sizes and anode conversions.

Radius (mm)	Reaction rate	Carbon conversion %				
		0	20	40	60	80
0.05	First order	0.81	0.85	0.89	0.94	0.98
	L-H	0.75	0.79	0.86	0.93	0.97
0.5	First order	0.49	0.64	0.79	0.88	0.94
	L-H	0.44	0.60	0.75	0.86	0.93
1.0	First order	0.45	0.63	0.77	0.87	0.93
	L-H	0.38	0.57	0.71	0.81	0.90
2.0	First order	0.43	0.59	0.74	0.86	0.92
	L-H	0.36	0.53	0.68	0.81	0.89

The distributions of the effectiveness factor in a fixed-bed reactor at multiple heights are presented in Fig. 14. The factor fluctuates at around 0.900–0.959. For the first and second steps, it gradually increases from the wall to 0.001 m distance and decreases from 0.001 m to the reactor center, where the lowest value emerges. According to the definition of effectiveness factor, the control of gasification follows the reactants' mass-fraction distributions because the temperature gradient inside the particles is not included. Taking the comparatively small temperature near the wall at the fixed-bed reactor's center, a relatively low reaction remains. By distancing the fluid from the wall and increasing the temperature gradually, the temperature that positively affects the intraparticle transfer exceeds the value shown for the reaction rate. The concentration gradient within the anode particles is weakened by continuing this process, so the effectiveness factor increases with increased distance from the wall [27]. However, nearer to the reactor's center, a higher temperature increases the reaction rate. At 0.001 m distance from the reactor's wall, the reaction rate is positively affected by temperature exceeding that for intraparticle transfer, which in turn causes the enhancement in concentration gradient within the particles. Hence, the effectiveness factor decreases when approaching the center of the reactor. As a result, Fig. 14 shows the reverse trend of the effectiveness factor. Additionally, at a height of 0.030 m, the maximum temperature causes the effectiveness factor to be minimized at the center of the reactor.

4.6. Temperature profiles

Figs. 15 and 16 exhibit the temperature distributions at various positions and directions (axial and radial). Fig. 15 demonstrates that the hotspot is located close to the reactor exit. Prior to the hotspot, the solid temperature is higher than that of the gas because of the solid's warm-up effect on the feed gas. This phenomenon is reversed after the hotspot as heat transfers from gas to solid; in the vicinity of the hotspot, gas temperature increases rapidly, although the solid temperature changes fairly slowly [21,49,52,56]. Based on Fig. 16, the temperature increases at the center and decreases on both sides in a parabolic manner because of the wall heat sinks. The solid temperature is remarkably higher than the gas temperature before the hotspot, whereas it is lower after the hotspot. Furthermore, Fig. 16 shows a noticeable temperature change in the gas phase, although a small temperature change can be observed solely in the solid phase [57]. In practical applications, the above temperature variations are due to the much higher thermal-conductivity performance and heat capacity of the solid phase than those of the gas phase.

Fig. 17a–c demonstrate the simulation outcomes at multiple flow rates. The hotspot temperature rises as flow rates increase. Moreover, the outlet temperature increases slightly. Whenever the volume flow rate of the material increases, the Reynolds number in the bed significantly increases. Consequently, the axial and radial heat-transfer rates to

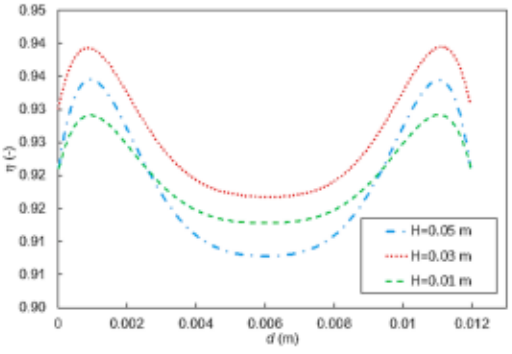

Fig. 14. Effectiveness factor distribution in the radial-bed direction for different bed heights. (r = 1 mm, R = 6 mm, Q = L·min^{-1}, T = 1233 K).

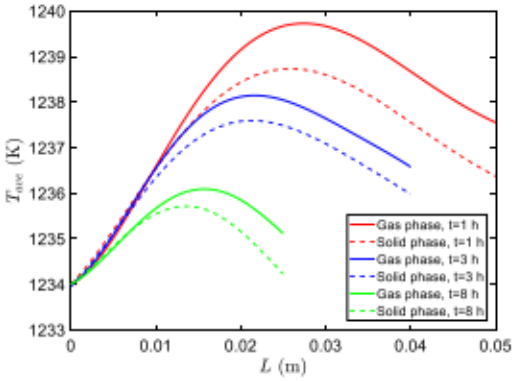

Fig. 15. Temperature profiles in the reactor. Temperature distributions along the axial direction of the reactor (r = 1 mm, Q = 1 L·min^{-1}, H = 5 cm, T = 1233 K).

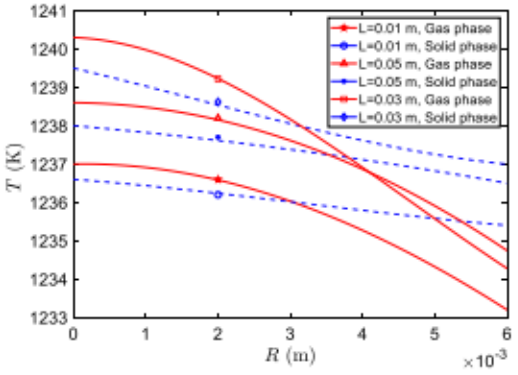

Fig. 16. Temperature profiles in the reactor. Temperature distributions along the radial direction of the reactor (r = 1 mm, Q = 1 L·min^{-1}, H = 5 cm, T = 1233 K).

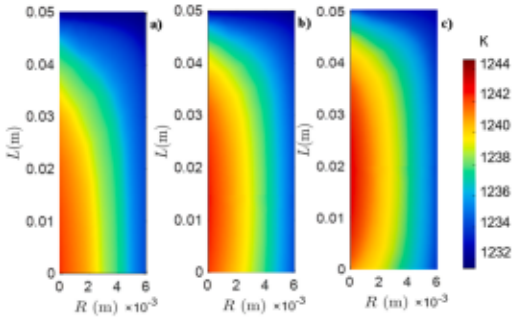

Fig. 17. Temperature distribution of the hotspot at multiple flow rates: a) 0.5 L·min^{-1}, b) L·min^{-1} and c) 2 L·min^{-1} (r = 1 mm, R = 6 mm, Q = 1 L·min^{-1}, H = 5 cm, T = 1233 K).

increase, whereas the radial-temperature difference and hot-spot temperature decrease to their original value.

4.7. Particle shrinkage

Fig. 18 illustrates the evolving particle size during the process through the shrinkage effect. As expected, the particle size is fixed and identical to the initial value at any point inside the domain when no shrinking exists. By contrast, the particle size decreases with gasification progress. Similar to the apparent density, the particle shrinkage's greatest gradient is observed near the inlet area where the reactions primarily occur. The simulation reveals that the mean particle diameters decrease to 3 mm after 10 h at the reactor's bottom side. As a consequence of particle shrinkage, they fall and the height of the bed begins to decrease throughout gasification.

4.8. Particle tracking

The movement trajectory for selected particles is shown in Fig. 19. The moving direction of the particle changes and falls into the bed because of gas–particle interactions, particle–particle collisions, and boundary effects in the vicinity of the bed top [23]. Fig. 19 compares the tracking at multiple flow rates. The figures show that for a smaller particle size r = 0.5 mm (Fig. 19a and b), either the passing direction or processing time remains lower than those of other tests (9 h). Clearly, with increased flow rate, the passing direction and processing time decrease (Fig. 19c and d). In each figure, particle tracking is simulated in three different bed positions. The particles existing in the reactor's central position vanish in less time and tracing pad, which may stem from a higher chemical reaction in such regions.

5. Conclusion

This research addresses the development of a reaction-transport model to simulate anode CO_2-reactivity dynamics using the FEM-DEM model. To explain the gasification process of anode particles within a fixed-bed gasifier, mass, heat transfer, and momentum equations were used. A particle-shrinkage pattern was rigorously applied to determine how density and size variation affect the main performance parameters, such as specific surface area, particle porosity, carbon anode conversion, and process time of the fixed bed. CO_2 and CO concentration distributions inside particles and throughout the bed were analyzed, and simulations of gas velocity and pressure were conducted. With increased flow rate, gasification time decreased. Results revealed that conversion drastically increased in the reaction's early stages. The gas distribution showed that the maximum change occurred in the first steps, and this change was primarily due to the existing surface reactions. Accordingly, the distribution decreased owing to pore merges. Anode consumption during the process included internal and external gasification and consequently led to the shrinkage of particles and bed height. In the initial steps, internal gasification was prominent; as the reaction progressed, the external gasification increased. The model results indicated that the CFD–DEM model can predict the bed scale and the complete microscale inside the particle. An inventive particle-tracking technology based on the CFD-DEM approach was illustrated in this work to quantitatively evaluate the real process time and the passing direction of particles.

CRediT authorship contribution statement

Mohammad Kavand: Conceptualization, Methodology, Software, Data curation, Writing - original draft, Visualization, Investigation, Supervision, Software, Validation, Writing - review & editing.

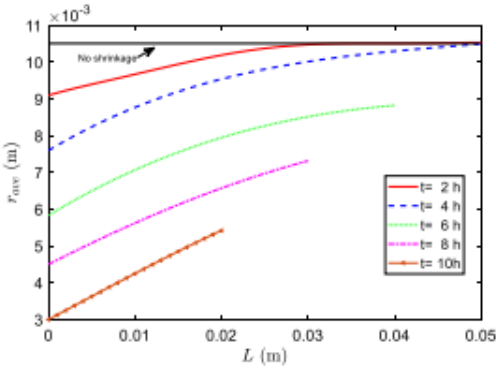

Fig. 18. Evolving particle size for the shrinking pattern (Q = 1 L. min^{-1}, H = 5 cm, T = 1233 K).

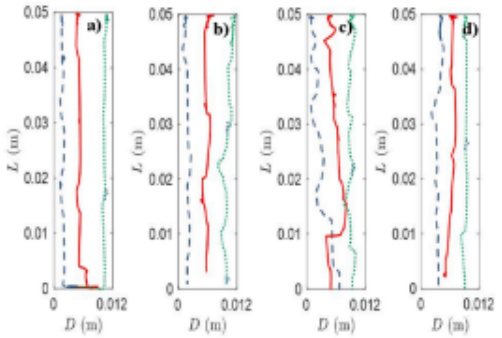

Fig. 19. Comparison of particle trajectories in the bed of particles at a) 0.5 L·min^{-1}, r = 1 mm, b) 0.5 L·min^{-1}, r = 0.5 mm, c) 1.0 L·min^{-1}, r = 1 mm, and d) 2 L·min^{-1}, r = 1 mm.

Declaration of Competing Interest

The authors declare that they have no known competing financial interests or personal relationships that could have appeared to influence the work reported in this paper.

Acknowledgments

The authors acknowledge the financial support of Alcoa and the Aluminium Research Centre-REGAL. The authors would like to express their appreciation to Guillaume Gauvin for his technical support.

References

[1] Azari K. Investigation of the materials and paste relationships to improve forming process and anode quality, Metallurgy and Materials Department. PhD. Canada: Laval University; 2013.
[2] Chevarin F. Relation entre les propriétés physico-chimiques de l'anode en carbone et sa vitesse de réaction sous CO_2. Metallurgy and Materials Department. PhD. Canada: Laval University; 2015.
[3] Chevarin F, Azari K, Lemieux L, Ziegler D, Fafard M, Alamdari H. Active pore sizes during the CO_2 gasification of carbon anode at 960°C. Fuel 2016;178:93–102. https://doi.org/10.1016/j.fuel.2016.03.044.
[4] Chevarin F, Azari K, Ziegler D, Gauvin R, Fafard M, Alamdari H. Substrate effect of coke particles on the structure and reactivity of coke/pitch mixtures in carbon anodes. Fuel 2016;183:123–31. https://doi.org/10.1016/j.fuel.2016.06.070.

[5] Chevarin F, Lemieux L, Ziegler D, Fafard M, Alamdari H. Air and CO2 reactivity of carbon anode and its constituents: an attempt to understand dusting phenomenon. Light Metals 2015. Springer; 2015, p. 1147–52.
[6] Engvoll MA. Reactivity of anode raw materials and anodes for production of aluminium. Science and Engineering. PhD. Norway: the Norwegian University of science and technology (NTNU); 2001.
[7] Houston G, Øye H. Consumption of anode carbon during aluminium electrolysis. Aluminium 1985;61(5):346–9.
[8] Sadler BA, Algie SH. Porosimetric study of sub-surface carbony oxidation in anodes. TMS. New Orleans, LA, USA: Minerals, Metals & Materials Soc 1991.
[9] Fedkiw RP. Coupling an Eulerian fluid calculation to a Lagrangian solid calculation with the ghost fluid method. J Comp Phys 2002;175(1):200–24. https://doi.org/10.1006/jcph.2001.6935.
[10] Jiang Y, Khadilkar MR, Al-Dahhan MH, Dudukovic MP. CFD modeling of multiphase flow distribution in catalytic packed bed reactors: scale down issues. Catal Today 2001;66(2):209–18. https://doi.org/10.1016/S0920-5861(00)00642-8.
[11] Potapov AV, Hunt ML, Campbell CS. Liquid–solid flows using smoothed particle hydrodynamics and the discrete element method. Powder Technol 2001;116(2–3):204–13. https://doi.org/10.1016/S0032-5910(00)00395-8.
[12] Salmi T, Warna J. Modelling of catalytic packed-bed reactors—comparison of different diffusion models. Comput Chem Eng 1991;15(10):715–27. https://doi.org/10.1016/0098-1354(91)85017-O.
[13] Thomas JR, Fucher F. Thermal modeling of microwave heated packed and fluidized bed catalytic reactors. J Microwave Power 2000;35(3):165–74. https://doi.org/10.1080/08327823.2000.11688433.
[14] Wehinger G, Eppinger T, Kraume M. Detailed numerical simulations of catalytic fixed-bed reactors: heterogeneous dry reforming of methane. Chem Eng Sci 2015;122:197–209. https://doi.org/10.1016/j.ces.2014.09.007.
[15] Singhal A, Cloete S, Quinta-Ferreira R, Amini S. Multiscale modeling of a packed bed chemical looping reforming (pbclr) reactor. Energies 2017;10(12):2056. https://doi.org/10.3390/en10122056.
[16] Fç L, Iliuta I, Bellkacemi K. Catalytic wet air oxidation with a deactivating catalyst analysis of fixed and sparged three-phase reactors. Catal Today 2001;64(3):309–20. https://doi.org/10.1016/S0920-5861(00)00534-4.
[17] Larachi Fç, Cassanello M, Laurent A, Midoux N, Wild G. Gas–liquid interfacial areas in three-phase fixed bed reactorsIPaper presented by André laurent at the 12th International Congress of Chemical and Process Engineering CHISA 1996, Praha, Czech Republic, 25-30 August, 1996.1. Chem Eng Process 1997;36(6):497–504. https://doi.org/10.1016/S0255-2701(97)00028-7.
[18] Ortiz-Arroyo A, Larachi F, Grandjean BPA, Roy S. CFD modeling and simulation of clogging in packed beds with nonaqueous media. AIChE J 2002;48(8):1596–609. https://doi.org/10.1002/(ISSN)1547-5905.10.1002/aic.v48:810.1002/aic.690480803.
[19] Valkov B, Rycroft CH, Kamrin K. Eulerian method for multiphase interactions of soft solid bodies in fluids. J Appl Mech 2015;82(4):041011. https://doi.org/10.1115/1.4029765.
[20] Pastopour B, Dixon AG. Integrated multiscale modeling of fixed bed reactors: studying the reactor under dynamic reaction conditions. Chem Eng J 2019;377:119738. https://doi.org/10.1016/j.cej.2018.08.124.
[21] Gao X, Zhu Y-P, Luo Z-H. CFD modeling of gas flow in porous medium and catalytic coupling reaction from carbon monoxide to diethyl oxalate in fixed-bed reactors. Chem Eng Sci 2011;66(23):6028–38. https://doi.org/10.1016/j.ces.2011.08.031.
[22] Hou Q, E D, Yu A. Discrete particle modeling of lateral jets into a packed bed and micromechanical analysis of the stability of raceways. AIChE J 2016;62(12):4240–50. https://doi.org/10.1002/aic.15358.
[23] Xu X, Li T, Lovas T. CFD-DEM simulation of biomass gasification with steam in a fluidized bed reactor. Chem Eng Sci 2015;122:270–83. https://doi.org/10.1016/j.ces.2014.08.045.
[24] Rabbani S, Sassi M, Shamim T. Modeling of hydrodynamics of fine particles deposition in packed-bed reactors. J Comput Multiphase Flows 2017;9(4):157-68. https://doi.org/10.1177/1757482X17716045.
[25] Wolfrum C, Josten A, Götz P. Optimization and scale-up of oligonucleotide synthesis in packed bed reactors using computational fluid dynamics modeling. Biotechnol Progress 2014;30(5):1048–56. https://doi.org/10.1002/btpr.1966.
[26] Wang L, Wu C, Ge W. Effect of particle clusters on mass transfer between gas and particles in gas-solid flows. Powder Technol 2017;319:221–7. https://doi.org/10.1016/j.powtec.2017.06.046.
[27] Huang K, Lin S, Wang J, Luo Z. Numerical evaluation on the intraparticle transfer in butylene oxidative dehydrogenation fixed-bed reactor over ferrite catalysts. J Ind Eng Chem 2015;29:172–84. https://doi.org/10.1016/j.jiec.2015.04.001.
[28] Petera J, Nowicki L, Ledakowicz S. New numerical algorithm for solving multidimensional heterogeneous model of the fixed bed reactor. Chem Eng J 2013;214:237–46. https://doi.org/10.1016/j.cej.2012.10.020.
[29] Pozzetti G, Jasak H, Besseron X, Rousset A, Peters B. A parallel dual-grid multiscale approach to CFD–DEM couplings. J Comput Phys 2019;378:708–22. https://doi.org/10.1016/j.jcp.2018.11.030.
[30] Santana ER, Pozzetti G, Peters B. Application of a dual-grid multiscale CFD-DEM coupling method to model the raceway dynamics in packed bed reactors. Chem Eng Sci 2019;205:46–57. https://doi.org/10.1016/j.ces.2019.04.025.
[31] Zhu Y-P, Chen G-Q, Luo Z-H. Iterative multiscale computational fluid dynamics-single-particle model for intraparticle transfer and catalytic hydrogenation reaction of dimethyl oxalate in a fluidized-bed reactor. Ind Eng Chem Res 2013;53(1):110–22. https://doi.org/10.1021/ie403227z.
[32] Ziaasi M, Ghafouri Roozbahani MA, Khandan N. New method of rigorous modeling and CFD simulation for methanol—steam reforming in packed-bed reactors. Chem Eng Commun 2016;203(10):1359–73. https://doi.org/10.1080/00986445.2016.1198333.
[33] Norouzi HR, Zarghami R, Sotudeh-Gharebagh R, Mostoufi N. Coupled CFD-DEM modeling: formulation, implementation and application to multiphase flows. John Wiley & Sons; 2016.
[34] Dixon AG, Taskin ME, Nijemeisland M, Stitt EH. CFD method to couple three-dimensional transport and reaction inside catalyst particles to the fixed bed flow field. Ind Eng Chem Res 2010;49(19):9012–25. https://doi.org/10.1021/ie100298q.
[35] Gómez-Barea A, Ollero P. An approximate method for solving gas-solid non-catalytic reactions. Chem Eng Sci 2006;61(11):3725–35. https://doi.org/10.1016/j.ces.2005.12.023.
[36] Gudekar KG. Modeling, control, and optimization of fixed bed reactors, Chemical Engineering Department. PhD. Texas Tech University; 2002.
[37] Bird RB, Stewart WE, Lightfoot EN. Transport phenomena. Wiley; 2006.
[38] Gómez-Barea A, Ollero P, Arjona R. Reaction-diffusion model of TGA gasification experiments for estimating diffusional effects. Fuel 2005;84(12–13):1695–704. https://doi.org/10.1016/j.fuel.2005.02.003.
[39] Kavand M, Mollaabbasi R, Ziegler D, Larachi F, Picard D, Alamdari H. Reaction–diffusion model for gasification of a shrinking single carbon-anode particle. ACS Omega 2021. https://doi.org/10.1021/acsomega.0c05297.
[40] Xu Q, Pang S, Levi T. Reaction kinetics and producer gas compositions of steam gasification of coal and biomass blend chars, part 2: Mathematical modelling and model validation. Chem Eng Sci 2011;66(10):2232–40. https://doi.org/10.1016/j.ces.2011.02.054.
[41] Garner FH, Grafton RW. Mass transfer in fluid flow from a solid sphere. Proc Royal Soc London Ser A, Math Phys Sci (1934–1990) 1954;224(1156):64–82. https://doi.org/10.1098/rspa.1954.0141.
[42] Gunn D, De Souza J. Heat transfer and axial dispersion in packed beds. Chem Eng Sci 1974;29(6):1363–71. https://doi.org/10.1016/0009-2509(74)80160-0.
[43] Aissa A, Abdelouahab M, Noureddine A, El Ganaoui M, Pateyron B. Ranz and Marshall correlations limits on heat flow between a sphere and its surrounding gas at high temperature. Thermal Sci 2015;19(5):1521–8. https://doi.org/10.2298/TSCI120912090A.
[44] Tamer C, Isci A, Kutlu N, Sakiyan O, Sahin S, Sumnu G. Effect of drying on porous characteristics of orange peel. Int J Food Eng 2016;12(9):921–8. https://doi.org/10.1515/ijfe-2016-0075.
[45] Kavand M, Fakoor E, Mahzoon S, Soleimani M. An improved film–pore–surface diffusion model in the fixed-bed column adsorption for heavy metal ions: Single and multi-component systems. Process Saf Environ Prot 2018;113:330–42. https://doi.org/10.1016/j.psep.2017.11.009.
[46] Pirnia P, Duhaime F, Ethier Y, Dubé J-S. ICY: an interface between COMSOL multiphysics and discrete element code YADE for the modelling of porous media. Comput Geosci 2019;123:38–46. https://doi.org/10.1016/j.cageo.2018.11.002.
[47] Abdulmohsin RS, Al-Dahhan MH. Pressure drop and fluid flow characteristics in a packed pebble bed reactor. Nuclear Technol 2017;198(1):17–25. https://doi.org/10.1080/00295450.2017.1292818.
[48] Ahmadi S, Sefidvash F. Study of pressure drop in fixed bed reactor using a computational fluid dynamics (CFD) code. ChemEngineering 2018;2(2):14. https://doi.org/10.3390/chemengineering2020014.
[49] Miroliaei AR, Shahraki F, Atashi H. Computational fluid dynamics simulations of pressure drop and heat transfer in fixed bed reactor with spherical particles. Korean J Chem Eng 2011;28(6):1474–9. https://doi.org/10.1007/s11814-010-0507-x.
[50] Jafari A, Zamankhan P, Mousavi SM, Pietarinen K. Modeling and CFD simulation of flow behavior and dispersivity through randomly packed bed reactors. Chem Eng J 2008;144(3):476–82. https://doi.org/10.1016/j.cej.2008.07.033.
[51] Taskin ME, Dixon AG, Nijemeisland M, Stitt EH. CFD study of the influence of catalyst particle design on steam reforming reaction heat effects in narrow packed tubes. Ind Eng Chem Res 2008;47(16):5966–75. https://doi.org/10.1021/ie800315d.
[52] Singhal A, Cloete S, Quinta-Ferreira R, Amini S. Verification of heat and mass transfer closures in industrial scale packed bed reactor simulations. Energies 2018;11(4):805. https://doi.org/10.3390/en11040805.
[53] Feng B, Bhatia SK. Variation of the pore structure of coal chars during gasification. Carbon 2003;41(3):507–23. https://doi.org/10.1016/S0008-6223(02)00357-3.
[54] Matsumoto K, Takeno K, Ichinose T, Ogi T, Nakanishi M. Gasification reaction kinetics on biomass char obtained as a by-product of gasification in an entrained-flow gasifier with steam and oxygen at 900–1000 C. Fuel 2009;88(3):519–27. https://doi.org/10.1016/j.fuel.2008.09.022.
[55] Mani T, Mahinpey N, Murugan P. Reaction kinetics and mass transfer studies of biomass char gasification with CO_2. Chem Eng Sci 2011;66(1):36–41. https://doi.org/10.1016/j.ces.2010.09.033.
[56] Behnam M, Dixon AG, Nijemeisland M, Stitt EH. A new approach to fixed bed radial heat transfer modeling using velocity fields from computational fluid dynamics simulations. Ind Eng Chem Res 2013;52(44):15244–61. https://doi.org/10.1021/ie4000568.
[57] Sadooghi P, Rauch R. Experimental and modeling study of catalytic steam reforming of methane mixture with propylene in a packed bed reactor. Int J Heat Mass Transfer 2014;78:515–21. https://doi.org/10.1016/j.ijheatmasstransfer.2014.06.084.